



JOHANNES GUTENBERG  
UNIVERSITÄT MAINZ

DOCTORAL THESIS

# TENSOR NETWORK SIMULATIONS WITH GLOBAL $SU(2)$ SYMMETRY

Dissertation submitted in fulfillment of the requirements  
for the degree of Doctor of Natural Sciences

to the

Department of Physics, Mathematics and Computer Science  
Johannes Gutenberg University

PHILIPP SCHMOLL

born in Oberwesel

Mainz

July 2020

Tensor Network Simulations with Global  $SU(2)$  Symmetry

PHILIPP SCHMOLL

Mainz, July 2020

# List of Publications

## Statement of Contributions to Co-Authored Works Contained in the Thesis

1. *A Programming Guide for Tensor Networks with Global  $SU(2)$  Symmetry*  
**P. Schmoll, S. Singh, M. Rizzi and R. Orús**  
 Annals of Physics **419**, 168232 (2020)  
 The implementation of  $SU(2)$  symmetry as described in the manuscript was developed by myself with support from all authors. Simulations to test and benchmark the code as well as the anyonic simulations were implemented by myself. Most of the manuscript was prepared by R. Orús and myself, including figures and plots. The project was accompanied by S. Singh and M. Rizzi at all stages, including preparation of the manuscript.
2. *Quantum Criticality on a Chiral Ladder: an  $SU(2)$  infinite DMRG Study*  
**P. Schmoll, A. Haller, M. Rizzi and R. Orús**  
 Physical Review B **99**, 205121 (2019)  
 The numerical simulations with  $SU(2)$  symmetry were developed and performed by myself. M. Rizzi worked out and prepared the section about Kadanoff coarse-graining. Exact diagonalization results were obtained by A. Haller and myself in equal parts. A. Haller generated the bosonization results and prepared the corresponding section in the manuscript. The main manuscript was composed by R. Orús and myself, with many contributions from the other two authors. R. Orús summarized the field theory results in the appendix.
3. *Fine-Grained Tensor Network Methods*  
**P. Schmoll, S. S. Jahromi, M. Hoehrmann, M. Mühlhauser, K. P. Schmidt and R. Orús**  
 Physical Review Letters **124**, 200603 (2020)  
 The implementation of the fine-PEPS algorithm as well as the associated simulations were performed by myself. S. Jahromi provided benchmarking gPEPS results and generated the final plots. All pCUT results were obtained by M. Hoehrmann, M. Mühlhauser and K. P. Schmidt. The initial manuscript was prepared by R. Orús with several contributions from all authors.
4. *Benchmarking Global  $SU(2)$  Symmetry in 2d Tensor Network Algorithms*  
**P. Schmoll and R. Orús**  
 Phys. Rev. B **102**, 241101(R) (2020)  
 All numerical simulations were developed and performed by myself, with support from R. Orús. The manuscript was initially prepared by R. Orús, and complemented by myself.
5. *A Tensor Network Study of the Classical Two-Dimensional Heisenberg Model*  
**P. Schmoll, A. Kshetrimayum, J. Eisert, R. Orús and M. Rizzi**  
 Manuscript in preparation  
 The implementation of the partition function for the classical Heisenberg model and all computations were done by myself, with support from M. Rizzi and R. Orús. Large parts of the manuscript were prepared by myself, complemented by all other authors.



*“Der Inhalt der Physik geht die Physiker an, die Auswirkungen alle Menschen.”*

Friedrich Dürrenmatt



# Zusammenfassung

## Tensornetzwerk Simulationen mit Globaler $SU(2)$ Symmetrie

Die theoretische Beschreibung und Untersuchung von Quanten-Vielteilchensystemen ist ein essentieller Bestandteil der Erforschung von Quantensystemen bei niedrigen Temperaturen, in denen das Zusammenspiel vieler individueller Teilchen zu erstaunlichen kollektiven Effekten führt. Aufgrund des exponentiellen Anstiegs der Anzahl an Parametern, die zur Beschreibung solcher Systeme nötig sind, kann ein Verständnis dieser Phänomene oftmals nur mit Hilfe numerischer Simulationstechniken gewonnen werden. In den letzten Jahren haben sich Tensornetzwerke als hochentwickelte numerische Techniken etabliert, die auf der Lokalität der Wechselwirkungen und Symmetrien von physikalischen Systemen basieren. Tensornetzwerke erfassen die genaue Struktur der Quantenkorrelationen der Vielteilchensysteme bei niedrigen Temperaturen und machen sie daher zur natürlichen Sprache, um Quantenzustände zu beschreiben und neue exotische Phasen von Quantenmaterialien zu simulieren. In dieser Dissertation werden Tensornetzwerk-Algorithmen eingesetzt, um Vielteilchensysteme auf ein-, zwei- und dreidimensionalen Gitterstrukturen zu simulieren. Die physikalischen Modelle unterscheiden sich in der Art der Wechselwirkung zwischen den Teilchen, der Geometrie des Gittersystems, sowie der lokalen Freiheitsgrade. Insbesondere untersuchen wir verschiedene Spinmodelle mit einer globalen  $SU(2)$ -Symmetrie, d.h. einer Invarianz unter einer globalen Rotation der Spins. Die Tensornetzwerke mit  $SU(2)$  Symmetrie werden für die Untersuchung eines quasi eindimensionalen Leitermodells mit chiraler drei-Spin Wechselwirkung, des bilinearen-biquadratischen Modells auf einem zweidimensionalen Rechtecksgitter und des rätselhaften antiferromagnetischen Heisenberg Modells auf einem Kagome Gitter genutzt. Unsere Untersuchungen der zuvor genannten physikalischen Modelle erlauben es, den Nutzen der Implementierung physikalischer Symmetrien in zweidimensionalen Tensornetzwerk-Algorithmen zu beurteilen. Zusätzlich stellen wir einen neuen Tensornetzwerk-Algorithmus für Gittersysteme mit hoher Konnektivität vor. Dessen Vorteile und Nützlichkeit wird Anhand von mehreren magnetischen und bosonischen Quantensystemen auf zwei- und dreidimensionalen Dreiecksgittern demonstriert. Abschließend konstruieren wir das  $SU(2)$ -invariante Tensornetzwerk, das die Partitionsfunktion des klassischen Heisenberg Modells analytisch darstellt. Unser Tensornetzwerk Ansatz erlaubt es, das Heisenberg Modell direkt im thermodynamischen Grenzfall zu simulieren und hilft dabei, die seit langem geführte Diskussion über einen möglichen Phasenübergang bei endlichen Temperaturen zu klären.





# Abstract

## Tensor Network Simulations with Global $SU(2)$ Symmetry

The theory of quantum many-body systems plays an important role in the study of quantum systems at low temperatures. In such settings the interplay of many individual constituents stimulates remarkable, collectively emergent phenomena. Due to an inherent exponential scaling of required resources in the number of constituents, insights can oftentimes be achieved only with the help of numerical simulation techniques. In recent years, tensor networks have emerged as sophisticated numerical techniques that are based on locality and symmetry, two concepts deeply rooted in physical theories. Tensor networks faithfully capture the structure and amount of quantum correlations in the system, making them the natural language to describe quantum states and study new exotic phases of matter.

In this thesis we employ tensor network algorithms in one, two and three spatial dimensions to study many-body lattice models with different kinds of interactions, lattice geometries and local degrees of freedom. In particular, we study different spin models with a global  $SU(2)$  symmetry, i.e. an invariance under a global rotation of spins that is directly incorporated into the tensor network. The algorithms are applied to study a quasi one-dimensional ladder model with chiral three-spin interaction, the bilinear-biquadratic model on a two-dimensional square lattice, and the enigmatic antiferromagnetic Heisenberg model on a Kagome lattice. Our studies of the aforementioned physical models allow us to assess the utility of implementing physical symmetries in two-dimensional tensor network algorithms. Additionally, we propose a new tensor network algorithm for lattices with high connectivity, and prove its usefulness for several magnetic and bosonic models on triangular lattices in two and three dimensions. Finally, we construct analytically the  $SU(2)$ -invariant tensor network that represents the partition function of the classical Heisenberg model. Our tensor network approach allows to study the system directly in the thermodynamic limit and helps to resolve the long-standing discussion about a possible finite-temperature phase transition.



# Contents

<b>1</b>	<b>Introduction</b>	<b>1</b>
<b>2</b>	<b>Entanglement and Tensor Networks</b>	<b>5</b>
2.1	Entanglement and Quantum Many-Body Systems . . . . .	5
2.1.1	Schmidt Decomposition and Singular Value Decomposition . . . . .	8
2.2	Quantum Phase Transitions . . . . .	10
2.3	Tensor Network Theory . . . . .	11
2.3.1	The Importance of Tensor Networks . . . . .	12
2.3.2	Tensor Network Representation of the Wave Function . . . . .	13
2.4	Matrix Product States (MPS) . . . . .	15
2.5	Projected Entangled Pair States (PEPS) . . . . .	16
2.6	Summary . . . . .	17
<b>3</b>	<b>Symmetry-Preserving Tensors</b>	<b>19</b>
3.1	Implementation of Symmetries . . . . .	19
3.2	SU(2)-Symmetric Tensors . . . . .	22
3.2.1	Fusion Trees . . . . .	23
3.2.2	Decorations of Fusion Trees with Quantum Numbers . . . . .	26
3.2.3	F-Moves . . . . .	27
3.3	Handling of Symmetric Tensors . . . . .	30
3.3.1	Reversal of Indices . . . . .	30
3.3.2	Permutation of Indices . . . . .	31
3.3.3	Reshaping of Indices . . . . .	31
3.4	Contractions of Symmetric Tensors . . . . .	33
3.4.1	Matrix-Matrix Multiplication . . . . .	34
3.4.2	General Tensor Contractions . . . . .	34
3.5	Matrix Factorizations . . . . .	37
3.5.1	Symmetric Singular Value Decomposition . . . . .	38
3.5.2	SVD Based Truncation . . . . .	38
3.6	Extension to Anyonic Theories . . . . .	39
3.7	Comments on Abelian Symmetries . . . . .	40
3.8	Summary . . . . .	41
<b>4</b>	<b>Quantum Criticality on a Chiral Ladder</b>	<b>43</b>
4.1	Motivation and Model . . . . .	44
4.1.1	Effective Low-Energy Physics with Kadanoff Coarse-Graining . . . . .	45
4.2	Density Matrix Renormalization Group . . . . .	47
4.3	Results . . . . .	50
4.3.1	Ground State Energy . . . . .	50
4.3.2	Entanglement Properties . . . . .	51
4.3.3	Correlation Functions . . . . .	54
4.3.4	Entanglement Spectrum . . . . .	56
4.4	Conclusion and Outlook . . . . .	57

<b>5</b>	<b>Global SU(2) Symmetry in 2d</b>	<b>59</b>
5.1	Tensor Network Algorithms in 2d . . . . .	59
5.2	Spin-1 Bilinear-Biquadratic Model . . . . .	61
5.2.1	Ground State Energy . . . . .	62
5.2.2	Structure of the Ground State . . . . .	64
5.3	Heisenberg Model on the Kagome Lattice . . . . .	65
5.3.1	Spin-1/2 Heisenberg Antiferromagnet . . . . .	66
5.3.2	Spin-2 Heisenberg Antiferromagnet . . . . .	70
5.4	Conclusion and Outlook . . . . .	71
<b>6</b>	<b>Fine-Grained Tensor Networks</b>	<b>73</b>
6.1	Fine-Graining of the Physical Sites . . . . .	73
6.1.1	General Fine-Graining Procedure . . . . .	73
6.1.2	Application to the Triangular Lattice . . . . .	74
6.1.3	Corner Transfer Matrix Scheme and Expectation Values . . . . .	76
6.2	Transverse-Field Ising Model . . . . .	77
6.3	Bose Hubbard Model . . . . .	79
6.4	Extension of the Fine-Graining to Three Dimensions . . . . .	82
6.5	General Comments and other Applications . . . . .	84
6.5.1	Efficiency of the Method . . . . .	84
6.5.2	Choice of Isometries . . . . .	85
6.6	Further Applications . . . . .	85
6.7	Conclusion and Outlook . . . . .	85
<b>7</b>	<b>Classical Partition Function for the Heisenberg Model</b>	<b>87</b>
7.1	The Partition Function as a Tensor Network . . . . .	88
7.1.1	Application to a 1d Chain . . . . .	88
7.1.2	Application to the 2d Square Lattice . . . . .	89
7.2	Computing the Partition Function with CTM . . . . .	91
7.3	Computation of Expectation Values . . . . .	93
7.3.1	Bond Energy . . . . .	95
7.3.2	Spin-Spin Correlations . . . . .	97
7.4	Thermodynamic Quantities . . . . .	99
7.4.1	Partition Function per Site . . . . .	99
7.4.2	Thermodynamic State Functions . . . . .	102
7.5	Discussion of the Approximations . . . . .	104
7.6	Conclusion and Outlook . . . . .	106
<b>8</b>	<b>Final Conclusion and Outlook</b>	<b>107</b>
8.1	Thesis Overview . . . . .	107
8.2	Prospects and Outlook . . . . .	109
<b>A</b>	<b>Details for Symmetric Tensors</b>	<b>111</b>
A.1	Representation Theory of SU(2) . . . . .	111
A.1.1	Irreducible Representations . . . . .	112
A.1.2	Reducible Representations . . . . .	113
A.2	Fusion Tree Transformations . . . . .	115
A.3	Construction of Matrix Product Operators . . . . .	116
A.3.1	Bilinear Interaction . . . . .	117
A.3.2	Chiral Three Spin Interaction . . . . .	119
A.3.3	Bilinear-Biquadratic Interaction . . . . .	121

<b>B</b>	<b>Tensor Network Algorithms in 2d</b>	<b>125</b>
B.1	iPEPS Simple Update . . . . .	125
B.2	Effective Environments and Expectation Values . . . . .	129
B.2.1	Mean-Field Environment . . . . .	130
B.2.2	Corner Transfer Matrix Renormalization Group Scheme . . . . .	131
B.2.3	Computation of Expectation Values using CTM Environments	135
B.3	iPESS Simple Update . . . . .	135
B.3.1	General iPESS Algorithm . . . . .	136
B.3.2	SU(2)-Symmetric iPESS Algorithm . . . . .	137
B.4	Effective Environments and Expectation Values . . . . .	138
B.4.1	iPESS Coarse-Graining . . . . .	138
B.4.2	Computation of Expectation Values using CTM Environments	139
	<b>Bibliography</b>	<b>141</b>



## Chapter 1

# Introduction

Important developments and achievements that facilitate and accelerate the evolution of mankind are often linked to new ideas and applications of fabricated materials. It is not by chance that particular eras of human evolution are named after commonly used basic materials, such as the three-age system including the Stone Age, Bronze Age and Iron Age. On a more recent time scale though, the evolution of our society has been advanced due to many groundbreaking inventions and developments of synthetic plastic materials, and even more so due to the digital revolution in the field of micro-electronic devices. Alongside, the new field of quantum information and technology is on a rise since the beginning of the 21<sup>st</sup> century, and we are currently experiencing the start of a new technological era based on quantum mechanical principles.

From a technological perspective, there is hardly anything modern society relies on more than microelectronic devices – they found their way into almost every utensil we use on a daily basis. The immense success and capabilities of available microelectronic technologies is due to the astonishing miniaturization of components. While early computer processors contained several thousand transistors, state of the art processors host several billion transistors. This trend, commonly described by Moore's law [1], is however expected to exhaust the limit of technological feasibility in the years to come. The ongoing miniaturization of electronic components also surfaces quantum mechanical effects such as the tunneling effect, that need to be controlled to avoid a stagnancy of the technological advancement. An alternative approach however would be to use those quantum effects to our advantage. New technologies that take over and pave the way for future applications could be found in quantum technologies, a flourishing field of physics and engineering. In this respect, the search for appropriate materials with suitable properties is an important step in the development of such quantum devices. Moreover, it is also possible to engineer so-called synthetic quantum matter that features the desired, tailored characteristics [2]. The quest for new materials is pursued in the field of quantum many-body physics, which has already found and produced a variety of highly complex and interesting materials with promising properties for future quantum applications.

The idea to exploit quantum effects is by no means recent, and the consequences of quantum mechanics have already been used in some of our everyday devices for more than fifty years. Particular examples are light-emitting diodes (LEDs), lasers or magnetic resonance imaging scanners (MRIs). Those systems make use of quantum mechanical effects of individual particles, such as discrete energy levels and the alignment of magnetic moments in external magnetic fields. However, quantum mechanics offers far more than just individual effects and reveals its full richness only in the setting of many-body quantum physics. While properties of the individual constituents are generally well understood, the collective behaviour of many particles

is oftentimes drastically different and far less understood. This concept of collective emergence leads to remarkable phenomena such as superconductivity, superfluidity, quantum magnetism or exotic quasi-particle excitations. The key ingredient for the stimulation and appearance of such effects is quantum entanglement, a multipartite phenomenon that describes non-local correlations and causes stunning interplay among the quantum particles. The disparity between classical and quantum physics is to be found precisely in the absence of entanglement in classical mechanics. Nowadays entanglement is even seen as a resource that will fuel the so-called *second quantum revolution*. Importantly, the most interesting effects in quantum matter are found in low-dimensional systems due to the presence of strong quantum fluctuations. One-dimensional (1d) quantum many-body systems bear a great potential of interplay between quantum objects and have helped to build a better understanding of how microscopic interactions of particles can lead to collective behaviour. In two spatial dimensions (2d) there is even a greater richness of possible effects, stimulated by the second extended dimension and the accrual of the notion of topology [3]. So-called topologically-ordered quantum states [4] could be a key ingredient for the successful implementation of quantum computation [5, 6], one of the ultimate goals in quantum technology [7]. The interest and fundamental importance of such topological phases has been highlighted by the 2016 Nobel Prize in Physics, awarded for the theoretical discovery of topological phases of quantum matter and topological phase transitions [8]. Certainly, there are also interesting properties in 3d materials that are oftentimes linked to topology. One particular instance are topological insulators, which exhibit edge or surface conductivity while being insulating in the bulk.

A proper understanding of the quantum many-body theory is crucial in order to utilize quantum phenomena to our advantage. Unfortunately, the study of quantum many-body systems is naturally impeded by the *curse of the system size*, which implies that the number of parameters required to study realistic materials scales exponentially in the number of constituents. Since the number of constituents in realistic materials is of the order of the Avogadro number  $N_0 \approx 6.022 \times 10^{23}$ , exact calculations are impossible in most cases, with only a few exceptions of exactly solvable systems. The understanding is therefore oftentimes acquired by numerical simulations of the systems under certain approximations, that can be systematically refined. Simulations are an essential tool in modern computational and theoretical research due to the great flexibility in the microscopic settings of the systems, such as local degrees of freedom (e.g. different particles), geometric structure or nature and range of the interactions. In recent years tensor networks have been developed for the description and simulation of low-dimensional quantum many-body systems [9]. They have been immensely successful due to their intrinsic structure and properties that permit to accurately capture the relevant physical information [10]. Additionally, tensor networks naturally allow the preservation of symmetries [11] which are ubiquitous in nature and hence in physical theories. For instance, the hydrogen atom, one of the few exactly solvable quantum mechanical systems, has an  $SO(4)$  rotational symmetry [12] in the non-relativistic case. In the field of condensed matter physics, and more specifically in quantum-many body physics, the systems often exhibit lattice symmetries such as invariance under (discrete) translations and rotations, particle number conservation or invariance under spin rotations. On a conceptual level the preservation of symmetries in tensor networks allows for a complete classification of gapped phases of matter in 1d [13] using Matrix Product States, and a partial classification in 2d [14]. For numerical simulations the preservation of symmetries does not only guarantee to target the correct structure of the model at hand, it also leads to a large gain in



computational efficiency. The increased computational efficiency goes hand in hand with an enhanced precision of the tensor network simulations, which in turn improves the accuracy of the results.

In this thesis we implement standard tensor network simulation techniques with a global symmetry of the Hamiltonian. While Abelian symmetries like  $U(1)$  or  $\mathbb{Z}_n$  have been used in tensor network studies for several years now, there are much fewer instances of tensor network simulations with non-Abelian symmetries, whose implementations are considerably more involved. We will focus on one of the most relevant non-Abelian symmetries in quantum mechanics, which is  $SU(2)$ . The  $SU(2)$  symmetry describes invariance under spin rotation and is inherent to many quantum many-body lattice models [15]. For instance, one of the most studied, yet most enigmatic models of frustrated quantum antiferromagnetism – the spin-1/2 nearest-neighbour Heisenberg model on the Kagome lattice – possesses an  $SU(2)$  symmetry. Its ground state is conjectured to be a type of spin liquid, which in turn provides a possible mechanism to explain high-temperature superconductivity [16]. While symmetries have been extensively and successfully leveraged in 1d tensor network simulations [17], their implementation in 2d versions fall behind due to the higher overall complexity of algorithms. In this respect, we develop a general  $SU(2)$ -symmetric tensor network framework which is used to implement  $SU(2)$ -symmetric versions of the famous Density Matrix Renormalization Group and the Projected Entangled Pair State methods. These two tensor network representations are well-established tools for the simulation of one- and two-dimensional lattice systems respectively. The symmetric tensor network framework is expected to be crucial for future studies of strongly correlated materials using tensor networks, especially when expanded to include other symmetries and products of symmetries. In the following we will outline the organization of the thesis.

In Chapter 2 we introduce general concepts of quantum many-body systems and tensor networks. In particular, we discuss the concept of quantum entanglement and its quantification with the help of the Schmidt decomposition, an important tool in tensor network algorithms. The concept of quantum phase transitions and local order parameters is introduced and exemplified for a 1d quantum Ising model. Furthermore, we introduce tensor networks, a sophisticated representation of quantum states and classical partition functions. We outline the historical development and motivation behind the technique and present two of the most prominent families of tensor network states, namely the Matrix Product State as well as the Projected Entangled Pair State.

In Chapter 3 we describe the general procedure to implement physical symmetries in tensor networks and focus on the group  $SU(2)$ . The symmetry will constrain the individual tensors, which decompose into a part that includes the remaining variational parameters and a part that is completely specified by the underlying symmetry. The symmetry part will be represented by a fusion tree, an analytic form of the Clebsch-Gordan coefficients of the group. We describe how standard tensor operations can be implemented for symmetric tensors. Furthermore, extensions to other symmetries and products of symmetries, as well as the incorporation of anyonic theories, are discussed.

Chapter 4 reports the results for a quasi-1d spin system on a two-leg ladder, that is studied with an  $SU(2)$ -invariant version of the Density Matrix Renormalization Group algorithm. A preliminary analysis with Kadanoff coarse-graining provides a first physical intuition, which is supported by numerical simulations. We study the

ground state energy, as well as different entanglement properties and correlation functions that uncover the nature of the ground state. A comparison to the entanglement spectrum of the spin-1/2 Heisenberg model in 1d reveals the Conformal Field Theory underlying the ladder model.

Chapter 5 presents the results we obtained for tensor network simulations in two spatial dimensions with  $SU(2)$  symmetry. The Projected Entangled Pair State ansatz is used to simulate a bilinear-biquadratic spin-1 Hamiltonian on the square lattice. Our results are compared to non-symmetric and  $U(1)$ -symmetric simulations. Furthermore, the Projected Entangled Simplex State ansatz is used to study a spin-1/2 and a spin-2 model on the Kagome lattice. Based on the study of the three models we evaluate the utility of implementing the symmetry in 2d tensor network algorithms.

In Chapter 6 we introduce a new tensor network algorithm for the simulation of lattices with a high connectivity, i.e. a large number of nearest-neighbour lattice sites. Reversing the established procedure of coarse-graining, our fine-graining approach represents local degrees of freedom in terms of smaller entities. A suitable transformation of this kind leads to a tensor network that is more amenable to standard simulation techniques. The utility of the proposed method is demonstrated for different magnetic and bosonic models on the 2d triangular and the 3d stacked triangular lattice. A discussion of the efficiency of the algorithms and further applications is presented.

In Chapter 7 we investigate a classical spin model by writing its partition function in terms of a 2d tensor network. In particular, we construct analytically the  $SU(2)$ -invariant tensors representing the partition function of the classical Heisenberg model, which can therefore be studied directly in the thermodynamic limit. We address the long-standing question of a finite-temperature phase transition with our tensor network approach.

Finally, the thesis is concluded in Chapter 8 and an outlook for future applications of the symmetric tensor network framework is presented. In addition to the main part of the thesis we elaborate details for  $SU(2)$ -symmetric tensors, as well as a review about the employed 2d tensor network algorithms in the appendix.

## Chapter 2

# Entanglement and Tensor Networks

Several highly interesting systems in condensed matter physics, typically involving interactions between many quantum particles, are not fully understood. Prominent examples are fractional quantum Hall states [18], topologically ordered quantum spin liquids [4] or frustrated quantum antiferromagnets [19]. Current investigations of these systems essentially rely on numerical methods which all have specific limitations. In recent years new numerical and theoretical techniques to treat those kind of problems in quantum many-body physics have been developed in the field of tensor networks. Based on quantum information concepts, tensor networks overcome many of the limitations of other methods and will be introduced in this chapter. Nowadays they have applications beyond condensed matter in related fields such as the AdS/CFT correspondence in quantum gravity, machine learning, high-energy physics or quantum chemistry [9].

### 2.1 Entanglement and Quantum Many-Body Systems

Entanglement is a quantum-mechanical property that occurs in situations where individual parts of a composite quantum system can no longer be described independently of one another. Thus the quantum state of the whole system needs to be considered and it is said to be entangled. Contrary to classical phenomena, entanglement has been a strongly debated topic after its first discussion in a paper by Einstein, Podolski and Rosen in 1935 [20]. With the construction of the famous Einstein-Podolski-Rosen paradox (EPR) they concluded that quantum mechanics was incomplete. Einstein even referred to entanglement as a "spooky action at a distance" [21]. In 1964 Bell proved that one of the key assumptions in the EPR paper, the principle of locality, is not compatible with a quantum theory. Furthermore he derived a set of Bell inequalities based on local realism and predicted a quantum theory to violate the limits in the inequalities for certain entangled systems [22]. Experimental tests of Bell's predictions showed indeed a violation of the limits, all proving that the theory of local realism is not correct [23, 24]. As a consequence, the quantum theory is complete and entanglement is a valid concept.

Nowadays entanglement is even seen both as a resource and a necessary ingredient in new technological ideas based on the principles of quantum mechanics. For instance, it makes quantum protocols such as quantum key distribution [25, 26] or the first quantum teleportation [27] experiments possible. Full quantum algorithms such as Grover's search [28] or Shor's factorization algorithm [29] are able to outperform any classical algorithms because they fall into completely different complexity classes [7]. While the lack of independence of different particles is precisely what leads to remarkable phenomena, it is also at the root of the success of tensor networks. Therefore,

we will give a more concise definition of entanglement in the following. Consider two quantum states  $|\psi_A\rangle \in \mathcal{H}_A$  and  $|\psi_B\rangle \in \mathcal{H}_B$  defined in two separate Hilbert spaces. A generic state in the composite system is an element of the tensor product of the two subspaces, i.e.

$$|\psi_{AB}\rangle \in \mathcal{H}_A \otimes \mathcal{H}_B . \quad (2.1)$$

The dimension of the composite Hilbert space  $\mathcal{H}_{AB} = \mathcal{H}_A \otimes \mathcal{H}_B$  is the product of the dimensions of the individual Hilbert spaces,  $\dim(\mathcal{H}_{AB}) = \dim(\mathcal{H}_A) \cdot \dim(\mathcal{H}_B)$ . In terms of basis states  $|i_{A/B}\rangle \in \mathcal{H}_{A/B}$ , the state  $|\psi_{AB}\rangle$  can be generally written as

$$|\psi_{AB}\rangle = \sum_{i_A=1}^{p_A} \sum_{i_B=1}^{p_B} c_{i_A, i_B} |i_A\rangle \otimes |i_B\rangle , \quad (2.2)$$

where  $p_A$  and  $p_B$  are the physical dimensions of the two subsystems respectively. Eq. (2.2) can now be used to define separable and entangled states.

### Definition of Entangled and Separable States

Given an arbitrary quantum state  $|\psi_{AB}\rangle$  of a composite system we say that the wave function is *entangled*, if it is not a product state of the wave functions of the subsystems. This implies

$$|\psi_{AB}\rangle \in \mathcal{H}_A \otimes \mathcal{H}_B \text{ is entangled} \quad \longleftrightarrow \quad |\psi_{AB}\rangle \neq |\psi_A\rangle \otimes |\psi_B\rangle . \quad (2.3)$$

In contrast the wave function is called *separable*, if  $c_{i_A, i_B} = c_{i_A} c_{i_B}$  for all values of  $(i_A, i_B)$  such that Eq. (2.2) becomes

$$|\psi_{AB}\rangle = \sum_{i_A=1}^{p_A} c_{i_A} |i_A\rangle \otimes \sum_{i_B=1}^{p_B} c_{i_B} |i_B\rangle = |\psi_A\rangle \otimes |\psi_B\rangle . \quad (2.4)$$

Due to Eq. (2.4), separable states are also called product states since they are simply a tensor product of the two quantum states of the subsystems.

In order to illustrate several concepts and relations throughout this section we consider two  $p = 2$  level systems (e.g. spin-1/2 particles) as a recurring example. For this composite system a complete set of basis states is given by the eigenstates of the Pauli  $\sigma^z$  operator as

$$\begin{aligned} \{|0_A\rangle, |1_A\rangle\} &\in \mathcal{H}_A & \{|0_B\rangle, |1_B\rangle\} &\in \mathcal{H}_B \\ \{|0_A\rangle \otimes |0_B\rangle, |0_A\rangle \otimes |1_B\rangle, |1_A\rangle \otimes |0_B\rangle, |1_A\rangle \otimes |1_B\rangle\} &\in \mathcal{H}_{AB} . \end{aligned} \quad (2.5)$$

Let us now define two paradigmatic states in the composite Hilbert space  $\mathcal{H}_{AB}$  given by

$$\begin{aligned} |\psi\rangle &= \frac{1}{\sqrt{2}} (|0\rangle |0\rangle + |0\rangle |1\rangle) , \\ |\phi\rangle &= \frac{1}{\sqrt{2}} (|0\rangle |0\rangle + |1\rangle |1\rangle) , \end{aligned} \quad (2.6)$$

where we have used a shorthand for the tensor product of two quantum states to simplify the notation. According to the definition in Eq. (2.3) we see that  $|\phi\rangle$  is an

entangled state, whereas  $|\psi\rangle$  is a separable state since it can be written as

$$|\psi\rangle = \frac{1}{\sqrt{2}} (|0\rangle|0\rangle + |0\rangle|1\rangle) = \frac{1}{\sqrt{2}} |0\rangle (|0\rangle + |1\rangle) = |0\rangle|+\rangle . \quad (2.7)$$

Here  $\{|+\rangle, |-\rangle\}$  with  $|\pm\rangle = 1/\sqrt{2}(|0\rangle \pm |1\rangle)$  are the eigenvectors of the Pauli  $\sigma^x$  operator. In this thesis we focus on bipartite entanglement only, e.g. the entanglement between two subsystems like defined above. There are however also more general concepts of entanglement for multipartite systems, like the geometric entanglement [30] or "three-way tangle" [31] for tripartite systems.

Entanglement comes as a binary concept, i.e. a quantum state can either be separable or entangled – the amount of entanglement can however be quantified. In general separability of a quantum system can be determined using a Schmidt decomposition, which will be explained in the next section. From the Schmidt decomposition we can further define a measure of entanglement known as the *von Neumann entropy*, an extension of the classical *Gibbs entropy*. It quantifies entanglement in a bipartite system as a continuous measure and is therefore also called the *entanglement entropy*. For a pure state  $|\psi_{AB}\rangle \in \mathcal{H}_A \otimes \mathcal{H}_B$  we can define the reduced density matrices for each subsystem by tracing out the degrees of freedom of the other subsystem according to

$$\rho_A = \text{tr}_B (|\psi_{AB}\rangle \langle \psi_{AB}|) \quad \rho_B = \text{tr}_A (|\psi_{AB}\rangle \langle \psi_{AB}|) . \quad (2.8)$$

The trace of a subsystem is given by  $\text{tr}_x(\cdot) = \sum_{i_x=1}^{p_x} \langle i_x| \cdot |i_x\rangle$ , for a orthonormal set of basis states  $|i_x\rangle \in \mathcal{H}_x$  and  $x = \{A, B\}$ . The von Neumann entropy for both of the subsystems is defined by

$$S(\rho_A) \equiv -\text{tr}(\rho_A \ln \rho_A) = -\text{tr}(\rho_B \ln \rho_B) \equiv S(\rho_B) . \quad (2.9)$$

The equality holds because the entanglement is only shared between two partitions, so that the entanglement entropy for each partition has to be the same. Making use of the spectral decomposition we can write the reduced density matrices as

$$\rho_i = \sum_{\alpha=1}^{\chi} \nu_{\alpha} |\alpha_i\rangle \langle \alpha_i| \quad (2.10)$$

where  $\nu_{\alpha}$  is the eigenvalue for the eigenvector  $|\alpha_i\rangle$  with  $i = \{A, B\}$  and  $\chi$  is the rank of the reduced density matrix. Inserting this equation in Eq. (2.9) yields the von Neumann entropy

$$S(\rho_A) = -\sum_{\alpha=1}^{\chi} \nu_{\alpha} \ln \nu_{\alpha} . \quad (2.11)$$

One important property of the von Neumann entropy is that it is upper bounded by

$$S(\rho_A) \leq \ln \chi . \quad (2.12)$$

In the two limiting cases of separable states and maximally entangled states it yields  $S = 0$  and  $S = \ln \chi$  respectively, as we will show below. There are also different measures for the entanglement such as the Rényi entropies

$$S_{\alpha} = \frac{1}{1-\alpha} \ln \text{tr}(\rho_A^{\alpha}) \quad \text{with } \alpha \geq 0 , \quad (2.13)$$

which approaches the von Neumann entanglement entropy for  $\alpha \rightarrow 1$  [32], or the single copy entanglement [33, 34].

### 2.1.1 Schmidt Decomposition and Singular Value Decomposition

The Schmidt decomposition can be used to compute the reduced density matrix for a bipartite system, which in turn can be used to obtain the entanglement entropy or its spectrum.

#### Theorem: Schmidt Decomposition

Given a pure quantum state  $|\psi_{AB}\rangle$  of a bipartite system with subsystems  $A$  and  $B$ , there exist orthonormal states  $|\alpha_A\rangle$  for system  $A$  and orthonormal states  $|\alpha_B\rangle$  for system  $B$  such that

$$|\psi_{AB}\rangle = \sum_{\alpha=1}^{\chi} \lambda_{\alpha} |\alpha_A\rangle |\alpha_B\rangle \quad (2.14)$$

with non-negative *Schmidt coefficients*  $\lambda_{\alpha}$  satisfying  $\sum_{\alpha} \lambda_{\alpha}^2 = 1$ . The *Schmidt rank*  $\chi$  is the number of non-zero Schmidt coefficients and  $|\alpha_A\rangle$  and  $|\alpha_B\rangle$  are called the *Schmidt vectors*.

The Schmidt coefficients are closely related to the eigenvalues of the reduced density matrix in Eq. (2.10). The relation unfolds as we use Eq. (2.8) and insert the Schmidt decomposition, which yields

$$\begin{aligned} \rho_A &= \text{tr}_B(|\psi_{AB}\rangle \langle \psi_{AB}|) = \sum_{\alpha=1}^{\chi} |\lambda_{\alpha}|^2 |\alpha_A\rangle \langle \alpha_A| , \\ \rho_B &= \text{tr}_A(|\psi_{AB}\rangle \langle \psi_{AB}|) = \sum_{\alpha=1}^{\chi} |\lambda_{\alpha}|^2 |\alpha_B\rangle \langle \alpha_B| . \end{aligned} \quad (2.15)$$

The Schmidt coefficients  $\nu_{\alpha}$  of a bipartition are therefore the square roots of the eigenvalues of the reduced density matrix for both subsystems.

Coming back to the example introduced previously we can now compute the Schmidt decomposition for the quantum states in Eq. (2.6), for which we find

$$\begin{aligned} |\psi\rangle : \quad \chi &= 1 & \lambda_1 &= 1 \\ |\phi\rangle : \quad \chi &= 2 & \lambda_1 &= \lambda_2 = 1/\sqrt{2} . \end{aligned} \quad (2.16)$$

The separable quantum state  $|\psi\rangle$  has a Schmidt rank of  $\chi = 1$ , a property which is valid for all separable states. Furthermore the entanglement entropy is given by  $S_{|\psi\rangle} = 0$  and  $S_{|\phi\rangle} = \ln 2$ , so that  $|\phi\rangle$  is a maximally-entangled state.

The Schmidt decomposition can be proven using a singular value decomposition (SVD), a mathematical tool in linear algebra to factorize real and complex matrices.

#### Theorem: Singular Value Decomposition

Any rectangular matrix  $M \in \mathcal{C}^{m \times n}$  of arbitrary size can be decomposed into

$$M = U \Lambda V^{\dagger} , \quad (2.17)$$

where  $U \in \mathcal{C}^{m \times m}$  and  $V^\dagger \in \mathcal{C}^{n \times n}$  are unitary matrices and  $\Lambda \in \mathcal{R}^{m \times n}$  is a diagonal matrix containing the singular values of  $M$ . The singular values are arranged in descending order  $\lambda_1 \geq \lambda_2 \geq \dots \lambda_r$  and  $r = \min(m, n)$ . In an economic version of the SVD the lower part of  $\Lambda$  is discarded, so that  $\Lambda$  is diagonal and square. A graphical representation of the SVD is shown in Fig. 2.1.

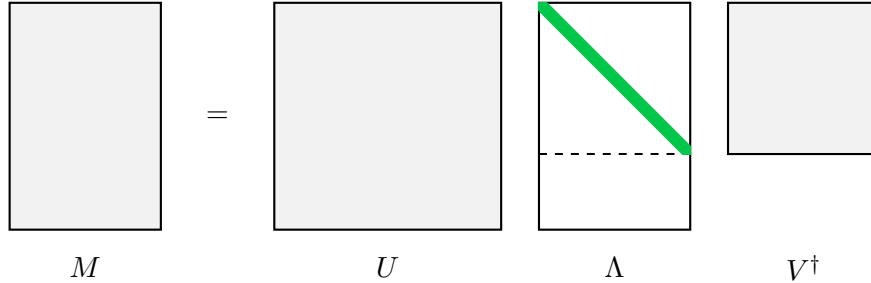


FIGURE 2.1: Graphical representation of the SVD of an  $(m \times n)$ -dimensional matrix  $M$ . The diagonal matrix  $\Lambda$  contains the singular values in descending order, indicated as a green line.

The singular value decomposition can be used to compute the Schmidt decomposition of a bipartition. Furthermore it represents an essential tool in tensor network simulations because it provides a method to extract the relevant physical information of quantum states based on their entanglement properties. Using an SVD to form a bipartition enables the approximation of quantum states by selecting the largest singular values, and therefore the most relevant part of the system in terms of contributions to the entanglement. Less important information encoded in very small singular values can be discarded to keep tensor network simulations manageable.

### Proof of the Schmidt Decomposition

Consider a system consisting of two subsystems  $A$  and  $B$ . Similarly as before, the composite quantum state can be written as

$$|\psi_{AB}\rangle = \sum_{i_A=1}^{p_A} \sum_{i_B=1}^{p_B} c_{i_A, i_B} |i_A\rangle |i_B\rangle, \quad (2.18)$$

where  $|i_A\rangle$  and  $|i_B\rangle$  are orthonormal basis states. Here  $c_{i_A, i_B}$  is a matrix containing the (complex) probability amplitudes of the expansion. Naturally, this matrix can be decomposed using an SVD so that Eq. (2.18) becomes

$$|\psi_{AB}\rangle = \sum_{i_A=1}^{p_A} \sum_{i_B=1}^{p_B} \sum_{\alpha=1}^{\chi} U_{i_A, \alpha} \Lambda_{\alpha, \alpha} V_{\alpha, i_B}^\dagger |i_A\rangle |i_B\rangle, \quad (2.19)$$

where  $\chi = \min(p_A, p_B)$ . Since  $U$  and  $V^\dagger$  are unitary matrices we can define rotated bases for subsystem  $A$  and  $B$  according to

$$|\alpha_A\rangle = \sum_{i_A=1}^{p_A} U_{i_A, \alpha} |i_A\rangle, \quad |\alpha_B\rangle = \sum_{i_B=1}^{p_B} V_{\alpha, i_B}^\dagger |i_B\rangle, \quad (2.20)$$

and with  $\Lambda_{\alpha, \alpha} = \lambda_\alpha$  the quantum state takes the form of the Schmidt decomposition as in Eq. (2.14).

## 2.2 Quantum Phase Transitions

Quantum phase transitions (QPT) describe transitions between different phases of matter at zero temperature. They are driven by quantum fluctuations and can be provoked by varying physical parameters of the system, such as the magnetic field. A transition appears at a quantum critical point (QCP), at which the energy gap between the lowest-energy state – the ground state – and the first excited state vanishes [35]. At the QCP the system is said to be critical, it exhibits scale-invariance that comes with a large amount of entanglement at all length scales.

To illustrate the phenomenon of a quantum phase transition we will briefly present the one-dimensional Ising model in a transverse field (TFIM) [36]. This example of a quantum many-body system is well-understood in condensed matter physics. It is exactly solvable and often serves as a benchmark. Consider a 1d chain of spin-1/2 degrees of freedom that are subject to nearest-neighbour interaction and a transverse magnetic field. The Hamiltonian is given by

$$H_{\text{TFIM}} = - \sum_{\langle i,j \rangle} \sigma_i^z \sigma_j^z - h_x \sum_i \sigma_i^x, \quad (2.21)$$

where  $\sigma_i^{x,z}$  are the spin-1/2 Pauli matrices for site  $i$  and  $\langle i, j \rangle$  denotes interaction between nearest neighbours, e.g. between site  $i$  and site  $j = i+1$ . The quantum phase transition occurs due to competing terms in the Hamiltonian. The first, interacting term favors parallel alignment of neighbouring spins along the  $z$ -direction to lower the total energy, due to the ferromagnetic coupling whose coupling strength is set to unity. The second term tends to align the spins parallel to the magnetic field along the  $x$ -direction to lower the total energy. Therefore tuning the strength of the transverse magnetic field  $h_x$  can drive the phase transition, as we will explain now.

Consider the two limiting cases of  $h_x = 0$  and  $h_x \rightarrow \infty$ . For  $h_x = 0$  the interacting term remains and the ground state is a product state of all spins pointing either up or down (a product state of eigenstates of the  $\sigma^z$  operator), i.e.

$$|\psi(h_x = 0)\rangle = \bigotimes_i |\uparrow\rangle_i \quad \text{or} \quad |\psi(h_x = 0)\rangle = \bigotimes_i |\downarrow\rangle_i. \quad (2.22)$$

The two-fold degeneracy reveals a  $\mathbb{Z}_2$  symmetry of the model at  $h_x = 0$  which is generally broken in the thermodynamic limit, so that one of the two ground states is selected. This is known as *spontaneous breaking* of the  $\mathbb{Z}_2$  symmetry. In the second limit  $h_x \rightarrow \infty$  the interacting term can be neglected and the ground state is a product state of  $+1$  eigenstates of the  $\sigma^x$  operator

$$|\psi(h_x \rightarrow \infty)\rangle = \bigotimes_i |+\rangle_i = \bigotimes_i \frac{1}{\sqrt{2}} (|\uparrow\rangle_i + |\downarrow\rangle_i). \quad (2.23)$$

The two ground states for the limiting cases cannot be adiabatically connected without closing the gap in the energy spectrum. Therefore a quantum phase transition occurs at the quantum critical point  $h_c$ , at which the model is gapless and critical. The QPT can be identified by a suitable *local order parameter*<sup>1</sup> that detects the spontaneous symmetry breaking. For the TFIM a possible local order parameter is the  $\sigma^z$  operator. The expectation value  $\langle \psi | \sigma^z | \psi \rangle$  should be non-zero in the ordered phase ( $h_x < h_c$ ) and zero for the disordered phase ( $h_c < h_x$ ). However not only the transition between

<sup>1</sup>There are quantum phase transitions that cannot be detected by *local* order parameters – these are called topological phase transitions (TPT).



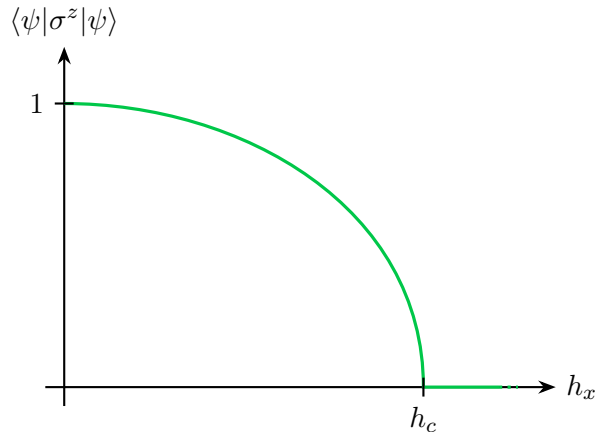


FIGURE 2.2: Sketch of the order parameter  $m_z = \langle \psi | \sigma_z | \psi \rangle$  for the 1d Ising model in a transverse field. The one-dimensional phase diagram exhibits a QCP at  $h_x = h_c$ .

different phases, but also the phases themselves can spark a lot of interest and we will investigate an example of a highly debated *spin liquid* phase in Chapter 5. In general, quantum many-body systems can also comprise more than one QPT and we will encounter models with multiple phases transitions in Chapter 6.

## 2.3 Tensor Network Theory

Numerical techniques are essential in many areas of modern research since often relevant problems are far too complex to be solved analytically. Some important problems like high-temperature superconductivity even lack a complete theoretical understanding [37], so that numerical simulations can provide tools to study these kind of systems and build that understanding. Additionally an inherent problem of quantum many-body systems is the exponential scaling of the complexity in the number of particles involved. Over time many different techniques have been developed to study a wide range of problems in condensed matter physics, but every method comes with its limitations. Exact diagonalization [38] is limited to only small systems sizes far away from the thermodynamic limit where quantum phase transitions occur, mean-field theory fails to capture very important quantum correlations between the particles in one and two dimensions and quantum Monte Carlo [39] suffers from the infamous sign problem for fermionic and frustrated systems. Certainly there are many more numerical techniques like Density Functional Theory (DFT) [40], Dynamical Mean-Field Theory (DMFT) [41], series expansion [42] or continuous unitary transformations [43], to name a few.

Tensor networks (TNs) include different families of numerical methods originally developed in the context of condensed matter physics that overcome several of the aforementioned limitations of other methods. Based on quantum information concepts, the systems are described by networks of interconnected tensors that convey the correlations in the system. Nowadays tensor networks are applied beyond their original scope of quantum many-body physics in fields like quantum chemistry [44], mathematics, machine learning [45], relations to quantum gravity [46] or even linguistics [47].

The most prominent tensor network algorithm is the Density Matrix Renormalization Group (DMRG) introduced by White [48, 49]. It is the foundation of almost all recent results for 1d gapped quantum systems and is also applied to 1d critical systems and used to study 2d systems on cylinder geometries. Besides DMRG there are various

other important tensor network algorithms to study 1d and 2d quantum matter, such as Time Evolving Block Decimation (TEBD) [50, 51], Projected Entangled Pair States (PEPS) [52], the Multiscale Entanglement Renormalization Ansatz (MERA) [53], Tree Tensor Networks (TTN) [54, 55, 56], continuous MPS [57] or MERA [58], and many more. Importantly, tensor networks also provide methods to simulate lattice systems in the thermodynamic limit without suffering from finite-size effects. Furthermore, in recent years tensor networks became more and more important to compute classical partition functions and study classical spin models with very high accuracy. In this thesis we will primarily focus on MPS and PEPS tensor networks to study 1d and 2d systems respectively. The following review on tensor networks is based on Refs. [59, 10, 60, 9].

### 2.3.1 The Importance of Tensor Networks

Tensor networks are able to simulate systems in the thermodynamic limit where phase transitions occur [35], they are able to simulate fermionic systems by including additional constraints that account for the fermionic exchange statistics and they can also handle frustration<sup>2</sup>. The only limitation inherent to tensor networks is the amount of entanglement they can capture, which translates to a limitation due to finite computational power. This makes them widely applicable and very competitive to strongly tailored methods. For instance, simulations of the 2d Hubbard model using projected entangled pair states provide one of the best variational energies to date [61].

The success of tensor network methods is not by chance. It has been noticed that they are the natural language to describe quantum states of many-body systems based on quantum information arguments. The wave function of a system of  $N$  particles lives in an exponentially large Hilbert space which sets an early limit for the approachable system sizes. Fortunately perspectives from the field of quantum information revealed very strong restrictions on the physically meaningful size of the Hilbert space. In fact, Hamiltonians of physical states appearing in nature are usually strongly constrained by locality of the interactions and symmetry – two concepts we will be using to our advantage in this thesis. For the low-energy states of local and gapped Hamiltonians in 1d one can show that the constraints are manifested in an area-law for the entanglement entropy. In 2d, this statement is even true for all temperatures. For these area-law states the entanglement entropy for any sub-region scales with the boundary  $S \sim \partial A$  between the region and its environment rather than with its volume. This is illustrated in Fig 2.3. The strong constraint of area-law entanglement confines phys-

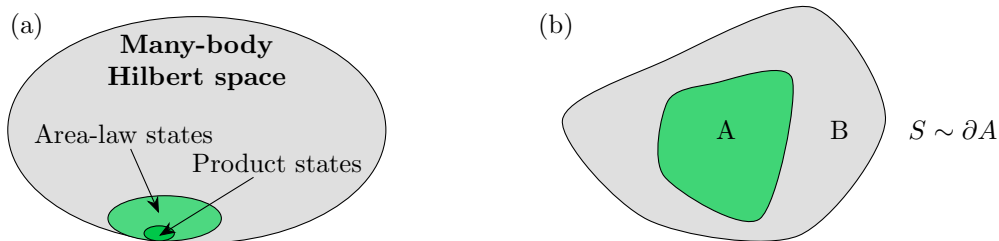


FIGURE 2.3: (a) Exponentially large Hilbert space with a tiny corner of area-law states. Most tensor networks satisfy the area-law by construction. (b) Area-law for the entanglement entropy for a region  $A$  of some general quantum system.

<sup>2</sup>Frustration in quantum lattice systems can arise due to geometric conditions (geometric frustration) or due to competing interaction terms in the Hamiltonian (exchange frustration). See Chapter 5 for details of frustration on the Kagome lattice.

ical states of quantum many-body systems to live in an exponentially small corner of the whole Hilbert space. Therefore they can often be efficiently represented in a sense that they do not need an exponential number of parameters to be accurately approximated, thus overcoming the exponential barrier.

Besides representing the physically relevant corner of the Hilbert space, tensor networks also have the correct structure of the entanglement in the system. Moreover they are beautifully simple in a sense that the physical structure is revealed naturally and everything can be drawn pictorially, as we will show in the next section.

### 2.3.2 Tensor Network Representation of the Wave Function

For our purposes a tensor is defined as a multi-dimensional array of complex numbers, whose rank is the number of its indices. A 0-index tensor is therefore a scalar, a 1-index tensor is a vector, a 2-index tensor is a matrix, and so on. We can introduce a more convenient diagrammatic representation that gives us a powerful visualization for tensor networks. Elementary tensors with up to three indices are depicted in Fig. 2.4. The ball represents the tensor, its legs represent the indices of the tensor. For now we will assume that every index of a tensor can take up to  $D$  different values,



FIGURE 2.4: Diagrammatic notation of elementary tensors up to rank-3, i.e. with at most three indices.

so that a 1-index tensor would be a  $D$ -dimensional vector, a 2-index tensor a  $(D \times D)$ -dimensional matrix and so on. Using this diagrammatic notation we can write down basic tensor operations very conveniently. Let us define an index contraction, which is a sum over all possible values of repeated indices in a tensor network. For the simple example of a matrix-matrix multiplication we have

$$C_{ik} = \sum_{j=1}^D A_{ij} B_{jk} = A_{ij} B_{jk} , \quad (2.24)$$

where we have used Einstein's summation convention in the last equation. In Eq. (2.24) one has to sum over or contract the single common index  $j$ . More complicated contractions of tensor networks could for example involve the summation over three indices as in

$$F_{ijkl} = \sum_{m,n,o=1}^D A_{ijmn} B_{mok} C_{onl} \quad (2.25)$$

resulting in a four-index tensor. This can be visualized using the pictorial representation introduced above as shown in Fig. 2.5, where the ordering of indices is fixed without following a labeling convention. Common indices in a set of tensors are the ones to contract over, unconnected or so-called open indices define the resulting rank. For simplicity we assumed that every index has a dimension of  $D$ , this is typically not the case in realistic applications. Clearly, the pictorial representation is an elegant way to write down equations in the form of Einstein's summation convention

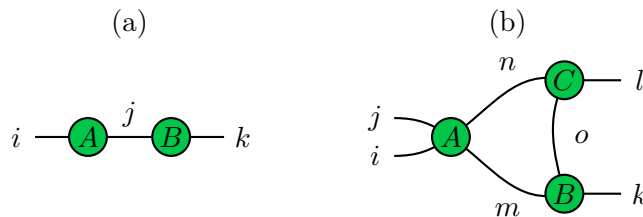


FIGURE 2.5: Example of a matrix-matrix multiplication written as a contraction in (a) and a contraction over three indices in a set of three tensors in (b), resulting in a matrix and a four-index tensor respectively. The ordering of indices is fixed and does not follow any convention in these examples.

and makes the operations directly visible. A quantum state written in the form of a tensor network will therefore directly reflect the system's entanglement structure, as we will see below.

At this point we would like to mention that the order in which contractions are performed affects the efficiency of algorithms significantly. Therefore consider the example in Fig. 2.6, a contraction of a set of four tensors. While the leading cost of the

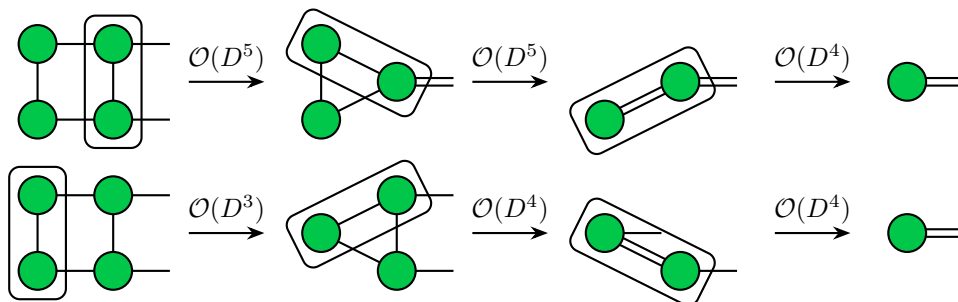


FIGURE 2.6: The order in which contractions of a tensor network are carried out is not unique and may result in different efficiencies of the overall operation. A contraction of two tensors that involves  $n$  indices has a cost that scales as the product of all  $n$  bond dimensions.

summations in the first row is  $\mathcal{O}(D^5)$ , it is only  $\mathcal{O}(D^4)$  in the second row which is therefore more efficient. A general proceeding to find the optimal contraction sequence is a very hard problem, in fact it is known to be an NP-complete problem [62, 63].

We now turn to the representation of quantum many-body states as tensor networks. The wave function for the whole composite system can be expressed as a superposition of tensor products of all the  $N$  single-particle states according to

$$|\psi\rangle = \sum_{i_1, i_2, \dots, i_N} c_{i_1, i_2, \dots, i_N} |i_1\rangle \otimes |i_2\rangle \otimes \dots \otimes |i_N\rangle . \quad (2.26)$$

Assuming that every particle lives in a finite dimensional Hilbert space  $\mathcal{H}_i$  of dimension  $p$ , the expansion has at the order of  $\mathcal{O}(p^N)$  terms. Therefore we need just as many complex coefficients  $c_{i_1, i_2, \dots, i_N}$  to represent the many-body quantum state. Those coefficients can be seen as the entries of an  $N$ -index tensor  $\mathcal{C}$ , where every index has dimension  $p$ . This tensor includes all the physical information of the quantum state, yet it is a very inefficient representation thereof due to the exponential scaling in the number of particles.

In the motivation of tensor networks we claimed that they can be an efficient representation that overcomes this exponential barrier. In what follows we will elaborate on how this is manifested in the tensor network and where this property is rooted. Tensor networks have been developed for the description and simulation for quantum lattice systems. The lattice morphology is now used to give the condensed tensor  $\mathcal{C}$  an inner structure resembling the lattice. To this end the large tensor  $\mathcal{C}$  is decomposed into smaller local tensors for the sites of the lattice, which are connected among each other. This transformation is exact and does not eliminate the exponential scaling of parameters per se. However by making the connection to the area-law for the entanglement entropy (see Sec. 2.3.1) we will explain the reduction. In the following sections we will introduce two of the most common tensor networks, Matrix Product States (MPS) in one spatial dimension and Projected Entangled Pair States (PEPS) in two spatial dimensions.

## 2.4 Matrix Product States (MPS)

Matrix Product States are one of the most famous tensor networks. They are tailored for the representation and simulation of quantum states of 1d gapped Hamiltonians with methods like the Density Matrix Renormalization Group (DMRG) [48, 49], Time-Evolving Block Decimation (TEBD) [50, 51] or variational methods like Variational Uniform MPS (VUMPS) [64]. The MPS consists of an array of local tensors, where each tensor represents a lattice site or a collection of lattice sites for the simulation of ladder systems. An examples for a six-site system with open boundary conditions is shown in Fig. 2.7. The physical indices, those that label the single particle basis

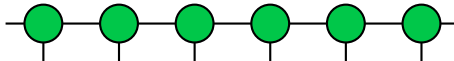


FIGURE 2.7: Matrix product state for a lattice of six sites with open boundary conditions. By connecting the first and the last site the MPS can also be used with periodic boundary conditions.

$|i_k\rangle$  with  $i_k = 1, \dots, p$  are given by the vertical tensor indices. The horizontal indices connecting the tensors are called virtual indices or bond indices and the maximum value of these indices is referred to as the *bond dimension*  $\chi$  of the MPS. For a finite MPS the number of parameters contained in the tensors is therefore  $\mathcal{O}(Np\chi^2)$ . The exponential scaling of the number of parameters  $\mathcal{O}(p^N)$  is now hidden in the bond dimension  $\chi$ , which needs to be exponentially large in order to reconstruct the exact expansion in Eq. (2.26) and explore the full Hilbert space. However, due to the constraint of the area-law it can be shown that the bond dimension  $\chi$  only scales polynomially in the system size [65] for low-energy states of gapped Hamiltonians (see also Fig. 2.3), so that MPS can really be an efficient representation of quantum states that overcomes the exponential scaling. Matrix product states obey the area-law for the entanglement entropy by construction. Forming a bipartition by cutting one link in the tensor network of an open system, the entanglement entropy is upper-bounded by the rank of the reduced density matrix. This rank is determined by the bond dimension of the cut open link, so that  $S \leq \ln \chi$  (see also Fig. 2.8). In 1d the area-law is just a constant because the area is of order  $\mathcal{O}(1)$ .

Matrix product states cannot represent quantum states of critical or gapless systems exactly, since those states violate the area-law and overshoot the capabilities of the MPS. Critical states come with a diverging correlation length and a scale-invariance, meaning that the quantum state and the entanglement structure is similar on all

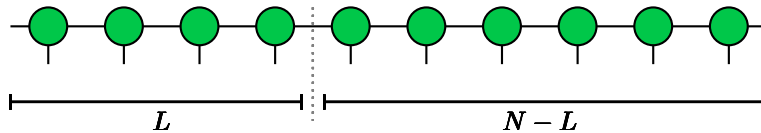


FIGURE 2.8: A bipartition of an MPS can be formed by cutting one link only. The entanglement entropy for a subsystem of size  $L$  is therefore independent of its size and only bounded by  $S(L) \leq \ln \chi$ . Since  $S(L)$  is a constant it fulfills an area-law in 1d, where the area of the region is of  $\mathcal{O}(1)$ .

length scales. Matrix product states however are known to have a finite correlation length [66], so that correlations always decay exponentially over distance. Nevertheless the scope of MPS is not limited to gapped systems. By increasing the bond dimension it is possible to approach and to study gapless, critical systems [65, 67, 68] and also two-dimensional systems [69]. Furthermore matrix product states can be used to study systems in the thermodynamic limit by repeating a unit cell of tensors periodically. An algorithm that makes use of this translational invariance will be used in Chapter 4. A geometric generalization of MPS to two spatial dimensions will be described in the next section.

## 2.5 Projected Entangled Pair States (PEPS)

Projected Entangled Pair States are the generalization of MPS to two spatial dimensions [52]. In principle tensor networks are not limited to any dimension, and any graph with vertices and edges can be treated as a tensor network. However quantum fluctuations are less important in higher dimensions, so that TNs are mostly used in one and two dimensions [70]. Again, the local tensors represent one lattice site

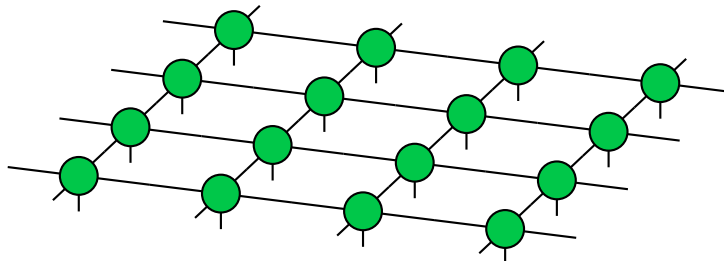


FIGURE 2.9: Projected entangled pair state for a square lattice of four times four sites with open boundary conditions. It is also possible to apply periodic boundary conditions in both directions, which results in a non-trivial torus geometry. However, the PEPS ansatz is typically used as an ansatz for infinite systems.

each and the virtual bond indices connecting the tensors resemble the structure of the underlying lattice. The square lattice is particularly convenient to work with from an algorithmic perspective, but PEPS states can also be defined on honeycomb, triangular, Kagome or other lattices. For a square lattice PEPS as in Fig. 2.9 the number of coefficients in the ansatz for the wave function is in the order of  $\mathcal{O}(NpD^4)$ , where  $D$  is used for the bond dimension of the PEPS and  $p$  is again the dimension of the physical Hilbert space. Just as for matrix product states, projected entangled pair states can represent low-energy states of local Hamiltonians with only a polynomial number of coefficients. They obey the area-law by construction which can be seen for a bipartition of a patch of size  $L \times L$  and the rest of the system, as visualized in Fig. 2.10. Assuming a uniform bond dimension of  $D$ , the entanglement entropy is

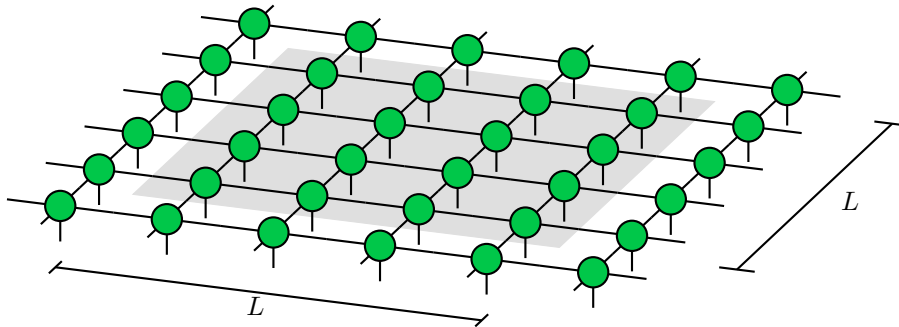


FIGURE 2.10: Bipartition of a PEPS into a patch of size  $L \times L$  and the rest of the system. The entanglement entropy is upper bounded by the rank of the reduced density matrix for the inner system that is at most  $D^{4L}$ . Therefore the entanglement entropy is  $S(L) \leq 4L \ln(D)$  and scales as the area of the inner system, and not with its volume (volume-law entanglement scales as  $S(L) \propto L^2$ ).

upper bounded by  $S(L) \leq 4L \ln D$ , which is proportional the length of the boundary. In contrast, volume-law entanglement would scale extensively as  $S(L) \propto L^2$ . Contrary to MPS, PEPS can represent critical quantum states and algebraically decaying correlations – already for a bond dimension of  $D = 2$  [60].

Most PEPS algorithm can be sorted into two groups. The first group of algorithms concerns the simulation of PEPS wave functions, i.e. obtaining the coefficients in the PEPS tensors that represent the target state. Important algorithms are schemes based on iTEBD [71, 72] and variational methods [73, 74]. The second group describes algorithms concerned with the contraction of the PEPS network to calculate physical observables, such as different tensor renormalization schemes (Tensor Renormalization Group (TRG) [75], Second Renormalization Group (SRG) [76], Higher-Order TRG (HOTRG) [77]), and other techniques based on Corner Transfer Matrices and Corner Tensors [78, 79, 80, 81]. Of particular interest to us will be the infinite PEPS (iPEPS) ansatz which we will use in Chapters 5, 6 and 7 together with a Corner Transfer Matrix scheme.

## 2.6 Summary

In this chapter we introduced a numerical simulation technique that is based on the structure and amount of entanglement in many-body systems. These so called tensor networks resemble the physical lattice in terms of local interconnected tensors that contain the variational parameters to represent the wave function of the system. The ability to capture the correct entanglement pattern as well as the amount of quantum correlations is a limitation of the method. TNs can be written in a very convenient pictorial form which makes the description of quantum states, algorithms and various calculations intuitive.

Two prominent families of tensor networks have been presented. While matrix product states are a tool for quantum many-body systems in one spatial dimension, projected entangled pair states are the generalization to two or higher dimensions. Both tensor networks obey the area-law for the entanglement entropy which makes them well suited for the simulation of Hamiltonians with local interactions.





## Chapter 3

# Symmetry-Preserving Tensors

The concepts of locality of interactions and symmetry are deeply rooted in physical systems appearing in nature. Locality has already been exploited in the formulation of the area-law which is the basis for the efficient representation of quantum many-body states using tensor networks. Additionally, the symmetry of certain systems can be exploited too, and will impose even more constraints on the Hilbert space in which the quantum states can live. One of the most important symmetries is the invariance under a rotation of spins, described by the continuous symmetry group  $SU(2)$  (the special unitary group of degree two). It appears frequently in quantum mechanics for several important spin models and it is also present in the standard model of particle physics, which has a local  $SU(3) \times SU(2) \times U(1)$  gauge symmetry [82].

Physical symmetries can be directly incorporated into tensor networks. The basic idea is to use symmetry preserving tensors, which causes the whole quantum state to be invariant under the action of the symmetry group. In the following sections we will describe a formalism to implement general symmetries in tensor networks following Refs. [11, 83], and we will focus then on the case of the non-Abelian group  $SU(2)$ . The disparity to Abelian groups like  $U(1)$  is briefly discussed in Sec. 3.7 and for an introduction to the representation theory of  $SU(2)$  we refer to Appendix A.1.

### 3.1 Implementation of Symmetries

Considering a lattice  $\mathcal{L}$  made of  $N$  sites, where each lattice site is described by a finite Hilbert space  $\mathbb{V}$  of dimension  $p$ . A pure state  $|\psi\rangle \in \mathbb{V}^{\otimes N}$  in the total Hilbert space can always be expanded in terms of the single-particle states  $|i_k\rangle$  with  $k = 1, \dots, p$  according to

$$|\psi\rangle = \sum_{i_1, i_2, \dots, i_N} c_{i_1, i_2, \dots, i_N} |i_1\rangle \otimes |i_2\rangle \otimes \dots \otimes |i_N\rangle . \quad (3.1)$$

A tensor network description of the state  $|\psi\rangle$  consists of a set of tensors and a graph or network of edges which determines how the tensors can be contracted together to recover the probability amplitudes  $c_{i_1, i_2, \dots, i_N}$ . Furthermore we consider a compact, completely reducible group  $\mathcal{G}$  with  $U : \mathcal{G} \rightarrow L(\mathbb{V})$  a unitary matrix representation of  $\mathcal{G}$  on the space  $\mathbb{V}$  of one site. For each element  $g$  of the group,  $U_g : \mathbb{V} \rightarrow \mathbb{V}$  denotes a unitary matrix and  $U_{g_1} U_{g_2} = U_{g_1 g_2}$ <sup>1</sup>. The vector space  $\mathbb{V}$  on each site decomposes as

$$\mathbb{V} \cong \bigoplus_j d_j \mathbb{V}_j \cong \bigoplus_j (\mathbb{D}_j \otimes \mathbb{V}_j) \quad (3.2)$$

<sup>1</sup>We do not consider projective representations here, for which  $U_{g_1} U_{g_2} = \omega(g_1, g_2) U_{g_1 g_2}$  holds. If projective representations are needed, one could use the corresponding covering group  $R(\mathcal{G})$ , where the projective representations of  $\mathcal{G}$  are linear representations of  $R(\mathcal{G})$ .

under the action of the symmetry. Here  $j$  are the charges or quantum numbers of  $\mathcal{G}$ ,  $\mathbb{V}_j$  denotes a subspace for the corresponding irreducible representation (irrep) and  $d_j$  counts the copies of  $\mathbb{V}_j$  in  $\mathbb{V}$ . The decomposition can also be conveniently written in terms of a  $d_j$ -dimensional degeneracy subspace  $\mathbb{D}_j$  (see Eq. (3.2)). Instead of using the single-particle basis  $|i_k\rangle$  with  $i_k = 1, \dots, p$ , we can now use the basis  $|j, t_j, m_j\rangle$  in  $\mathbb{V}$ , where  $t_j$  denotes states within the degeneracy space  $\mathbb{D}_j$  and  $m_j$  label states within the irrep space  $\mathbb{V}_j$ . This formalism is very general, for the concrete example of  $\mathcal{G} = SU(2)$  we will be focusing on the charges  $j$  correspond to the total spin, and  $m_j$  corresponds to the spin projection along a quantization axis.

We are interested in quantum states  $|\psi\rangle \in \mathbb{V}^{\otimes N}$  that are *invariant* under a global on-site symmetry, so that

$$(U_g)^{\otimes N} |\psi\rangle = |\psi\rangle \quad \forall g \in \mathcal{G}. \quad (3.3)$$

Here  $U_g$  is an element of the group  $\mathcal{G}$  that acts on the vector space of the physical degrees of freedom, as visualized for an MPS in Fig. 3.1. The invariance under the

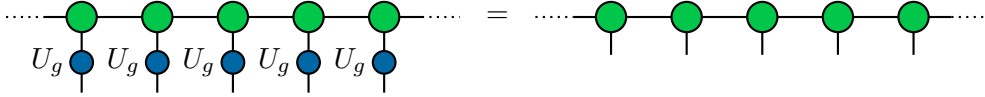


FIGURE 3.1: A global on-site symmetry for an MPS, where  $U_g$  acts on the vector space of the physical degrees of freedom. The invariance under the action of a group  $\mathcal{G}$  is achieved by purely symmetric tensors in the representation of  $|\psi\rangle$ .

action of  $\mathcal{G}$  will be achieved by a representation of  $|\psi\rangle$  in terms of purely symmetric tensors. A tensor is a multi-linear map between tensor product vector spaces, and each index of the tensor labels a basis on one of these spaces. In order to introduce the action of a symmetry, we will also assign a direction  $w_i \in \{-1, +1\}$  to each index  $i$  using the convention

$$w_i = \begin{cases} -1 & \text{if } i \text{ is an incoming index} \\ +1 & \text{if } i \text{ is an outgoing index} \end{cases}. \quad (3.4)$$

The direction determines how the symmetry acts on the index. Since an outgoing index of one tensor needs to be connected with an incoming index of another one, the symmetry acts as the identity on the link between the tensors. A symmetric tensor is defined by being invariant under the simultaneous action of  $\mathcal{G}$  on all its indices, that is, on the vector spaces associated with these indices. This is shown in Fig. 3.2,

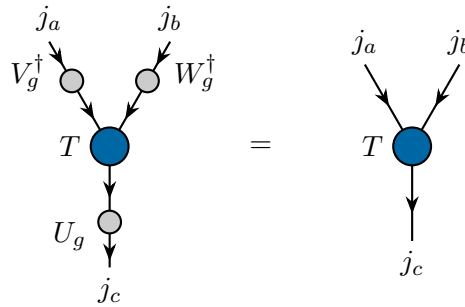


FIGURE 3.2: A symmetric tensor is invariant under the simultaneous action of  $\mathcal{G}$  on all its indices for fixed values of the charges  $j_a$ ,  $j_b$  and  $j_c$ . The directions of the tensor indices determine how the group acts on them.

where we use the convention that the group acts with its adjoint representation on

incoming indices. We now fix the basis of symmetric tensors to the one corresponding to the irrep basis  $\{|j, t_j, m_j\rangle\}$  for all tensor indices. Instead of simply labeling the basis states, every index  $i$  then corresponds to a set of triples  $i \equiv (j_i, t_{j_i}, m_{j_i})$ , i.e. each index can carry multiple irreps  $j_i$  that come with degeneracies  $t_{j_i}$  and  $m_{j_i}$ . The symmetric bond dimension of an index  $i$  is then the number of different irreps counting multiple copies separately, given by

$$\chi_{\text{sym}} = \sum_{j_i} t_{j_i}. \quad (3.5)$$

The total, effective bond dimension  $|i|$  can however be larger if the irreps of the group  $\mathcal{G}$  are degenerate. Generally, it is given by

$$\chi_{\text{eff}} = \sum_{j_i} t_{j_i} \times |m_{j_i}|, \quad (3.6)$$

where  $|m_{j_i}|$  is the size of index  $m_{j_i}$ . For the case of  $SU(2)$  we have  $m_{j_i} = [-j_i, \dots, +j_i]$  and therefore  $|m_{j_i}| = 2j_i + 1$ , so that the effective bond dimension will generally be larger than the symmetric one. In the chosen basis a symmetric tensor can be decomposed according to the Wigner-Eckart theorem. This implies that the degrees of freedom that are not fixed by the present symmetry can be isolated in a set of *degeneracy tensors*  $\{P\}$ , while everything that is entirely determined by the symmetry is transferred into a set of *structural tensors*  $\{Q\}$ . In practice, this means that only the degeneracy tensors  $P$  encode the variational parameters in a symmetric tensor network optimization, which implies a reduction in memory cost as well as a computational speed-up in TN algorithms.

Let us consider the case of a three-index tensor  $T_{abc}$ , where each index carries a set of quantum numbers with corresponding degeneracies  $(j_i, t_{j_i}, m_{j_i})$ . By fixing particular values of the charges  $j_a, j_b$  and  $j_c$  we can select one block of components from the tensor, denoted by  $T_{j_a j_b j_c}$ . The Wigner-Eckart theorem separates this block into a tensor product of its variational parameters and the structural parameters of the symmetry according to

$$T_{j_a j_b j_c} = P_{j_a j_b j_c} \otimes Q_{j_a j_b j_c}. \quad (3.7)$$

Here the dimensions of  $P$  and  $Q$  are determined by the dimensions of the degenerate subspaces  $\mathbb{D}_{j_i}$  and the dimensions of the irrep spaces  $\mathbb{V}_{j_i}$  respectively. The decom-

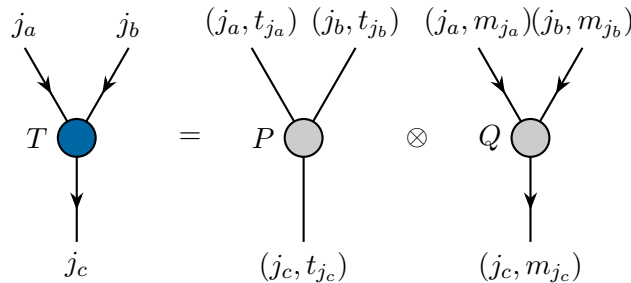


FIGURE 3.3: For fixed values of the charges a symmetric tensor decomposes into a *degeneracy part*  $P$  and a *structural part*  $Q$ , where  $P$  holds the unconstrained parameters of  $T$  and  $Q$  is entirely determined by the symmetry (it is an intertwiner of the symmetry group). Both  $P$  and  $Q$  are labeled by the quantum numbers  $j_a, j_b, j_c$ , their dimensions are however specified by  $t_{j_a}, t_{j_b}, t_{j_c}$  and  $m_{j_a}, m_{j_b}, m_{j_c}$ .

position in Eq. (3.7) is visualized in Fig. 3.3. The full symmetric tensor  $T_{abc}$  can be written in terms of block of components  $T_{j_a j_b j_c}$  as

$$T_{abc} = \bigoplus_{j_a j_b j_c} (P_{j_a j_b j_c})_{t_{j_a} t_{j_b} t_{j_c}} \otimes (Q_{j_a j_b j_c})_{m_{j_a} m_{j_b} m_{j_c}} \quad (3.8)$$

for compatible combinations of  $(j_a, j_b, j_c)$ , which are determined by the fusion rules of the symmetry. Exploiting the decomposition of symmetric tensor is crucial in improving existing tensor network implementations and will lead to reduced memory requirements and computational speedup, as we will demonstrate later.

This formalism can be used to decompose tensors of arbitrary rank. It is important to notice however that the decomposition is generally no longer unique for tensors with more than three indices. This is due to the pairwise combination of vector spaces. Consider a four-index tensor for which the three vector spaces  $\mathbb{V}_a$ ,  $\mathbb{V}_b$  and  $\mathbb{V}_c$  merge into  $\mathbb{V}_d$ . The composite vector space  $\mathbb{V}_d$  can be constructed as  $(\mathbb{V}_a \otimes \mathbb{V}_b) \otimes \mathbb{V}_c$  or as  $\mathbb{V}_a \otimes (\mathbb{V}_b \otimes \mathbb{V}_c)$ . Since the intermediate vector spaces  $\mathbb{V}_i = \mathbb{V}_a \otimes \mathbb{V}_b$  or  $\mathbb{V}_j = \mathbb{V}_b \otimes \mathbb{V}_c$  can again be decomposed as a direct sum of vector spaces as in Eq. (3.2), it is necessary to keep the intermediate quantum numbers to identify the tensor blocks. A symmetric tensor with  $k$  indices can generally be written as a direct sum of symmetric blocks

$$T_{j_1, \dots, j_k}^{j_1^{\text{int}}, \dots, j_l^{\text{int}}} = P_{j_1, \dots, j_k}^{j_1^{\text{int}}, \dots, j_l^{\text{int}}} \otimes Q_{j_1, \dots, j_k}^{j_1^{\text{int}}, \dots, j_l^{\text{int}}}, \quad (3.9)$$

where each block is labeled by the charges  $j_1, \dots, j_k$  associated to the  $k$  indices and additional  $l = k - 3$  internal charges  $j_1^{\text{int}}, \dots, j_l^{\text{int}}$ . Even though  $P$  and  $Q$  are labeled by the full set of quantum numbers  $(j_1^{\text{int}}, \dots, j_l^{\text{int}}, j_1, \dots, j_k)$ , they only have  $k$  indices each with dimensions given by  $t_{j_i}$  and  $|m_{j_i}|$  respectively.

Notice that in the presented description of symmetric tensors we implicitly assumed a multiplicity-free group  $\mathcal{G}$ , this is however not the most general case. Generally, the tensor product of two irreps with charges  $j_a$  and  $j_b$  decomposes as

$$\mathbb{V}_{j_a} \otimes \mathbb{V}_{j_b} \cong \bigoplus_{j_c} N_{j_a j_b}^{j_c} \mathbb{V}_{j_c}, \quad (3.10)$$

where  $N_{j_a j_b}^{j_c}$  counts the copies of  $\mathbb{V}_{j_c}$  that appear in the direct sum. If  $N_{j_a j_b}^{j_c} \geq 2$  for any combination of irreps, one needs to extend the formalism by introducing additional indices for the multiplicities at each intersection of two vector spaces.

This completes the theoretical description of symmetric tensors. From now on we will focus on the group  $\mathcal{G} = SU(2)$ , an infinite non-Abelian group that does not have multiplicities. We will show how the ambiguity of combining vector spaces can be resolved by the formalism of *fusion trees* - a kind of a tree graph decorated with charge labels - which completely specify the structural part of a symmetric tensor.

## 3.2 SU(2)-Symmetric Tensors

For  $\mathcal{G} = SU(2)$  the charges  $j$  correspond to the total spin, e.g.  $j \in 0, \frac{1}{2}, 1, \dots$  and  $m_j$  corresponds to a projection along a quantization axis. The effect of the symmetry will be incorporated into the structural tensors  $Q$ , which describe the coupling of different spins in terms of Clebsch-Gordan coefficients. The coupling coefficients  $\langle j_1 m_1 j_2 m_2 | j m \rangle$  then appear as entries of the structural tensors  $Q$ , which can be

stored as standard numerical arrays. Alternatively, the structural part can be described by a fusion tree decorated by quantum numbers of the group. This has several advantages compared to a regular implementation. First of all, since the fusion trees are an algebraic construct they are memory-efficient and no actual coefficients for structural tensors have to be stored. Second, manipulation of tensors are mostly impacted by manipulations of the fusion trees which are exact and virtually free of numerical errors that could occur when manipulating structural tensors as numerical arrays. Additionally, fusion trees are the natural language to describe *anyonic systems*, so that an implementation based on fusion trees can be readily extended to support so called quantum groups, that underly anyonic theories (see Sec. 3.6).

### 3.2.1 Fusion Trees

The structural tensors are the intertwiners of the symmetry group  $\mathcal{G}$  [84]. The elementary objects - three-index structural tensors - are tensors whose components are the Clebsch-Gordan coefficients of the group. They are connected to the unique mapping between three vector spaces  $\mathbb{V}_{j_a} \otimes \mathbb{V}_{j_b} \cong \mathbb{V}_{j_c}$ . We refer to these elementary three-index tensors as Clebsch-Gordan tensors. A Clebsch-Gordan tensor  $C^{\text{fuse}}$  describes a (unitary) change of basis from the tensor product of two irreps  $j_a$  and  $j_b$  to a total irrep  $j_c$  according to

$$|j_c m_{j_c}\rangle = \sum_{m_{j_a} m_{j_b}} \left( C^{\text{fuse}} \right)_{(j_a, m_{j_a}), (j_b, m_{j_b})}^{(j_c, m_{j_c})} |j_a, m_{j_a}\rangle \otimes |j_b, m_{j_b}\rangle . \quad (3.11)$$

This is denoted by  $j_a \times j_b \rightarrow j_c$ . The Clebsch-Gordan coefficients in Eq. (3.11) vanish unless the *fusion rules* of the symmetry

$$j_c \in j_a \otimes j_b = \{|j_a - j_b|, \dots, j_a + j_b\} \quad (3.12)$$

are satisfied. The possible symmetric blocks labeled by  $(j_a, j_b, j_c)$  that appear in the decomposition of a three-index symmetric tensor are therefore determined by compatible configurations where  $j_c$  belongs to the set above. The inverse operation, where

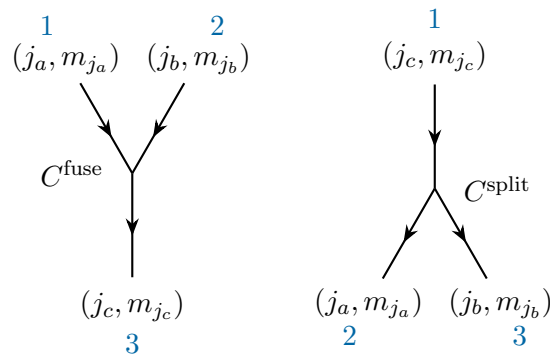


FIGURE 3.4: Graphical representation of the elementary three-index Clebsch-Gordan tensors that fuse two irreps  $j_a \times j_b \rightarrow j_c$  or split an irrep  $j_c \rightarrow j_a \times j_b$ . The blue labels indicate the order in which the legs will to be specified.

irrep  $j_c$  splits into a tensor product of irreps  $j_a$  and  $j_b$  ( $j_c \rightarrow j_a \times j_b$ ) is denoted by a Clebsch-Gordan tensor  $C^{\text{split}}$ . The definitions of these elementary building blocks of fusion trees are shown in Fig. 3.4. Structural tensors (or intertwiners) with more than three indices can always be decomposed in terms of these elementary tensors, which corresponds to a pairwise combination of vector spaces. Every intertwiner can

be described in terms of directed trivalent tree graphs that are generated by combinations of fusion and splitting tensors. Therefore  $C^{\text{fuse}}$  and  $C^{\text{split}}$  are the trivalent nodes of the fusion tree, and the irreps that are being fused or split are those carried by the indices of the symmetric tensor. The Clebsch-Gordan tensors obey some useful

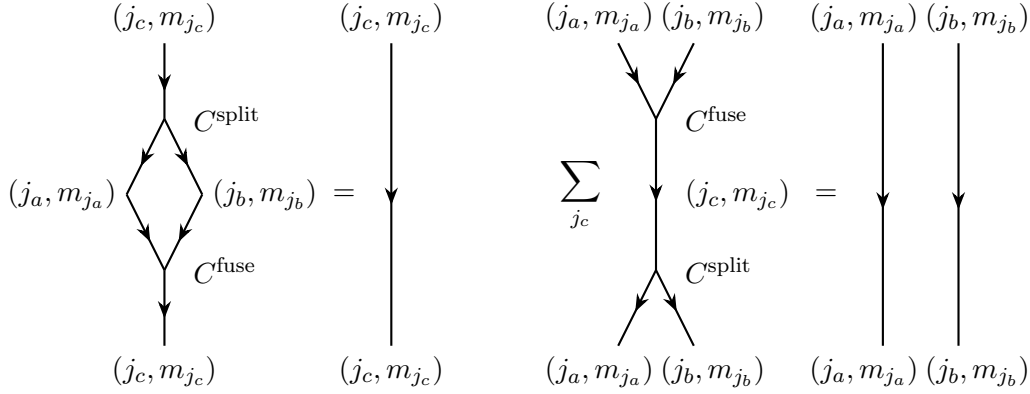


FIGURE 3.5: Identity relations for the Clebsch-Gordan tensors  $C^{\text{fuse}}$  and  $C^{\text{split}}$ . The sums over all spin projections  $m_{j_a}$ ,  $m_{j_b}$  and  $m_{j_c}$  are implicit.

identity relations depicted in Fig. 3.5 which will be utilized in Sec. 3.2.3 to transform different fusion trees into each other.

In order to store a fusion tree for a general tensor one needs a list of nodes specifying which indices intersect at the given vertex, and a list of node types specifying whether the node is a fusion or a splitting node. This is necessary to avoid ambiguities as we will show below. To this end, we label incoming and outgoing edges of the symmetric tensor by negative numbers  $-1, -2, \dots$ , whereas edges carrying the intermediate irreps (the various pairwise fusion outcomes) are labeled by positive numbers  $1, 2, \dots$ . The edges labeled by negative integers correspond to the indices of the corresponding structural tensors while edges labeled by positive numbers are the additional quantum numbers that occurred in the general decomposition of Eq. (3.9). Each node  $i$  of the tree is specified by a three-component vector  $\tau_i$ , whose entries correspond to the labels of the three edges that intersect at the node. The position in the node is fixed for both elementary nodes and the position is indicated in Fig. 3.4 by blue numbers. The label to distinguish fusion nodes from splitting nodes is stored in a separate vector  $\sigma$  where for each node

$$\sigma_i = \begin{cases} -1 & \text{if node } i \text{ is a fusion node} \\ +1 & \text{if node } i \text{ is a splitting node} \end{cases} \quad (3.13)$$

Therefore, for  $\sigma_i = -1$  the first and the second edge of  $\tau_i$  fuse to the third edge, and for  $\sigma_i = +1$  the first edge of  $\tau_i$  is split into the second and the third edge. A complete fusion tree is then specified by a list of nodes  $\tau$  and the corresponding vector  $\sigma$ . As an example let us consider the possible fusion trees for a four-index tensor. Their structural parts are special in so far, as they represent combinations of two fusion and/or splitting nodes which form a full list of all possible tree structures available. They are also the smallest possible trees for which the ambiguity of combining vector spaces appears and will allow us to establish transformations between differently coupled vector spaces. First we make the observation that we can further classify trees according to the property of separating incoming and outgoing edges. Fig. 3.6

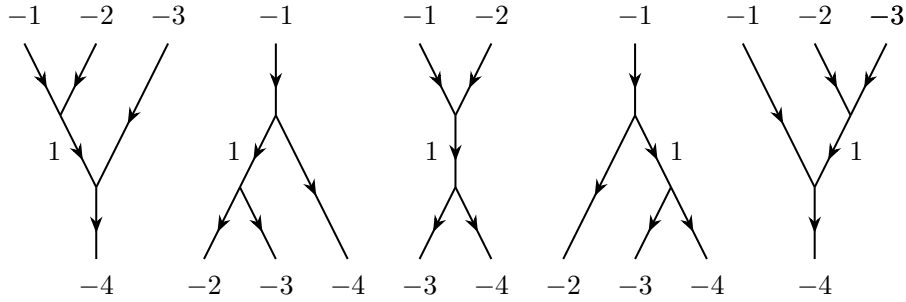


FIGURE 3.6: Different fusion trees representing the structural part of a four-index tensor. Since all incoming edges are separated from outgoing edges either immediately or by cutting only one internal edge, these trees are called *simple trees*.

lists all four-index fusion trees for which incoming and outgoing edges are either automatically separated, or can be separated by cutting a single edge of the tree. We refer to these kind of structures as *simple trees*. However the set in Fig. 3.6 is not the most general one, since we can also build the trees in Fig. 3.7. Cutting a single

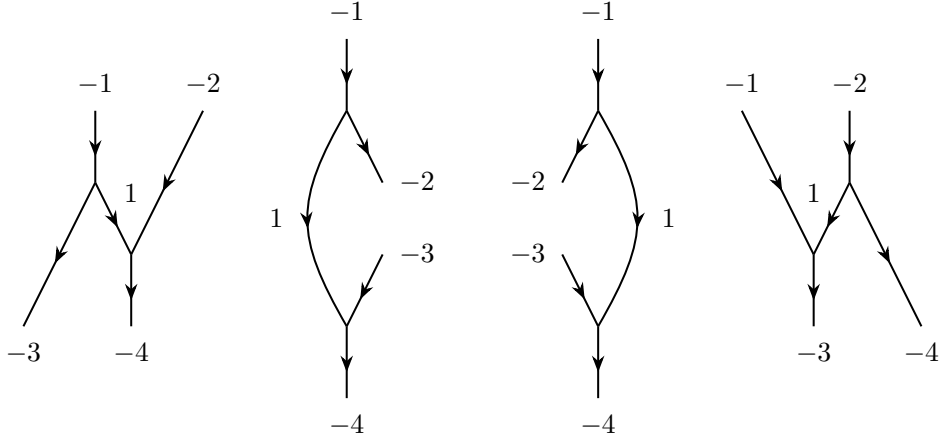


FIGURE 3.7: Different fusion trees representing the structural part of a four-index tensor. Since incoming and outgoing edges can no longer be separated by cutting one internal edge, these trees are called *advanced trees*.

branch of those trees will no longer separate incoming and outgoing edges, and we refer to those structures as *advanced trees*. We now make some concrete examples for the specification of the fusion trees using our convention in terms of  $\tau$  and  $\sigma$  vectors and the labelling of nodes defined in Fig. 3.4. The first, third and the fourth fusion tree in Fig. 3.6 are constructed by

$$\begin{aligned}
 \tau_1 &= \{[-1, -2, 1], [1, -3, -4]\} & \sigma_1 &= [-1, -1] \\
 \tau_3 &= \{[-1, -2, 1], [1, -3, -4]\} & \sigma_3 &= [-1, +1] \\
 \tau_4 &= \{[-1, -2, 1], [1, -3, -4]\} & \sigma_4 &= [+1, +1].
 \end{aligned}
 \tag{3.14}$$

Here the importance of the  $\sigma$  vector becomes apparent since the trees are all specified by the same  $\tau$  vectors. Using this convention it is possible to construct arbitrary trees, and also more general graphs that can contain loops<sup>2</sup>.

<sup>2</sup>For symmetric tensors graphs are a less efficient representation of the structure of the group and we will be confined to only using fusion trees without the loss of generality. However graphs with loops can occur for the contraction of several tensors, which we will address in a dedicated chapter.

### 3.2.2 Decorations of Fusion Trees with Quantum Numbers

The internal structure and the symmetric part of symmetry-preserving tensors can be conveniently described in terms of fusion trees. Moreover, the fusion rules of the group in Eq. (3.12) also determine the possible symmetric blocks that appear in the decomposition of the full tensor

$$T = \bigoplus_{\substack{j_1, \dots, j_k \\ j_1^{\text{int}}, \dots, j_l^{\text{int}}}} T_{j_1, \dots, j_k}^{j_1^{\text{int}}, \dots, j_l^{\text{int}}} = \bigoplus_{\substack{j_1, \dots, j_k \\ j_1^{\text{int}}, \dots, j_l^{\text{int}}}} P_{j_1, \dots, j_k}^{j_1^{\text{int}}, \dots, j_l^{\text{int}}} \otimes Q_{j_1, \dots, j_k}^{j_1^{\text{int}}, \dots, j_l^{\text{int}}}. \quad (3.15)$$

Each block of the symmetric tensor is labeled by the set of all quantum numbers  $\{j_1^{\text{int}}, j_2^{\text{int}}, \dots, j_l^{\text{int}}, j_1, j_2, \dots, j_k\}$ , which is a complete decoration of the fusion tree in terms of quantum numbers of the group. For such a decoration the irreps intersecting at any node obey the fusion rules. Each block in the tensor is labeled by one unique decoration, which we also refer to as *charge sector*.

In order to find the possible charge sectors it is necessary to determine the quantum numbers on internal edges first. For the case of  $\mathcal{G} = SU(2)$  the intermediate vector spaces can always be constructed with non-degenerate vector spaces of irreducible representations since there are no multiplicities. Once all quantum numbers in the fusion tree are known (external ones specified by the initialization of the symmetric tensor and internal ones obtained by pairwise fusion), one can apply the fusion rules of the symmetry to each node individually. The final set of tree decorations is obtained by combining the possible quantum numbers for every node in such a way that the quantum numbers on the connecting, internal edges are in agreement. An example for a four-index fusion tree with different quantum numbers on incoming and outgoing edges is given in Fig. 3.8. Here the intermediate vector space would carry  $j_1^{\text{int}} = [0, 1, 2]$  for the fusion of the two incoming vector spaces, however due to the splitting into the two outgoing spaces  $\mathbb{V}_3$  and  $\mathbb{V}_4$  it is limited to carry only spin zero and one. A symmetric four-index tensor initialized with the external quantum num-

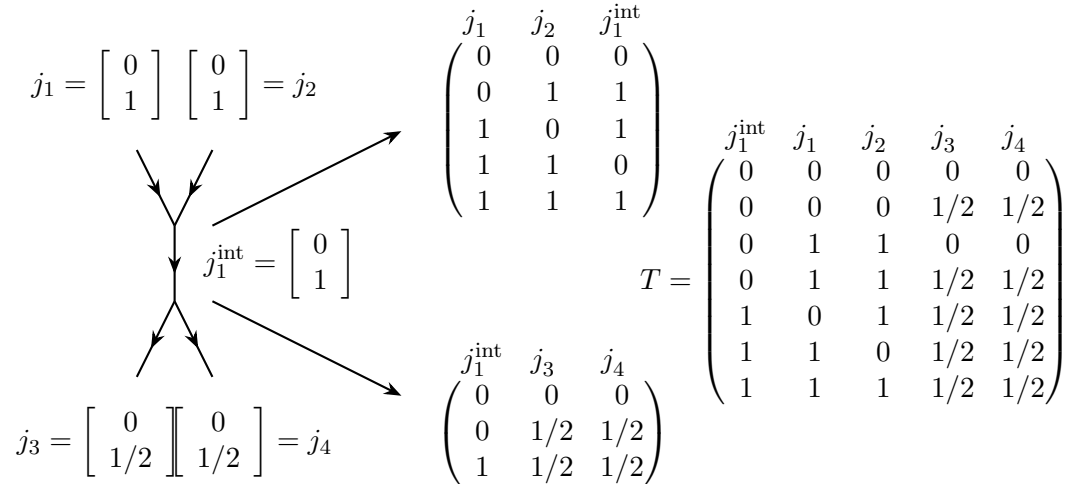


FIGURE 3.8: Construction of all fusion tree decorations (charge sectors) that label the blocks of a symmetric tensor with chosen external quantum numbers. Once the irreps for all internal edges are determined one can construct possible decorations for every node using the fusion rules of the group. These are then assembled to the full list of charge sectors.



bers  $j_i$  as in Fig. 3.8 would therefore consist of seven separate blocks, each of which labeled by one row of the matrix  $T$ . The individual dimensions of the degeneracy tensors  $\{P\}$  then corresponds to the degeneracies  $t_{j_i}$  of  $j_i$  that are not specified here.

### Building Structural Tensors

One of the main advantages of the fusion tree approach is that no actual Clebsch-Gordan coefficients have to be stored, and tensor manipulations are rendered as analytic operations on the trees. However it is always possible to build the actual structural tensors from the information that is stored, namely the fusion tree itself and the decorated quantum numbers. For every tree decoration - i.e. every symmetric block in the tensor - a Clebsch-Gordan tensor is assigned to each fusion and splitting node respectively. The structural tensor is then obtained by contracting all the numerical fusing and splitting tensors according to the fusion tree. This operation is required when computing the full tensor from the symmetric tensor decomposition.

### 3.2.3 F-Moves

In this section we will describe how different fusion trees can be transformed into each other via so-called  $F$ -moves. This is an important operation since the decomposition of tensors with more than three legs is not unique and the vector spaces can be pairwise fused in different ways. All these possibilities are equivalent from the perspective of the symmetric tensor - i.e. it does not matter which fusion tree is chosen as an internal structure - but some tree decompositions are more useful than others in certain situations.

A given fusion tree can be transformed into another fusion tree by applying a sequence of elementary transformations known as  $F$ -moves. They act on fusion trees with four open edges, leaving their direction as well as their ordering unaffected. Therefore not all of the elementary four-index fusion trees in Figs. 3.6 and 3.7 can

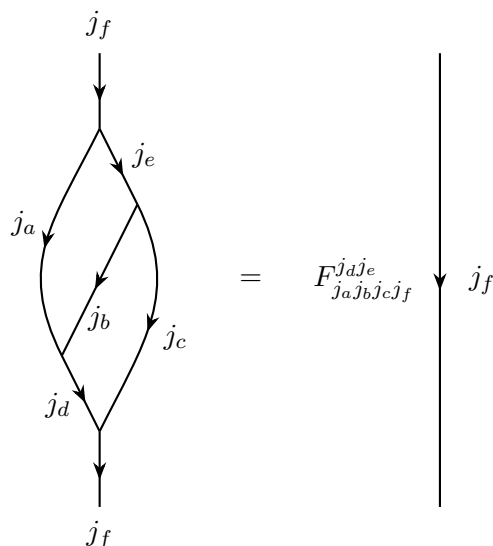


FIGURE 3.9: Evaluating the spin network on the left is proportional to the identity on the right, with a factor given by the recoupling coefficients  $F$ , that relate two differently coupled bases to one another.

be transformed into each other. An  $F$ -move is a (unitary) change of basis for the

structural tensors that relates two fusion trees to one another via the *recoupling coefficients* of the group. For  $SU(2)$  they are defined in Fig. 3.9 via the overlap of differently coupled bases. They are also closely related to the Wigner 6- $j$  symbols according to

$$F_{j_a j_b j_c j_f}^{j_d j_e} = (-1)^{j_a + j_b + j_c + j_f} \sqrt{(2j_d + 1)(2j_e + 1)} \cdot \left\{ \begin{matrix} j_a & j_b & j_d \\ j_c & j_f & j_e \end{matrix} \right\}, \quad (3.16)$$

where  $\{\dots\}$  denotes a 6- $j$  symbol. In total there are ten different types of  $F$ -moves which are necessary to transform among different internal structures of symmetric tensors. They are listed in Fig. 3.10. The actual relation between differently coupled bases for all  $F$ -moves can be deduced by applying different resolutions of the identity and using Fig. 3.9. A detailed chapter about  $F$ -moves can be found in Appendix A.2. For general fusion trees with more than four indices, the tree transformation can al-

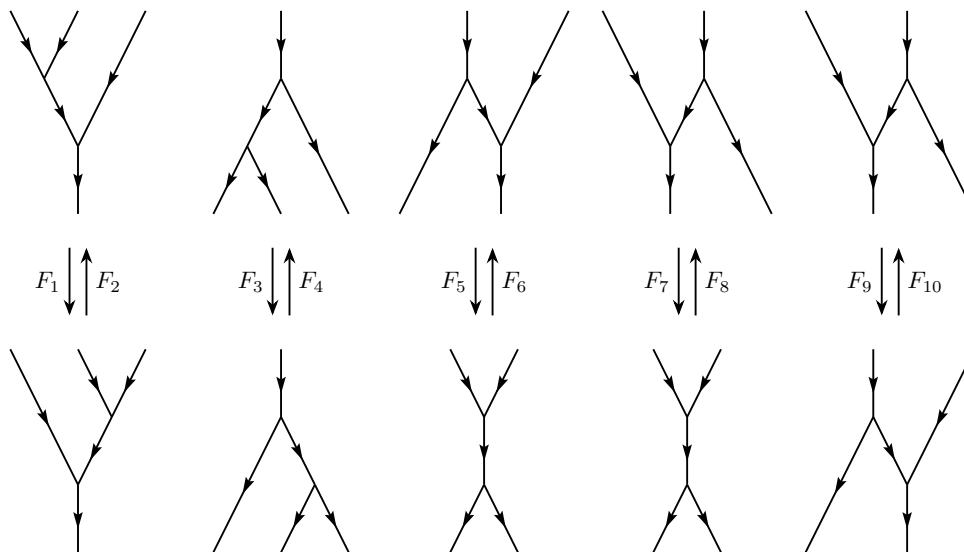


FIGURE 3.10: Full set of possible  $F$ -moves to transform different fusion trees into each other.

ways be reduced to a concatenation of single  $F$ -moves like the ones in Fig. 3.10. In doing so the sequence of  $F$ -moves is not unique and the same overall transformation may even require a different number of single moves. It is therefore important to find an optimal transformation sequence.

### Finding the Optimal Sequence of $F$ -Moves

In general a given fusion tree can be transformed into a final fusion tree with different concatenations of  $F$ -moves. The determination of the best suitable  $F$ -moves and their sequence is one of the core tasks for the transformation of trees and we will outline how this operation can be performed. For every fusion tree we can define a clockwise (anticlockwise) ordering of the open edges by starting at one leaf and traversing the tree. Every leaf is connected to its neighbour by a certain path inside the tree that consists of different nodes to be traversed. Collecting this information for all open edges, one can define a measure of distance between two fusion trees, e.g. the difference in the path length to traverse every edge to its clockwise or anticlockwise neighbours. As a concrete example let us consider the five-index fusion tree in Fig. 3.11, where it is obvious that the sequence of  $F_5$  on internal edge 1 and  $F_4$  on internal edge 2 yields the desired final tree. The optimal sequence should be found automatically for all possible

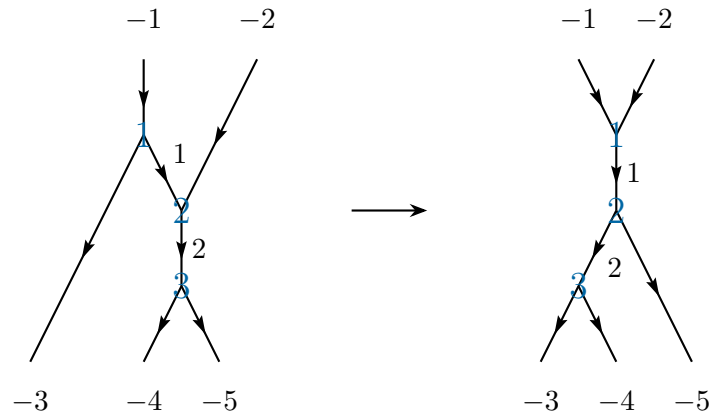


FIGURE 3.11: The sequence of  $F$ -moves to transform an input tree into an output tree can be found using a kind of cost function that measures how far two trees are apart from each other. More details are given in the text.

trees using the cost function mentioned previously. For the two trees in Fig. 3.11 we have the set of data for a traversal in clockwise order shown in Table 3.1. The first cost function  $C_1$  is the collective difference in path lengths between the initial and the final tree which needs to be zero when the correct sequence of  $F$ -moves has been found. This information is however not sufficient. Consider for example the two fusion trees that can be transformed into each other by only  $F_9$  (or  $F_{10}$  equivalently) in Fig. 3.10. The cost function  $C_1$  for these two trees is already zero because the distance between

pathID	1	2	3	4	5
connected edges	-1 $\rightarrow$ -2	-2 $\rightarrow$ -5	-5 $\rightarrow$ -4	-4 $\rightarrow$ -3	-3 $\rightarrow$ -1
path length I	2	2	1	3	1
path length F	1	2	2	1	3
path difference ( $C_1$ )	1	0	1	2	2
node types I	+1, -1	-1, +1	+1	+1, -1, +1	+1
node types F	-1	-1, +1	+1, +1	+1	+1, +1, -1
node difference ( $C_2$ )	[1 0]	[0 0]	[0 0]	[0 0]	[0 1]

TABLE 3.1: Tree traversal information that is used to define a cost function to minimize the distance between two fusion trees. Both trees are traversed in clockwise order.

neighbouring edges is identical, however the full trees are not identical. Therefore a second cost function  $C_2$  is required that measures the distance of the two trees in terms of node types that need to be traversed, i.e. whether the nodes along the path are in the same sequence of fusion and/or splitting nodes. Since the number of nodes in the paths is in general not the same, the cost function  $C_2$  measures the agreement of nodes in clockwise and anticlockwise order. This results in two values for  $C_2$  as shown in Table 3.1, where a discrepancy of node types is penalized. In the automated process all possible  $F$ -moves for the internal edges are tested successively, the distance measures  $C_1$  and  $C_2$  are computed for the resulting tree and compared against the initial tree. If the cost functions improve, e.g. lower collective distance or better overlap in terms of node types the  $F$ -move is accepted. Otherwise it is rejected and the next  $F$ -move is tested. The most efficient transformation is then the one with the smallest number of individual transformations.

### 3.3 Handling of Symmetric Tensors

Summarizing the description in the previous sections, a symmetric tensor is an object with a given set of quantum numbers and corresponding degeneracies for every tensor index, and a fusion tree that represents the internal structure of the tensor in terms of Clebsch-Gordan coefficients of the underlying symmetry group  $\mathcal{G}$ . The fusion rules of  $\mathcal{G}$  determine the possible symmetric blocks in the tensor, each of which factorizes into a part  $P$  holding the remaining variational parameters of the symmetric tensor and a structural part  $Q$  represented by a decorated fusion tree instead of a numerical array filled with Clebsch-Gordan coefficients.

For the discussion of tensor network algorithm and the application of  $SU(2)$ -symmetric tensors therein we can treat them essentially as elementary building blocks. Notice however that the standard set of tensor operations, such as reshaping or permuting tensor indices, factorizing matrices (using e.g. an SVD or an eigendecomposition) and ultimately multiplications and general tensor contractions have to be adapted for symmetric tensors and are significantly more involved. For a very detailed description of the complete set of tensor operations we refer the interested reader to Ref. [85], a programming guide for tensor networks with  $SU(2)$  symmetry. Here we briefly describe the operations and highlight where the symmetry puts additional complications. In the following, all tensor operations that are used in tensor networks algorithm will be presented. Notice that the transformation of fusion trees in terms of  $F$ -moves is not listed below, since it only affects the internal decomposition of the tensor which should be dealt with automatically in actual algorithms. Tensor manipulations applied by the programmer are the ones listed below.

#### 3.3.1 Reversal of Indices

Reversal of indices is a trivial operation for non-symmetric tensors which have no directions assigned to them. For symmetric tensors however, a reversal acts on the structural part and changes a fusion node into a splitting node (or vice versa) for the node where the index is attached. This in turn changes the Clebsch-Gordan coefficients for this particular node. In the fusion tree picture the change of the node type results in an algebraic factor derived from the recoupling coefficients of the group, that can be absorbed into the associated degeneracy part. The reversal of tensors with many

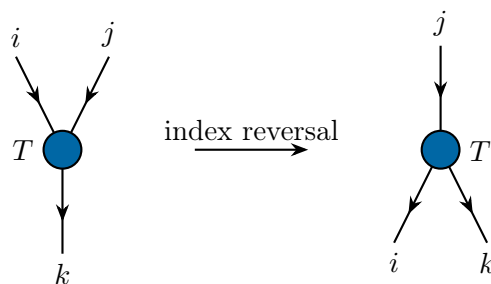


FIGURE 3.12: Reversing the incoming index  $i$  for a three-index tensor  $T$  transforms the fusion node into a splitting node. The resulting numerical factors are absorbed into the set of updated degeneracy tensors of  $T'$ .

indices works similarly because the factors for the symmetric blocks can be derived only from the node that is affected. Detailed information about the reversal factors can be found in Ref. [85].

### 3.3.2 Permutation of Indices

The second important operation which is frequently used in tensor network algorithms is the permutation of indices. We limit the discussion here to indices that have the same direction, e.g. that are both incoming or both outgoing. If this is not preexisting, a reversal operation is performed before and after the permutation. A permutation of a regular numerical array is simply a reshuffling of the tensor entries. This is the case for the degeneracy part of the symmetric blocks as well, however permutations of the quantum numbers in the decorated fusion trees leads to additional numerical factors<sup>3</sup>. These factors are given by the  $R$ -symbols of  $SU(2)$

$$R_{j_a \times j_b \rightarrow j_c} = R_{j_c \rightarrow j_a \times j_b} = (-1)^{j_a + j_b - j_c} . \quad (3.17)$$

As for reversal, a permutation of indices introduces a single factor per symmetric block that can again be absorbed into the degeneracy parts. For tensors with an arbitrary

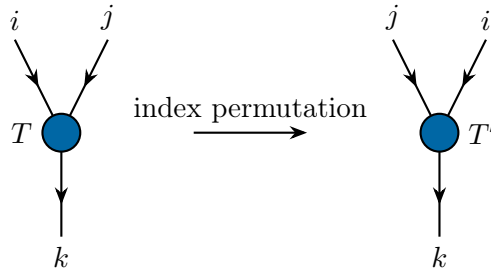


FIGURE 3.13: Permutation of two incoming indices of a three-index tensor  $T$ . The corresponding  $R$ -factors are absorbed into the updated degeneracy tensors of  $T'$ .

number of indices, a general permutation of indices with the same direction can always be composed of pairwise permutations. However, since the pairwise permutations need to be performed on indices belonging to the same node in the fusion tree, there are additional  $F$ -moves necessary to ensure this property. Details are given in Ref. [85].

### 3.3.3 Reshaping of Indices

A tensor is treated as a multidimensional array in the language of tensor networks. In order to be able to use them properly in algorithms it is necessary to reshape tensors, e.g. combine several indices to one or split a certain index into others. This can for example be required prior to matrix factorizations or contractions. Reshaping of non-symmetric tensors is a simple operation which changes the dimensions of the array. In the symmetric counterpart, a reshaping operation leads to a concatenation of multiple individual blocks for a fusion, or a separation of a single block into multiple ones for a splitting operation. Typically, a splitting of tensor indices is the exact inverse operation to a preceding fusion operation and does not occur as a standalone process. We will therefore make an example of a fusion operation to demonstrate the reshaping of  $SU(2)$ -symmetric tensors. Due to the underlying fusion tree structure, the fusion of indices is restricted to indices with the same direction. In this way the splitting of a previously fused index with given direction results in separate indices with the same direction. General reshaping operations can be constructed out of index reversal, index permutations and index reshaping as described below.

<sup>3</sup>For anyonic theories the permutation is described in terms of braiding operations, for which clockwise and anticlockwise braidings generally correspond to different factors.

### Fusion of Two Indices

We demonstrate an elementary fusion operation of two indices for the example of a three-index tensor. In this way the two indices that will be fused are already attached to the same node in the fusion tree. The handling of tensors with more than three

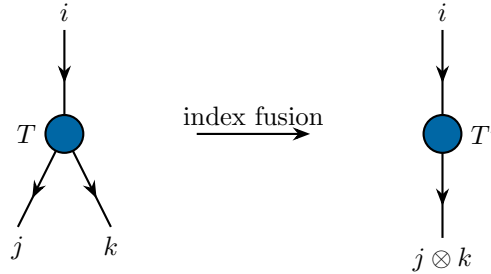


FIGURE 3.14: Fusion of the two outgoing indices of a three-index tensor. The symmetric blocks of  $T'$  result from a concatenation of reshaped symmetric blocks of  $T$ , as demonstrated in the main text.

indices is explained in detail in our programming guide [85]. For the concrete example we choose the arbitrary irreps and degeneracies for each index of tensor  $T$  in Table 3.2. Applying the fusion rules of the symmetry group (see Eq. (3.12)) determines the list

index	irreps with degeneracies $\{j_{t_j}\}$
$i$	$[0_1, 1_2, 2_3]$
$j$	$[0_1, 1_4]$
$k$	$[0_1, 1_6]$

TABLE 3.2: Quantum numbers and degeneracies for a three-index tensor whose outgoing indices will be fused together.

of possible charge sectors of  $T$ , which in turn label the various degeneracy tensors

$$\{P_{0,0,0}, P_{0,1,1}, P_{1,0,1}, P_{1,1,0}, P_{1,1,1}, P_{2,1,1}\}. \quad (3.18)$$

Fusing outgoing indices  $j \times k \rightarrow l$  results in a new index that carries the fused quantum numbers shown in Table 3.3. Here the degeneracies of the fused quantum numbers are determined by all combinations leading to a specific fusion outcome, e.g.  $1_{34} = (0_1 \otimes 1_6) + (1_4 \otimes 0_1) + (1_4 \otimes 1_6)$ . Again, the list of possible charge sec-

index	irreps with degeneracies $\{j_{t_j}\}$
$i$	$[0_1, 1_2, 2_3]$
$l$	$[0_{25}, 1_{34}, 2_{24}]$

TABLE 3.3: Quantum numbers and degeneracies for the two-index tensor obtained by fusing two indices of the three-index tensor of Table 3.2.

tors determines and labels the degeneracy blocks of tensor  $T'$ , which are given by  $\{P'_{0,0}, P'_{1,1}, P'_{2,2}\}$ . In order to relate the degeneracy tensors of  $T_{ijk}$  to the ones of  $T'_{il}$  one has to identify which input charge sectors will be assigned to which output charge sector according to the fusion rules. This assignment is however not unique due to the non-Abelian character of  $SU(2)$ , it is shown in Table 3.4. In the fusion operation an output degeneracy tensor is composed by reshaping the contributing degeneracy tensors and concatenating them. For the degeneracy block  $P'_{0,0}$  the contributing degeneracy tensors  $P_{0,0,0}$  and  $P_{0,1,1}$  are reshaped by fusing together indices  $t_j$  and  $t_k$

output charge sector	contributing input charge sector
[0, 0]	[0, 0, 0], [0, 1, 1]
[1, 1]	[1, 0, 1], [1, 1, 0], [1, 1, 1]
[2, 2]	[2, 1, 1]

TABLE 3.4: Map between the input charge sectors of  $T$  and the output charge sectors of  $T'$  for the fusion of two indices. Each output degeneracy tensor corresponding to an output charge sector is composed of transformed input degeneracy tensors associated to the contributing input charge sectors.

and the resulting matrices are concatenated. This operation is denoted by

$$P'_{0,0} = P_{0,(0,0)} \circ P_{0,(1,1)} , \quad (3.19)$$

where the indices in brackets denote the fusion of these two indices and  $\circ$  denotes the concatenation of the resulting arrays along the fixed dimensions. In this example  $P_{0,(0,0)}$  yields a  $(1 \times 1)$ -dimensional array,  $P_{0,(1,1)}$  yields a  $(1 \times 24)$ -dimensional array which are concatenated along the fixed row. This yields the final  $(1 \times 25)$ -dimensional degeneracy tensor  $P'_{0,0}$  for the output tensor. Similarly the remaining degeneracy tensors are constructed by

$$\begin{aligned} P'_{1,1} &= P_{1,(0,1)} \circ P_{1,(1,0)} \circ P_{1,(1,1)} \\ P'_{2,2} &= P_{2,(1,1)} . \end{aligned} \quad (3.20)$$

This formalism can be extended to tensors with an arbitrary number of indices, for which a generic fusion operation can be performed by pairwise fusion of indices. The transformation on the fusion tree is done by removing the node where the two indices are attached, and promoting the internal edge connected to the removed node to an external edge (special treatment for tensors less than four indices is required).

### Splitting of Indices

The splitting of indices is the inverse operation to the fusion of indices. The elementary split operation separates an index – that was previously fused – into the two original indices. On the level of the fusion tree this corresponds to promoting the split index to an internal edge, and attaching a new node for the two separate indices. In terms of the degeneracy tensors one can use the same map as for the fusion operation (see Table 3.4), only now the input degeneracy tensors have to be broken into different pieces, that are reshaped according to the degeneracies of the corresponding quantum numbers and associated to the output charge sectors. Due to the possibility of concatenated fusion operations one needs to keep track of the fusion history, which is unraveled again in the split operations.

## 3.4 Contractions of Symmetric Tensors

One of the most important operations in tensor network algorithms is the efficient contraction of two tensors or generally larger networks of tensors. For regular, non-symmetric tensors contractions can be implemented via matrix-matrix or matrix-vector multiplications using permutation and reshaping operations to prepare the input tensors and transform the output tensor to the desired form. For symmetric tensors however, contractions are more involved due to the internal structure of the tensors and the underlying fusion trees. Here we will explain the essential procedure

and steps, but we will spare technical details that – though being very relevant – strongly depend on the actual implementation.

### 3.4.1 Matrix-Matrix Multiplication

One of the most elementary operation is the multiplication of two matrices, to which every general contraction of two tensors can be related. We will present this example here to exemplify some first complications due to the symmetry. Additionally this operation unveils the core benefit of implementing symmetries, as we will see below. Consider two  $SU(2)$ -symmetric matrices carrying quantum numbers  $j_{t_j} = [0_4, 1/2_6, 1_3]$  on both indices respectively. The decomposition based on the fusion rules leads to a block-diagonal structure, because the only possible blocks are the ones for which the quantum numbers on the indices match. Therefore both matrices look like

$$T = \begin{pmatrix} \left( P_{0,0} \right)_{4 \times 4} & & \\ & \left( P_{\frac{1}{2}, \frac{1}{2}} \right)_{6 \times 6} & \\ & & \left( P_{1,1} \right)_{3 \times 3} \end{pmatrix}, \quad (3.21)$$

where the dimensions of the blocks are given by the degeneracies of the quantum numbers. The multiplication of the full matrices is now reduced to the multiplication of the individual blocks of the symmetric decomposition. This is clear from the block-diagonal structure, however it implies that only blocks with matching quantum number on the contracted leg are multiplied. This is a general property for the contraction of arbitrary tensors, where all quantum numbers on the contracted indices need to match.

Before going to more general contractions let us note that the computational speedup obtained by implementing symmetries originates precisely in the matrix-matrix multiplication or generally in contractions. The symmetric decomposition reduces the computational cost by trading the operation on full, non-symmetric tensors with multiple, but much cheaper operations on small blocks of tensors.

### 3.4.2 General Tensor Contractions

One important contribution of the symmetric tensor could be neglected in the previous example of a matrix-matrix multiplication – the fusion tree. For general contractions however, the so called spin network, i.e. the network of fusion trees of the contracted tensor leads to numerical factors for the degeneracy tensors. Since a fully general contraction can always be achieved by sequential contractions of only two tensors we will restrict to that case. Furthermore, the possible contractions of two tensors can be classified into a class that does not exhibit loops in the contracted fusion tree and a class that exhibits loops in the spin network.

#### Loop-Free Contractions

Loop-free contractions always involve only one contracted index. An example of this is the matrix-matrix multiplication in Sec. 3.4.1, or the contraction of two four-index tensors as shown in Fig. 3.15. In the case of loop-free contractions the final fusion tree is a direct combination of both input fusion trees. The charge sectors labeling the new degeneracy blocks (i.e. the fusion tree decorations) are constructed by the quantum numbers of the input blocks where the contracted index is promoted to an additional internal edge. In the present example, new blocks are the combination of



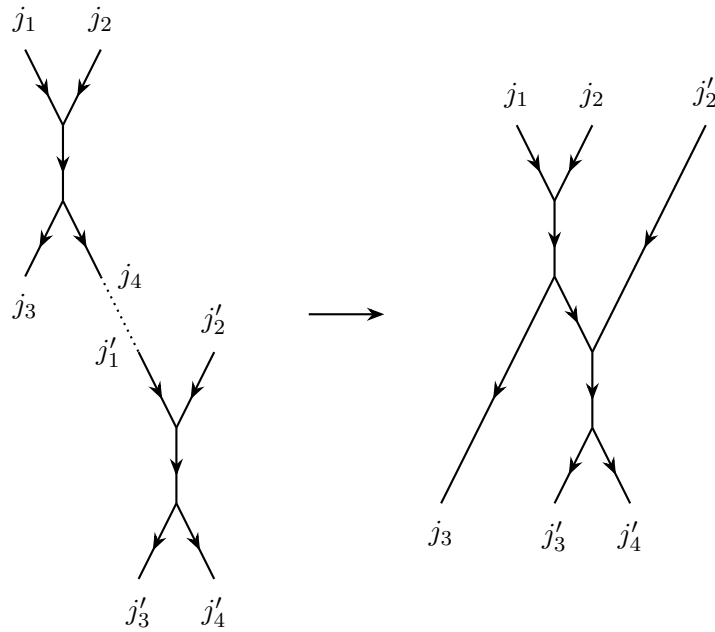


FIGURE 3.15: Contraction of two four-index tensors resulting in a six-index tensor. No loops appear in the contractions when only one index is summed over.

input blocks for which  $j_4 = j'_1$ . Here the new degeneracy tensors originate from a contraction of a single pair of input degeneracy tensors.

### Contractions with Loops

The general and common case is a contraction of two or more indices, resulting in loops in the spin networks. This operation is different from loop-free contractions in-

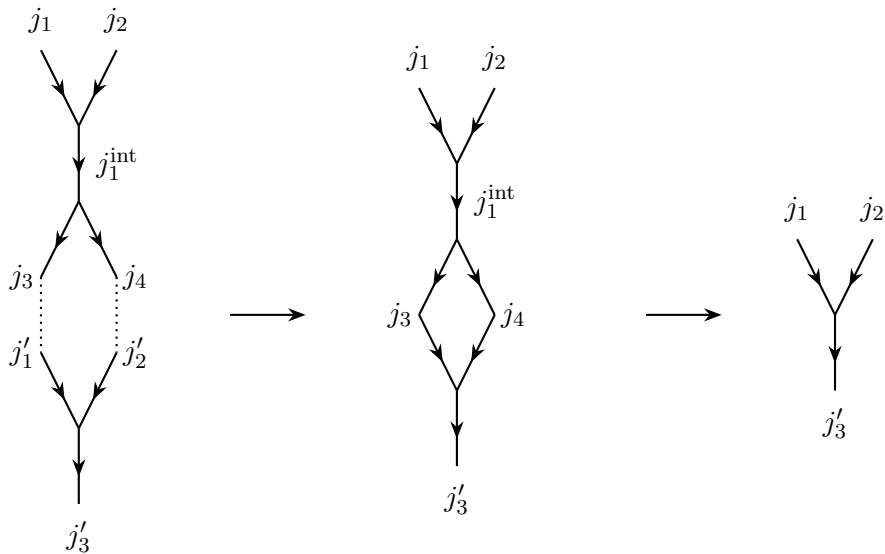


FIGURE 3.16: Contraction of a four-index tensor and a three-index tensor. The loop in the spin network can always be eliminated by exploiting the orthogonality relation for Clebsch-Gordan coefficients, resulting in a three-index tensor.

so far, as loops can lead to additional numerical factors for the contracted blocks, and the map between pairs of input degeneracy tensors and output degeneracy tensors is no longer in one-to-one correspondence. We will demonstrate the two intricacies with

some examples in the following. First, let us again consider the contraction of a four-index with a three-index tensor, this time along two indices. This is shown in Fig. 3.16 where the resulting spin network exhibits a loop. Spin networks that include loops are commonly referred to as graphs, they are however an inefficient representation of the symmetric tensor and a reduction to a fusion tree without loops is desirable. The loop appearing in the present contraction is the smallest one possible, consisting of only one splitting and one fusion node. It is denoted as a *bubble*. Making use of the orthogonality relation for Clebsch-Gordan coefficients this loop reduces exactly to the identity for  $j_1^{\text{int}} = j'_3$ , and vanishes otherwise (refer to Fig. 3.5). It can therefore be removed from the spin network, which then results in a simple three-index Clebsch-Gordan tensor. However, as stated above, loops in the network lead to a many-to-one

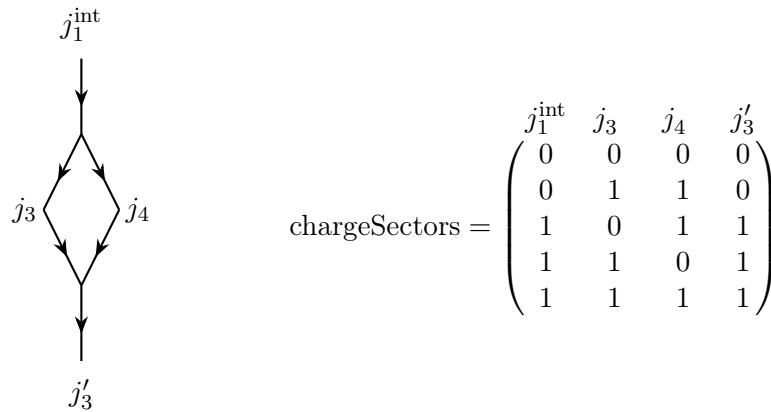


FIGURE 3.17: Possible charge sectors for the diamond shaped loop consisting of a splitting and a fusion node. The orthogonality relation for Clebsch-Gordan coefficients enforces  $j_1^{\text{int}} = j'_3$  and has already been applied for the charge sectors.

correspondence for the charge sectors and therefore the degeneracy tensors as well. To demonstrate this let us consider a concrete example in which we choose to assign  $j = [0, 1]$  to all external indices. For input tensor  $A$  corresponding to the upper fusion tree, the internal edge can carry  $j_1^{\text{int}} = [0, 1, 2]$ . In order to illustrate the relation between input and output charge sectors we can focus on the loop in the network. The table of charge decorations for this structure is shown in Fig. 3.17, where the orthogonality of Clebsch-Gordan coefficients has already been exploited. Due to the elimination of the loop the two first charge sectors in the list will be assigned to the same charge sector in the contracted tensor, and the same goes for the last three charge sector. For instance, the final charge sector  $[0, 0, 0]$  of the contracted tensor consists of sectors  $[0, 0, (0, 0, 0, 0)]$  and  $[0, 0, (0, 1, 1, 0)]$ , where the quantum numbers in parenthesis are the ones for the loop configuration, and the other ones are for  $j_1$  and  $j_2$ . Consequently, it follows that the corresponding degeneracy tensor  $P_{0,0,0}$  is the sum of two pairs of tensors that are contracted along the marked indices each.

For arbitrary contractions the loops in the spin networks are however not always simple loops, in the sense that the corresponding Clebsch-Gordan coefficients reduce to the identity. Instead the evaluation or simplification of the spin network yields additional numerical factors that can be absorbed into the degeneracy tensors, as we have done before. As a more involved example we consider the contraction of two five-index tensors depicted in Fig. 3.18. Here the spin network exhibits two loops, which are not easily removable. However, the resulting loop structure is precisely the one which defines an  $F$ -move (see also Fig. 3.9). Therefore, applying the appropriate

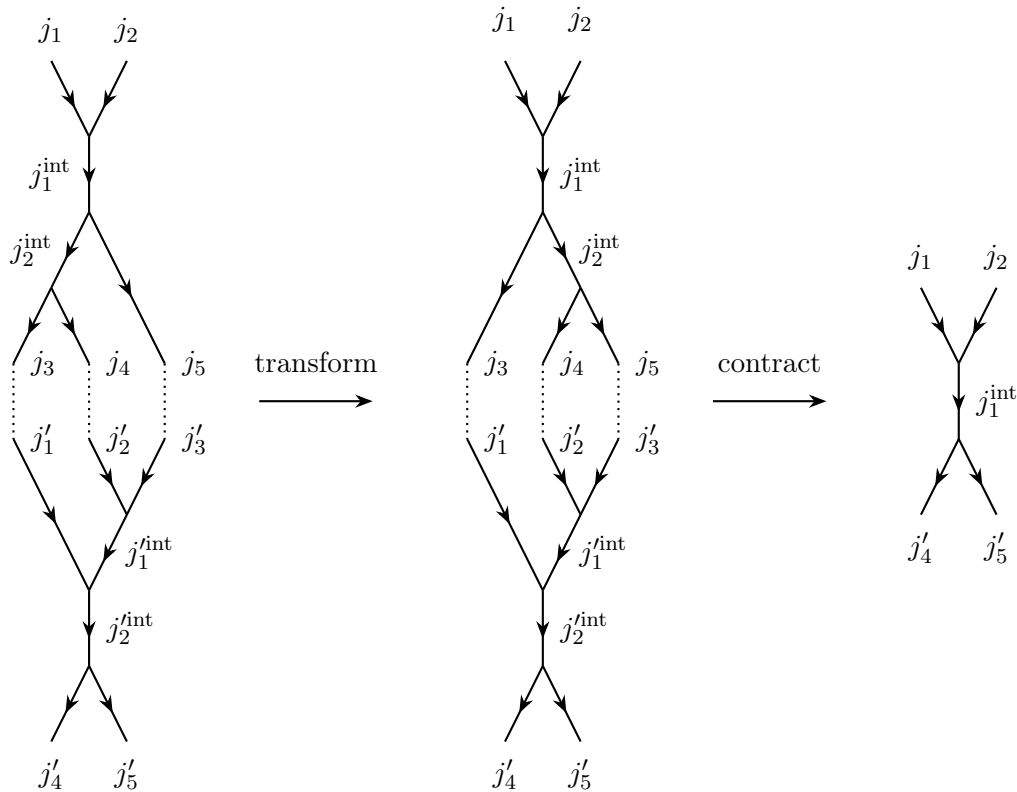


FIGURE 3.18: Contraction of two five-index tensors that results in non-trivial loops in the spin network. These structures can be simplified to simple loops (bubbles) using  $F$ -moves, afterwards they can be easily eliminated.

$F$ -move to either one of the input tensors simplifies the loops to two nested bubbles, which can be removed. Here the first, small bubble implies  $j_2^{\text{int}} = j_1'^{\text{int}}$  and the second, large bubble implies  $j_1^{\text{int}} = j_2'^{\text{int}}$ . This discussion sums up the challenges arising for the contraction of  $SU(2)$ -symmetric tensors. There are some more subtleties and special cases which can occur, and we refer the interested reader to Ref. [85] for a detailed elaboration of the subject.

### 3.5 Matrix Factorizations

Matrix factorizations are an important part of tensor network calculations. As shown in Sec. 2.1.1, decompositions like the singular value decomposition enable the calculation of relevant properties like the entanglement entropy. Besides that the SVD has a high significance for the approximation of matrices and quantum states based on the spectrum of singular values. It is frequently used in TN algorithms to implement truncation schemes that discard irrelevant degrees of freedom to keep simulations manageable [86]. The SVD has already been introduced along with its visual interpretation in Fig. 2.1. Let us consider an  $SU(2)$ -invariant matrix with one incoming and one outgoing index that can be written in a block-diagonal form

$$M = \bigoplus_j (M_j \otimes \mathbb{I}_{2j+1}) . \quad (3.22)$$

Due to the fusion rules the quantum numbers on both indices need to match, so that  $j$  is the only relevant quantum number and the Clebsch-Gordan coefficients simplify

to the  $(2j + 1)$ -dimensional identity. The matrix blocks  $M_j$  and therefore the whole matrix does not need to be square.

### 3.5.1 Symmetric Singular Value Decomposition

Exploiting the block-diagonal structure of an  $SU(2)$ -invariant matrix as in Eq. (3.22), the SVD of the full matrix reduces to an individual SVD for each degeneracy block. This is illustrated in Fig. 3.19 for the case of an *economic SVD*, that discards all vanishing singular values. This procedure can be equivalently applied to other matrix

$$\begin{pmatrix} \square & & \\ & \square & \\ & & \square \end{pmatrix} = \begin{pmatrix} \square & & \\ & \square & \\ & & \square \end{pmatrix} \cdot \begin{pmatrix} \square & & \\ & \square & \\ & & \square \end{pmatrix} \cdot \begin{pmatrix} \square & & \\ & \square & \\ & & \square \end{pmatrix}$$

$M \qquad \qquad U \qquad \qquad \Lambda \qquad \qquad V^\dagger$

FIGURE 3.19: The SVD of an  $SU(2)$ -symmetric matrix can be performed on individual blocks leading to increased performance for large matrices. The green line indicates the singular values in the block-diagonal matrix  $\Lambda$ .

factorizations, such as eigenvalue decomposition, polar decomposition, and others.

### 3.5.2 SVD Based Truncation

As mentioned previously, the SVD can be used to approximate a matrix by another matrix with fewer singular values. To this end, singular values that are smaller than a given error  $\epsilon$  are discarded and the matrices  $U$  and  $V^\dagger$  are truncated accordingly, as visualized in Fig. 3.20. The truncated matrix  $M'$  is a good approximate to the

$$\square = \square \cdot \square \cdot \square$$

$M \qquad \qquad U \qquad \qquad \Lambda \qquad \qquad V^\dagger$

FIGURE 3.20: Truncation of the matrices  $U$ ,  $\Lambda$  and  $V^\dagger$  obtained from an SVD. Only the largest singular values are retained and the parts right of and below the dotted lines are deleted.

original matrix  $M$  if the error  $\epsilon$  is small. The accuracy of the approximation – called the *discarded weight* – is typically given by the normalized sum of the discarded squared singular values.

Similarly to the symmetric version of the SVD, the truncation of a symmetric tensor containing the singular values can be performed on each block. However it is important to remember that the truncation needs to be performed in a way that minimizes the trace loss of the total matrix  $M$ . Let  $\lambda_{j,k}$  denote the  $k$ -th singular value in the various blocks labeled by quantum number  $j$ . According to the decomposition of an  $SU(2)$ -invariant matrix in Eq. (3.22), every singular value  $\lambda_{j,k}$  appears  $(2j + 1)$  times in the

singular value spectrum of  $M$ . The trace of  $M^\dagger M$  is therefore given by

$$\mathrm{tr}(M^\dagger M) = \sum_{j,k} (2j+1) \lambda_{j,k}^2 . \quad (3.23)$$

The approximation in the singular values  $\lambda_{j,k}$  then needs to take the weight of  $(2j+1)$  into account, because a small singular value with a large weight can contribute more to the trace than a larger singular value with smaller weight. Ultimately this may lead to a different amount of truncation in the various blocks. Some blocks might require no truncation at all, in other blocks all the singular values might be irrelevant and therefore discarded. In this case the corresponding irrep  $j$  can be removed from  $U$ ,  $\Lambda$  and  $V^\dagger$ .

In the SVD based truncation we see yet another advantage of keeping the symmetry in tensor network simulations. Based on the singular values, algorithms can automatically determine relevant symmetry sectors and discard others, e.g. keeping only integer and discarding half-integer spin sectors. This can be useful to determine different phases of matter based on the quantum numbers on the virtual legs of a TN [87].

### 3.6 Extension to Anyonic Theories

One of the main advantages of working with algebraic fusion trees as described in Sec. 3.2.1 is that the formalism can be readily generalized to anyonic systems as well. Anyons are quasi-particle excitations of many-body systems that can only be found in two-dimensional systems, exhibiting extended particle exchange statistics. This means that anyons neither behave as bosons nor as fermions, for which the phase of the wave function is  $+1$  or  $-1$  for a particle exchange respectively. Anyons can be classified as Abelian or non-Abelian. For Abelian anyons the phase for the wave function can be anything  $|\psi_1\psi_2\rangle = e^{i\theta} |\psi_2\psi_1\rangle$ , hence their name. For non-Abelian anyons the exchange statistics is even more involved and leads to a linear unitary transformation in the space of necessarily degenerate ground states.

Non-Abelian anyonic theories are described by so called quantum symmetries or quantum groups. Those groups will generally include multiplicities which is not treated in this thesis. There are however examples of multiplicity-free quantum groups, for instance deformations of the group  $SU(2)$  denoted by  $SU(2)_k$ . Here the usual fusion rules are altered to be

$$j_a \times j_b \in \{|j_a - j_b|, \dots, k - j_a - j_b\} . \quad (3.24)$$

As an example we consider Fibonacci anyons described by  $SU(2)_3$ . Fibonacci anyons<sup>4</sup> are the simplest anyons with non-Abelian braiding statistics [88]. The charges of the group are now called *topological charges* instead of irreducible representations. There are two different quasi-particles (charges) labeled  $\mathbf{1}$  for the vacuum and  $\tau$  for the only non-trivial particle. The fusion rules are given by

$$\begin{aligned} \mathbf{1} \otimes \tau &= \tau \\ \tau \otimes \mathbf{1} &= \tau \\ \tau \otimes \tau &= \mathbf{1} \oplus \tau , \end{aligned} \quad (3.25)$$

---

<sup>4</sup>The name 'Fibonacci' originates from the number  $F_n$  of decorated fusion trees for the fusion of  $n$  of such anyons. This results in a recursive relation  $F_{n+1} = F_n + F_{n-1}$ , which is exactly the Fibonacci sequence [88].

here the non-Abelian property is manifested in the last equation. As demonstrated in Fig. 3.21 the underlying structure is conveniently represented in terms of fusion trees. The fusion rules can be incorporated by representing the trivial particle by a spin-0

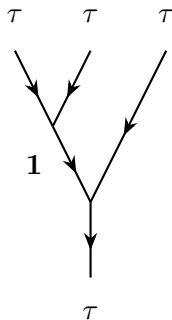


FIGURE 3.21: Fusion trees are the natural language to describe the Hilbert space and fusion rules of anyonic systems. Here an example of Fibonacci anyons is given.

and the  $\tau$  particle by a spin-1. In order to adapt the  $SU(2)$ -symmetric implementation to  $SU(2)_k$  there are some more changes in order. Contrary to the irreducible representations of  $SU(2)$ , the topological charges of anyonic theories typically come with a quantum dimension different from one. Here we have

$$d_{\mathbf{1}} = 1 \quad d_{\tau} = (1 + \sqrt{5}) / 2 , \quad (3.26)$$

where the value for  $d_{\tau}$  is also called the golden ratio. They have to be included for certain operations, such as reversal or fusion and splitting of tensor indices. Furthermore, the permutation of charges needs to be described in terms of a braiding tensor  $R_c^{ab}$  which is generally different for a clockwise or anticlockwise swap operations. Additionally the recoupling coefficients, described by  $F$ -moves have to be adapted (they replace the Wigner 6- $j$  symbols).

### 3.7 Comments on Abelian Symmetries

The implementation of non-Abelian symmetries in TNs poses a significantly more complex challenge than the implementation of Abelian symmetries. A comparison with one of the most common Abelian symmetries in quantum many-body physics, the conservation of the number of particles in the system described by the symmetry group  $U(1)$ , shows the disparity. Similarly to the case of  $SU(2)$ , the single-particle basis  $|i_k\rangle$ , with  $k = 1, \dots, p$  can be labeled by  $|n, t_n, m_n\rangle$ , where  $n$  are the charges,  $t_n$  labels the states in the degeneracy subspace  $\mathbb{D}_n$ , and  $m_n$  labels the states in the irrep space  $\mathbb{V}_n$  (see also Sec. 3.1). For the group  $U(1)$  the charges  $n$  correspond to the particle number and since all irreducible representations are non-degenerate, i.e.  $m_n = 1$  for all  $n$ , we can omit the last quantum number. The three-index structural tensors again describe the unique mapping between the vector spaces  $\mathbb{V}_{n_a} \otimes \mathbb{V}_{n_b} \cong \mathbb{V}_{n_c}$ , denoted by  $n_a \times n_b \rightarrow n_c$ . Here the fusion rules of the symmetry group  $U(1)$  are given by

$$n_c = n_a + n_b , \quad (3.27)$$

so that the structural tensors are simply given by  $Q_{n_a n_b n_c} = \delta_{n_a + n_b, n_c}$ . As a consequence, the full formalism of fusion trees described for  $SU(2)$ -symmetric tensors is not

required when dealing with  $U(1)$ , or generally with Abelian symmetries [17]. Nevertheless, our implementation of  $SU(2)$  symmetry can be readily extended to include Abelian symmetries as well.

### 3.8 Summary

In this chapter we have presented a general formalism to include arbitrary symmetries in tensor networks. Focusing on  $\mathcal{G} = SU(2)$  we demonstrated how the structure of the group can be accounted for by fusion trees decorated with charge labels, that are an analytic representation for the coupling of different spins. For numerical purposes the functions contained in the regular tensor network toolbox, e.g. permutation and reshaping of tensor indices, tensor contractions and factorizations have to be modified to respect the internal decomposition of symmetric tensors. The symmetric blocks of the tensors are determined by the fusion rules of the symmetry and factorize into degeneracy tensors holding the variational parameters, and decorated fusion trees representing the structural part of the symmetry. The formalism can be readily extended to deal with anyonic theories and also to groups with multiplicities, if required.

The  $SU(2)$ -invariant tensor network framework developed during the time of the PhD is utilized to study a quasi-1d spin-1/2 ladder model in Chapter 4, as well as different spin models on 2d lattices using different tensor network techniques in Chapter 5. Furthermore, the symmetric framework is also suitable for the representation of partition functions of classical spin models, with a demonstrative example presented in Chapter 7.





## Chapter 4

# Quantum Criticality on a Chiral Ladder

The  $SU(2)$ -invariant tensor network framework was first used to implement a symmetric version of the famous infinite Density Matrix Renormalization Group algorithm (iDMRG), used to study one-dimensional quantum lattice systems predominantly. The plain spin-1/2 antiferromagnetic Heisenberg model described by the Hamiltonian

$$H_{\text{HB}} = J \sum_j \vec{S}_j \vec{S}_{j+1} \quad (4.1)$$

served as a validation and benchmark of the  $SU(2)$ -symmetric code. In principle other models could serve as a benchmark as well, the 1d Heisenberg model is however one of the simplest interacting models with  $SU(2)$  symmetry. Consider the operator

$$S^z = \sum_j S_j^z, \quad (4.2)$$

which measures the number of up and down spins, e.g. the total magnetization along the  $z$ -axis. This operator commutes with the Hamiltonian  $H_{\text{HB}}$  so that one can restrict to a fixed total magnetization, which corresponds to a  $U(1)$  symmetry of the model. Targeting an  $U(1)$ -symmetric ground state selects a state with vanishing magnetization  $\langle S^z \rangle = 0$ . The Heisenberg Hamiltonian also commutes with the total spin operator

$$\vec{S} = \sum_j \vec{S}_j, \quad (4.3)$$

which reveals the  $SU(2)$ -symmetry mentioned above. The ground state of the spin-1/2 Heisenberg model is known to be critical [89]. In critical systems the energy gap between the ground and the first excited state vanishes [35]. This has profound consequences as compared to gapped systems, such as scale-invariance, violation of the area-law for the entanglement entropy, and long-range correlations in the system. We have argued that gapped quantum states are efficiently represented by an MPS due to the fulfillment of the area-law (refer to Sec. 2.4). In symmetric tensor network simulations the bond dimension can be exhausted far more than in non-symmetric simulations, hopefully enough to represent even critical quantum states accurately. Critical quantum states are therefore challenging applications for TNs, and as a more interesting physical model beyond the Heisenberg model we studied a spin-1/2 model on a ladder geometry, as presented in this chapter.

## 4.1 Motivation and Model

The Hubbard model, a minimal microscopic description for interacting electrons is often the starting point for the study of electronic lattice systems. The ordinary Hubbard Hamiltonian takes the form

$$H_{\text{Hubbard}} = -t \sum_{\langle i,j \rangle, \sigma} \left( c_{i\sigma}^\dagger c_{j\sigma} + c_{j\sigma}^\dagger c_{i\sigma} \right) + U \sum_i n_{i\uparrow} n_{i\downarrow}. \quad (4.4)$$

Here  $\sigma = \{\uparrow, \downarrow\}$  are the spin projections of the electrons and  $\langle i, j \rangle$  denotes nearest neighbours. The first term describes hopping of both species on the lattice, the second term is a repulsive interaction if two electrons occupy the same site. Consider the Hubbard model to live on a Kagome lattice that is subject to a magnetic field. Due to the magnetic field the Hamiltonian is extended by a Zeeman term  $h_z$  as well as complex hopping amplitudes  $t_{ij}$ , that generate a flux  $\Phi$  through each elementary plaquette of the lattice. The extended Hubbard Hamiltonian is now given by

$$H_{\text{Hubbard}} = - \sum_{\langle i,j \rangle, \sigma} \left( t c_{i\sigma}^\dagger c_{j\sigma} + t^* c_{j\sigma}^\dagger c_{i\sigma} \right) + U \sum_i n_{i\uparrow} n_{i\downarrow} + \frac{h_z}{2} \sum_i (n_{i\uparrow} - n_{i\downarrow}). \quad (4.5)$$

In the particular limit of large on-site interaction  $U$  the Hamiltonian can be expanded in terms of  $t/U$  at half-filling which results in the spin Hamiltonian

$$H = J_{\text{HB}} \sum_{\langle i,j \rangle} \vec{S}_i \cdot \vec{S}_j + h_z \sum_i S_i^z + J_\chi \sum_{i,j,k} \vec{S}_i \cdot (\vec{S}_j \times \vec{S}_k), \quad (4.6)$$

where  $J_{\text{HB}} \sim t^2/U$  and  $J_\chi \sim \Phi t^3/U^2$  to lowest order in perturbation theory [90]. The three-spin term  $\chi_{ijk} = \vec{S}_i \cdot (\vec{S}_j \times \vec{S}_k)$  is denoted as the scalar spin chirality [91], it breaks time-reversal symmetry and parity but preserves  $SU(2)$  symmetry. Without any time-reversal symmetry breaking, e.g.  $h_z = 0$  and  $J_\chi = 0$  the Hamiltonian in Eq. (4.6) reduces to the standard Heisenberg Hamiltonian and the resulting model on the Kagome lattice is a paradigmatic example of a frustrated quantum antiferromagnet. This model will be subject to analysis in Chapter 5, exploiting  $SU(2)$  symmetry in a 2d tensor network algorithm.

Tuning the spin Hamiltonian to the opposite limit, e.g.  $J_{\text{HB}} = 0$  and  $h_z = 0$  yields a chiral spin liquid phase on the Kagome lattice that is not time-reversal symmetric, as explained in Ref. [91]. The isolated study of the scalar spin chirality term is quiet unrealistic in existing materials. However, it could be implemented in a tight-binding model with density-assisted hopping terms [68], which has been realized experimentally in the framework of ultracold atoms [92]. Here we want to pick up the chiral part  $\chi_{ijk}$  of the Hamiltonian and study it in a one-dimensional limit of a two-dimensional lattice, namely on a ladder geometry as shown in Fig. 4.1. Unlike the Kagome lattice,

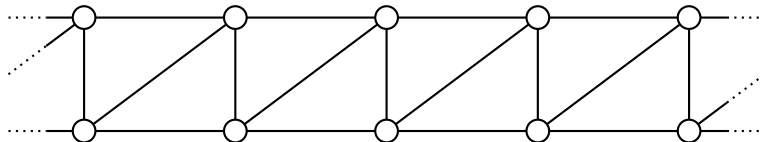


FIGURE 4.1: The chiral Hamiltonian of Eq. (4.7) is defined on a ladder geometry with side-sharing triangles (instead of corner-sharing triangles as in the Kagome lattice).

the spin ladder features side-sharing triangles, however it can serve as a starting point

to study chiral interactions in spin chains with increasing number of legs in order to reveal the transition to true 2d physics. Due to the quasi-1d form of the ladder we can label the sites in a snake-like pattern, as shown in the details of the ladder in Fig. 4.2. The model that we want to study is then described by the chiral Hamiltonian

$$H = \sum_i J_i \vec{S}_i \cdot (\vec{S}_{i+1} \times \vec{S}_{i+2}) \quad (4.7)$$

with  $\vec{S}_i$  the spin-1/2 operator at site  $i$  and individual coupling constants  $J_i$  for each triangle. Focusing on the smallest unit cell of four sites we will consider the cases where  $J_i \in \{-1, +1\}$  and choose the coupling coefficients depending on the traversal of the triangles. A triangle consisting of sites  $i$ ,  $i+1$  and  $i+2$  is traversed in

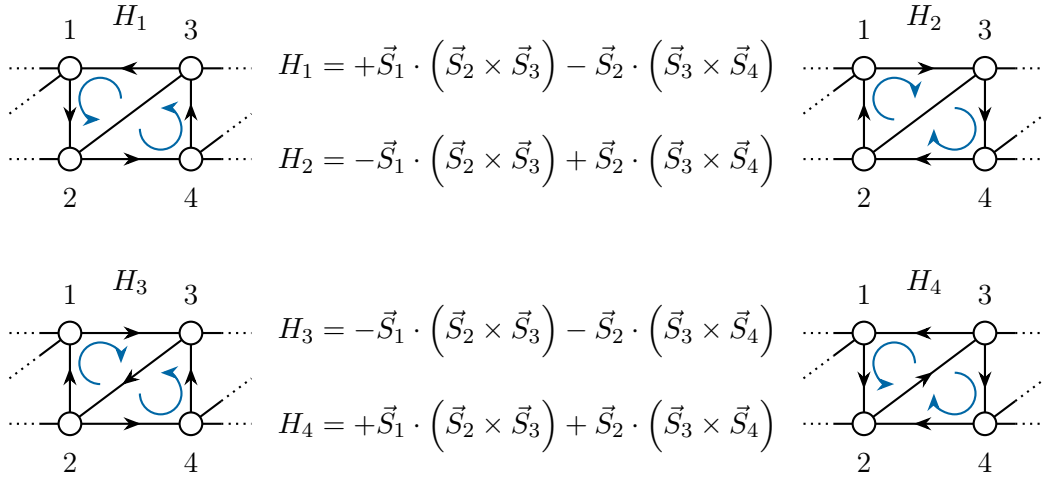


FIGURE 4.2: The chiral Hamiltonian of Eq. (4.7) for clockwise and anticlockwise configurations of the triangles. For  $H_1$  and  $H_2$  the orientation is the same, e.g. both clockwise or anticlockwise, for  $H_3$  and  $H_4$  the orientation is opposite.

(against) the direction of the labels if  $J_i = +1$  ( $J_i = -1$ ). This can be recast into a clockwise/anticlockwise ordering of triangles. For  $J_i = (-1)^i$  all triangles in the ladder are in a clockwise configuration, and for  $J_i = -(-1)^i$  they are all anticlockwise. In contrast,  $J_i = 1$  or  $J_i = -1$  results in a staggered distribution of triangles. In Fig. 4.2 the four possible Hamiltonians on a unit cell of two triangles are shown. Since  $H_1 = -H_2$  and  $H_3 = -H_4$  both pair of Hamiltonians have the same spectrum and only the relative orientation between the two triangles matters. We can therefore restrict to  $H_1$  and  $H_3$  as different cases.

Let us analyze the symmetries of the Hamiltonian. Clearly it has an  $SU(2)$  symmetry which we will exploit in the numerical analysis. Both Hamiltonians are however odd under time-reversal symmetry ( $\vec{S}_i \rightarrow -\vec{S}_i$ ), which results in  $\mathcal{T}H_i\mathcal{T}^{-1} = -H_i$ . The inversion at the center of the chain leaves  $H_1$  invariant, whereas  $\mathcal{P}H_3\mathcal{P}^{-1} = -H_3$ . This leads to a different behaviour between the two cases with different relative triangle orientations ( $H_1$  and  $H_3$ ) for observables and the eigenstates. For instance, the spin currents of  $H_1$  are expected to be counter-propagating (even under parity), whereas they propagate in the same direction for  $H_3$  (odd under parity) [68].

#### 4.1.1 Effective Low-Energy Physics with Kadanoff Coarse-Graining

As a first step to analyze the model we perform a Kadanoff coarse-graining procedure to expose the dominant physics. To this end the  $2^3$ -dimensional Hilbert space of the

spins on a triangle  $n$  starting at site  $i = 3n - 2$  is projected onto the two-dimensional subspace with lowest energy using the isometry

$$W_n : \frac{1}{2} \otimes \frac{1}{2} \otimes \frac{1}{2} \longrightarrow \frac{1}{2}. \quad (4.8)$$

Using this isometry we can construct the operators in the relevant spin-1/2 subspace and find the emerging effective Hamiltonian. Let us start by writing the chiral Hamiltonian for one triangle in terms of projectors

$$\vec{S}_1 \cdot (\vec{S}_2 \times \vec{S}_3) = \sum_{\alpha=\pm} \alpha \frac{\sqrt{3}}{4} \mathbb{P}_{1/2,\alpha} + 0 \mathbb{P}_{3/2}. \quad (4.9)$$

The three spins on every triangle can couple according to  $(1/2)^{\otimes 3} = 1/2_- \oplus 1/2_+ \oplus 3/2$ , where  $1/2_{\pm}$  denotes subspaces of spin-1/2 with positive and negative energy. In order to project onto the subspace with lowest energy the sought-after isometry depends on the sign of the triangle  $n$  and becomes

$$W_n W_n^\dagger = \mathbb{P}_{1/2, -\text{sign}(J_{3n-2})}. \quad (4.10)$$

Using this isometry we can construct the coarse-grained spin operators involved in the interaction between triangle  $n$  and  $n + 1$ . Using a suitable unitary transformation it turns out that the projectors can be chosen such that for all sites  $j \in \{3n-2, 3n-1, 3n\}$  and  $\alpha \in \{\pm\}$

$$\begin{aligned} W_{1/2,\alpha} \vec{S}_j W_{1/2,\alpha}^\dagger &= \frac{1}{3} \tilde{S}_n \\ W_{1/2,\alpha} (\vec{S}_j \times \vec{S}_{j+1}) W_{1/2,\alpha}^\dagger &= \frac{\alpha}{\sqrt{3}} \tilde{S}_n, \end{aligned} \quad (4.11)$$

where  $\tilde{S}_n$  is the spin-1/2 operator in the relevant subspace. The effective spin-1/2 model resulting from the coarse-graining procedure is then given by

$$H_{\text{eff}} = -\text{sign}(J_1 J_2) \frac{|J_1| + |J_2|}{3\sqrt{3}} \sum_{n=1}^N \tilde{S}_n \tilde{S}_{n+1} - \frac{\sqrt{3}}{4} \frac{|J_1| + |J_2|}{2} N \quad (4.12)$$

with an additive constant that can be omitted. Here  $N \simeq L/3$  is the number of effective triangles in the original model. In the low-energy subspace we obtain an effective spin-1/2 Heisenberg model, whose magnetic character (ferromagnetic or antiferromagnetic) depends on the mutual sign of the couplings  $J_1$  and  $J_2$  of the two triangles in the unit cell. We can now resort to known properties of the Heisenberg model to foresee the behaviour of the triangle model.

Configuring all triangle to be (anti)clockwise ( $H_1$  and  $H_2$ ) leads to an antiferromagnetic model, which is expected to be gapless with central charge<sup>1</sup>  $c = 1$ , and the ground state tends to minimize the total spin of the chain. Thus for  $N$  even it will be in the total spin zero sector. In contrast, choosing a uniform pattern of coupling coefficients ( $H_3$  and  $H_4$ ) yields an effective ferromagnetic model so that the ground state is likely to maximize the total spin of the chain. Although this low-energy projection is a strong simplification we will confirm the predictions for  $H_1$  with our numerical

<sup>1</sup>The central charge  $c$  is an important property of the Conformal Field Theory describing the scale-invariant critical ground state of the 1d spin-1/2 quantum Heisenberg model, or models in the same universality class.

findings. Additional analysis with exact diagonalization as well as bosonization for  $H_1$  and  $H_3$  further validates the first intuition, these results are presented in Ref. [68].

## 4.2 Density Matrix Renormalization Group

The Density Matrix Renormalization Group (DMRG) and its version for infinite lattices (iDMRG) are numerical simulation techniques to approximate low-energy eigenstates of quantum many-body systems, mostly used to simulate ground states [48, 49]. It is based on the idea that these quantum states can be described efficiently by the degrees of freedom that are most important for the target state. For short-range and gapped Hamiltonians there is always an efficient representation due to the area-law for the entanglement entropy, so that DMRG naturally operates on the family of matrix product states and is nowadays the standard tool in 1d [66, 93]. Its application is however not limited to gapped 1d quantum states. (i)DMRG is also widely used to study critical systems that are approximable by sufficiently large bond dimensions as we will show in this chapter, and can also be used to study 2d quantum states. Here the local interactions in 2d are mapped to long-range interactions in the 1d representation, in which one lattice direction is chosen to be periodic instead of infinite.

The standard DMRG algorithm is based on finite MPS, the idea behind it however extends to infinite systems as well. Based on a Hamiltonian with local interactions, the idea of DMRG is to find a quantum state  $|\psi_0\rangle$  written as an MPS, that minimizes the energy

$$E_0 = \min_{|\psi\rangle} \frac{\langle\psi|H|\psi\rangle}{\langle\psi|\psi\rangle} . \quad (4.13)$$

This problem can be expressed as finding the state  $|\psi\rangle$  for which  $\langle\psi|H|\psi\rangle$  is minimal under the constrained that the state is normalized, i.e.  $\langle\psi|\psi\rangle = 1$ . Using Lagrangian multipliers to enforce normalization we find

$$E_0 = \min_{|\psi\rangle} (\langle\psi|H|\psi\rangle - \lambda \langle\psi|\psi\rangle) . \quad (4.14)$$

Importantly this optimization does not need to be performed globally. Instead the tensors in the MPS representation can be optimized sequentially, fixing everything except one or only a few tensors and optimizing the parameters of these tensors at a time.

Here we will give an introduction to the infinite DMRG algorithm used in the present chapter. It is strictly speaking not a true algorithm in the thermodynamic limit but rather approximates the translational invariant state by the center of a finite chain that is grown extensively. Figure 4.3 illustrates the two-site MPS ansatz, where the unit cell consisting of tensors  $A = (\Gamma\Lambda)_A$  and  $B = (\Gamma\Lambda)_B$  is repeated all over the lattice. Here the diagonal tensors  $\Lambda$  contain the singular values for a bipartition along

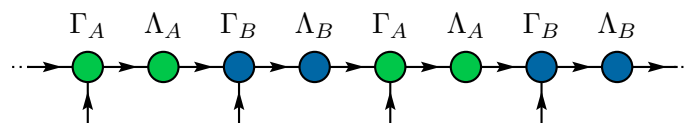


FIGURE 4.3: Two-site  $SU(2)$ -symmetric MPS ansatz used for the iDMRG study in this chapter. The unit cell consists of two MPS tensors  $\Gamma_A$  and  $\Gamma_B$  with corresponding diagonal matrices  $\Lambda_A$  and  $\Lambda_B$  containing the singular values for a bipartition along the respective link. In this case the MPS is said to be in canonical form.

the respective cut and the MPS is in its canonical form [66]. Notice that an MPS ansatz with two different tensors is mandatory to represent antiferromagnetic states, e.g. one tensor for each sublattice site. The iDMRG algorithm we use is a two-site growing DMRG code. Starting from two initial sites the system is grown towards both directions by inserting a pair of spins at the center of the chain, extending the chain to length  $L = 4, 6, 8, \dots$ . After sufficiently many absorption steps the central tensors of the chain are assumed to represent the translational invariant state. Since those central tensors are of particular interest, the rest of the chain is represented by an effective environment on both sides. This is shown in Fig. 4.4 where the Hamiltonian is written in the form of a four-index Matrix Product Operator (MPO), the extension of MPS to operators (see for instance Ref. [60]). At each growing step the two in-

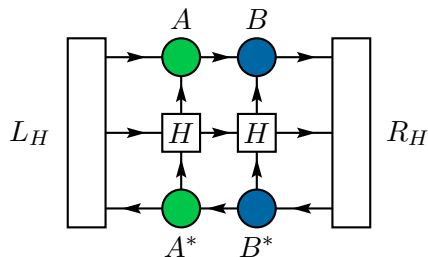


FIGURE 4.4: Two-site iDMRG algorithm. The expectation value  $\langle \psi | H | \psi \rangle$  written in terms of left and right environment tensors ( $L_H$ ,  $R_H$ ), two local tensors  $A$  and  $B$  as well as the Hamiltonian in the form of a matrix product operator.

serted tensors are optimized collectively with a two-site update in the vicinity of the surrounding tensors. The key problem here is to find the optimized tensors by solving a two-site eigenvalue problem. Differentiating the expectation value in Fig. 4.4 with respect to the complex conjugate tensors yields an eigenvalue problem of the form

$$H^{\text{eff}} M = \lambda M, \quad (4.15)$$

where  $H^{\text{eff}}$  denotes the effective Hamiltonian. It is shown as the collection of white tensors in Fig. 4.5, where the eigenvalue problem is written as a tensor network. Eq. (4.15) is solved for the eigenvector  $M$  with smallest eigenvalue  $\lambda$  to find a better approximation to the true ground state. In order to split the new eigenvector  $M$  back into two

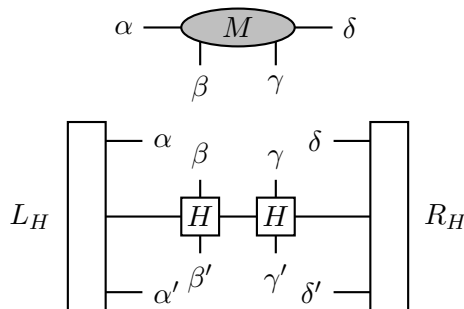


FIGURE 4.5: Two-site iDMRG algorithm. The optimized MPS tensors are constructed by solving an eigenvalue problem for the effective Hamiltonian, written in tensor network form. Arrows due to the  $SU(2)$  symmetry are omitted in this figure.

MPS tensors it can be reshaped into a matrix  $(M)_{(\alpha\beta),(\gamma\delta)}$  of dimension  $(\chi d) \times (d\chi)$  and an SVD separates it into tensors  $A$  and  $B$ . In general one needs to truncate the singular values in this step due to the enlarged index between tensor  $A$  and  $B$  back to

the bond dimension  $\chi$ . The two-site update with truncation is particularly useful in an iDMRG implementation with symmetries because it allows the algorithm to adapt to the relevant symmetry sectors necessary to describe the target state automatically (the truncation of the singular values controls which quantum numbers are kept on the virtual indices, as described in Sec. 3.5.2). To grow the chain further the newly optimized tensors are then absorbed into the left and right environment respectively. Repeating these steps in an iterative procedure yields better approximations of the two-site translational invariant state in each iteration<sup>2</sup>, and the ground state search can be terminated once the difference in singular values falls below a certain threshold.

The  $SU(2)$ -symmetric iDMRG implementation is based on the fusion tree formalism presented in Chapter 3. In order to represent the two-legged ladder as an MPS, the two sites on each rung of the ladder are coarse-grained into one physical site, see Fig. 4.6. Therefore the physical indices of the resulting MPS tensors carry quantum

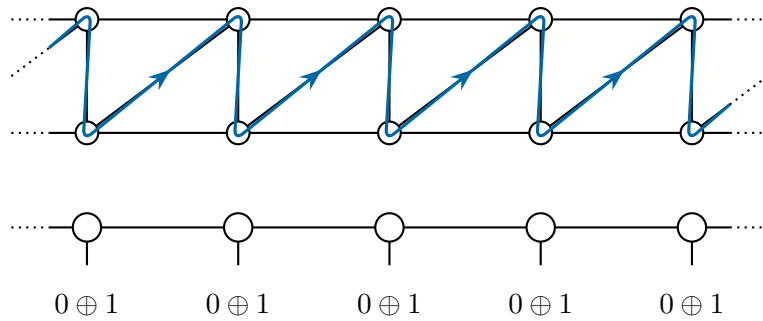


FIGURE 4.6: The sites of the spin-1/2 chiral ladder are labeled consecutively, indicated by the blue line. Two sites on the rungs are coarse-grained for the simulation with an MPS, whose physical indices carry  $1/2 \otimes 1/2 = 0 \oplus 1$ .

numbers  $0 \oplus 1$ . The  $SU(2)$ -invariant matrix product operator, the formulation of the Hamiltonian in the language of MPS, is presented in Appendix A.3. Since we

$\chi_{\text{sym}}$	$\chi$	virtual bond irreps
50	148	$0_{14} \oplus 1_{24} \oplus 2_{11} \oplus 3_1$
100	312	$0_{26} \oplus 1_{46} \oplus 2_{24} \oplus 3_1$
150	480	$0_{37} \oplus 1_{68} \oplus 2_{38} \oplus 3_7$
200	652	$0_{48} \oplus 1_{89} \oplus 2_{52} \oplus 3_{11}$
250	834	$0_{58} \oplus 1_{110} \oplus 2_{65} \oplus 3_{16} \oplus 4_1$
300	1008	$0_{69} \oplus 1_{130} \oplus 2_{80} \oplus 3_{20} \oplus 4_1$
350	1184	$0_{80} \oplus 1_{149} \oplus 2_{96} \oplus 3_{24} \oplus 4_1$

TABLE 4.1: Symmetric and effective bond dimensions for several simulations together with the quantum numbers and their degeneracies  $j_{t_j}$  on the virtual bonds of the MPS.

target an  $SU(2)$ -invariant ground state, the symmetric simulations are restricted to an antiferromagnetic configuration of the triangle ladder, and we choose to work with  $H_1$ . Simulations were performed with symmetric bond dimensions up to  $\chi_{\text{sym}} = 350$ , which amounts to an effective bond dimension of  $\chi \sim 1200$  due to the intrinsic degeneracies of  $SU(2)$  quantum numbers (refer to Sec. 3.1). In Table 4.1 we list the

<sup>2</sup>Provided that the landscape of the optimization is sufficiently simple, so that the algorithm does not get trapped in local minima.

distribution of singular values in the different spin sectors for some of the simulations performed. In the next section we will report on numerical results.

## 4.3 Results

### 4.3.1 Ground State Energy

At first we analyze the energy of the  $SU(2)$ -invariant ground state. A low energy generally indicates a reasonable approximation to the ground state due to the variational principle

$$\langle \psi | H | \psi \rangle \geq E_0 \quad \forall |\psi\rangle . \quad (4.16)$$

Here  $E_0$  is the true ground state energy, i.e. the lowest energy eigenvalue in the spectrum of  $H$ . It is therefore a useful quantity to compare between different numerical methods and verify that the bond dimension of the tensor network is sufficient to extract accurate physical information. Fig. 4.7 shows the ground state energy versus the inverse MPS bond dimension. In the figure convergence is only reached for large bond dimensions  $\chi \geq 1000$ , a value that would be very difficult to reach without exploiting  $SU(2)$  symmetry. An estimation of the error of the energy data points is

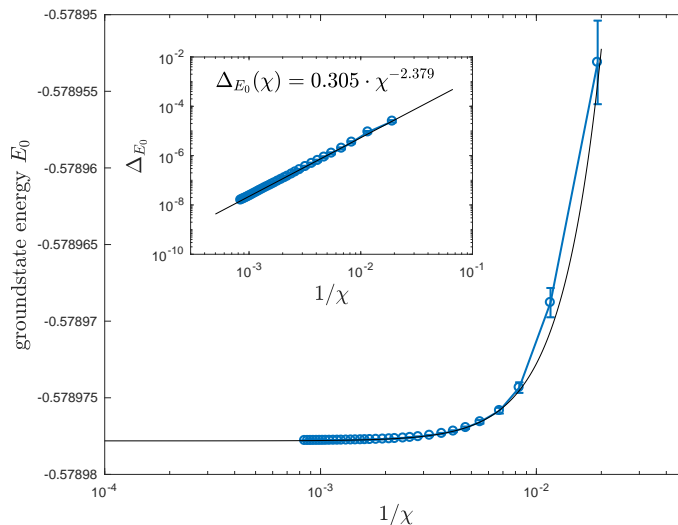


FIGURE 4.7: Ground state energy  $E_0$  versus the inverse MPS bond dimension  $1/\chi$ . The estimation of the error for the data points is based on the discarded weight, as explained in the text. The inset shows the convergence of the error  $\Delta E_0 = E_0 - E_0(\chi \rightarrow \infty)$ .

given by the discarded weight  $\delta$  of each simulation, i.e. the amount of entanglement that needs to be truncated in order to comply with the specified bond dimension. It is a measure of the accuracy of the simulation and the true ground state is reached for  $\delta \rightarrow 0$ , also refer to Sec. 3.5.2. In Fig. 4.8 the ground state energy is plotted directly against the discarded weight. In both of the figures the ground state energy is fitted with a polynomial function of the form  $E_0(x) = a \cdot x^b + c$  to extract the extrapolated energy at infinite bond dimension  $E_0(\chi \rightarrow \infty)$  and  $E_0(\delta \rightarrow 0)$  respectively. This results in an averaged value of

$$E_0 = -0.578978(2) . \quad (4.17)$$



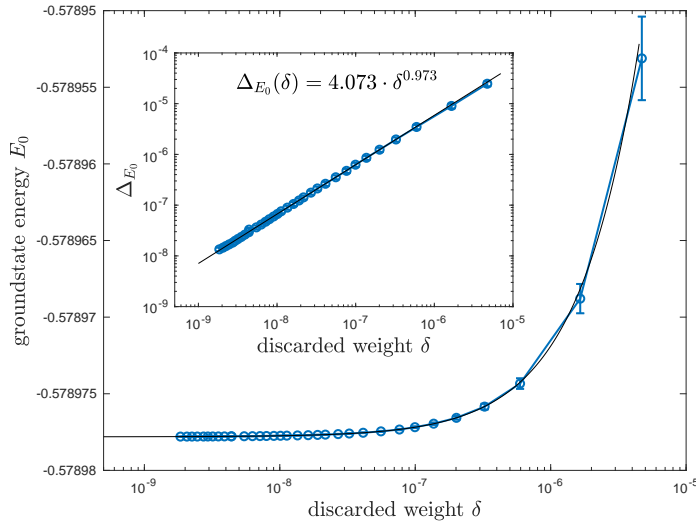


FIGURE 4.8: Ground state energy  $E_0$  versus the discarded weight  $\delta$ . In the inset we show the convergence of the error  $\Delta_{E_0} = E_0 - E_0(\delta \rightarrow 0)$ .

The inset of Fig. 4.7 and Fig. 4.8 show the convergence of the ground state energy towards the extrapolated value  $E_0$ . According to Ref. [66] the convergence of the ground state energy with respect to the discarded weight  $\Delta_{E_0}(\delta)$  should be fitted with a linear function. This is in good agreement with our power-law fit showing an exponent of 0.973(3). Concluding the ground state energy analysis, the chosen bond dimension of  $\chi \sim 1200$  is sufficiently large to even represent the critical ground state of  $H_1$  despite the intrinsic gapped nature of the matrix product state.

### 4.3.2 Entanglement Properties

The description of the low-energy physics of the chiral ladder in Section 4.1.1 resulted in an effective Heisenberg model on coarse-grained triangles. Based on the mutual sign of the coupling coefficients of  $H_1$  – which was chosen in the iDMRG study – the model is expected to be critical, with a central charge of  $c = 1$ . These prospects are now complemented by a more sophisticated analysis of entanglement properties. First we study the scaling of the entanglement entropy  $S(L)$  of a block of length  $L$  with two open edges. Typically one would have to construct the reduced density matrix for the

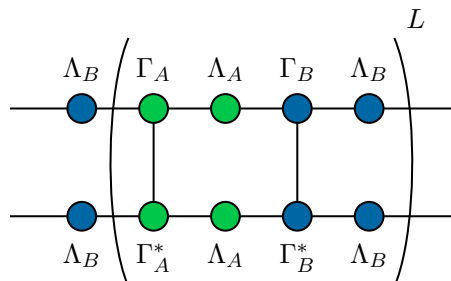


FIGURE 4.9: Extracting the entanglement entropy  $S(L)$  of a block of length  $L$ . The MPS is in canonical form, written in terms of tensors  $\Gamma$  and diagonal matrices  $\Lambda$ .

$L$  sites by tracing over the complement part, which causes an exponential growth in  $L$ . Fortunately, since the entanglement entropy needs to be the same for both parts of the bipartition one can trace over the relevant part of the system and exploit the

canonical form of the MPS to compute the entanglement entropy. The block is then grown by multiplying the transfer matrix multiple times as visualized in Fig. 4.9. The computational cost of this operation is  $\mathcal{O}(\chi^5)$ , in contrast to the  $\mathcal{O}(\chi^3)$  cost of the infinite DMRG algorithm. An eigenvalue decomposition of the transfer matrix of  $L$  sites with respect to upper and lower indices yields the eigenvalue spectrum, from which the entanglement entropy is computed according to

$$S = - \sum_{\alpha=1}^{\chi^2} \nu_{\alpha} \ln \nu_{\alpha} . \quad (4.18)$$

The intrinsic degeneracies of the eigenvalues  $\nu_{\alpha}$  due to the spin sectors have to be considered here. As expected from Conformal Field Theory (CFT) predictions the entanglement entropy should follow a scaling [94, 95, 96]

$$S(L) \sim \frac{c}{3} \log L . \quad (4.19)$$

Here  $c$  is the *central charge* of the underlying conformal theory of the Heisenberg and the chiral ladder model. As introduced in Sec. 2.3.1, matrix product states obey the area-law for the entanglement entropy by construction. Separating a block of size  $L$  from the infinite chain can be achieved by cutting two bond indices of the MPS, so that the entanglement entropy is expected to be a constant. This is however only the case for gapped quantum states and for the critical state of the chiral ladder the entanglement entropy is expected to scale logarithmically in the size of the block according to Eq. (4.19). This behaviour is indeed found in our simulations for moderate

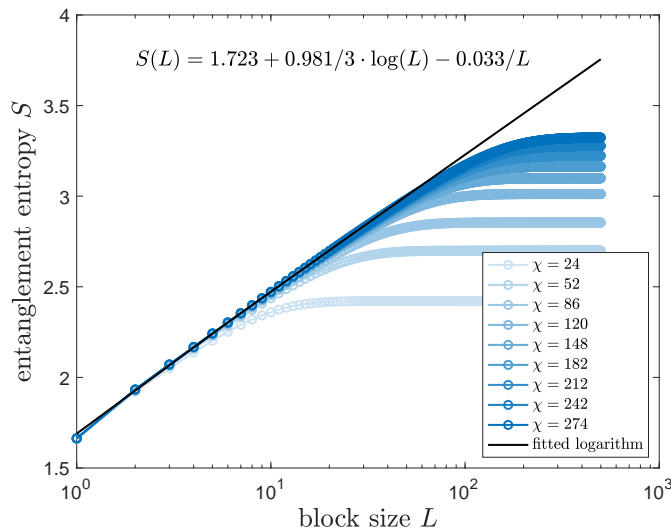


FIGURE 4.10: Scaling of the entanglement entropy  $S(L)$  of a block of size  $L$  for different bond dimensions. Due to the intrinsic area-law behaviour of the MPS the entanglement entropy saturates for large  $L$ , the central charge can be extracted from the slope of the curves.

block sizes  $L$ . However for large block sizes the entanglement entropy saturates due to the finite amount of entanglement in the system and the intrinsic area-law. The larger the bond dimension of the MPS the more quantum correlations can be captured and the predicted behaviour is recovered for larger block sizes. A fitted logarithm with an  $\mathcal{O}(1/L)$  correction is used to extract the central charge of the ground state, which is

determined to be  $c = 0.981(4)$ . This value is in very good agreement with a central charge of  $c = 1$  expected for the ground state of the antiferromagnetic Heisenberg model. The same information can be extracted from the scaling of the entanglement entropy of half an infinite chain with the MPS correlation length  $\xi$ , a calculation that scales as  $\mathcal{O}(\chi^3)$ . The correlation length measures how far correlations can spread in the lattice and for an MPS it is always finite due to its intrinsic properties. However by increasing the bond dimension we can approach critical states and therefore larger correlations lengths. Here, results from CFT [97] predict a behaviour that is given by

$$S(\xi) \sim \frac{c}{6} \log(\xi) . \quad (4.20)$$

In the numerical simulations the entanglement entropy for half an infinite chain is readily available due to the canonical form of the MPS, it can be computed from the diagonal tensors  $\Lambda$ . The correlation length is determined by

$$\frac{1}{\xi} = -\log \left| \frac{\lambda_2}{\lambda_1} \right| , \quad (4.21)$$

where  $\lambda_1$  and  $\lambda_2$  are the two largest eigenvalues computed by an eigenvalue decomposition of the transfer matrix [60] in Fig. 4.11. The result is shown in Fig. 4.12 and

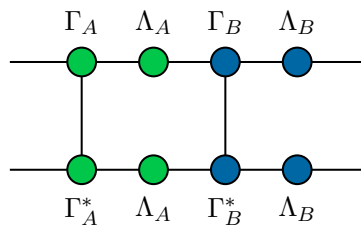


FIGURE 4.11: Transfer matrix of the MPS used to compute the correlation length.

nicely resembles the expected logarithmic behaviour. A fit reveals a central charge of

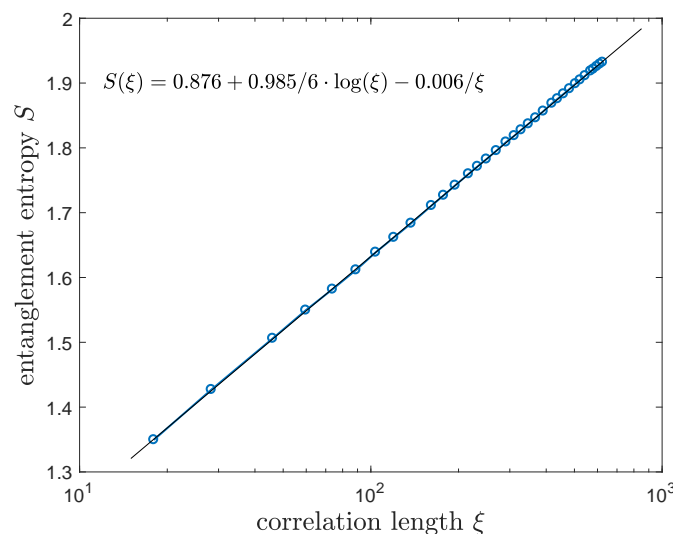


FIGURE 4.12: Scaling of the entanglement entropy of half an infinite chain  $S(\xi)$  with the MPS correlation length  $\xi$ . The expected logarithmic growth is found in the numerical data, from which the central charge can be extracted.

$c = 0.985(5)$  that is again in good agreement with  $c = 1$ . The critical nature of the ground state can be further fortified by calculations of correlation functions, presented in the next section.

### 4.3.3 Correlation Functions

In order to characterize different phases of matter one can compute correlation functions, which uncover how particles at different positions in space are related<sup>3</sup>. In particular, correlation functions are expected to behave very differently for gapped and gapless quantum states. While gapped phases typically have short-range, exponentially decaying correlations, those of critical, gapless systems are expected to decay polynomially over distance. Several correlations functions have been computed for the critical ground state of the triangle model. The first measured observable is the spin-spin correlation  $\langle \psi | \vec{S}_i \vec{S}_j | \psi \rangle$  for spins in the same and in different legs of the ladder. The ground state  $|\psi\rangle$  is the one with highest bond dimension of  $\chi_{\text{sym}} = 350$ . Results are shown in Fig. 4.13 and Fig. 4.14. The algebraic decay is fitted with a

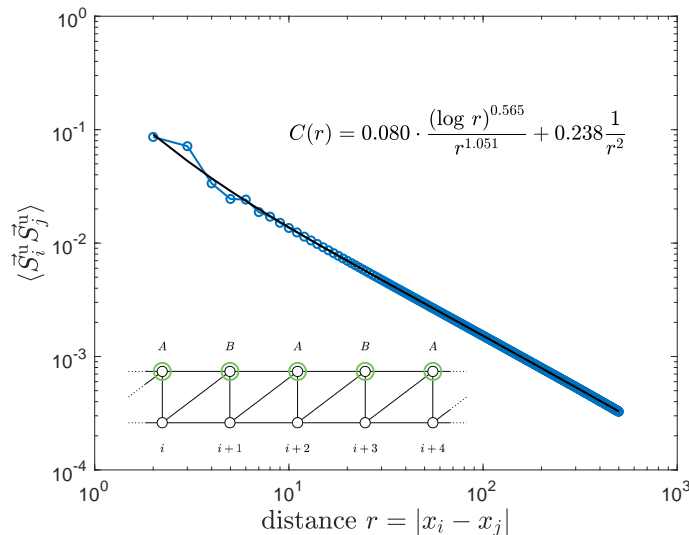


FIGURE 4.13: Spin-spin correlation function for spins in the same leg of the ladder. The expected behaviour of  $C(r) \sim (\log r)^{1/2}/r$  is well reproduced by the numerical data, for the fit we fixed the exponent of the short-distance term.

polynomial function with logarithmic corrections as shown in the figures. Our numerical findings agree well with the expected behaviour  $C(r) \sim (\log r)^{1/2}/r$  derived for the Heisenberg model [98, 89], the effective low-energy model. The decay of the correlation functions follows the prediction for very large distances indicating a good approximation of the critical ground state. Furthermore we computed the expectation value of the dimer-dimer correlation function on different rungs of the ladder. The four-body expectation value is corrected by all disconnected parts according to

$$\begin{aligned} \langle \psi | (\vec{S}_i^u \vec{S}_i^d) (\vec{S}_j^u \vec{S}_j^d) | \psi \rangle_c &= \langle \psi | (\vec{S}_i^u \vec{S}_i^d) (\vec{S}_j^u \vec{S}_j^d) | \psi \rangle - \langle \psi | \vec{S}_i^u \vec{S}_i^d | \psi \rangle \langle \psi | \vec{S}_j^u \vec{S}_j^d | \psi \rangle \\ &\quad - \frac{1}{3} \langle \psi | \vec{S}_i^u \vec{S}_j^u | \psi \rangle \langle \psi | \vec{S}_i^d \vec{S}_j^d | \psi \rangle - \frac{1}{3} \langle \psi | \vec{S}_i^u \vec{S}_j^d | \psi \rangle \langle \psi | \vec{S}_i^d \vec{S}_j^u | \psi \rangle . \end{aligned} \quad (4.22)$$

<sup>3</sup>In dynamic systems one can and also compute time-dependent correlation functions at the same, or at different positions in space.

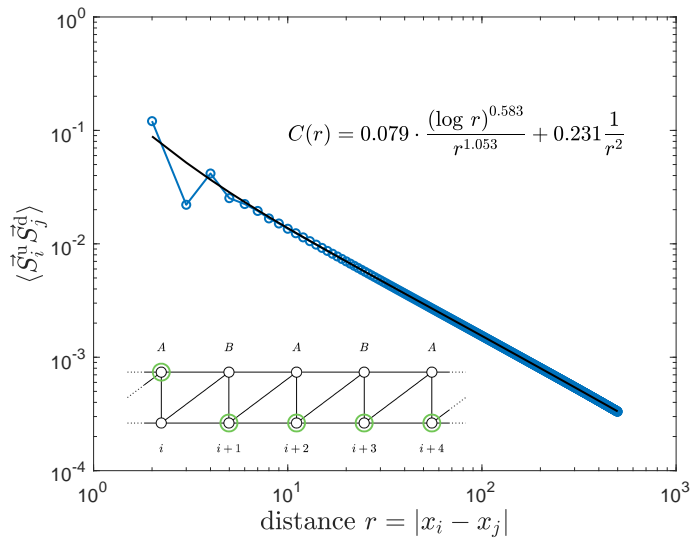


FIGURE 4.14: Spin-spin correlation function for spins in different legs of the ladder. The expected behaviour of  $C(r) \sim (\log r)^{1/2}/r$  is well reproduced by the numerical data, for the fit we fixed the exponent of the short-distance term.

The result is shown in Fig. 4.15, again with a polynomial fit and a logarithmic correction as suggested in Ref. [98] for four-body expectation values. Plotting the same quantity for smaller bond dimensions reveals the intrinsic finite correlation length of the MPS, which causes an exponential decay of correlations eventually. Summarizing

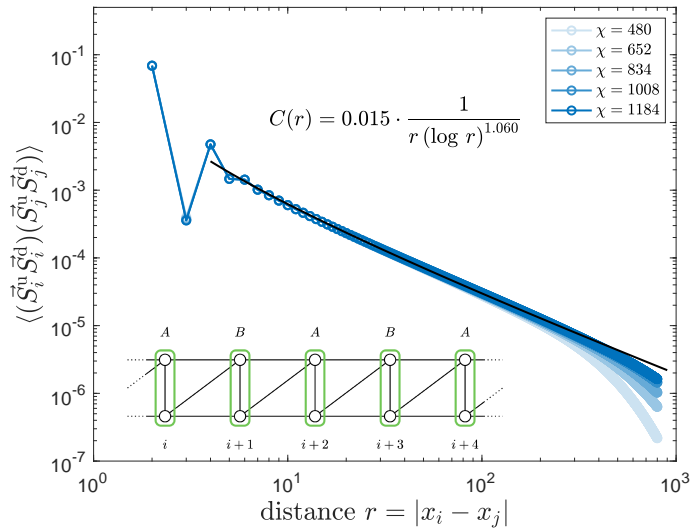


FIGURE 4.15: Dimer-dimer correlation function for the vertical rungs of the ladder. The data points are fitted with a polynomial function with a logarithmic correction, as suggested in Ref. [98].

the results in this section the correlation functions follow an algebraic decay expected for criticality, also in good agreement with analytic predictions. This further supports our analysis of the entanglement properties and matches all known characteristics of the low-energy effective Heisenberg model.

### 4.3.4 Entanglement Spectrum

In order to further characterize the chiral spin-1/2 ladder model and demonstrate its similarities to the plain Heisenberg model, we investigate the entanglement structure of half an infinite chain. In Sec. 4.3.2 we have analyzed the entanglement entropy, a collective quantity that discards the structure of the spectrum. The entanglement spectrum is directly obtained from the singular values of the MPS and their distribution is according to the virtual bond irreps shown in Table 4.1. Each spin sector  $j$  in this table comes with a  $(2j + 1)$ -fold degeneracy and by construction  $j$  is an integer due to the coarse-graining of the two spin-1/2 degrees of freedom on each rung. In Fig. 4.16 we plot the entanglement energies  $\epsilon_\alpha \equiv -\log \lambda_\alpha^2$  with  $\lambda_\alpha$  the Schmidt coefficients. The data points are sorted according to the different spin sectors  $j = 0, 1, 2, 3, 4$ , and each point is actually  $(2j + 1)$ -fold degenerate. Data points

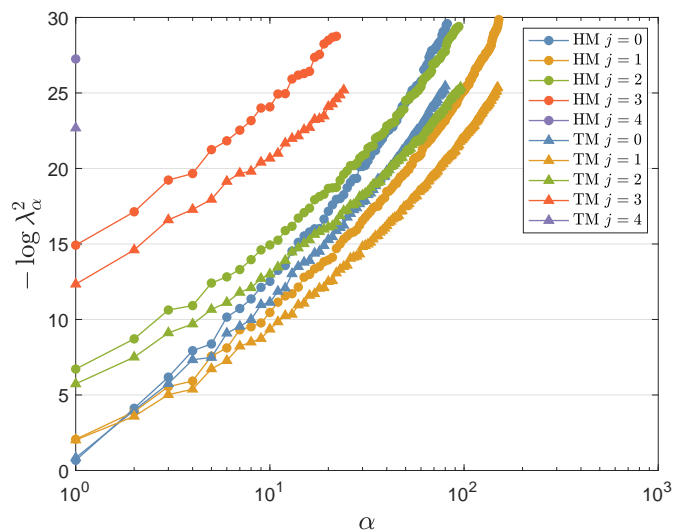


FIGURE 4.16: Entanglement spectrum for the triangle ladder model (TM, triangles) and the Heisenberg spin chain (HM, circles), with multiplets organized according to their spin sector  $j$ . Every point is a  $(2j + 1)$ -plet.

for the triangle model (TM) shown as triangles are compared to the corresponding spectrum of entanglement energies for the ground state of the regular spin-1/2 Heisenberg model (HM). A coarse-graining of two lattice sites similarly to the triangle model ensures integer quantum numbers on the virtual legs, and the same iDMRG algorithm is used for the simulation of the Heisenberg model. Up to an overall rescaling the two entanglement spectra show exactly the same features. In particular the structures for the lowest part of the spectrum, i.e. the largest singular values resemble each other in appearance. This is a numerical verification that the effective low-energy theory of both models is the same, and that both models are likely to be described by the same boundary CFT [99]. Accordingly, this is a strong indication that the triangle model in configuration  $H_1$  is described by the  $(1 + 1)$ -dimensional CFT of the Heisenberg spin-1/2 chain, i.e. an  $SU(2)_1$  WZW theory (Wess–Zumino–Witten). This would be in agreement with our previous findings and also with the  $SU(2)$  symmetry of the triangle ladder model.

## 4.4 Conclusion and Outlook

The iDMRG study of the spin-1/2 chiral ladder described in this chapter was the first concrete application of our  $SU(2)$ -invariant tensor network framework. The ground state of the antiferromagnetic Hamiltonian  $H_1$  is found to be critical with a central charge that is compatible with  $c = 1$ . This can be concluded from the results we obtained for the scaling of entanglement entropies, the entanglement spectrum as well as different correlation functions that all decay algebraically. It is also in good agreement with previous studies of the continuum limit [100]. Our analysis of the model is complemented by exact diagonalization results studying ground state degeneracies and edge currents, as well as bosonization results revealing the critical nature of the ground state and the origin of the edge currents for both  $H_1$  and  $H_3$  [68].

This work motivates further investigations along different directions. Extensions to multi-leg ladders and higher spin systems would be straightforward. In this context it would be interesting to study how the gapped/gapless nature of the chiral system depends on both the spin and the number of chains. Ultimately one could study the transition to 2d physics. Since the  $SU(2)$ -symmetric iDMRG code can only access the configuration  $H_1$ , investigation of  $H_3$  possibly with  $U(1)$ -symmetric or  $SU(2)$ -covariant MPS methods would complement the analysis of the chiral ladder model. Moreover, configuration  $H_3$  with the same couplings  $J_1 = J_2$  for the two triangles is expected to be exactly solvable by Bethe ansatz.

The chiral Hamiltonian of Eq. (4.7) can also be defined and explored on different lattice geometries, such as on the thin-torus limit of the Kagome lattice, illustrated in Fig. 4.17. The motivation for this project originated in the study of the chiral Hamiltonian on the Kagome lattice that revealed a chiral spin liquid, a type of ground state that features chiral edge modes. These chiral modes have been found in the triangle model as well [68], however in order to study the transition of a quasi-1d strip to two spatial dimensions and the behaviour of the edge currents, it could be beneficial to use corner-sharing triangles right away.

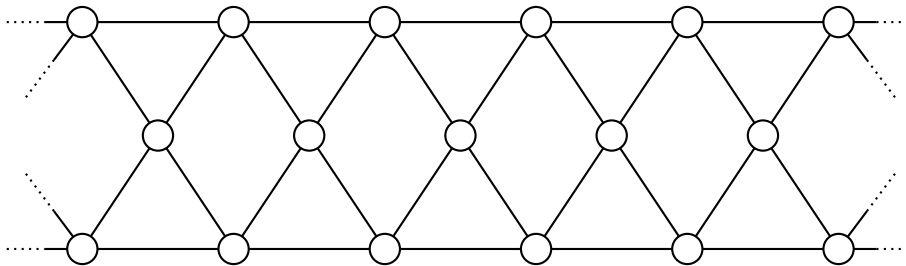


FIGURE 4.17: Thin-torus limit of the Kagome lattice which could serve as a starting point to study the cross-over between quasi-1d and 2d physics.





## Chapter 5

# Global $SU(2)$ Symmetry in 2d

The implementation of the  $SU(2)$  symmetry of the chiral ladder model presented in Chapter 4 has clearly proven the benefits. Exploiting the symmetry and representing tensors as symmetric blocks allows to simulate much larger bond dimensions compared to non-symmetric TN simulations, which in turn increases the accuracy of the results. Exploiting physical symmetries in 1d TN simulations is widespread these days, whereas the statement does not apply for 2d TN simulations. At the same time, 2d TN computations are computationally much more expensive [9] due to more complicated algorithms and tensors with many indices, so that the implementation of physical symmetries is expected to be greatly beneficial.

In this chapter we apply the  $SU(2)$ -invariant tensor network framework to tensor network algorithms in two spatial dimensions, namely in the famous infinite Projected Entangled Pair State (iPEPS) and the infinite Projected Entangled Simplex State (iPESS) ansatz. In order to assess the utility of implementing the symmetry, the two simulation tools are benchmarked for three different spin systems on different lattice geometries with unexpected outcomes. In Sec. 5.1 we will present the iPEPS and iPESS algorithms, with more details given in Appendix B. Sec. 5.2 reports the results for the spin-1 bilinear-biquadratic model on the square lattice using iPEPS, with a comparison to  $U(1)$ -symmetric simulations. Finally, in Sec. 5.3 the iPESS algorithm is used to simulate a spin-1/2 and a spin-2 Heisenberg model on the Kagome lattice.

### 5.1 Tensor Network Algorithms in 2d

Matrix product states have been immensely successful in the study of one-dimensional quantum many-body systems. Due to their intrinsic properties and the canonical form, expectation values can be computed exactly in a very efficient way, and even without symmetries the accessible bond dimensions are reasonably high to extract precise results. In two dimensions the situation is somewhat different. First of all, due to the second dimension and the increased number of nearest neighbours involved, tensor network simulations in 2d are considerably more computationally expensive. This is especially true for the computation of expectation values, where approximations are inevitable in order to avoid an exponential scaling.

The infinite Projected Entangled Pair State (iPEPS) ansatz has already been introduced in Sec. 2.5. In this chapter we use iPEPS on a square lattice to study a spin-1 model, where a unit cell of  $2 \times 2$  tensors is repeated periodically to construct the infinite lattice. The iPEPS tensors are optimized with a *simple update* procedure to represent the ground state of the model Hamiltonian [71]. The simple update provides an efficient algorithm also when combined with  $SU(2)$  symmetry. It falls

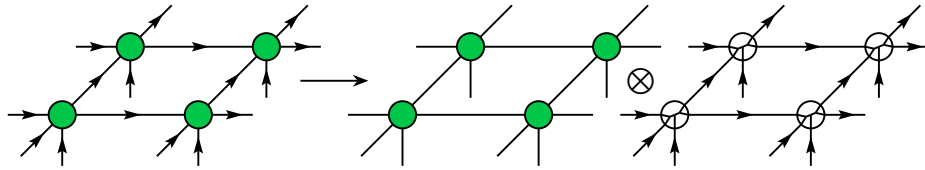


FIGURE 5.1: Symmetric decomposition of a  $2 \times 2$  unit cell of iPEPS tensors into a network of degeneracy and structural tensors. The structural tensors are described by a spin network, where arrows describe incoming and outgoing indices.

behind more sophisticated update schemes like the full update [72] or variational update schemes [73, 74], but serves our purpose here to benchmark the utility of  $SU(2)$  symmetry in 2d TN algorithms. Expectation values for the infinite PEPS network are computed with a Corner Transfer Matrix Renormalization Group (CTM) scheme, that approximates the contraction of the infinite lattice with effective fixed-point environment tensors. The simple update and the CTM procedure are explained in detail in Appendix B.

The second algorithm used in this chapter to study two spin systems on the Kagome lattice is the infinite Projected Entangled Simplex State (iPESS) ansatz [101]. Contrary to iPEPS, here the local tensors do not resemble the lattice structure. In-

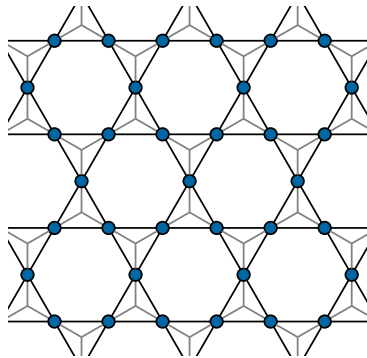


FIGURE 5.2: The 2d Kagome lattice in black, with its dual honeycomb lattice shown in gray. While the lattice sites reside on the vertices of the original Kagome lattice, they reside on the links in the honeycomb lattice.

stead of assuming local iPESS tensors on the lattice sites of the Kagome lattice, one can imagine the tensors to sit on the links of the dual honeycomb lattice (see Fig. 5.2). Consequently, the tensors for the physical sites of the Kagome lattice now only have two instead of four virtual indices. However, in order to connect them together the ansatz requires additional three-index *simplex tensors*, which are the ones in the triangles of the Kagome lattice. An iPESS ansatz with a three-site unit cell is shown in Fig. 5.3, where the three lattice site tensors are connected by two simplex tensors to build the honeycomb lattice. The iPESS ansatz on the honeycomb lattice does not resemble the original Kagome lattice and therefore its entanglement structure. Nevertheless it has been noted that it captures the correlation on the triangles in the Kagome lattice, thus being a suitable tool for its simulation. As for the iPEPS ansatz we use a simple update scheme to optimize the tensor coefficients that is presented in detail in Sec. B.3. For the computation of observables a coarse-graining to a regular square lattice is used, where the structure shown in Fig. 5.4 is contracted together to form an iPEPS tensor. More details for the computation of expectation values are given in Appendix. B.4. For some simulations with  $SU(2)$  symmetry a three-site

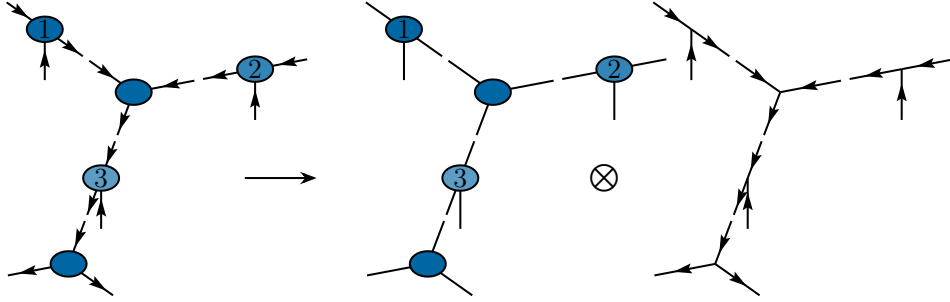


FIGURE 5.3: Symmetric decomposition of a three-site iPESS tensors into a network of degeneracy and structural tensors. The structural tensors are described by a spin network, where arrows describe incoming and outgoing indices. Apart from the three tensors on the lattice sites, the ansatz includes two simplex tensors connecting them.

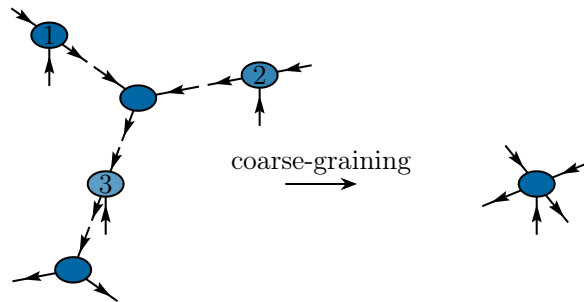


FIGURE 5.4: The full unit cell of three site tensors together with two simplex tensors is coarse-grained into a single iPEPS tensor. This iPEPS tensor can then be used in standard CTM procedures. The coarse-grained physical index represents the fusion of the three physical subspaces on the left.

unit cell iPESS is not adequate and the ansatz needs to be extended. The problem occurs if the iPESS unit cell is not compatible with a decoration in terms of  $SU(2)$  quantum numbers, explained in Sec. B.3.2. As a resort we employ a six-site iPESS ansatz for the simulation of the spin-1/2 Heisenberg model, and a coarse-graining of this structure leads to two different iPEPS tensors as demonstrated in Sec. B.4.

## 5.2 Spin-1 Bilinear-Biquadratic Model

In this section we study the spin-1 bilinear-biquadratic model (BLBQ) on a square lattice using  $SU(2)$ -symmetric iPEPS. This model features two kinds of competing nearest-neighbour interactions, the regular bilinear Heisenberg coupling and the biquadratic coupling, which is a squared Heisenberg term. The Hamiltonian reads

$$H = \sum_{\langle i,j \rangle} \left( \cos(\theta) (\vec{S}_i \cdot \vec{S}_j) + \sin(\theta) (\vec{S}_i \cdot \vec{S}_j)^2 \right), \quad (5.1)$$

where  $\langle i,j \rangle$  denotes nearest neighbour interactions,  $\vec{S}_i$  is the vector of spin-1 operators on site  $i$ , and  $\theta$  tunes the relative coupling strength of the bilinear and biquadratic terms. The spin-1 BLBQ model is the most general lattice model with lattice rotation, lattice translation and spin rotation symmetry<sup>1</sup>. It has generated a lot of

<sup>1</sup>All higher powers of  $\vec{S}_i \cdot \vec{S}_j$  can be recast into bilinear and biquadratic interaction terms for a system of spin-1 particles.

interest in recent years due to the presence of high symmetry points at  $\theta = \pi/4, 5\pi/4$  and  $\theta = \pi/2, 3\pi/2$ , for which the Hamiltonian is  $SU(3)$ -symmetric [102]. Also, some phases of the BLBQ model on the triangular lattice might be realized in materials such as  $\text{NiGa}_2\text{S}_4$  [103] and  $\text{Ba}_3\text{NiSb}_2\text{O}_9$  [104]. For the parameter range  $0 < \theta < \pi$  the model is inaccessible for quantum Monte Carlo simulations due to the negative sign problem, however TN simulations can be used to explore the full phase diagram. Let us now concentrate on the present spin rotation symmetry. Even though the Hamiltonian is fully  $SU(2)$ -symmetric, the ground state  $|\psi(\theta)\rangle$  can break the symmetry spontaneously and is not necessary symmetric as well. The model has been studied in Ref. [102] for all angles  $\theta \in [0, 2\pi)$ . For instance, the ground state of the plain spin-1 Heisenberg model ( $\theta = 0$ ) on the square lattice is in an antiferromagnetic phase, it is however only  $U(1)$ -symmetric around the axis of magnetization. For our investigation the BLBQ model is tuned to  $\theta = 0.21\pi$ , for which the ground state is believed to be in an  $SU(2)$ -symmetric phase reminiscent of a Haldane phase of coupled one-dimensional chains. In this phase, realized for  $0.189(2)\pi \leq \theta \leq 0.217(4)\pi$ , the magnetization vanishes exactly which is also an indication of an  $SU(2)$ -symmetric ground state. The iPEPS simulations were performed with a simple update on a unit cell of  $2 \times 2$  tensors and a corner transfer matrix renormalization group scheme for the computation of observables (refer to Sec. B.1 and Sec. B.2 for details about the simple update and CTM respectively).

### 5.2.1 Ground State Energy

We computed the ground state energy of the BLBQ model to benchmark the symmetric implementation to a non-symmetric one. In Fig. 5.5 the ground state energy is shown as a function of the inverse bond dimension  $1/D_{\text{eff}}$ . Additional numbers computed with  $U(1)$  symmetry are shown in comparison (provided by the authors of Ref. [102] and replotted with permission). The expectation values for the  $SU(2)$ -

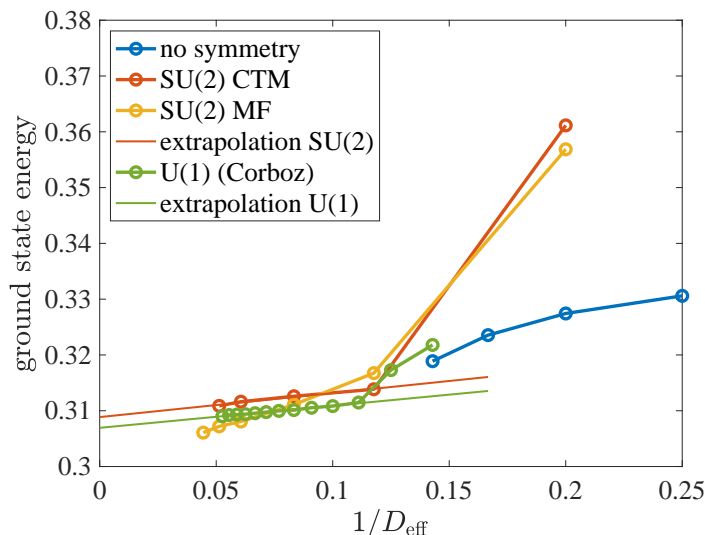


FIGURE 5.5: Ground state energy of the spin-1 BLBQ model on a square lattice as a function of  $1/D_{\text{eff}}$ . Data points with  $U(1)$  symmetry provided by the authors of Ref. [102] and replotted with permission.

symmetric simulations have been computed both with the mean-field environment, as well as with the variational CTM environment tensors explained in Sec. B.2.3. Even though the mean-field values are not variational they can provide a trend for larger

bond dimensions that are currently not accessible with a CTM procedure. Clearly, non-symmetric simulations yield lower energies for small bond dimensions, however due to the implementation of symmetries it is possible to access regimes that are impossible to reach without symmetries. Here the symmetric simulations produce lower overall results. Importantly, the  $SU(2)$  CTM data points are slightly higher than those with lower  $U(1)$  symmetry. This can be an indication that the  $SU(2)$ -symmetric iPEPS ansatz may be too restrictive, and the optimization to find an accurate ground state could be very limited. Before investigating the restrictiveness

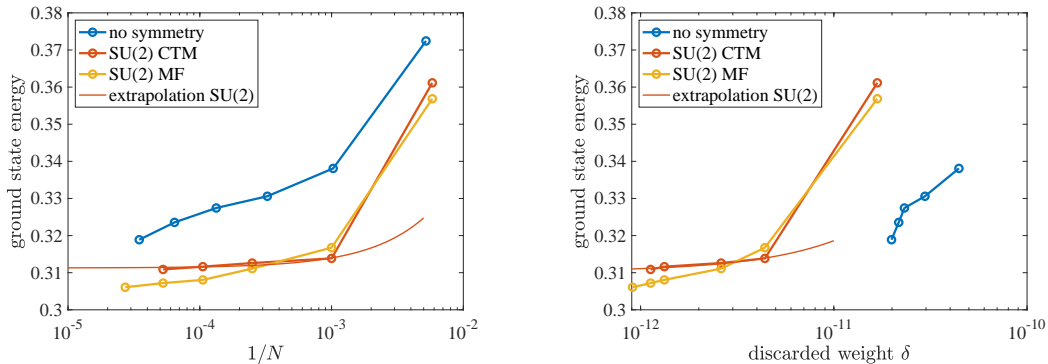


FIGURE 5.6: Ground state energy of the spin-1 BLBQ model on a square lattice as a function the inverse number of variational parameters  $1/N$  (left) and of the discarded weight  $\delta$  (right).

of the iPEPS ansatz, let us plot the data points in Fig. 5.5 versus the inverse number of variational parameters and the discarded weight [61]. In Fig. 5.6 we find that the  $SU(2)$ -symmetric simulations produce lower energies when compared with the number of free parameters in the ansatz. This behaviour is expected, since irrelevant degrees of freedom are eliminated due to the symmetry, which in turn captures the correct structure of the ground state. The discarded weight  $\delta$  is the amount of discarded squared singular values [93] in the simple update truncation step and rates the approximation of the ground state (see Sec. 3.5.2 for SVD based truncation and Sec. B.1 for the truncation in the iPEPS simple update). Fig. 5.6 reveals that the simulations without symmetries are not converged yet, so that an energy extrapolation of the data points is meaningless. For the extrapolation of the  $SU(2)$  CTM data we find

$$\begin{aligned}
 e_0(1/D_{\text{eff}} \rightarrow 0) &= 0.309 \pm 0.003 \\
 e_0(1/N \rightarrow 0) &= 0.311 \pm 0.004 \\
 e_0(\delta \rightarrow 0) &= 0.310 \pm 0.002,
 \end{aligned}
 \tag{5.2}$$

and the extrapolation of the  $U(1)$  data points yields  $e_0(1/D_{\text{eff}} \rightarrow 0) = 0.307 \pm 0.001$ . The numbers are very close, yet it is noticeable that the  $SU(2)$ -symmetric data points are systematically higher than the  $U(1)$ -symmetric ones. This could be rooted in the fact that a simple update scheme is used and overcome by more elaborate simulation schemes like the full update [72]. However, we also noticed that the iPEPS ansatz in 2d is very much restricted due to the implementation of the symmetry. In Fig. 5.7 we show the ratio between the remaining variational parameters in the symmetric iPEPS ansatz and the number of free parameters in the corresponding unconstrained TN, alongside the same information for the iDMRG study of the chiral ladder presented in Chapter 4. The comparison clearly shows a strong restriction of 1d iDMRG simulations, but even more so in 2d iPEPS simulations with only about 1% of variational parameters left

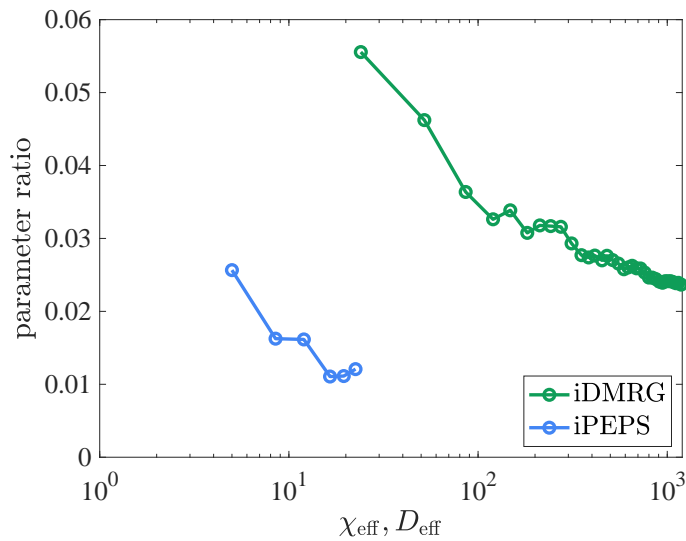


FIGURE 5.7: The ratio of parameters between an  $SU(2)$ -symmetric iDMRG and iPEPS ansatz and their corresponding unconstrained tensor networks, as a function of the effective bond dimension  $\chi_{\text{eff}}$  and  $D_{\text{eff}}$  respectively.

compared to an unconstrained ansatz. A priori this is expected and also desired when implementing the symmetry, and this also enables access to large bond dimensions in the first place. However, the trajectories in the space of remaining variational parameters are limited just as much. A ground state search in the unconstrained space of parameters might be better at circumnavigating local minima and finding low variational ground states, and therefore energies.

## 5.2.2 Structure of the Ground State

In order to explain the nature of the  $SU(2)$ -invariant ground state we plot the energy on each link of the iPEPS unit cell in Fig. 5.8. Our results indicate that the ground state cultivates anisotropic bonds, thus breaking lattice rotation symmetry. This yields different energies in  $x$ - and  $y$ -directions which is compatible with vertical

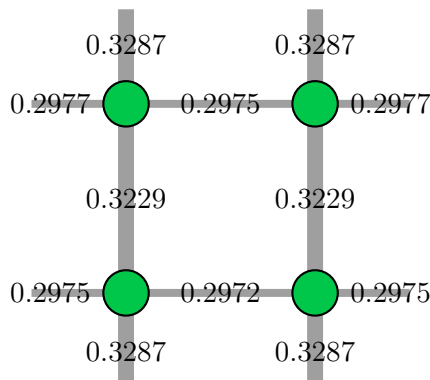


FIGURE 5.8: Bond energies for the ground state of the BLBQ model at  $\theta = 0.21\pi$  and  $D_{\text{sym}} = 5$ . The pattern with different energies on  $x$ - and  $y$ -bonds is compatible with a system of coupled one-dimensional Haldane chains, as reported in Ref. [102].

coupled Haldane chains, and in accordance with the findings in Ref. [102]. This difference in energy is caused by having different spin quantum numbers on horizontal

$x$ - and vertical  $y$ -bonds, to which the algorithm is converged. In detail we have

$$x\text{-links: } 0_1 \oplus 1_2 \oplus 2_2, \quad y\text{-links: } \frac{1}{2}_2 \oplus \frac{3}{2}_2 \oplus \frac{5}{2}_1 \quad (5.3)$$

and therefore different effective bond dimensions  $D^x = 17$  and  $D^y = 18$ . The differences in the numbers between link energies in the horizontal and vertical direction respectively is probably due to truncation effects.

### 5.3 Heisenberg Model on the Kagome Lattice

In this section we investigate two spin models on the Kagome lattice using the infinite projected entangled simplex state ansatz. In particular we study the spin-1/2 and the spin-2 nearest-neighbour antiferromagnetic Heisenberg model. The Kagome Heisenberg antiferromagnet (KHAF) is currently the defining problem in the research field of frustrated quantum antiferromagnetism, and the nature of the ground state has been under debate for a long time [105, 106, 107, 108, 109, 110]. The reason for this is the large amount of frustration generated by the corner-sharing triangles of the Kagome lattice. Frustration already arises for a single triangle, where the antiferromagnetic spin interaction can not be fulfilled simultaneously for all three bonds, as shown in Fig. 5.9. This generates so-called geometric frustration that originates due



FIGURE 5.9: Antiferromagnetic interaction on the triangle leads to geometric frustration, because the spins can not satisfy the AF exchange interaction for all bonds simultaneously. Antiferromagnetic interaction on the square lattice, or any other bipartite lattice does not lead to frustration.

to the Kagome lattice structure. An antiferromagnetic Heisenberg model on a square lattice, or any other bipartite lattice does not exhibit frustration, in contrast. The large amount of frustration in the KHAF causes strong quantum fluctuations around the ground state. Therefore, many quantum states are very close in energy and compete to be the true ground state, which makes the numerical simulation of the model challenging. There are two competing proposals for the ground state of the model, the first one being a Quantum Spin Liquid (QSL), the second one being a Valence Bond Crystal (VBC). Quantum spin liquids, proposed by Anderson [16], refer to quantum phases of matter that do not show any form of magnetic ordering down to zero temperature, therefore not breaking any kind of lattice symmetry. This, in turn, means that the state can not be detected with any local order parameter, and the identification of QSL phases proves to be difficult both in theory and experiment. Moreover these kind of states typically show long-range entanglement and exotic fractionalized excitations [111]. The second nominee, the valence bond crystal, is a state where all spins on the lattice are in a pairwise singlet configuration due to their antiferromagnetic interaction. Since every spin is paired in a singlet configuration, the overall state is  $SU(2)$ -invariant and non-magnetic, however it lacks the long-range order. Furthermore, by forming a specific arrangements of these valence bonds this state breaks the lattice symmetries. However, an equal superposition of all possible valence bond



crystal lattice decorations restores the lattice symmetries, and is known as a Resonating Valence Bond (RVB) state. In principle a quantum spin liquid can therefore be constructed by a superposition of valence bond crystals, where quantum fluctuations prevent the ground state to choose any specific VBC configuration. The nature of the spin-1/2 KHAF is still not fully clear. The study that obtained the energetically lowest ground state claims it is a  $\mathbb{Z}_2$  quantum spin liquid [112], while others studies favor a valence bond crystal [113]. Recent works on the KHAF show that the ground state could actually be a gapless spin liquid [114]. Experimental studies are based on investigations of different kind of materials such as *Herbertsmithite* ( $\text{ZnCu}_3(\text{OH})\text{Cl}_2$ ), *Volborthite* ( $\text{Cu}_3\text{V}_2\text{O}_7(\text{OH})_2 \cdot 2\text{H}_2\text{O}$ ) and *Vesignieite* ( $\text{BaCu}_3\text{V}_2\text{O}_8(\text{OH})_2$ ), that have a dominant spin-1/2 Heisenberg interaction and a Kagome lattice structure.

Different tensor network simulation tools have been applied to study the ground state of the spin-1/2 KHAF, such as DMRG [115, 112], PEPS [116] and the Multiscale Entanglement Renormalization Ansatz (MERA) [110]. Additionally, the iPESS ansatz has proven to be a suitable TN because it captures correctly the multipartite entanglement for the triangles in the Kagome lattice [117, 114]. Here we employ a six-site iPESS ansatz to study the ground state of the spin-1/2 KHAF and a three-site iPESS ansatz to study the ground state of the spin-2 KHAF. The Hamiltonian is given by

$$H = \sum_{\langle i,j \rangle} \vec{S}_i \cdot \vec{S}_j, \quad (5.4)$$

where  $\langle i,j \rangle$  denotes nearest-neighbours on the Kagome lattice, and  $\vec{S}_i$  is the spin operator at site  $i$ . A simple update scheme is used for the optimization of the iPESS tensors, for the evaluation of expectation values we use a coarse-graining of the iPESS unit cell and a standard CTM procedure, as described in Appendix. B.

### 5.3.1 Spin-1/2 Heisenberg Antiferromagnet

For the simulation of a spin-1/2 system a three-site iPESS unit cell is not compatible with a decoration in terms of  $SU(2)$  quantum numbers. Therefore a six-site ansatz is used. The issue here is that there is a conflict between the  $SU(2)$  symmetry and

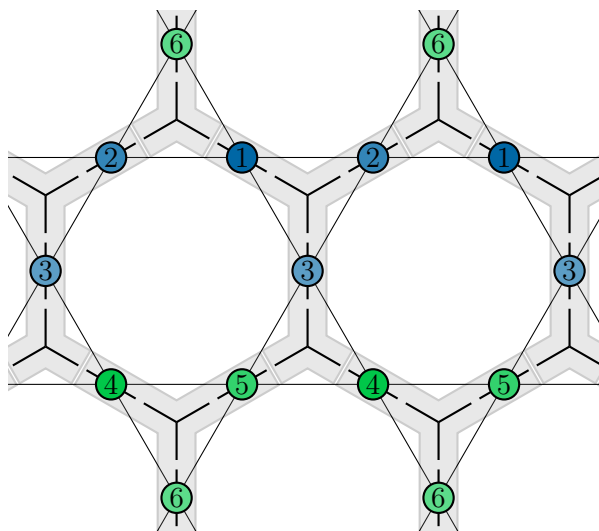


FIGURE 5.10: The six-site iPESS ansatz on the honeycomb lattice used to study the spin-1/2 KHAF. The unit cell consists of six lattice site tensors and four simplex tensors connecting them. Physical indices of the iPESS tensors are not shown.



translational invariance of the three-site iPESS ansatz for half-integer spin systems, much like the case for 1d MPS. More details are given in Appendix B.3.2. The six-site iPESS ansatz is shown in Fig. 5.10. Simulations were performed with a maximum symmetric bond dimension of  $D_{\text{sym}} = 7$ , which yields an effective bond dimension of  $D_{\text{eff}} = 17.75$ . The fractional value is due to an averaging of the different bond dimensions in the network. In Fig. 5.11 we plot the ground state energy versus the inverse bond dimension, and compare the values against non-symmetric three-site and six-site iPESS simulations. The ground state energy of the  $SU(2)$ -symmetric simu-

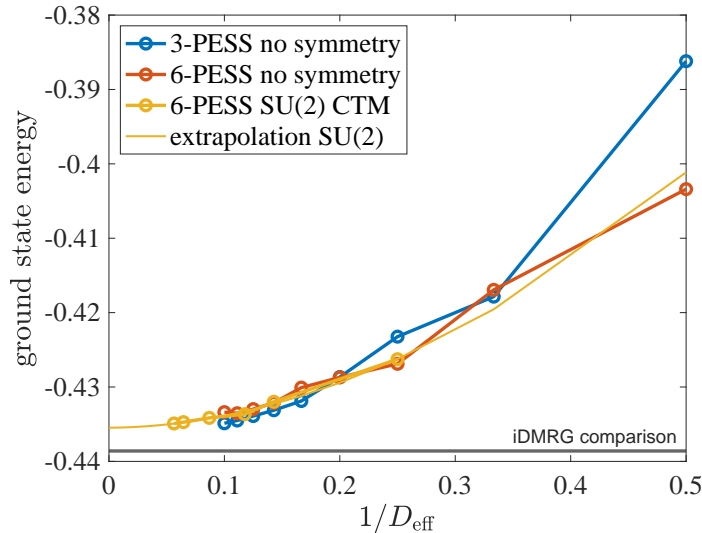


FIGURE 5.11: Ground state energy of the spin-1/2 KHAF as a function of the inverse bond dimension, computed with a six-site iPESS and  $SU(2)$  symmetry, and with a three-site and six-site iPESS without symmetry.

lation is compatible with the non-symmetric ones, which reinforces the observation that the ground state is indeed  $SU(2)$ -invariant and a quantum spin liquid. However,

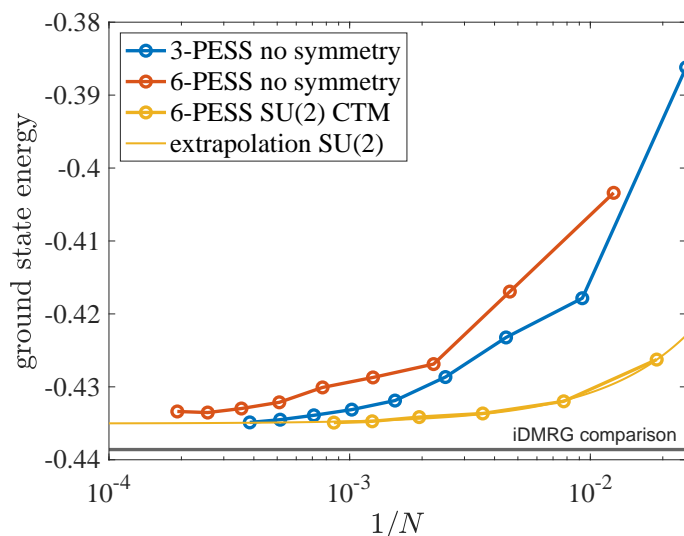


FIGURE 5.12: Ground state energy of the spin-1/2 KHAF as a function of  $1/N$ , computed with a six-site iPESS and  $SU(2)$  symmetry, and with a three-site and six-site iPESS without symmetry.

it is noticeable that the energies for the six-site iPESS simulations lie above those with a three-site unit cell for large bond dimensions. This is explainable with the analysis of spin-spin correlations on the bonds, which will be presented after the energy assessment. In Fig. 5.12 we show the ground state energy versus the number of free variational parameters in the ansatz. A polynomial fit is used to determine the extrapolated ground state energy in both figures, whereat the limit of infinite bond dimension is slightly better achieved in the  $SU(2)$ -invariant simulations as a function of  $1/N$ . For the extrapolated energy we find

$$\begin{aligned} e_0(1/D_{\text{eff}} \rightarrow 0) &= -0.435 \pm 0.004 \\ e_0(1/N \rightarrow 0) &= -0.435 \pm 0.002 . \end{aligned} \quad (5.5)$$

Unfortunately, a scaling in the discarded weight as performed for the iPEPS simulations in Sec. 5.2 can not be done, because the discarded weight was always too small. In both of the previous figures we show the comparison with the energetically lowest iDMRG energy of Ref. [112]. In the introduction of the frustrated Heisenberg model on the Kagome lattice we stated that the ground state is believed to be a quantum spin liquid that does not break any lattice symmetry. In order to investigate the very first check for this claim, we computed the spin-spin correlation on all the different bonds in the iPESS unit cells. Fig. 5.13 shows the nearest-neighbour spin correlations for

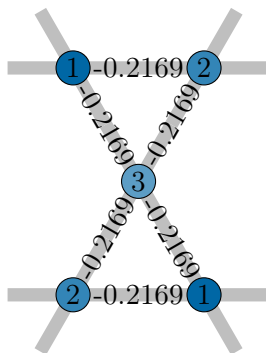


FIGURE 5.13: Nearest-neighbour spin-spin correlations on the bonds in the three-site iPESS for the spin-1/2 KHAF.

the three-site iPESS. As expected for a spin liquid, the ground state has very uniform bonds. Certainly this is not yet a proof for a spin liquid, and a lot of quantities could be checked to substantiate the claim [111]. However, it is a first indication for the expected nature of the ground state, and a numerical verification that iPESS is a suitable simulation tool. Moreover, we plot the spin correlations, or equivalently the bond energies, for the six-site iPESS with and without  $SU(2)$  symmetry in Fig. 5.14. For the non-symmetric simulation, the six-site iPESS state seems to produce a valence-bond crystal structure with strong and weak links, thus breaking invariance under lattice translations and rotations. This is however not unusual, since TN algorithms favor injective quantum states<sup>2</sup> over symmetric ones. In this respect, the symmetric ground state constructed from a superposition of all valence bond configurations would be non-injective and is therefore impossible to find in practice, unless lattice symmetries are explicitly conserved. For the  $SU(2)$ -symmetric simulations the spin-spin correlations are even more skewed without any recognizable pattern. Presumably this is due to the non-uniform bond dimensions caused by the mixture of integer and half-integer

<sup>2</sup>A PEPS is injective in a region  $R$ , if different linearly independent boundary conditions on the boundary  $\partial R$  lead to different linearly independent quantum states.

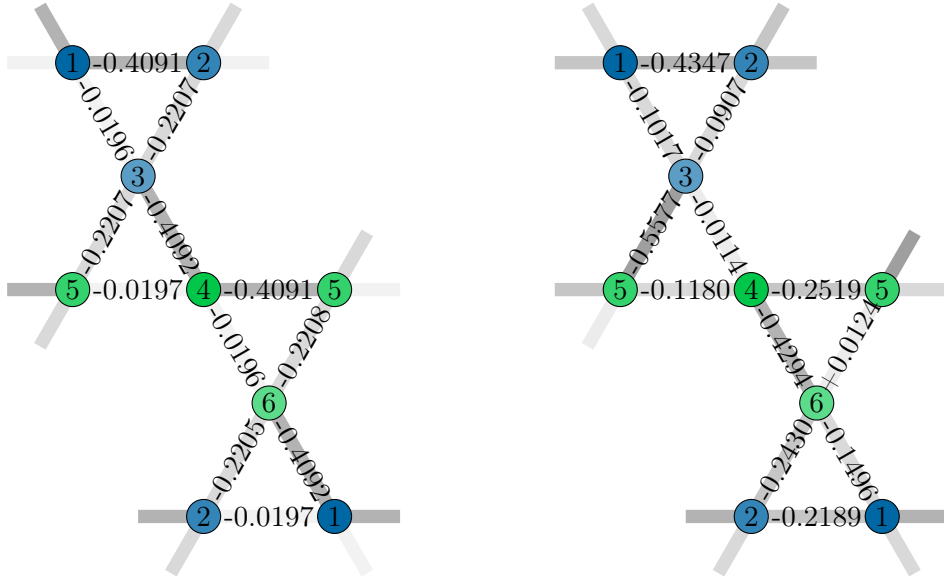


FIGURE 5.14: Nearest-neighbour spin-spin correlations on the bonds in the six-site iPESS ansatz, without symmetry (left) and with  $SU(2)$  symmetry (right).

quantum numbers on the virtual bonds. In any case, we observe that the valence bond crystal tends to melt as higher bond dimensions are reached. In Fig. 5.15 we show the correlator skewness, i.e. the difference between the strongest and the weakest link in the network for both six-site iPESS simulations. Clearly, in the  $SU(2)$ -symmetric

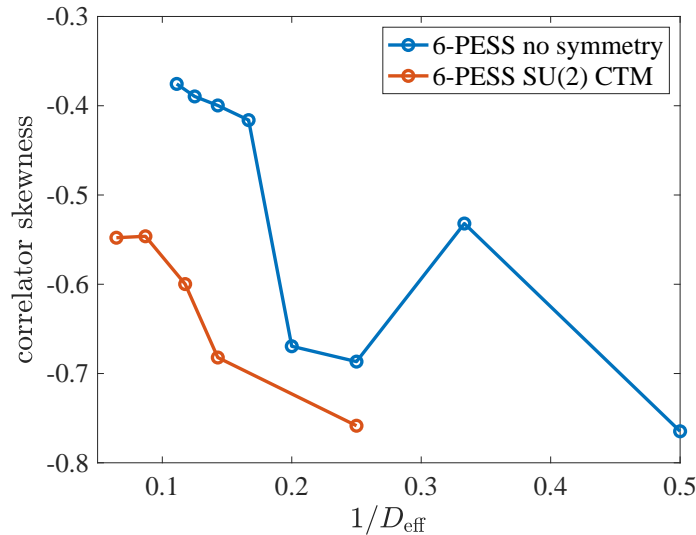


FIGURE 5.15: Difference between the strongest and the weakest link (correlator skewness) in the six-site iPESS unit cell with and without  $SU(2)$  symmetry.

simulations of the ground state the valence bond crystal tends to melt slower. This is again due to the mixed spin representations, and the difference in bond dimensions caused by the intrinsic degeneracies of the quantum numbers is expected to balance out with their degeneracies, as larger bond dimensions are accessible. The dip in the non-symmetric data is likely caused by the strong quantum fluctuation. For  $D = 4$  and  $D = 5$  the algorithm converges to a state that is close in energy to the remaining ones, with more pronounced valence bonds though.

### 5.3.2 Spin-2 Heisenberg Antiferromagnet

Although the spin-1/2 Heisenberg model on the Kagome lattice has generated a lot of research interest, there are also studies of spin- $S$  versions of the models. For instance, Ref. [118] studied the spin-1 KHAF with the conclusion that the ground state is a gapped simplex valence-bond crystal (SVBC). That is, the two simplexes or triangles in the Kagome lattice have different energies, therefore breaking the lattice inversion symmetry. In order to apply our implementation of the iPESS ansatz with

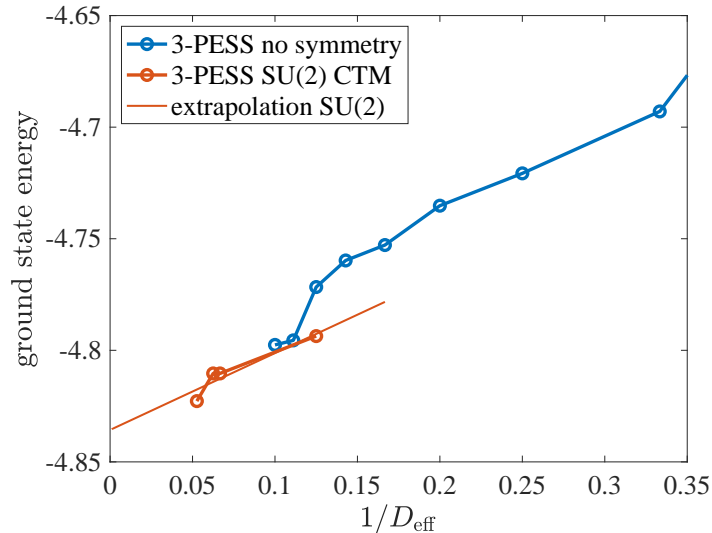


FIGURE 5.16: Ground state energy of the spin-2 KHAF as a function of the inverse bond dimension, computed with a three-site iPESS.

$SU(2)$  symmetry to an integer spin system, we instead settled for the spin-2 KHAF. Therefore we use the Hamiltonian in Eq. (5.4) and a three-site iPESS unit cell. The

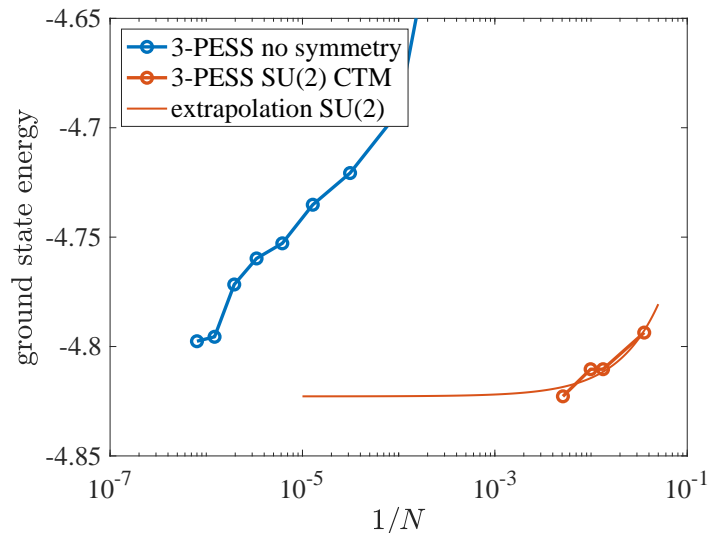


FIGURE 5.17: Ground state energy of the spin-2 KHAF as a function of  $1/N$ , computed with a three-site iPESS.

mismatch between symmetry and translational invariance does not appear for integer spin systems, and in principle the bond indices can carry mixed spin representations.

The ground state however converges to a configuration where only integer quantum numbers are kept, and the ground state energy for the non-symmetric and  $SU(2)$ -symmetric simulations is shown in Fig. 5.16. Due to the large local spin, the maximal symmetric bond dimension is  $D_{\text{sym}} = 5$ , corresponding to an effective bond dimension  $D_{\text{eff}} = 19$ . Although the local spins are non-degenerate, i.e.  $j_{\text{physical}} = 2_1$ , the large spin-2 produces many more internal symmetric blocks compared to the case with  $j_{\text{physical}} = (1/2)_1$ , therefore slowing down the calculations. In Fig. 5.16 the symmetric simulations can handle larger bond dimensions and produce lower variational energies compared to the non-symmetric simulations. The same data is plotted versus the inverse number of parameters  $1/N$  in Fig. 5.17. Here the difference between non-symmetric and symmetric simulations is very large, and the implementation of  $SU(2)$  leads to better results at a fraction of variational parameters. This is mainly owed to the three-site iPESS ansatz, which is able to represent the ground state well with a uniform distribution of only integer quantum numbers. The extrapolation to infinite bond dimension is only shown for completeness, since the simulations do not yet show convergence in the achievable bond dimensions.

Similarly to the spin-1/2 KHAF we computed the nearest-neighbour spin-spin correlations, i.e. the bond energies that are shown in Fig. 5.18. The observed pattern

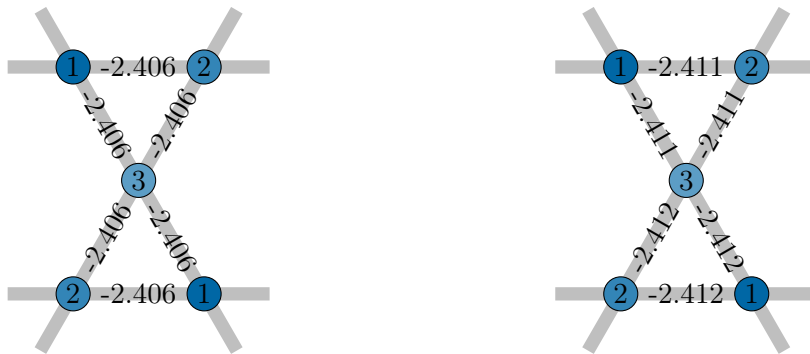


FIGURE 5.18: Nearest neighbour spin-spin correlations on all the bonds in the three-site iPESS unit cell for the ground state of the spin-2 KHAF, without symmetry (left) and with  $SU(2)$  symmetry (right).

is again compatible with a quantum spin liquid, supported by vanishing expectation values for the spin chiral operator  $\vec{S}_i \cdot (\vec{S}_j \times \vec{S}_k)$  on all of the Kagome triangles.

## 5.4 Conclusion and Outlook

In this chapter we implemented tensor network algorithms in two spatial dimensions with a global  $SU(2)$  symmetry. The iPEPS and iPESS TNs were used to study ground state properties of different spin models on the square and the Kagome lattice. Rather than surpassing existing studies of the models, the implementations provide an assessment of the utility of  $SU(2)$  symmetry in 2d. For the extraction of the most accurate numbers the simple update is anyway too inaccurate, and more sophisticated algorithms are needed. In this respect further investigations of the restrictiveness of the simulations is also required. The effects we observe for the spin-1 BLBQ model simulated with a simple update might disappear for full update iPEPS simulations, that are known to be more accurate [72].

Our studies generally show that the utility of the symmetry strongly depends on the problem at hand, and also on the nature of the ground state. With the currently

available computational power it seems that we are just at the border between a benefit and an equilibrium of symmetric versus non-symmetric simulations. For instance, implementing the  $SU(2)$  symmetry in iPESS simulations for half-integer models on the Kagome lattice leads to increased imbalances in the system due to the different intrinsic degeneracies of integer and half-integer quantum numbers. This effect is expected to decrease as larger bond dimensions become available, so that the full potential of symmetries in 2d becomes accessible. For the specific case of the spin-1/2 KHAF it would also be beneficial to exploit the point group symmetries of the lattice, such as invariance under rotation.

Concluding, the implementation of  $SU(2)$  symmetry in 2d TN algorithms allows to study the physical systems with a higher bond dimension compared to non-symmetric simulations. The net effect however strongly depends on the type of algorithm, the unit cells used to simulate the model, the model itself and the nature of the ground state.

## Chapter 6

# Fine-Grained Tensor Networks

In this chapter we study different quantum many-body systems using regular, non-symmetric infinite PEPS methods in two and three spatial dimensions. The systems under consideration are defined on a triangular lattice, a lattice structure that can host highly interesting phases of matter due to possible geometric frustration. In general though, lattices with high connectivity, i.e. a high number of nearest neighbours are very interesting since they are usually linked to exotic phases of quantum matter such as topological quantum spin liquids [119, 111]. Even though frustration will not be present in our analysis, the triangular lattice itself can pose some difficulties for tensor network simulations. Due to the high connectivity, tensor networks that resemble the lattice structure have to deal with many-index tensors that slow down calculations. This is especially relevant for simulations in three dimensions. Moreover the triangular lattice structure makes it complicated to define and compute effective environments needed to contract the whole 2d network, such as in CTM methods.

Based on our proposal in Ref. [120] we will introduce a physically motivated strategy to improve the utility of tensor network methods on lattices with high connectivity. To this end the Hilbert space of the physical degrees of freedom is fine-grained so that a tensor network ansatz with a lower connectivity is natural. This comes at the expense of increasing the range of the interactions in the original model, but has the additional advantage that standard 2d tensor network methods, such as CTM can be directly applied in the new fine-grained tensor network.

In this chapter we will describe the idea of the general fine-graining procedure for the specific example of a triangular lattice. In order to demonstrate its usefulness we study a spin model and a bosonic model using infinite PEPS and corner transfer matrix methods. As a first application of the procedure in 3d we consider a spin model on a stacked triangular lattice as well.

## 6.1 Fine-Graining of the Physical Sites

### 6.1.1 General Fine-Graining Procedure

The idea of fine-graining is quite simple yet very powerful. The physical degree of freedom on each lattice site is decomposed into smaller, more fundamental entities which, when coarse-grained again reproduce the original ones. The physical Hilbert space  $\mathcal{H}_p$  can therefore be understood as the coarse-grained space of multiple other fine-grained Hilbert spaces  $\mathcal{H}_f^{[i]}$  via an isometry

$$W : \bigotimes_{i=1}^N \mathcal{H}_f^{[i]} \longrightarrow \mathcal{H}_p, \quad (6.1)$$

where  $N$  is the number of fine-grained spaces. In this sense fine-graining is the inverse operation of coarse-graining, where multiple physical sites are combined as e.g. used in Chapter 4 and Chapter 5. The isometry  $W$  is given by

$$W = \sum_{f_1, f_2, \dots, f_N} \sum_{f_p} |f_1\rangle |f_2\rangle \dots |f_N\rangle \langle f_p| \quad (6.2)$$

with  $W^\dagger W = \mathbb{I}_p$  and  $\mathbb{I}_p$  the identity in the physical Hilbert space  $\mathcal{H}_p$ . The isometry  $W$  can be seen as an  $(N+1)$ -index tensor that maps the fine-grained spaces to the physical space and vice-versa. An example for  $N = 2$  is provided in Fig. 6.1. Importantly, operators in the physical Hilbert space  $O_p$  are mapped to operators on the fine-grained lattice  $O_f$  by

$$O_f = W O_p W^\dagger. \quad (6.3)$$

Naturally the support of operators, i.e. the region where an operator acts is increased due to the application of  $W$ . Particularly, an  $m$ -site operator on the original lattice is mapped to an  $(m \times N)$ -site operator on the fine-grained lattice. As long as the isometry

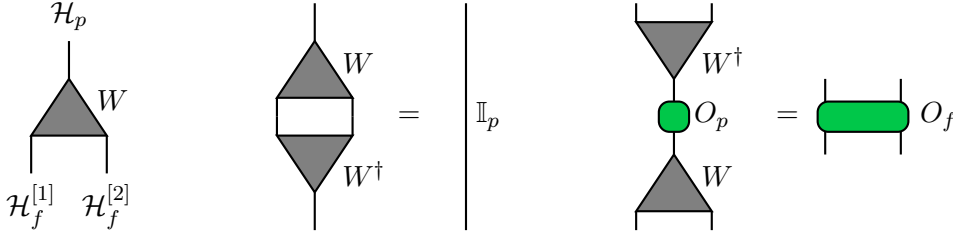


FIGURE 6.1: Isometry  $W$  with  $N = 2$  for the fine-graining of the physical Hilbert space  $\mathcal{H}_p$  into two other Hilbert spaces  $\mathcal{H}_f^{[1]}$  and  $\mathcal{H}_f^{[2]}$  and its identity relation. A one-site operator  $O_p$  on the original lattice is transformed to a two-site operator  $O_f$  on the fine-grained lattice.

$W$  is local, locality is also preserved by this mapping. Importantly, tensor network optimizations and evaluation of local expectation values can be fully performed in the fine-grained picture.

In order to utilize the presented idea, the isometry to fine-grain the physical degrees of freedom should be chosen such that the resulting tensor network structure is simpler, in a sense that it is more amenable to standard simulation techniques. The actual choice of  $W$  however depends on the problem at hand, and in general  $W$  can even have a tensor network structure itself.

### 6.1.2 Application to the Triangular Lattice

The fine-graining procedure presented in Sec. 6.1.1 is now applied to the paradigmatic example of a triangular lattice. The triangular lattice has a connectivity of six, i.e. every lattice site has six nearest neighbours which is already high enough to benefit from our method. Using an isometry that maps one physical lattice site to two fine-grained sites transforms the triangular lattice to the square lattice, as demonstrated in Fig. 6.2. A PEPS tensor for the triangular lattice with six virtual indices is thereby decomposed into two PEPS tensors with four virtual indices each with the help of an isometry as presented in Fig. 6.1. The choice of mapping is very convenient since the resulting fine-grained lattice is square. In particular we can exploit this simpler structure in standard algorithms to contract the infinite tensor network, such as CTM



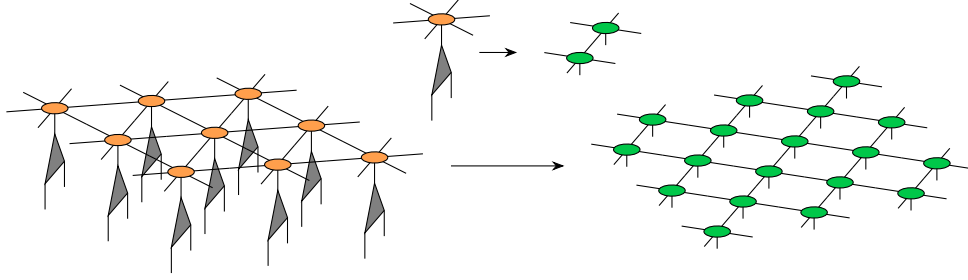


FIGURE 6.2: Fine-graining of the triangular lattice with an  $N = 2$  isometry as shown in Fig. 6.1. The resulting square lattice is more amenable for standard tensor network techniques. Notice that also the operator support is increased due to the fine-graining isometry.

methods. This is required to compute accurate expectation values, and also for more sophisticated iPEPS update schemes such as the full update. For the study of the different models in subsequent sections we used a non-symmetric simple update iPEPS scheme [51], the same type of algorithm used in the  $SU(2)$ -symmetric iPEPS study in Chapter 5. A comprehensive description of the simple update algorithm is presented in Appendix B.1, and we refer the unacquainted reader to this section before proceeding with the present description of the fine-grained simple update.

Choosing a unit cell of  $N_x \times N_y$  tensors on the triangular lattice results in an  $N_x \times (2N_y)$  tensor unit cell on the square lattice (for a fine-graining along the  $y$ -direction). In the triangular lattice there are three different directions along which the simple update steps have to be applied, and generally there are  $3N_x N_y$  different links. Due to the fine-graining of the lattice the simple update on the square lattice involves four fine-grained iPEPS tensors in every update step. Horizontal links in the triangular lattice are updated as shown in Fig. 6.3. The diagonal tensors in blue represent the mean-

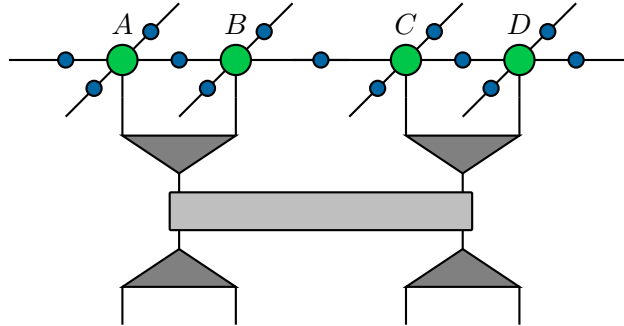


FIGURE 6.3: Simple update step of horizontal bonds in the fine-grained square lattice. The trotterized Hamiltonian gate shown in light gray acts on all four sites due to the isometries shown in deep gray.

field environment of the iPEPS tensors. For a computationally cheaper update scheme we can again collect all links that are not affected by the update and split them away to both sides. For this purpose tensors  $A$  and  $B$  on the left as well as tensors  $C$  and  $D$  on the right can be decomposed as shown in Fig. 6.4, so that the four-body gate can be applied to the middle tensors of smaller rank. These additional steps greatly benefit the efficiency of the simple update, as explained in detail in Sec. B.1. Nevertheless, the fine-grained simple update implicates some amount of overhead due to the maintenance of the fine-grained TN structure, and a discussion of the efficiency of the whole algorithm is presented in Sec. 6.5.1. The two other types of links – the diagonal links of the triangular lattice – are updated in a similar way.

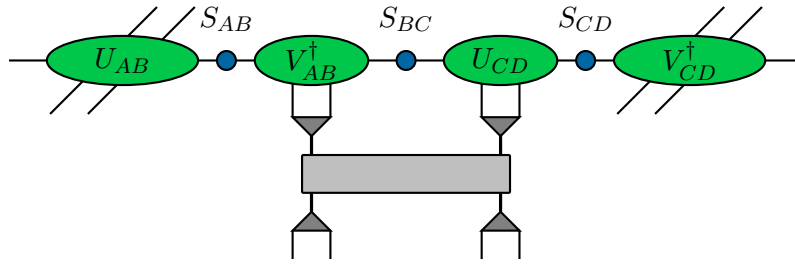


FIGURE 6.4: Simple update step of horizontal bonds applied to the reduced tensors in order to lower the computational cost. A certain amount of overhead is however introduced due to the maintenance of the fine-grained form of tensors.

### 6.1.3 Corner Transfer Matrix Scheme and Expectation Values

In order to fully utilize the fine-graining procedure it is convenient to choose an isometry that maps the original lattice to the square lattice. Thus one can directly apply standard tensor network techniques to contract the whole 2d network to e.g. compute expectation values. Notice that the unit cell on the square lattice does not repro-

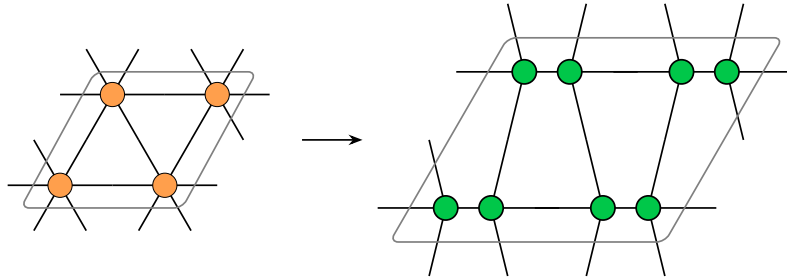


FIGURE 6.5: A unit cell of  $2 \times 2$  tensors on the triangular and the fine-grained unit cell on the square lattice. The unit cell does not reproduce a translational invariant state with respect to the orthogonal  $x$ - and  $y$ -directions on the square lattice.

duce a translational invariant state with respect to the orthogonal  $x$ - and  $y$ -lattice directions. This is however typically the case for systems on the square lattice and exploited in standard CTM procedures. In the fine-grained lattice we can easily fix this by doubling the unit cell to  $4 \times 4$  tensors, which are then absorbed directionally to compute the effective environment, illustrated in Fig. 6.6. A detailed description

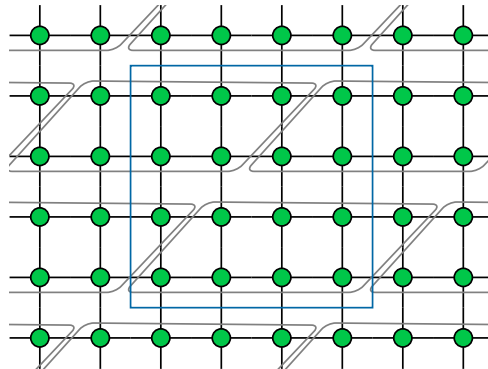


FIGURE 6.6: The unit cell of the fine-grained PEPS (gray borders) is not translational invariant with respect to the  $x$ - and  $y$ -directions of the square lattice. An extension of the unit cell (blue border) is therefore used in the CTM procedure.

about the CTM procedure can be found in Sec. B.2. For the computation of local

observables one can then use the fixed-point environment tensors. Due to the mapping via the isometry  $W$ , the range of the interaction increases as demonstrated in Fig. 6.1. Computing one-body expectation values such as the local magnetization or particle number results in the evaluation of a two-site operator. Two-body operators such as the energy per link are obtained by a contraction of tensor networks as shown in Fig. 6.7. The increased range of interactions is clearly disadvantageous for com-

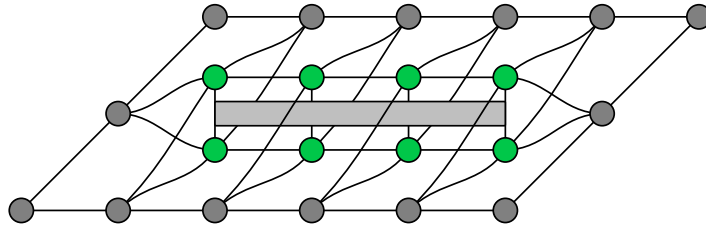


FIGURE 6.7: A two-site operator for the original triangular lattice results in a four-site operator for the fine-grained lattice. Gray tensors represent the fixed-point environment tensors, as computed with a CTM procedure.

putational reasons. However it is traded for the benefit of working on a lattice with lower connectivity compared to the original triangular lattice, which makes accurate calculations that involve the full environment much more amenable.

In the following sections we apply the fine-graining procedure to study the spin-1 transverse-field Ising model and two versions of the Bose Hubbard model on the triangular lattice. The fine-graining method will also be referred to as fine-PEPS.

## 6.2 Transverse-Field Ising Model

In this section we study the spin-1 ferromagnetic transverse-field Ising model (TFIM) on the triangular lattice. The model is described by the Hamiltonian

$$H_{\text{TFIM}} = - \sum_{\langle i,j \rangle} \sigma_i^z \sigma_j^z - h_x \sum_i \sigma_i^x, \quad (6.4)$$

where  $\sigma_i^\alpha$  describes the  $(3 \times 3)$ -dimensional spin-1 Pauli matrices at site  $i$  and  $h_x$  is the magnetic field along the  $x$ -direction. As argued in Sec. 2.2 the Ising model realizes a polarized phase for  $h_x > h_c$  and a symmetry-broken ordered phase for  $h_x < h_c$ , separated by a quantum phase transition. The precise value of the quantum critical point  $h_c$  depends on the lattice dimension and geometry. A perturbative Continuous Unitary Transformation (pCUT) series of the one-particle gap in the polarized phase using Dlog Pandé extrapolation yields a very accurate estimation of  $h_c^{\text{pCUT}} = 5.269(3)$  [120]. For the numerical fine-PEPS simulations we choose an isometry that represents the spin-1 degrees of freedom in terms of two spin-1/2 degrees of freedom projected into the spin-1 subspace in the coupled basis. Due to the  $SU(2)$  fusion rules we have  $1/2 \otimes 1/2 = 0 \oplus 1$ , i.e. a four-dimensional Hilbert space where the singlet state needs to be projected out. The actual isometry is then given by

$$W_{m_1, m_2}^m = \langle 1/2, m_1, 1/2, m_2 | 1, m \rangle \quad (6.5)$$

with  $m_{1/2} = \pm 1/2$  and  $m = -1, 0, +1$ . It is therefore a  $(2 \times 2 \times 3)$ -dimensional array filled with standard Clebsch-Gordan coefficients  $\langle j_1, m_1, j_2, m_2 | j, m \rangle$ . The fine-PEPS simulations were performed for bond dimensions up to  $D = 6$  and the results are compared to a tensor network method called graph-based PEPS (gPEPS) [121]. This

method is particularly suited since it can simulate arbitrary lattice structures with a simple update, but it uses only the mean-field environment to compute observables. Therefore, the benefit of using a CTM scheme in fine-PEPS simulations can be directly assessed. In Fig. 6.8 we show the ground state energy per site obtained by the

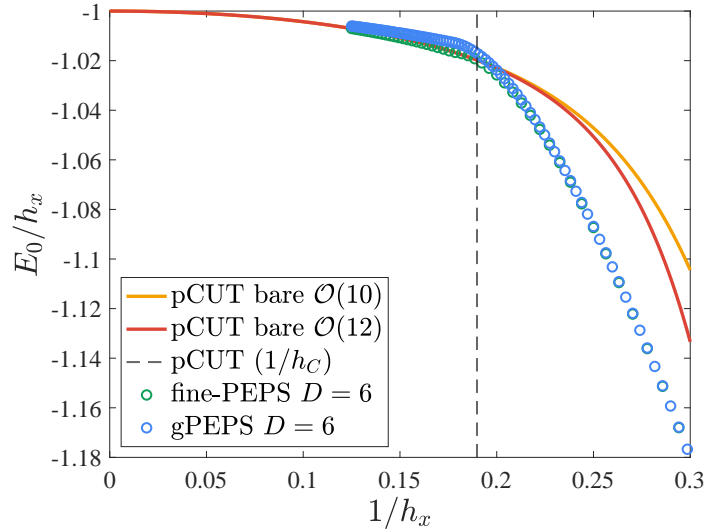


FIGURE 6.8: Ground state energy per site for the ferromagnetic spin-1 transverse-field Ising model on a triangular lattice compared to gPEPS and pCUT results.

two tensor network methods and compare it to a pCUT series expansion up to order  $\mathcal{O}(12)$ . The series expansion for the pCUT results is done in the polarized phase and the overlap with fine-PEPS for small  $1/h_x$  is perfect. Compared with gPEPS, fine-PEPS performs much better for magnetic fields slightly larger than  $h_c^{\text{pCUT}} = 5.269(3)$  due to the inclusion of the whole environment using CTM. In this regime the system

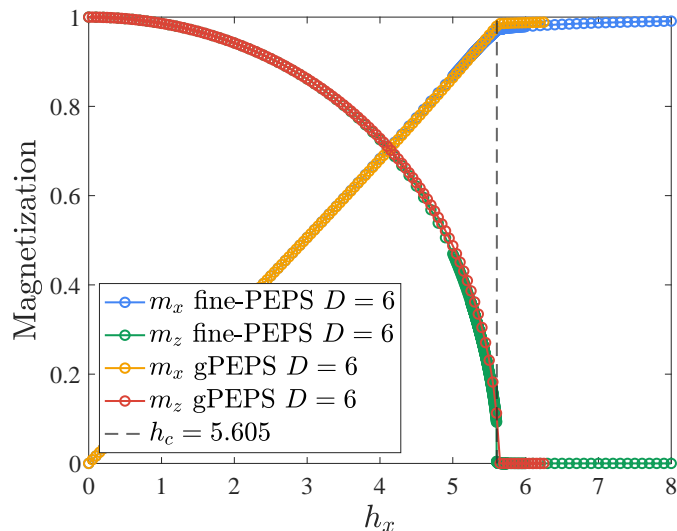


FIGURE 6.9: Longitudinal and transversal magnetization per site for the ferromagnetic spin-1 transverse-field Ising model on a triangular lattice. The observables correspond to  $\langle \sigma^x \rangle$  and  $\langle \sigma^z \rangle$  respectively.

is close to criticality and the correlation length becomes very large. Those correlations are much better captured by fine-PEPS and neglected in the gPEPS ansatz. For large

$1/h_x$  the amount of entanglement is again manageable by both TN approaches so that the energies coincide.

The phase transition can be determined very accurately by pCUT. In order to determine the transition in the TN simulations we computed the local transverse magnetization  $\langle \sigma_z \rangle$ , that can act as an order parameter to detect the spontaneous breaking of the  $\mathbb{Z}_2$  symmetry in the ordered phase (refer to Sec. 2.2). The results of the longitudinal magnetization  $\langle \sigma_x \rangle$  and transversal magnetization  $\langle \sigma_z \rangle$  for both fine-PEPS and gPEPS at  $D = 6$  are shown in Fig. 6.9, which agree very well. Computing expectation values with the full CTM environment has again a small effect so that the quantum critical point is extracted from fine-PEPS to be  $h_c = 5.60(5)$ . The discrepancy to the value obtained by pCUT lies in the simple update method that is used for both TN simulations. A more sophisticated procedure that utilized the full environment already in the simulation of the ground state is known to work more accurately near QCPs, and should reproduce the precise location of the phase transition.

### 6.3 Bose Hubbard Model

In order to test our approach for a bosonic system we consider two limiting cases of the bosonic Hubbard model on the triangular lattice. The general Bose-Hubbard model describes interacting spinless bosons on a lattice and is known to capture superfluid-insulator transitions [122]. The Bose-Hubbard Hamiltonian is given by

$$H_{\text{BH}} = -t \sum_{\langle i,j \rangle} (b_i^\dagger b_j + b_j^\dagger b_i) + \frac{U}{2} \sum_i n_i (n_i - 1) - \mu \sum_i n_i, \quad (6.6)$$

with the hopping parameter  $t$ , the repulsive density-density interaction strength  $U$  and a chemical potential  $\mu$  that controls the filling fraction. Here  $b_i^\dagger$  and  $b_i$  are bosonic creation and annihilation operators at site  $i$  and  $n_i = b_i^\dagger b_i$ . In the limit of large interaction  $U \rightarrow \infty$ , each site can be either occupied or empty but a double occupancy is suppressed – this is called the hardcore limit where the Hamiltonian simplifies to

$$H_{\text{HC}} = -t \sum_{\langle i,j \rangle} (b_i^\dagger b_j + b_j^\dagger b_i) - \mu \sum_i n_i. \quad (6.7)$$

The hardcore Bose-Hubbard model has a  $U(1)$  particle number symmetry, meaning that the Hamiltonian commutes with the total number operator. Transforming the bosonic operators  $b_j \rightarrow b_j^\dagger$  on all sites (duality transformation) maps  $H_{\text{HC}}(\mu)$  to  $H_{\text{HC}}(-\mu)$  up to an irrelevant additive constant. Therefore, for  $\mu = 0$  the model is self-dual and the model's properties for e.g.  $\mu > 0$  can be obtained from those for  $\mu < 0$ . The chemical potential  $\mu$  controls the ground state density

$$\rho = \frac{1}{N} \sum_j \langle b_j^\dagger b_j \rangle. \quad (6.8)$$

For  $\mu \ll 0$  the chemical potential forces the lattice sites to be unoccupied, i.e. the ground state is in a Mott phase with zero density. Contrary, and as expected from the duality transformation the case  $\mu \gg 0$  leads to a completely filled lattice, so that the ground state is in a Mott phase with density one. Both limits represent gapped phases, whereas in the intermediate phase with  $0 < \rho < 1$  the hopping terms

dominates and the cost of adding or removing bosons vanishes. The system is then in a gapless superfluid phase [122] that is characterized by a finite fraction of bosons in the lowest momentum mode

$$\tilde{b}_{k=0} = \frac{1}{N} \sum_j b_j, \quad (6.9)$$

where the phase in the Fourier transformation is always one due to vanishing momentum. This fraction of superfluid bosons is given by the *condensate fraction*

$$\rho_0 = \langle \tilde{b}_{k=0}^\dagger \tilde{b}_{k=0} \rangle = \frac{1}{N^2} \sum_{j,j'} \langle b_j^\dagger b_{j'} \rangle. \quad (6.10)$$

It is known that in thermodynamic limit a finite value of  $\rho_0$  is only possible in the presence of off-diagonal long-range order (ODLRO) [123], so that  $\langle b_j^\dagger b_{j'} \rangle \neq 0$  for large distances of  $|j - j'|$  and therefore

$$\rho_0 = \lim_{|j-j'| \rightarrow \infty} \langle b_j^\dagger b_{j'} \rangle. \quad (6.11)$$

At large distances the condensate fraction reduces to  $\rho_0 = |\langle b_j \rangle|^2$  and can be used as an order parameter to determine the spontaneous breaking of the  $U(1)$  symmetry in the superfluid phase.

Using the fine-graining as introduced in Sec. 6.1.2 every hardcore boson is represented in terms of two hardcore bosons via the isometry

$$W_{0,0}^0 = 1 \quad W_{1,0}^1 = W_{0,1}^1 = \frac{1}{\sqrt{2}}. \quad (6.12)$$

Therefore the physical site is empty if both fine-grained sites are empty and if the physical site is occupied, the hardcore boson can be in either of the fine-grained sites. In order to identify the phase transitions of the hardcore Bose-Hubbard model we

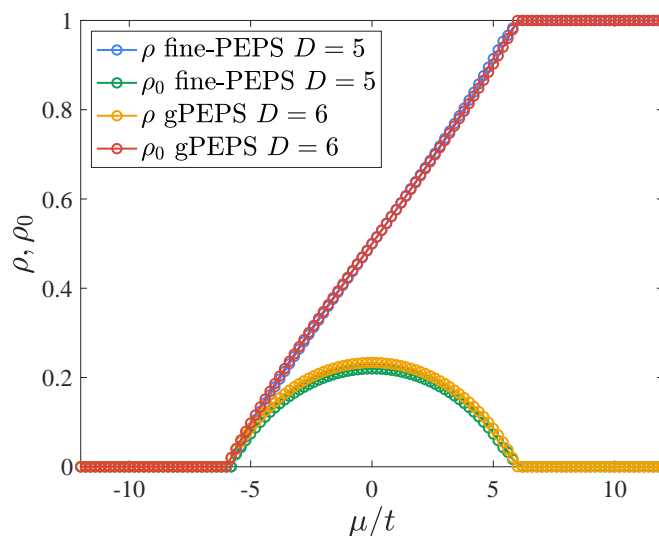


FIGURE 6.10: Particle density  $\rho$  and condensate fraction  $\rho_0$  for the hardcore Bose-Hubbard model on the triangular lattice. Both TN simulations use  $t = 1$  for the hopping amplitude.

compute numerically the particle density per site  $\rho = \langle b_j^\dagger b_j \rangle$ , as well as the condensate fraction  $\rho_0 = |\langle b_j \rangle|^2$  using fine-PEPS up to  $D = 5$ . The hopping amplitude is set to  $t = 1$ . Results are shown in Fig. 6.10 in comparison with gPEPS data for  $D = 6$ . Both TN approaches show excellent agreement and identify the location of the phase transitions at  $(\mu/t)_c = \pm 6$ . This value matches the exact location of the phase transitions computed from first-order perturbation theory for the one-particle gap of the two Mott phases [120].

Relaxing the hardcore constraint yields a softcore version of the Bose-Hubbard model, for which we consider at most two particles per lattice site. The Hamiltonian for the softcore model is the one in Eq. (6.6) where the local Hilbert space is of dimension three. The ground state is expected to have three gapped Mott phases with integer densities  $n_j \in \{0, 1, 2\}$  and two intermediate superfluid phases. Again we can use the particle density  $\rho$  as well as the condensate fraction  $\rho_0$  as order parameters to determine the phase transitions. The completely empty ( $n_j = 0$ ) and the completely filled ( $n_j = 2$ ) Mott states are exact eigenstates of the Hamiltonian and the corresponding one-particle gap  $\Delta_{n=0}^p = -\mu - 6t$  and the one-hole gap  $\Delta_{n=2}^h = -U + \mu - 12t$  can be calculated exactly. For the fine-PEPS simulations we choose the same fine-graining as for the hardcore version only now with the possibility of double occupancy of the physical site via the isometry

$$W_{0,0}^0 = 1 \quad W_{1,0}^1 = W_{0,1}^1 = \frac{1}{\sqrt{2}} \quad W_{1,1}^2 = 1. \quad (6.13)$$

Results are shown in Fig. 6.11, again in good agreement with compared gPEPS data. Near the critical points the fine-PEPS simulations show a better precision because

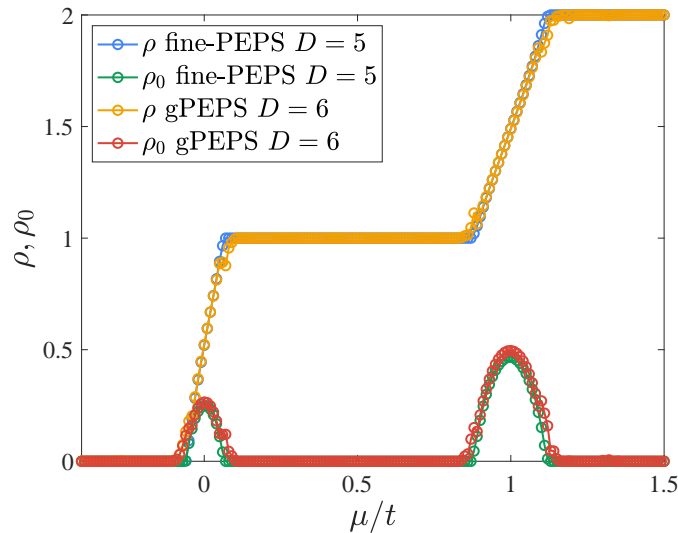


FIGURE 6.11: Particle density  $\rho$  and condensate fraction  $\rho_0$  for the softcore Bose-Hubbard model on the triangular lattice with  $t = 0.01$  and  $U = 1$ . The comparison with gPEPS shows a better accuracy of fine-PEPS results especially near the QCPs.

correlations are fully incorporated in the environment. The three gapped Mott phases with integer densities are clearly identified and the condensate fraction is non-zero only in the gapless superfluid phases in between.

## 6.4 Extension of the Fine-Graining to Three Dimensions

The fine-graining procedure was introduced as a physically motivated strategy to improve the utility of tensor networks on lattices with a high connectivity. In order to demonstrate that this approach works in three-dimensional TN simulations as well, we will consider a 3d stacked triangular lattice made of 2d triangular layers. The lattice sites are connected to six neighbours in plane and to two neighbours among the planes as shown in Fig. 6.12. This lattice structure is directly used in the gPEPS simple update, where each local tensor has one physical and eight virtual indices. For

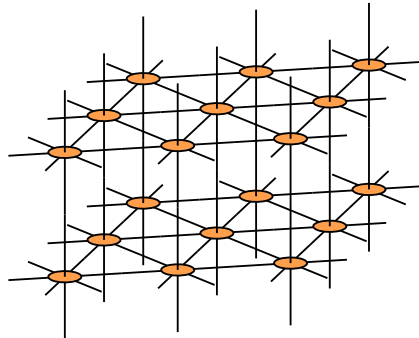


FIGURE 6.12: The 3d stacked triangular lattice consisting of layered triangular planes. Only the lattice structure is shown and not the tensor network, hence there are no physical indices.

fine-PEPS we employ the same fine-graining isometry as used for the 2d triangular TFIM in Sec. 6.2, and the local iPEPS tensors are split into two fine-grained tensors carrying five virtual indices each. The two virtual indices connecting the 2d planes are separated as shown in Fig. 6.13. Physical indices are drawn in snake form for a better

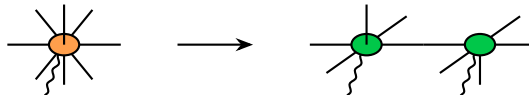


FIGURE 6.13: Fine-graining of the local iPEPS tensors on the stacked triangular lattice. Physical indices are drawn in snake form to distinguish them from virtual indices.

distinction with virtual indices. For the numerical simulations we consider a unit cell of  $N_x \times N_y \times N_z$  tensors with two tensors in each direction. This corresponds to a unit cell of  $N_x \times (2N_y) \times N_z$  tensors on the fine-grained cubic-type lattice, and a total number of  $4N_x N_y N_z$  different links to be considered in the simple update. Notice that the fine-graining does not result in a regular cubic lattice since every fine-grained tensor connects only to one other tensor in the  $z$ -direction.

The ferromagnetic spin-1 transverse-field Ising model serves again as a benchmarking model. Due to the reduced importance of quantum fluctuations in three dimensions [70] we compute all fine-PEPS expectation values using the mean-field environment, as done for the gPEPS simulations. Fig. 6.14 shows the ground state energy per site for fine-PEPS and gPEPS together with an  $\mathcal{O}(12)$  pCUT expansion. Due to the pCUT expansion in the polarized phase the overlap with both TN methods is excellent for magnetic field values above the critical point. The quantum critical point for the 3d stacked triangular lattice can be estimated precisely by pCUT to be



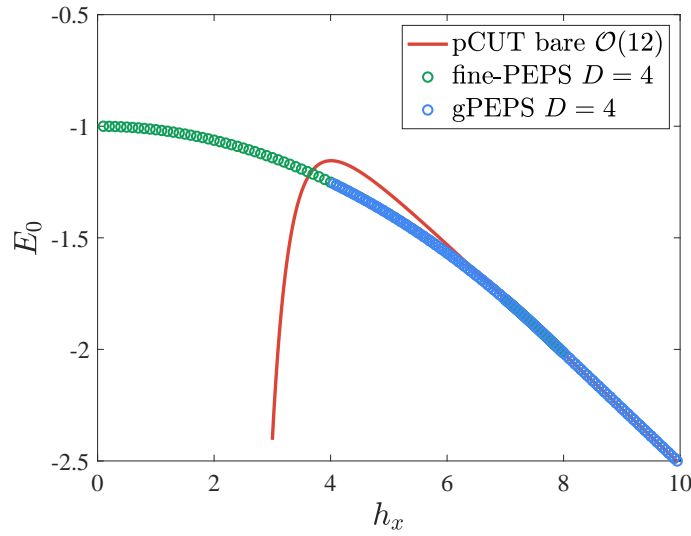


FIGURE 6.14: Ground state energy per site for the ferromagnetic spin-1 transverse-field Ising model on a stacked triangular lattice. The energy is compared to gPEPS and pCUT results at order twelve in the series expansion.

$h_c^{\text{pCUT}} = 7.45(1)$  [120]. Using TN methods we can again compute the order parameters to determine the location of the phase transition. The longitudinal and transverse magnetization is shown in Fig. 6.15. In both TN simulations the critical point is at

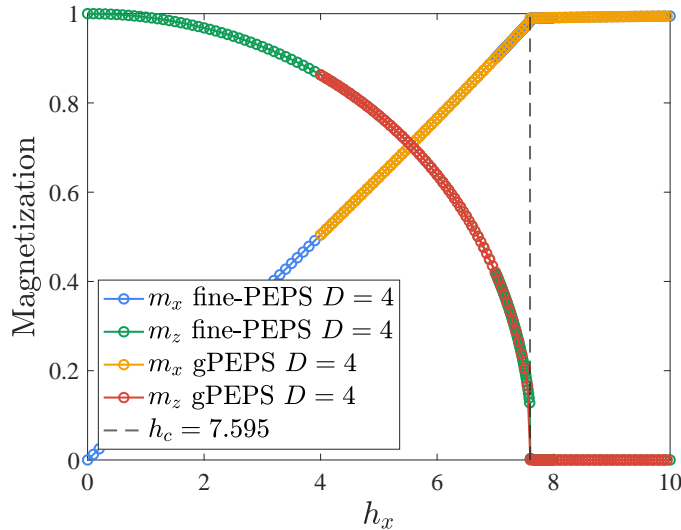


FIGURE 6.15: Longitudinal and transversal magnetization per site for the ferromagnetic spin-1 transverse-field Ising model on a stacked triangular lattice. The observables correspond to  $\langle \sigma^x \rangle$  and  $\langle \sigma^z \rangle$  respectively.

$h_c \approx 7.59$ , which is still not in agreement with pCUT. The reason lies again in the approximations introduced in the simple update, that neglects the full correlations while finding the iPEPS tensors representing the wave function. Nevertheless, the fine-graining procedure and the mapping to a cubic-like structure is very convenient for the implementation of a 3d corner transfer matrix renormalization group scheme, which is expected to unveil even larger differences in computational costs compared to a CTM for gPEPS or a fine-grained version of gPEPS.

## 6.5 General Comments and other Applications

### 6.5.1 Efficiency of the Method

One of the most important characteristics of new algorithms and methods is their computational efficiency. Since the accuracy of TN simulations is mostly controlled via the bond dimension, a smaller computational cost automatically implies the possibility of improved precision. Here we will comment on the efficiency of fine-PEPS and compare it to gPEPS.

#### Simple Update

The simple update for the fine-graining is explained in Sec. 6.1.2. For a reduced computational cost it is beneficial to split away uninvolved virtual indices and apply the gate only to the reduced tensors. The same preparation can and should be done for the

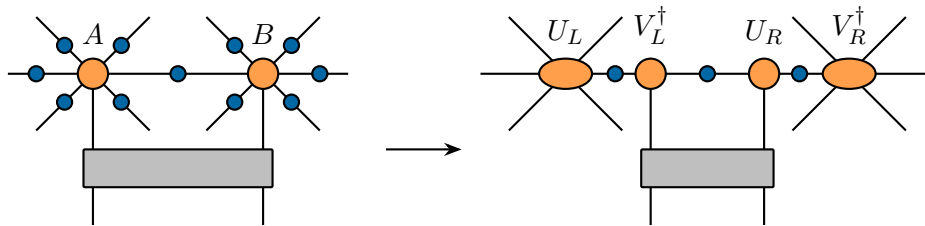


FIGURE 6.16: Simple update of a horizontal link in the original triangular lattice. An SVD can be used to split off uninvolved virtual indices and apply the gate on the reduced tensors only.

simple update on the triangular lattice, as used in gPEPS. The cost for an SVD of an  $(m \times n)$ -dimensional matrix with  $m \geq n$  scales as  $\mathcal{O}(mn^2)$ , so that the decomposition in Fig. 6.16 is  $\mathcal{O}(D^7 d_p^2)$ . This is the leading cost in the gPEPS algorithm. A naive implementation without reduced tensors would instead scale as bad as  $\mathcal{O}(D^{15} d_p^3)$ . In contrast, the leading cost of the fine-graining simple update is  $\mathcal{O}(D^7 d_f^4)$  with  $d_f < d_p$  typically. The leading costs are therefore comparable, however the fine-graining algorithm has additional steps that scale as  $\mathcal{O}(D^7 d_f^7)$  in the worst case. Due to the overhead of keeping and restoring the fine-grained structure in fine-PEPS, gPEPS is slightly more efficient for the simple update.

#### Corner Transfer Matrix Schemes

CTM procedures are essential to compute accurate expectation values taking the full environment into account. In fine-PEPS we can readily apply CTM schemes due to the simplified square lattice structure. In order to make a comparison to gPEPS we can use the gPEPS tensors obtained from the simple update, and use a regular SVD to split the tensors similarly to fine-graining. Generally the link connecting the two

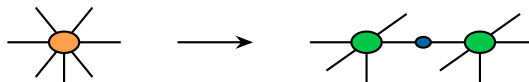


FIGURE 6.17: Splitting of an iPEPS tensor on the triangular lattice using isometry  $W$  and e.g. an SVD. In general the link between the two tensors can not be truncated without losing important physical information and its bond dimension is  $\mathcal{O}(D^3 d_f)$ .

separate tensors cannot be truncated without losing important physical information, so that the bond dimension for this link is  $\mathcal{O}(D^3 d_f)$ . The leading computational cost of a regular CTM procedure as used in the fine-PEPS algorithm is  $\mathcal{O}(D^7 \chi^2 d_f)$ , where

$D$  is the iPEPS bond dimension and  $\chi$  the bond dimension of the environment tensors. In contrast, the leading computational cost of a CTM for fine-grained gPEPS tensors scales as  $\mathcal{O}(D^{11}\chi^2d_f^3)$  due to the enlarged link. This limits calculations to smaller bond dimensions  $D$  and slows down CTM procedures significantly. Native CTM schemes on the triangular lattice are more involved and are expected to perform worse than square lattice CTM procedures due to the high connectivity of iPEPS tensors.

### 6.5.2 Choice of Isometries

In all applications provided in this chapter the isometry was chosen such that both fine-grained sites are embraced equally, i.e. we chose a symmetric fine-graining. In principle a spin-1 degree of freedom could also be fine-grained as  $1 \rightarrow 0 \otimes 1$ , so that one of the additional sites is trivial. For practical purposes we noticed however that a symmetric splitting is indeed favorable, and imbalances due to the isometry may negatively affect convergence of the simulations.

## 6.6 Further Applications

The two dimensional triangular lattice is a paradigm example that benefits from fine-graining. However there are other lattice structures where our method can be applied. For instance consider the lattice shown in Fig. 6.18, which is classified as the  $D(4, 8^2)$  Laves lattice [124] and also called the Tetrakis square tiling or Union Jack lattice. In

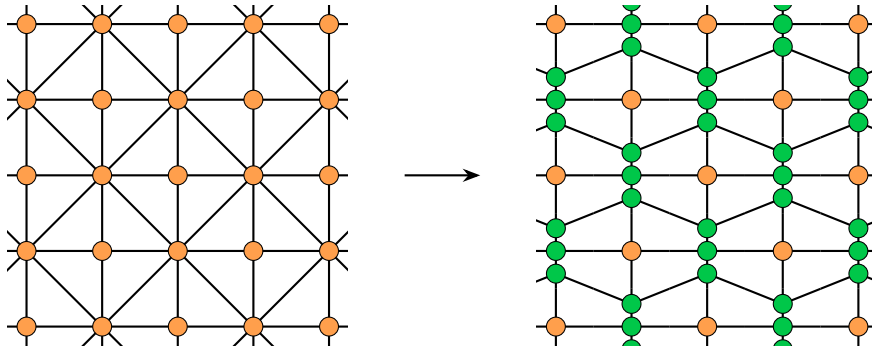


FIGURE 6.18: Application of the fine-graining procedure to the  $D(4, 8^2)$  Laves lattice. All lattice sites that connect to eight neighbours are decomposed using a 1-to-3 isometry which results in a square lattice.

order to map it to the square lattice a 1-to-3 isometry is used on all lattice sites that connect to eight neighbours.

## 6.7 Conclusion and Outlook

In this chapter we have introduced and described a new physically motivated strategy to deal efficiently with tensor network simulations of lattices with high connectivity. Based on the idea of fine-graining, the physical degrees of freedom are decomposed into smaller entities in such a way that the resulting tensor network structure is simpler and more suitable for standard simulation techniques. The method has been applied for different magnetic and bosonic models on the 2d triangular and 3d stacked triangular lattice, showing excellent agreement with other TN methods and pCUT results. The fine-graining technique is believed to advance the tensor network study of high-connectivity lattices, which can host highly interesting quantum phases.



## Chapter 7

# Classical Partition Function for the Heisenberg Model

Besides the established application of tensor networks as representations of quantum states and operators, it has been recently noted that they can provide an accurate portrayal of partition functions of classical models. For instance, two-dimensional PEPS-like tensor networks have been used to study the classical XY model of statistical mechanics [125, 126]. In Ref. [126] the TN ansatz exploited the full  $O(2)$  symmetry of the model by preserving explicitly the  $U(1)$  and charge conjugation symmetry  $\mathcal{C}$  in the tensors. In this respect, the symmetric tensor network framework developed during the time of the PhD can be used to study classical models of statistical mechanics with an  $SU(2)$  symmetry, such as the Heisenberg model. We restrict to the classical Heisenberg model on the square lattice to utilize all the algorithms developed in Chapter 5. This model has sparked a lot of interest since the 1960s. During that time, one of the most striking results was the Mermin-Wagner theorem [127], which states that continuous symmetries in one and two spatial dimensions cannot be spontaneously broken at finite temperatures. This rules out the possibility of spontaneous magnetization in the 2d classical Heisenberg model, and therefore phase transitions based on symmetry breaking. Around the same time, some studies found indications of a possible finite-temperature transition in the 2d Heisenberg model based on spin-wave arguments and high temperature expansions [128, 129]. The contradiction with the Mermin-Wagner theorem could be resolved by the possibility of a Berezinsky–Kosterlitz–Thouless transition [130, 131], where the absence of spontaneous symmetry breaking does not automatically imply the absence of quasi-long-range order. In fact, some studies indeed found evidences of a finite-temperature transition at  $T_c \sim 0.6$  with features similar to a Berezinsky–Kosterlitz–Thouless transition [132]. Although topological defects are likely to play an important role in the system, the mechanism behind a possible transition is fully unclear at the moment. More recent studies of the classical Heisenberg model using finite size scaling suggest a pseudo critical region [133] and quasi-long-range order [134]. With our method based on symmetric tensor networks we provide a fresh approach to this long-standing problem, which may in future help to resolve this question.

In the present chapter we will develop a strategy to write the partition function for the classical Heisenberg model in terms of  $SU(2)$ -symmetric tensors and compute different local and thermodynamic quantities from it. Besides providing a new line of action to simulate this delicate model, it is also a beautiful demonstration of the potential of symmetry-preserving tensors and the formalism developed in Chapter 3. Moreover, our tensor network study works directly in the thermodynamic limit, and does not suffer from finite-size effects.

## 7.1 The Partition Function as a Tensor Network

The classical antiferromagnetic Heisenberg model on the square lattice is defined by the Hamiltonian

$$H = \sum_{\langle i,j \rangle} \vec{S}_i \cdot \vec{S}_j, \quad (7.1)$$

where  $\langle i,j \rangle$  denotes nearest-neighbours and  $\vec{S}_i$  is the three-dimensional spin vector of unit length at site  $i$ , i.e.  $\vec{S}_i = (\sin \theta_i \cos \phi_i, \sin \theta_i \sin \phi_i, \cos \theta_i)^\top$ . Let us note that one can also study the ferromagnetic Heisenberg model instead, since the two versions can be mapped into each other via a suitable lattice transformation for the case of bipartite lattices. Our discussion therefore applies in large parts to both models. We now want to write the partition function

$$Z = e^{-\beta H} = \prod_k \int d\Omega_k e^{-\beta \sum_{\langle i,j \rangle} \vec{S}_i \cdot \vec{S}_j} = \prod_k \int d\Omega_k \prod_{\langle i,j \rangle} e^{-\beta \vec{S}_i \cdot \vec{S}_j} \quad (7.2)$$

at inverse temperature  $\beta = 1/T$  for the model as a tensor network. In order to shorten the notation we write  $d\Omega_k = d\theta_k d\phi_k \sin \theta_k$ . Using a plane wave expansion

$$\begin{aligned} e^{i\vec{k} \cdot \vec{r}} = e^{ikr \cos \theta} &= \sum_{\ell=0}^{\infty} (2\ell+1) (i)^\ell \sqrt{\frac{\pi}{2}} \frac{1}{\sqrt{kr}} J_{\ell+\frac{1}{2}}(kr) P_\ell(\cos \theta) \\ &= \sum_{\ell=0}^{\infty} \sum_{m=-\ell}^{+\ell} (i)^\ell (2\pi)^{3/2} \frac{1}{\sqrt{kr}} J_{\ell+\frac{1}{2}}(kr) Y_{\ell,m}^*(\hat{k}) Y_{\ell,m}(\hat{r}) \end{aligned} \quad (7.3)$$

we can write the Boltzmann factors on every link in the lattice as a linear combination of spherical harmonics. Here  $J_{\ell+1/2}(kr)$  are Bessel functions of the first kind, and  $Y_{\ell,m}(\theta, \phi)$  are the spherical harmonics, i.e., the representations of the 3d rotation group in terms of functions. Using  $\beta' = kr$  and making the substitution  $\beta' \rightarrow i\beta$  yields the plane wave expansion for the Boltzmann factors for the Heisenberg model, which become

$$\begin{aligned} e^{-\beta \vec{S}_i \cdot \vec{S}_j} = e^{-\beta \cos \theta_{ij}} &= \sum_{\ell=0}^{+\infty} (2\ell+1) (i)^\ell \sqrt{\frac{\pi}{2}} \frac{1}{\sqrt{i\beta}} J_{\ell+\frac{1}{2}}(i\beta) P_\ell(\cos \theta_{ij}) \\ &= \sum_{\ell=0}^{+\infty} \sum_{m=-\ell}^{+\ell} (i)^\ell (2\pi)^{3/2} \frac{1}{\sqrt{i\beta}} J_{\ell+\frac{1}{2}}(i\beta) Y_{\ell,m}^*(\hat{S}_i) Y_{\ell,m}(\hat{S}_j), \end{aligned} \quad (7.4)$$

with  $\theta_{ij}$  as the angle between spin  $\vec{S}_i$  and spin  $\vec{S}_j$ . This can also be written in terms of the modified Bessel function of the first kind  $I_{l+1/2}(\beta)$  to simplify the expression. Finally, the Boltzmann factors can be written according to

$$e^{-\beta \vec{S}_i \cdot \vec{S}_j} = \sum_{\ell=0}^{+\infty} \sum_{m=-\ell}^{+\ell} (i)^{2\ell} (2\pi)^{3/2} \frac{1}{\sqrt{\beta}} I_{\ell+\frac{1}{2}}(\beta) Y_{\ell,m}^*(\hat{S}_i) Y_{\ell,m}(\hat{S}_j). \quad (7.5)$$

### 7.1.1 Application to a 1d Chain

Consider first the case of a 1d classical Heisenberg model, where the spins on the chain are coupled to their left and right neighbours. The one-dimensional Heisenberg model is known to have an exact solution [135, 136, 137]. For every site  $j$  of the chain

there are two Boltzmann factors in the partition function, one for the left and one for the right bond. Using the plane wave expansion in Eq. (7.5) the partition function contains terms like

$$\sum_{\ell,m} \sum_{\ell',m'} I_{\ell+\frac{1}{2}}(\beta) I_{\ell'+\frac{1}{2}}(\beta) \int d\theta_j d\phi_j \sin \theta_j Y_{\ell,m}(\theta_j, \phi_j) Y_{\ell',m'}^*(\theta_j, \phi_j). \quad (7.6)$$

Using the orthogonality relation for spherical harmonics

$$\int_{\theta=0}^{\pi} \int_{\phi=0}^{2\pi} d\theta d\phi \sin \theta Y_{\ell,m}(\theta, \phi) Y_{\ell',m'}^*(\theta, \phi) = \delta_{\ell,\ell'} \delta_{m,m'} \quad (7.7)$$

we find that the angular momenta must coincide on both links, so that the  $\delta$  functions reduce to the identities on the lattice sites. Finally, the partition function for the 1d antiferromagnetic chain of Heisenberg spins can be written as

$$Z = \prod_{l \in \mathcal{L}} \left( \sum_{\ell_l=0}^{\infty} \sum_{m=-\ell_l}^{+\ell_l} (i)^{2\ell_l} (2\pi)^{3/2} (\beta)^{-1/2} I_{\ell_l+\frac{1}{2}}(\beta) \right), \quad (7.8)$$

i.e. the partition function reduces to a product over sums of Bessel functions on every link  $l$  in the chain. The partition function in Eq. (7.8) has been derived for the antiferromagnetic Boltzmann terms. For completeness, the partition function for ferromagnetic version of the Heisenberg chain is given by

$$Z = \prod_{l \in \mathcal{L}} \left( \sum_{\ell_l=0}^{\infty} \sum_{m=-\ell_l}^{+\ell_l} (2\pi)^{3/2} (\beta)^{-1/2} I_{\ell_l+\frac{1}{2}}(\beta) \right). \quad (7.9)$$

Ultimately, the expressions in Eq. (7.8) and Eq. (7.9) are the same, since the factors of  $(i)^{2\ell_l}$  cancel for an even number of links in the 1d chain. The expression in Eq. (7.9) furthermore matches the derivations in Refs. [136, 137].

### 7.1.2 Application to the 2d Square Lattice

If we now make the same transformation on all the links of the 2d square lattice, there are four terms per lattice site instead of only two. In Fig. 7.1 we show a square lattice vertex, with arrows labeling the direction of the two-body interaction  $\vec{S}_i \cdot \vec{S}_j$ . Again,

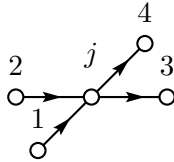


FIGURE 7.1: The four bonds in the square lattice connected to every lattice site  $j$ . Here the arrows indicate the direction of the two-body interaction.

by integrating over the two continuous variables  $\theta_j$  and  $\phi_j$  parameterizing the unit vector  $\hat{S}_j$  at site  $j$ , we write the partition function as

$$Z = \prod_{l \in \mathcal{L}} \left( \sum_{\ell_l=0}^{\infty} \sum_{m=-\ell_l}^{+\ell_l} (i)^{2\ell_l} (2\pi)^{3/2} (\beta)^{-1/2} I_{\ell_l+\frac{1}{2}}(\beta) \right) \prod_s F_{\ell_{s_1}, \ell_{s_2}}^{\ell_{s_3}, \ell_{s_4}}. \quad (7.10)$$

Here the first product runs over all links  $l$  in the lattice and the second product runs over all lattice sites  $s$ . Notice that the two terms are not independent of each other, the angular momenta appearing on the links are also the ones that are coupled on the sites. The object  $F$  on each lattice site is a four-index tensor given by

$$F_{\ell_1, \ell_2}^{\ell_3, \ell_4} = \int d\Omega_s Y_{\ell_1, m_1}(\theta_s, \phi_s) Y_{\ell_2, m_2}(\theta_s, \phi_s) Y_{\ell_3, m_3}^*(\theta_s, \phi_s) Y_{\ell_4, m_4}^*(\theta_s, \phi_s), \quad (7.11)$$

where  $\ell_{s_k}$  in Eq. (7.10) are the angular momenta appearing in the plane wave expansion on the links surrounding site  $s$ , see also Fig. 7.1. Tensor  $F$  ensures the coupling of angular momenta at each vertex of the lattice as prescribed by the product of spherical harmonics, i.e. are the two incoming values compatible with the two outgoing values. We now want to write the whole partition function as the contraction of an iPEPS tensor network on the 2d plane. Therefore we want to use  $SU(2)$ -symmetric tensors, whose group structure is described in terms of Clebsch-Gordan coefficients, i.e. the recoupling coefficients for  $SU(2)$  quantum numbers. The conservation of quantum numbers is natural in an  $SU(2)$ -invariant tensor network, where a four-index tensor on the lattice site incorporates only these symmetric blocks for which the fusion rules of the symmetry are satisfied. So far we have only worked with classical angular momenta and the corresponding spherical harmonics. Although both the spherical harmonics as well as the Clebsch-Gordan coefficients implement the fusion rules of angular momenta and spin quantum numbers respectively, we have to use the precise relation to convert between the two representations. The connection is established by

$$\begin{aligned} \int d\Omega Y_{\ell_1, m_1} Y_{\ell_2, m_2} Y_{\ell_3, m_3}^* &= f_{\text{SHCG}}(\ell_1, \ell_2, \ell_3) \begin{array}{c} (\ell_2, m_2) \searrow \\ \phantom{(\ell_2, m_2)} \\ (\ell_1, m_1) \nearrow \end{array} \longrightarrow (\ell_3, m_3) \\ \int d\Omega Y_{\ell_1, m_1} Y_{\ell_2, m_2}^* Y_{\ell_3, m_3}^* &= f_{\text{SHCG}}(\ell_2, \ell_3, \ell_1) (\ell_1, m_1) \longrightarrow \begin{array}{c} \phantom{(\ell_1, m_1)} \\ \nearrow \\ (\ell_3, m_3) \\ \searrow \\ (\ell_2, m_2) \end{array} \end{aligned} \quad (7.12)$$

for fusion and splitting vertices. Here  $f_{\text{SHCG}}$  are additional factors that appear and the three-index fusion and splitting nodes denote Clebsch-Gordan coefficients. The conversion factors are given by

$$f_{\text{SHCG}}(\ell_1, \ell_2, \ell_3) = \sqrt{\frac{(2\ell_1 + 1)(2\ell_2 + 1)}{4\pi(2\ell_3 + 1)}} \langle \ell_1 0 \ell_2 0 | \ell_3 0 \rangle. \quad (7.13)$$

Since every iPEPS tensor consists of two vertices (one fusion vertex fusing the incoming edges to an intermediate spin and a splitting vertex splitting the intermediate spin into the outgoing edges) the relation for one lattice site is given by

$$\begin{aligned} &\int d\theta d\phi \sin \theta Y_{\ell_1, m_1}(\theta, \phi) Y_{\ell_2, m_2}(\theta, \phi) Y_{\ell_3, m_3}^*(\theta, \phi) Y_{\ell_4, m_4}^*(\theta, \phi) \\ &= \sum_{\ell} f_{\text{SHCG}}(\ell_1, \ell_2, \ell) f_{\text{SHCG}}(\ell_3, \ell_4, \ell) \langle \ell_1 m_1 \ell_2 m_2 | \ell m \rangle \langle \ell_3 m_3 \ell_4 m_4 | \ell m \rangle. \end{aligned} \quad (7.14)$$

The correct prefactor for every block in the  $SU(2)$ -invariant tensor is then the product of two conversion factors, that will be absorbed into the degeneracy tensors. The sums over Bessel functions that appear on the links in Eq. (7.10) can also be absorbed into



the entries of the tensors sitting on the lattice sites. Finally we can construct the fully  $SU(2)$ -invariant iPEPS tensors on the square lattice, that represent the partition function of the Heisenberg model. The conservation of angular momentum quantum numbers is taken care of by the structural part of the tensor, so that the fusion of  $\ell_1$  and  $\ell_2$  is compatible with the splitting into  $\ell_3$  and  $\ell_4$ . The corresponding degeneracy tensors are defined by

$$\begin{array}{c}
 (\ell_4, m_4) \\
 \uparrow \\
 (\ell_2, m_2) \rightarrow \textcircled{\ell} \rightarrow (\ell_3, m_3) \\
 \uparrow \\
 (\ell_1, m_1)
 \end{array}
 = (i)^{2(\ell_1+\ell_2)} \prod_{i=1}^4 \left( (2\pi)^{3/2} (\beta)^{-1/2} I_{\ell_i+\frac{1}{2}}(\beta) \right)^{1/2} \cdot (7.15)$$

$$\times f_{\text{SHCG}}(\ell_1, \ell_2, \ell) f_{\text{SHCG}}(\ell_3, \ell_4, \ell)$$

Here  $\ell$  is the quantum number on the internal leg of the four-index fusion tree and the phase factors  $(i)^{2\ell}$  are accounted for on incoming links. The infinite sum on the links of the square lattice can be truncated in practice, the number of  $SU(2)$  quantum numbers kept on the virtual indices is then the parameter to refine the precision. The explicit sums over  $\ell$  and  $m$  in Eq. (7.10) is performed due to the contraction of the network of the iPEPS tensors, defined in Eq. (7.15). The degeneracy tensors to construct the partition function of the ferromagnetic Heisenberg model in 2d are similar to the ones in Eq. (7.15), just without the phase factors  $(i)^{2\ell}$ .

## 7.2 Computing the Partition Function with CTM

The classical partition function, written as a network of four-index iPEPS tensors can be computed approximately with a standard CTM procedure (for a detailed description of the CTM procedure see Appendix B.2.2). We initialize a single-site iPEPS tensor according to the prescription in Eq. (7.15). This tensor is exact due to the analytic construction and it directly enters the CTM procedure. Due to integer quantum numbers on the virtual indices of the iPEPS network, the CTM environment bond indices can generally carry integer, half-integer or mixed spin representations. The natural choice of only integer spin irreps worked out to be the best one, with smooth convergence of the environment tensors. The full partition function is then given by the expression in Fig. 7.2. Since the network is constructed out of a single iPEPS

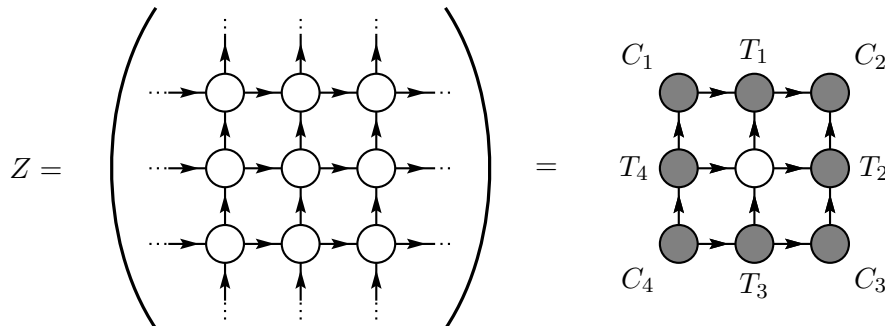


FIGURE 7.2: Computing the full partition function implies the contraction of the full 2d plane, which is approximated with fixed-point CTM tensors, shown in gray.

tensor, there is only one set of eight environment tensors representing the contraction

of the four corners, as well as the four half-infinite rows and columns. We have computed the partition function for several temperatures  $T \in [0.01, 100]$ . From the Bessel

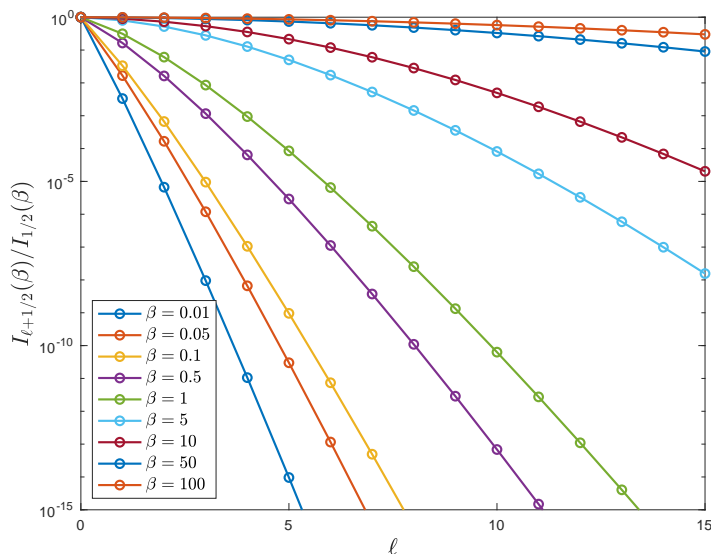


FIGURE 7.3: Decay of the Bessel functions  $I_{\ell+1/2}(\beta)$  normalized to  $I_{1/2}(\beta)$  as a function of the angular momentum  $\ell$ , for several values of the inverse temperature  $\beta = 1/T$ . For large  $\beta$  more values of the angular momentum  $\ell$  have to be kept on the virtual bond indices of the iPEPS tensors to achieve sufficient precision.

functions  $I_{\ell+1/2}(\beta)$  that enter the analytic construction it is expected that more spin representations have to be kept on the virtual indices of the network the larger  $\beta$ , or the smaller the temperature is. This is shown in Fig. 7.3. Therefore, for large  $T$  only a few spin irreps will be sufficient, while for small  $T$  a convergence of the plane wave expansion in  $\ell$  will not be achievable with available computational power.

In order to test if the classical antiferromagnetic Heisenberg model exhibits some interesting behaviour we first compute the corner entropy from the eigenvalue decomposition of the fixed-point tensors  $C \equiv C_1 \cdot C_2 \cdot C_3 \cdot C_4$ . This quantity is equivalent to the entanglement entropy of the ground state for the 1d quantum Heisenberg model. This is due to a general mapping between  $d$ -dimensional classical statistical mechanics models and  $(d-1)$ -dimensional quantum models [35]. The corner entropy is given by

$$S = - \sum_{\alpha} \omega_{\alpha} \log \omega_{\alpha} , \quad (7.16)$$

where the degeneracies of the eigenvalues  $\omega_{\alpha}$  in each spin sector need to be taken into account. The analytic iPEPS tensors were constructed with a maximum of six spin irreps, i.e.  $j_{\max} = 5$  on the virtual indices. Results are shown in Fig. 7.4. For temperatures  $T \geq 0.2$  the corner entropy is essentially converged in the virtual spin irreps, however for  $T \leq 0.2$  more quantum numbers would be needed to achieve convergence, as indicated by the separation of the data points. The environment bond dimension is fixed to  $\chi_E = 50$ , i.e. a maximum of fifty singular values are kept during the  $SU(2)$ -symmetric CTM procedure. This environment bond dimension is not sufficient for larger  $j_{\max}$ , as we demonstrate in the general discussion of the approximations in Sec. 7.5. The spin sectors on the CTM environment tensors are fixed to be integer and the truncation procedure adapts to the most relevant sectors. A collection

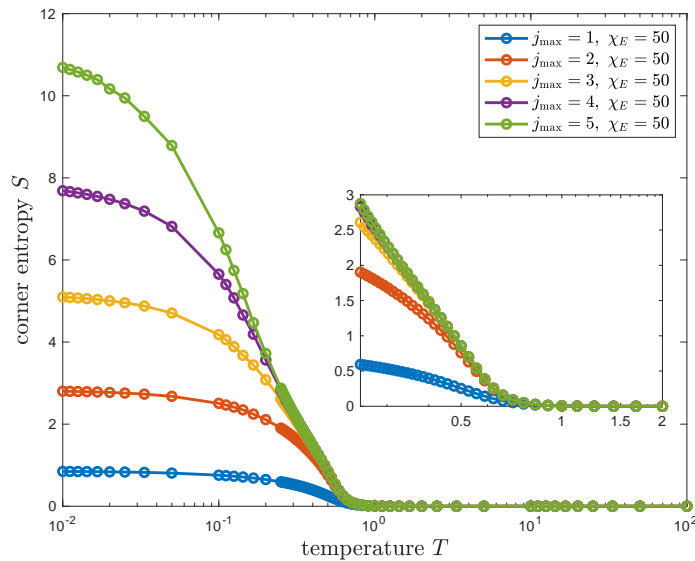


FIGURE 7.4: Corner entropy of the fixed-point CTM corner tensors for different maximal values of the spin in the plane wave expansion and the virtual bond indices. The slow decay of Bessel functions for small  $T$  is manifested in a slow convergence of the entropy with increasing  $j_{\max}$ .

of the  $SU(2)$  CTM data is provided in Table 7.1, where the fifty singular values are distributed across all sectors  $j_E = 0, 1, \dots, j_{E,\max}$ . For larger  $\chi_E$  the algorithm will also keep more spin sectors on the CTM bond indices, therefore increasing the precision. The trend of the corner entropy shows an onset of a finite amount of correlations for

iPEPS $j_{\max}$	iPEPS $D_{\text{eff}}$	CTM $j_{\max}$	CTM $\chi_{\text{eff}}$
1	4	4	208
2	9	7	302
3	16	9	392
4	25	11	452
5	36	13	520

TABLE 7.1: Maximal spin and effective bond dimension for the indices of the analytic iPEPS tensors, and for the CTM bond indices at  $T = 0.01$  and for  $\chi_E = 50$ .

temperatures in the interval  $0.1 \leq T \leq 1$ . In the following sections we compute local and thermodynamic quantities, to further investigate the behaviour of the classical Heisenberg model.

### 7.3 Computation of Expectation Values

We are mainly interested in one-site and two-site observables, like magnetization, the energy on the links of the lattice or spin-spin correlation functions. Therefore, we will describe the calculation of expectation values in the TN formalism first, before moving on to concrete quantities. For a general one-site operator  $O(\hat{S}_i)$  the expectation value is given by

$$\langle O(\hat{S}_i) \rangle = \frac{1}{Z} \prod_k \int d\Omega_k e^{-\beta E(\{\hat{S}_k\})} O(\hat{S}_i). \quad (7.17)$$

By integrating over all continuous variables  $\theta_k$  and  $\phi_k$  except at site  $i$ , the one-site expectation value can be written as

$$\langle O(\hat{S}_i) \rangle = \frac{1}{Z} \left( \begin{array}{c} \vdots \\ \circ \rightarrow \circ \rightarrow \circ \rightarrow \vdots \\ \vdots \\ \circ \rightarrow \square \rightarrow \circ \rightarrow \vdots \\ \vdots \\ \circ \rightarrow \circ \rightarrow \circ \rightarrow \vdots \\ \vdots \end{array} \right), \quad (7.18)$$

where the round tensors are the analytic iPEPS tensors of Eq. (7.15) and the one-site operator is given by the expression in Eq. (7.19).

$$\begin{aligned} & \begin{array}{c} (\ell_4, m_4) \\ \uparrow \\ (\ell_2, m_2) \rightarrow \square \rightarrow (\ell_3, m_3) \\ \uparrow \\ (\ell_1, m_1) \end{array} = (i)^{2(\ell_1 + \ell_2)} \prod_{i=1}^4 \left( (2\pi)^{3/2} (\beta)^{-1/2} I_{\ell_i + \frac{1}{2}}(\beta) \right)^{1/2} \\ & \times \int d\Omega_i O(\hat{S}_i) Y_{\ell_1, m_1}(\hat{S}_i) Y_{\ell_2, m_2}(\hat{S}_i) Y_{\ell_3, m_3}^*(\hat{S}_i) Y_{\ell_4, m_4}^*(\hat{S}_i) \end{aligned} \quad (7.19)$$

The only possible single-site operator is the local magnetization given by the expectation value of  $O(\hat{S}_i) = \hat{S}_i$ . We can write the spin operator as

$$\hat{S} = \begin{pmatrix} \sin(\theta) \cos(\phi) \\ \sin(\theta) \sin(\phi) \\ \cos(\theta) \end{pmatrix} = \sqrt{\frac{4\pi}{3}} \begin{pmatrix} \frac{1}{\sqrt{2}}(Y_{1,-1}(\theta, \phi) - Y_{1,+1}(\theta, \phi)) \\ \frac{i}{\sqrt{2}}(Y_{1,-1}(\theta, \phi) + Y_{1,+1}(\theta, \phi)) \\ Y_{1,0}(\theta, \phi) \end{pmatrix}. \quad (7.20)$$

From the expansion in terms of spherical harmonics we can see that every component of  $\hat{S}$  implies another spherical harmonics function  $Y_{1,x}(\theta, \phi)$  that enters the integration in Eq. (7.19). This integration leads to an altered form of the spin fusion, and a fifth index appears in the tensor representation which necessarily carries a spin-1 representation. Due to the preservation of  $SU(2)$  symmetry, the resulting local tensor is no longer invariant (the spin operator is not a scalar operator), and the local magnetization has to vanish.

In a similar way we can compute two-site observables  $O(\hat{S}_i, \hat{S}_j)$  using the tensor network representation of the partition function. Let us first describe the general procedure to compute the expectation value, and then focus on concrete quantities we can compute. The two-site observable is computed by

$$\langle O(\hat{S}_i, \hat{S}_j) \rangle = \frac{1}{Z} \prod_k \int d\Omega_k e^{-\beta E(\{\hat{S}_k\})} O(\hat{S}_i, \hat{S}_j). \quad (7.21)$$

By integrating over all spins except the ones at position  $i$  and  $j$ , we can write the two-site operator as a contraction of the tensor network

$$\langle O(\hat{S}_i, \hat{S}_j) \rangle = \frac{1}{Z} \left( \begin{array}{cccc} \vdots & \vdots & \vdots & \vdots \\ \cdots \rightarrow & \text{---} & \text{---} & \text{---} \rightarrow \cdots \\ \text{---} & \text{---} & \text{---} & \text{---} \\ \vdots & \vdots & \vdots & \vdots \end{array} \right), \quad (7.22)$$

which can be approximated with the fixed point CTM tensors. Again, the round tensors are the analytic iPEPS tensors of Eq. (7.15) and the two-site operator is given by the expression in Eq. (7.23).

$$\begin{array}{c} \begin{array}{ccc} \ell_6 & & \ell_5 \\ \uparrow & & \uparrow \\ \ell_3 \rightarrow \text{---} \ell_x \text{---} \rightarrow \ell_4 \\ \uparrow & & \uparrow \\ \ell_2 & & \ell_1 \end{array} \\ = (i)^{2(\ell_1+\ell_2+\ell_3)} \prod_{i=1}^6 \left( (2\pi)^{3/2} (\beta)^{-1/2} I_{\ell_i+\frac{1}{2}}(\beta) \right)^{1/2} \\ \times \int d\Omega_i \int d\Omega_j O(\hat{S}_i, \hat{S}_j) \left( \sum_{\ell_x=0}^{\infty} \sum_{m_x=-\ell_x}^{+\ell_x} (i)^{2\ell_x} (2\pi)^{3/2} (\beta)^{-1/2} I_{\ell_x+\frac{1}{2}}(\beta) \right) \\ \times Y_{\ell_1, m_1}(\hat{S}_j) Y_{\ell_2, m_2}(\hat{S}_i) Y_{\ell_3, m_3}(\hat{S}_i) Y_{\ell_4, m_4}^*(\hat{S}_j) Y_{\ell_5, m_5}^*(\hat{S}_j) Y_{\ell_6, m_6}^*(\hat{S}_i) \end{array} \quad (7.23)$$

The index connecting site  $i$  and site  $j$  still carries the plane wave expansion of the Boltzmann term, and the spherical harmonics have to be evaluated at the two different sites now. The only two  $SU(2)$ -invariant scalar operator are  $\mathbb{I}_i \cdot \mathbb{I}_j$  and  $\hat{S}_i \cdot \hat{S}_j$ . If the two-site operator  $O(\hat{S}_i, \hat{S}_j)$  is equal to the identity  $\mathbb{I}_i \cdot \mathbb{I}_j$ , the expression in Eq. (7.23) simplifies to the contraction of two regular iPEPS tensors as defined in Eq. (7.15). For  $O(\hat{S}_i, \hat{S}_j) = \hat{S}_i \cdot \hat{S}_j$  we can compute bond energies and spin-spin correlations, as demonstrated in Sec. 7.3.1 and Sec. 7.3.2 respectively.

### 7.3.1 Bond Energy

While the two-body operator  $\mathbb{I}_i \cdot \mathbb{I}_j$  is trivial and recovers the analytic expression for the partition function, the interesting case is the dot product  $\hat{S}_i \cdot \hat{S}_j$ . This measures the bond energy between nearest neighbours, and can also be used to compute correlations at a distance as described in Sec. 7.3.2. The dot product can be written in terms of spherical harmonics according to

$$\hat{S}_i \cdot \hat{S}_j = \frac{4\pi}{3} \sum_{m=-1,0,+1} Y_{1,m}^*(\theta_i, \phi_i) Y_{1,m}(\theta_j, \phi_j). \quad (7.24)$$

The spherical harmonics can be affiliated to either side and an integration of the free parameters  $(\theta_i, \phi_i)$  and  $(\theta_j, \phi_j)$  yields an additional index carrying spin-1 for both of the tensors on site  $i$  and site  $j$ . Combining the steps, we can define the left tensor (site  $i$ ) and the right tensor (site  $j$ ) as shown in Fig. 7.5 and Fig. 7.6. Shown are only the entries for the degeneracy tensors, the corresponding fusion trees ensure spin

$$\begin{aligned}
 & \begin{array}{c} (\ell_4, m_4) \\ \uparrow \\ (\ell_2, m_2) \rightarrow \square \rightarrow (\ell_3, m_3) \\ \uparrow \\ (\ell_1, m_1) \end{array} \rightarrow (\ell_3, m_3) \rightarrow (1, m) \\
 & = \sqrt{\frac{4\pi}{3}} (i)^{2(\ell_1+\ell_2)} \prod_{i=1}^4 \left( (2\pi)^{3/2} (\beta)^{-1/2} I_{\ell_i+\frac{1}{2}}(\beta) \right)^{1/2} \\
 & \quad \times f_{\text{SHCG}}(\ell_1, \ell_2, \ell_{a,1}) f_{\text{SHCG}}(\ell_{a,2}, \ell_4, \ell_{a,1}) f_{\text{SHCG}}(1, \ell_3, \ell_{a,2})
 \end{aligned}$$

FIGURE 7.5: Left tensor for the scalar product  $\hat{S}_i \cdot \hat{S}_j$ . The additional channel  $(1, m)$  mediates the interaction, the other four indices carry the quantum numbers of the plane wave expansion for the Boltzmann terms.

coupling rules and mediate the  $\hat{S}_i \cdot \hat{S}_j$  interaction via the additional spin-1 channel. The factors converting between spherical harmonics and Clebsch-Gordan coefficients

$$\begin{aligned}
 & \begin{array}{c} (\ell_4, m_4) \\ \uparrow \\ (\ell_2, m_2) \rightarrow \square \rightarrow (\ell_3, m_3) \\ \uparrow \\ (\ell_1, m_1) \end{array} \rightarrow (\ell_3, m_3) \rightarrow (1, m) \\
 & = \sqrt{\frac{4\pi}{3}} (i)^{2(\ell_1+\ell_2)} \prod_{i=1}^4 \left( (2\pi)^{3/2} (\beta)^{-1/2} I_{\ell_i+\frac{1}{2}}(\beta) \right)^{1/2} \\
 & \quad \times f_{\text{SHCG}}(1, \ell_2, \ell_{b,1}) f_{\text{SHCG}}(\ell_1, \ell_{b,1}, \ell_{b,2}) f_{\text{SHCG}}(\ell_3, \ell_4, \ell_{b,2})
 \end{aligned}$$

FIGURE 7.6: Right tensor for the scalar product  $\hat{S}_i \cdot \hat{S}_j$ . The additional channel  $(1, m)$  mediates the interaction, the other four indices carry the quantum numbers of the plane wave expansion for the Boltzmann terms.

are determined by the internal fusion tree decomposition shown in Fig. 7.7. We

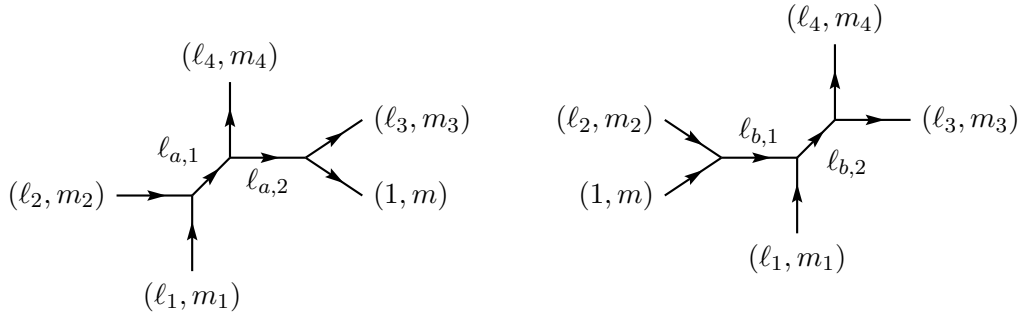


FIGURE 7.7: Fusion trees for the two tensors that generate the two-body scalar product  $\hat{S}_i \cdot \hat{S}_j$  via the additional spin-1 channel.

have computed the nearest-neighbour spin-spin correlation on horizontal and vertical bonds in the iPEPS network, using the two operators defined in Fig. 7.5 and Fig. 7.6. The nearest-neighbour spin-spin correlation is equivalent to the bond energy, and as expected from the analytic construction of the iPEPS tensors it should be rotational symmetric. This is indeed confirmed by the numerical simulation, and the bond energy is shown in Fig. 7.8 for the accessible bond dimensions. The behaviour of  $\langle \vec{S}_i \cdot \vec{S}_j \rangle$  for a fixed  $j_{\text{max}}$  only depends very weakly on the environment bond dimension  $\chi_E$ , so that the same results are already obtained for the smallest value of  $\chi_E = 10$ . However, it strongly depends on the number of angular momenta in the plane wave expansion of the Boltzmann terms, which leads to the spread of the data curves. The bond energy follows the expected behaviour. For large temperatures the classical Heisenberg model is completely disordered, and the bond energy is expected to vanish. In the

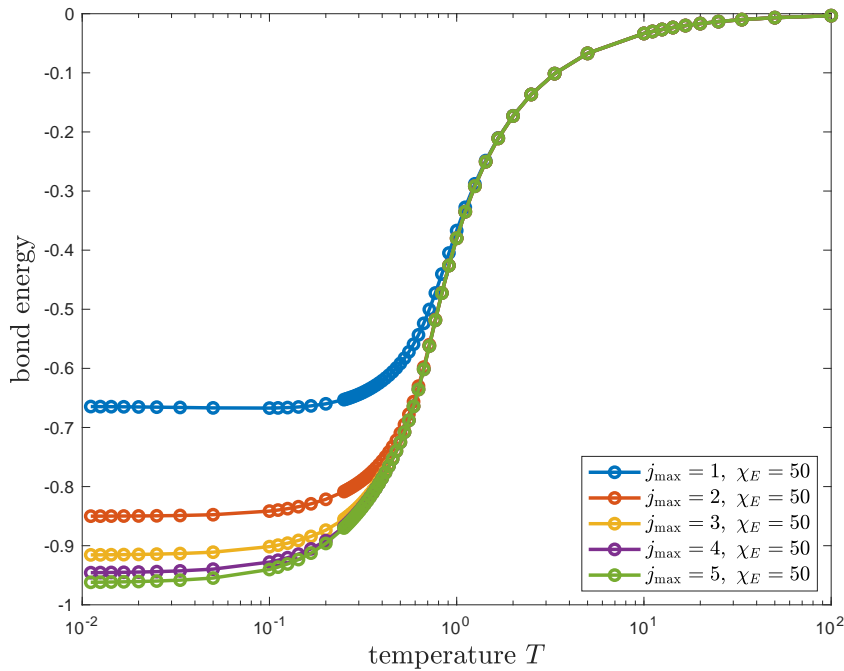


FIGURE 7.8: Bond energy on horizontal and vertical links in the iPEPS network of the partition function.

opposite limit of small temperatures, the antiferromagnetic spin interaction leads to an antiferromagnetic configuration, shown in Fig. 7.9. The total orientation is however

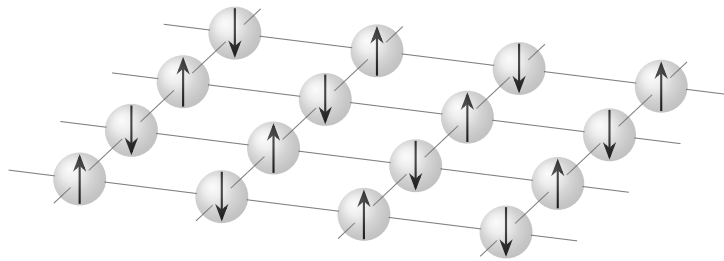


FIGURE 7.9: The ground state of the classical Heisenberg model for  $T \rightarrow 0$  is in an antiferromagnetic configuration. The orientation of the spins is not fixed, they can be rotated on the unit sphere collectively without losing the antiferromagnetic character.

not necessarily aligned with any coordination axis as shown in the figure, a possible rotation of all spins on the unit sphere is a likewise ground state. For the ferromagnetic Heisenberg model, the bond energy is exactly mirrored along the horizontal axis, and it converges to  $+1$  for large  $j_{\max}$  due to the parallel alignment of spins. The bond energy should be equivalent to the internal energy  $U$ , a thermodynamic quantity that can be computed directly from the partition function  $Z(\beta)$ . Those calculations can readily be performed using the CTM fixed-point tensors and are presented in Sec. 7.4.

### 7.3.2 Spin-Spin Correlations

The two operators in Figs. 7.5 and 7.6 can be used to compute the spin-spin correlation at a distance. In order to do this, the regular iPEPS tensor for the partition function

is inserted in between the sites where the spin operators act. Therefore, the actual spin-spin correlations are then computed by a contraction of the TN in Fig. 7.10, divided by the norm, i.e. the same network without any operators. We have computed

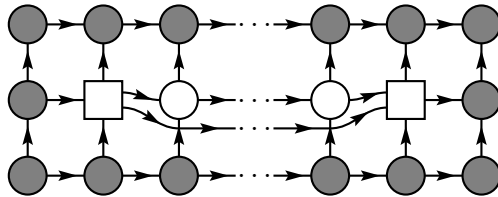


FIGURE 7.10: Computation of the spin-spin correlation function at site  $i$  and  $j$ . The expectation value has to be divided by the same expressions without the operators.

the spin-spin correlation function for the accessible bond dimensions and a maximal separation distance of  $L_{\max} = 50$ . The correlations have alternating signs for the antiferromagnetic, and positive signs for the ferromagnetic Heisenberg model, with the same rate of decay for both versions. The absolute values of the expectation values match an exponential decay of correlations for large temperatures, and a quasi-algebraic decay of correlations for low temperatures. It is important to keep in mind that the results for low temperatures are strongly approximated due to the limited number of angular momenta in the plane wave expansion. The scaling of the correlations at low  $T$  with the iPEPS bond dimension however indicates a shift to a cleaner algebraic decay at larger  $j_{\max}$ . The most interesting features is the cross-over between exponential and power-law correlations, which indicates a change in fundamental properties. The clear exponential decay for large temperatures is blurred out when lowering  $T$ , so that we use a fit in the form of

$$C(r) \sim c \cdot e^{-r/\xi} \cdot r^{-\kappa} . \quad (7.25)$$

Here  $\xi$  is the correlation length and  $\kappa$  is the exponent of the power-law fit. The combination of both terms is necessary especially in the temperature range  $T \leq 1$ . For high temperatures one expects a strong exponential decay due to the disordered alignment of spins. In contrast, for low temperatures Fig. 7.8 clearly shows an antiferromagnetic alignment of spins, so that the correlation length is expected to increase. The spin-spin correlation functions for all available  $j_{\max}$  and  $\chi_E = 50$  have been computed and fitted to extract the relevant information, which is shown in Fig. 7.11. In the figure the upper curves show the correlation length  $\xi(T)$ , while the lower curves show the power-law exponent  $\kappa(T)$ . The correlation length increases towards lower temperatures, and saturates to a finite value eventually. This saturation can have different explanations. First, let us assume that the model features quasi-long-range order as reported for instance in Ref. [134]. The correlation length is then expected to diverge, before saturating to a large, but finite value. While this scenario is within the possibilities of our numerical outcome, it is certain that the saturation is also due to the approximations in the TN study. An actual diverging correlation length could only be observed in the limit  $j_{\max} \rightarrow \infty$  and  $\chi_E \rightarrow \infty$ , as expected from Fig. 7.3. The maximal bond dimension of  $j_{\max} = 5$  is not sufficient, so that even quasi-long-range order would likely not be fully captured by our approximation. Furthermore the wobbly behaviour of  $\xi(T)$  for  $T \leq 0.3$  and  $j_{\max} \geq 4$  is probably due to the fact that the simulations are not yet fully converged in the environment bond dimension  $\chi_E$  (see also Sec. 7.5 for a detailed discussion of the approximations).



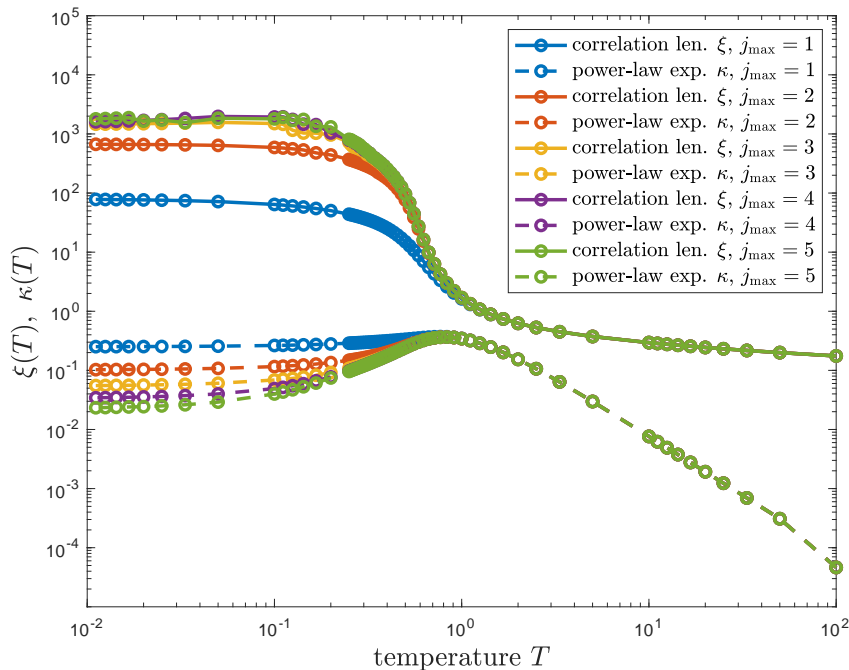


FIGURE 7.11: Correlation length  $\xi(T)$  and power-law exponent  $\kappa(T)$  extracted from the fits of the spin-spin correlation functions, using Eq. (7.25).

With our current numerical simulations it is too vague to speculate about a possible finite temperature transition in the model. Moreover, due to the strong approximations in the low temperature regime we cannot distinguish between a large, but finite correlations length and a truly diverging, i.e. infinite correlation length in the limit  $j_{\max} \rightarrow \infty$ . To gain more evidence or disproof of a finite temperature transition, one could for instance study the spin stiffness of the Heisenberg model. This is however not possible in an  $SU(2)$ -invariant setting, because the required magnetic field would break the continuous symmetry [126]. A small magnetic field could only be introduced in non-symmetric simulations, where the access to large angular momenta is even more restricted due to the loss of the efficient symmetric form of the tensors. Ultimately, if more evidence for a finite temperature transition is found, it would be extremely interesting to identify a possible mechanism behind it. Due to the limited expressiveness of the presented data, we postpone concrete conclusions until further study has been conducted.

## 7.4 Thermodynamic Quantities

### 7.4.1 Partition Function per Site

Performing the contraction of the infinite 2d lattice as shown in Fig. 7.2 yields the full partition function as a function of the inverse temperature  $\beta$ . The problem however is the normalization of the environment tensors, which is necessary in every CTM step to prevent a divergence of the tensor entries. Without this normalization the contraction of the infinite lattice would be infinite, consistent with what one would expect for the full partition function  $Z(\beta)$ . Since we are working directly in the thermodynamic limit, the relevant quantity is the partition function per site, from which we can compute thermodynamic properties like the free energy  $F$ , the internal

energy  $U$  or the thermodynamic entropy  $S$ , also per site. Let us denote the partition function per site as  $z(\beta)$ , defined by

$$\ln(z(\beta)) = \lim_{N_x N_y \rightarrow \infty} \frac{1}{N_x N_y} \ln(Z(\beta)) . \quad (7.26)$$

The partition function can be computed from the transfer operator  $T(\beta)$  according to

$$Z(\beta) = |\text{tr}(T(\beta)^{N_x})| , \quad (7.27)$$

where  $T(\beta)$  is the a column of PEPS tensors and  $N_x$  the number of horizontal copies. For  $N_x \gg 1$  the partition function is expected to scale with the dominant eigenvalue  $\mu$  of  $T(\beta)$ , so that  $Z(\beta) \sim |\mu^{N_x}|$ . This expression can be written in terms of the dominant left and right eigenvectors of the transfer operator according to

$$Z(\beta) \approx \left| \frac{\langle \Psi_L | T(\beta) | \Psi_R \rangle}{\langle \Psi_L | \Psi_R \rangle} \right|^{N_x} . \quad (7.28)$$

We can express this equation in tensor network form, as illustrated in Fig. 7.12. Here  $\langle \Psi_L |$  and  $|\Psi_R\rangle$  are the left and right eigenvectors, which are not necessarily

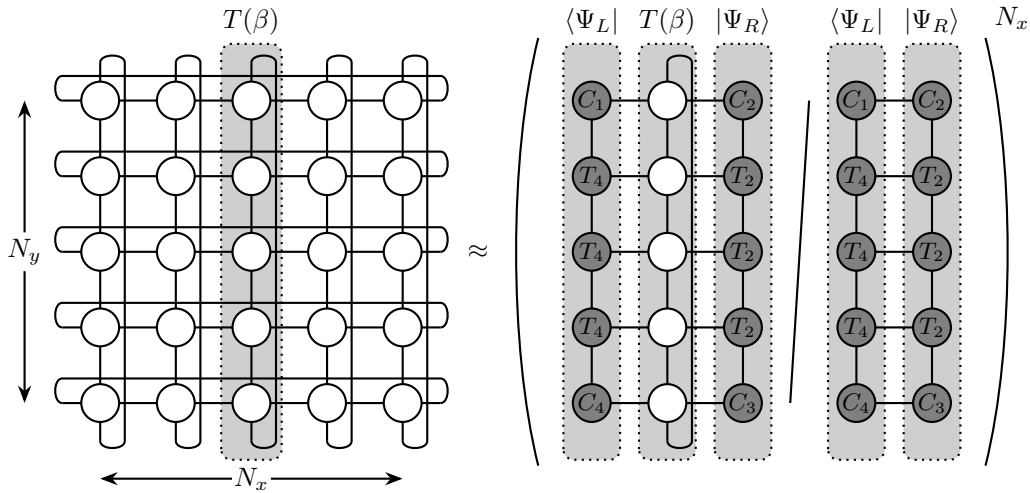


FIGURE 7.12: Equation (7.28) written as a tensor network.

normalized. Therefore, the denominator is required. The numerator in Eq. (7.28) can be understood as the expectation value of an MPO for the one-dimensional transfer operator, computed with an MPS given by the eigenvectors. This yields

$$\langle \Psi_L | T(\beta) | \Psi_R \rangle = \text{tr}(E^{N_y}) , \quad (7.29)$$

where  $E$  is the zero-dimensional transfer operator defined in Fig. 7.13. In the limit  $N_y \gg 1$  this can be formulated in terms of the dominant eigenvalue  $\nu$  of  $E$ , and  $\langle \Psi_L | T(\beta) | \Psi_R \rangle \sim \nu^{N_y}$ . Using the corresponding dominant eigenvectors we find

$$\langle \Psi_L | T(\beta) | \Psi_R \rangle \approx \left( \frac{\langle \Sigma_U | E | \Sigma_D \rangle}{\langle \Sigma_U | \Sigma_D \rangle} \right)^{N_y} , \quad (7.30)$$

where  $\langle \Sigma_U |$  and  $|\Sigma_D\rangle$  denote the left and right eigenvectors of  $E$  respectively. They are again not necessarily normalized, hence we have to divide by  $\langle \Sigma_U | \Sigma_D \rangle$ . The tensor network expression of Eq. (7.30) is shown in Fig. 7.13. A similar reformulation

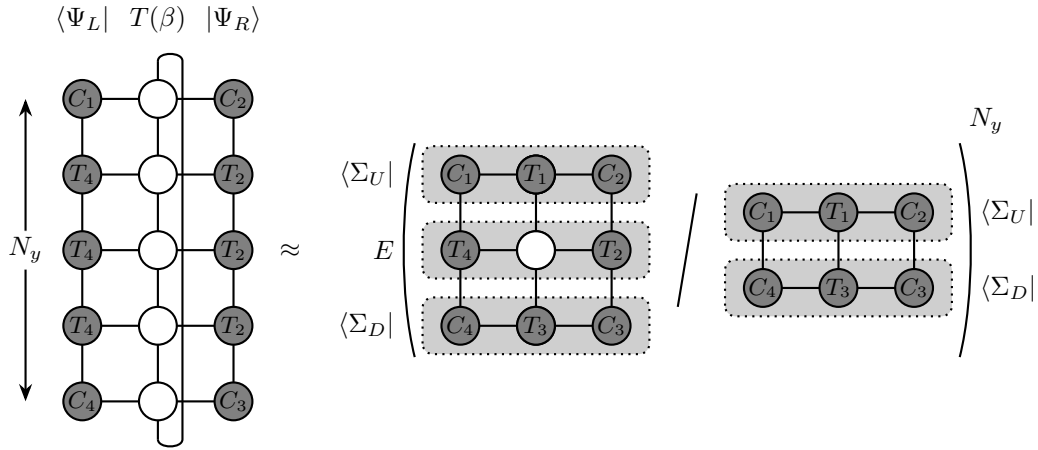


FIGURE 7.13: Equation (7.30) written as a tensor network.

can be performed for the denominator of Fig. 7.12. Here, the tensor network can be interpreted as a product of two MPS, equivalent to the overlap of the left and right eigenvalue of the 1d transfer operator  $T(\beta)$ . With the definition of the second zero-dimensional transfer operator  $K$  in Fig. 7.14, the denominator becomes

$$\langle \Psi_L | \Psi_R \rangle = \text{tr}(K^{N_y}). \quad (7.31)$$

Using the dominant eigenvalue  $\sigma$  of  $K$ , this expression scales as  $\langle \Psi_L | \Psi_R \rangle \sim \sigma^{N_y}$  in the limit  $N_y \gg 1$ . We can therefore express the denominator in terms of the left and right dominant eigenvector of  $K$  denoted by  $\langle \Omega_U |$  and  $|\Omega_D\rangle$ , which yields

$$\langle \Psi_L | \Psi_R \rangle \approx \left( \frac{\langle \Omega_U | K | \Omega_D \rangle}{\langle \Omega_U | \Omega_D \rangle} \right)^{N_y}. \quad (7.32)$$

Since also  $\langle \Omega_U |$  and  $|\Omega_D\rangle$  are not necessarily normalized, we have to divide by the product of all four CTM corner tensors, as shown in Fig. 7.14. The steps outlined

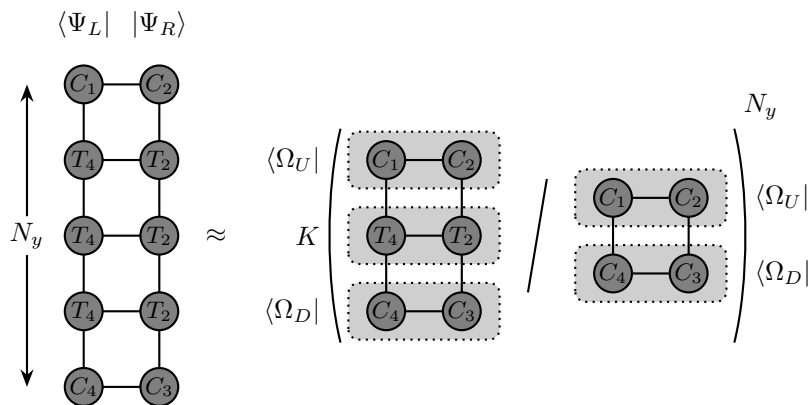


FIGURE 7.14: Equation (7.32) written as a tensor network.

above can be combined and inserted into Eq. (7.26), which then becomes

$$\ln(z(\beta)) = \lim_{N_x N_y \rightarrow \infty} \frac{1}{N_x N_y} \ln \left( \left| \frac{\langle \Sigma_U | E | \Sigma_D \rangle \langle \Omega_U | \Omega_D \rangle}{\langle \Sigma_U | \Sigma_D \rangle \langle \Omega_U | K | \Omega_D \rangle} \right|^{N_x N_y} \right). \quad (7.33)$$

Finally, the relevant quantity, the partition function per site  $z(\beta)$  is simply given by

$$z(\beta) = \frac{\langle \Sigma_U | E | \Sigma_D \rangle \langle \Omega_U | \Omega_D \rangle}{\langle \Sigma_U | \Sigma_D \rangle \langle \Omega_U | K | \Omega_D \rangle}, \quad (7.34)$$

or equivalently by the contraction shown in Fig. 7.15. Fortunately, by doing the

$$z(\beta) = \left( \begin{array}{c} \text{Diagram 1} \\ \text{Diagram 2} \end{array} \right) / \left( \begin{array}{c} \text{Diagram 3} \\ \text{Diagram 4} \end{array} \right)$$

FIGURE 7.15: The partition function per site can be computed conveniently from the CTM tensors. In this equation all normalizations in the environment tensors cancel.

derivation above, the normalization in the CTM tensors is canceled out.

### 7.4.2 Thermodynamic State Functions

From the partition function we can compute thermodynamic properties such as entropy  $S$ , the free energy  $F$  and internal energy  $U$ . First, let us show the behaviour for  $\ln(z(\beta))$  in Fig. 7.16, computed according to Fig. 7.15. The curves are smooth, and

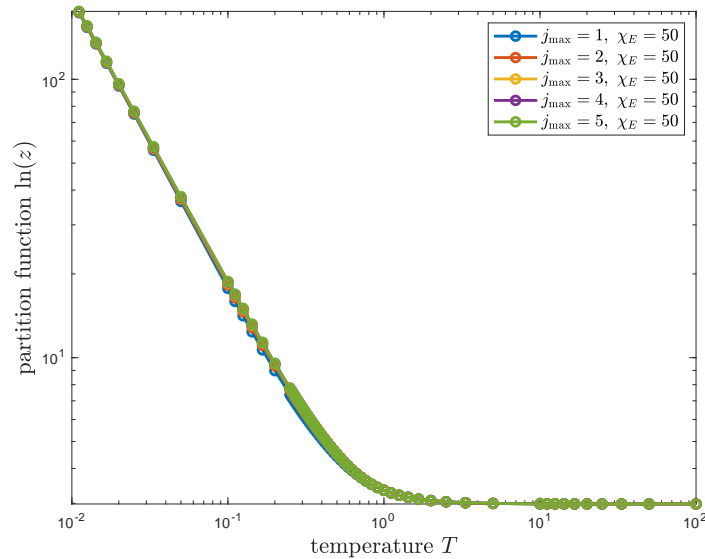


FIGURE 7.16: Partition function per site  $\ln(z(\beta))$  computed as shown in Fig. 7.15.

as expected from the Bessel functions the partition function diverges exponentially for low temperatures. The free energy is readily available from the partition function by  $F = -\ln(z)/\beta$ , and its behaviour is shown in Fig. 7.17. It is known that thermodynamic potentials are concave functions of their intensive variables, and convex functions of their extensive variables [138]. Although this is satisfied in Fig. 7.17 for larger  $j_{\max}$  (the temperature is an intensive variable), the free energy is also expected to decrease monotonically a priori. This is rooted in the fact that the thermodynamic

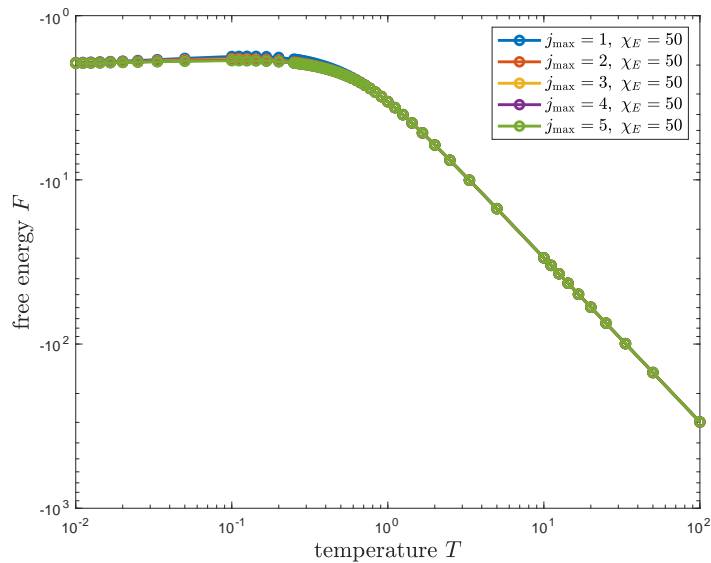


FIGURE 7.17: Free energy  $F$  computed from the partition function  $\ln(Z(\beta))$ .

entropy  $S$ , obtained by  $S = -\partial F/\partial T$  is positive semidefinite. Therefore, temperatures below  $T = 0.2$  are directly disqualified, as already expected from the rather rough approximations in the plane wave expansion.

Taking the first derivative  $U = -\partial \ln(z)/\partial \beta$  yields the internal energy per site. The derivative is performed numerically and the result is shown in Fig. 7.18. The

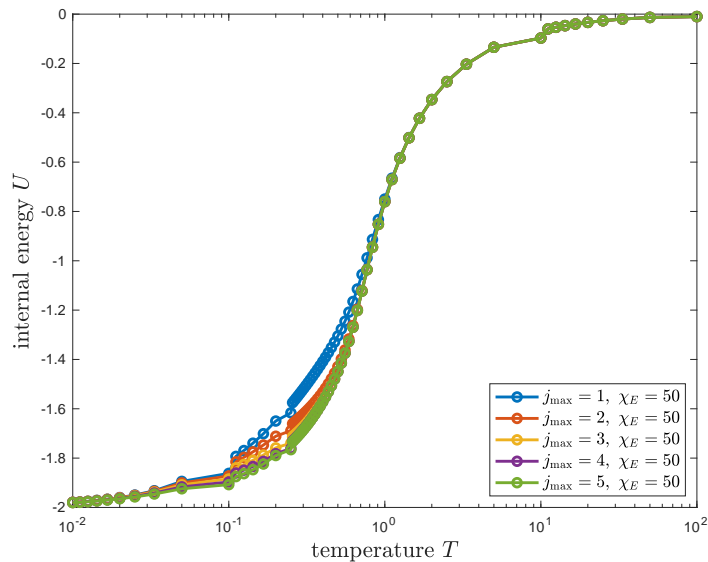


FIGURE 7.18: Internal energy  $U$  computed from the partition function  $\ln(z(\beta))$ .

simulations converge to  $U(T \rightarrow 0) \rightarrow -2$  for low temperatures, which is twice the value we have found for the expectation value of the bond energies (see Sec. 7.3.1). The factor of two is simply the number of independent nearest neighbours in the square lattice. Due to the single-site iPEPS unit cell, there are only two independent lattice links and the results are therefore consistent. Interestingly, the bond energy

in Fig. 7.8 shows a separation of the data curves for low temperatures, whereas the internal energy shows a spread around the mid-temperature range. This discrepancy is due to the different approximations performed in the calculations, and they are expected to give the same result for the correct limits of  $j_{\max} \rightarrow \infty$  and  $\chi_E \rightarrow \infty$ . In particular, the internal energy is given by

$$\begin{aligned} U &= \lim_{N_x N_y \rightarrow \infty} \frac{1}{N_x N_y} E = \lim_{N_x N_y \rightarrow \infty} \frac{1}{N_x N_y} \langle H \rangle \\ &= \langle h_x \rangle + \langle h_y \rangle = \frac{1}{Z} \text{tr} \left( (h_x + h_y) e^{-\beta H} \right). \end{aligned} \quad (7.35)$$

This is precisely equal to the derivative of the partition function

$$U = - \lim_{N_x N_y \rightarrow \infty} \frac{1}{N_x N_y} \frac{\partial \log Z}{\partial \beta}. \quad (7.36)$$

Finally, we can compute the thermodynamic entropy  $S$  from the free energy  $F$  by  $S = -\partial F/\partial T$ , shown in Fig. 7.19. For large temperatures, the entropy saturates

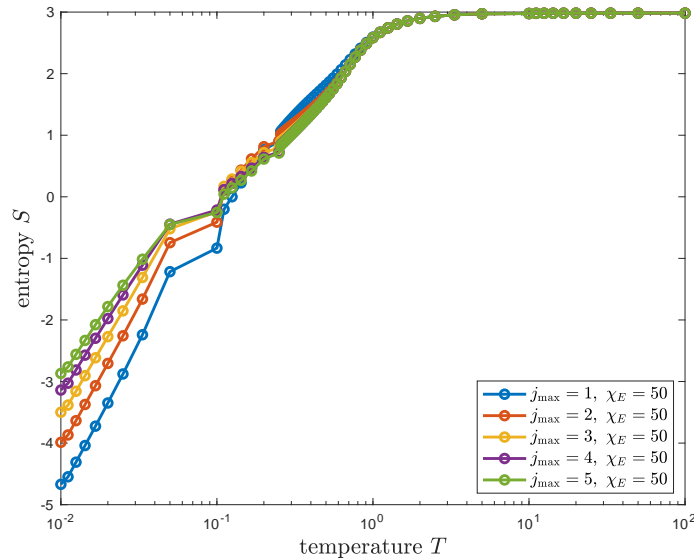


FIGURE 7.19: Thermodynamic entropy  $S$  computed from the free energy in Fig. 7.17. Negative entropies for  $T < 0.2$  are unphysical, and a consequence of the approximations in the TN ansatz.

to  $S(T \rightarrow \infty) = \ln(z(T \rightarrow \infty))$ , whereas the entropy becomes negative for low temperatures. This seems to be unphysical at first sight, however it is a typical pathology for classical models. For instance, the entropy for a classical 1d Heisenberg chain follows  $S(T \rightarrow 0) \rightarrow -\infty$  [138]. Nevertheless, temperatures below  $T = 0.2$  are untrustworthy in our tensor network simulations. We can only assess the behaviour in  $j_{\max}$ , which indicates a convergence towards  $S(T \rightarrow 0) \rightarrow 0$ .

## 7.5 Discussion of the Approximations

The tensor network approach to study the classical Heisenberg model in 2d has the particular advantage, that it does not suffer from finite size effects. Nevertheless, there are two main approximations necessary in order to keep the calculations manageable.

The first, and obvious approximation is the bond dimension of the TN, which controls how many spin representations are used in the plane wave expansion of the Boltzmann terms. As demonstrated in Fig. 7.3, the lower the temperature is, the more terms are relevant due to the slow decay of the Bessel functions. Therefore, setting  $j_{\max} = 5$  is a rather rough approximation for  $T < 1$ . As it turns out, the approximation seems to be still well justified down to  $T = 0.2$ , supported by calculations of the corner entropy in Fig. 7.4, and the bond energy in Fig. 7.8.

Besides the approximations in  $j_{\max}$ , a second refinement parameter is introduced by the bond dimension  $\chi_E$  of the CTM environment tensors. Since the CTM tensors represent the approximation of the infinite 2d lattice, it is important to converge the simulations in  $\chi_E$  for any fixed  $j_{\max}$ . Again, the required environment bond dimensions depend on the temperature, and for low  $T$  it was not possible to reach full convergence due to a high computational cost of the methods. This is shown in Fig. 7.20 for a fixed  $j_{\max} = 5$ . In this figure, the corner entropy is essentially converged

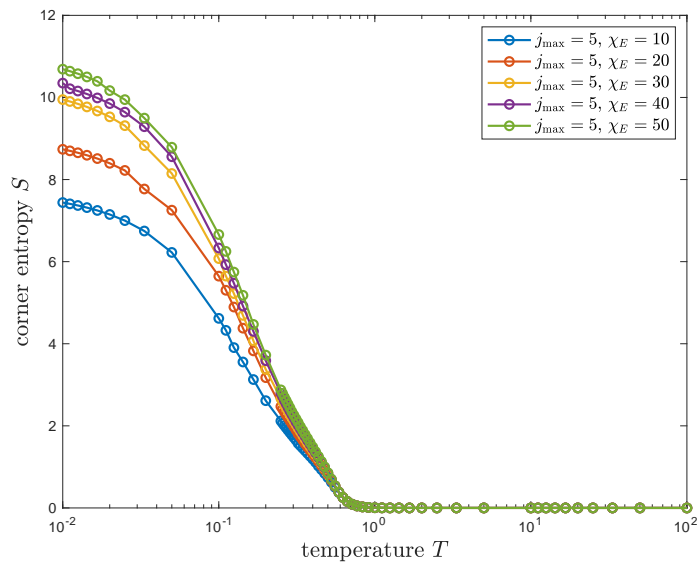


FIGURE 7.20: Convergence of the corner entropy  $S$  with the environment bond dimension  $\chi_E$ , at a fixed  $j_{\max} = 5$ . At low temperatures, the maximal bond dimension  $\chi_E = 50$  is not yet sufficient to reach convergence.

for  $T \geq 0.2$ , and starts to separate below that. Combining the observations for both the approximations in  $j_{\max}$  as well as  $\chi_E$ , we can conclude that the calculations for  $T \geq 0.2$  are to be trusted.

Certainly, the limit  $\beta \rightarrow \infty$  is of particular interest. Unfortunately, simulations in this limit are too inaccurate in our tensor network approach, and the results need to be interpreted carefully. On the other hand, and fortunately for our study, the most interesting and disputed property is a possible thermal phase transition of the classical Heisenberg model in the temperature range  $0.1 \leq T \leq 1.0$ . Here, the accessible bond dimensions are sufficiently large to extract accurate results, and an increase in quantum numbers for the Boltzmann terms is not expected to change the outcomes significantly.

## 7.6 Conclusion and Outlook

In this chapter we have applied the  $SU(2)$ -invariant tensor network formalism to study a classical spin model in the thermodynamic limit. In particular, we derived an analytic form of tensors, that represent the partition function of the classical Heisenberg model on the square lattice. The bond dimension of the resulting infinite PEPS network controls the precision of the simulations, due to the maximal spin used in the plane wave expansion of the Boltzmann terms. We applied a standard CTM method to contract the whole 2d plane and obtain the partition function, from which we computed local, non-local and thermodynamic properties.

The results of our numerical investigation of the 2d classical Heisenberg model reveals a strong increase for the correlation length of the spin-spin correlations in a temperature range  $0.1 \leq T \leq 1.0$ . Due to the unavoidable approximations in the TN representation of the partition function, it is purely speculative whether the correlation length tends to diverge for larger bond dimensions, or if it is an indication for the presence of quasi-long-range order. Moreover, an adequate mechanism behind a possible thermal phase transition is unknown for the Heisenberg model. Therefore, further analysis of the low temperature properties is in order. The behaviour of the correlation length could be studied with boundary MPS methods [71]. Provided that our observations hold true for low temperatures, the boundary MPS is expected to represent a (quasi-)critical state with a very large correlation length. Naturally, an MPS has an intrinsic finite correlation length, but hopefully the MPS bond dimension can be increased sufficiently to not suffer from a finite- $\chi$  approximation like the CTM procedure. Furthermore, it would be interesting to identify a mechanism and an order parameter for a possible transition, if further evidence for such a transition is found.



## Chapter 8

# Final Conclusion and Outlook

### 8.1 Thesis Overview

In this thesis we have applied tensor network algorithms for the study of different spin systems, with a focus on the preservation of the non-Abelian  $SU(2)$  symmetry. As a concrete output of the PhD, we developed an  $SU(2)$ -symmetric tensor network library that is able to deal with arbitrary-rank tensors, therefore providing an essential and flexible tool for numerical simulations. The implementation of the symmetry is based on a fusion tree approach, in which the structural part of symmetric tensors is encoded in analytic descriptions of the Clebsch-Gordan coefficients of the symmetry group. The chosen approach offers a memory-efficient solution that is virtually free from floating-point errors that could accumulate in an opposing numerical implementation of Clebsch-Gordan coefficients. Moreover, the approach is readily extensible to include other symmetries, such as  $U(1)$ ,  $\mathbb{Z}_n$  or  $SU(3)$ , and products of symmetries. It is also capable of accommodating so-called quantum groups, e.g. deformed versions of regular symmetry groups such as  $SU(2)_k$ , that underly anyonic theories. The  $SU(2)$ -invariant formalism has been recapitulated in a programming guide (P. Schmoll et al., *Annals of Physics* **419**, 168232 (2020)), and the corresponding  $SU(2)$ -invariant tensor network framework is planned to be made public.

The physical part of the thesis consists of four independent parts, three of which are based on the  $SU(2)$ -invariant tensor formalism. We will draw a final conclusion of the chapters below, and give further directions of research in Sec. 8.2.

Using the  $SU(2)$ -invariant tensor network framework we have studied a spin-1/2 ladder with chiral three-spin interactions in Chapter 4. The preservation of symmetry allows us to reach bond dimensions of  $\chi \sim 1200$ , a value that would be nearly impossible to reach without the symmetry. As a result, the physical information we extracted is very precise and the ground state of the model is found to be critical, with a central charge compatible with  $c = 1$ . This finding is supported by an algebraic decay of correlations, and backed by detailed studies of the model using Kadanoff coarse-graining, exact diagonalization and Abelian bosonization. The ladder system considered can provide a good starting point to study the cross-over to 2d systems with chiral interactions. The main results of the study have been published in P. Schmoll et al., *Physical Review B* **99**, 205121 (2019).

Based on the experience we gained in the previous project, the  $SU(2)$ -invariant tensor network framework was used to implement symmetric versions of the two-dimensional iPEPS and iPESS algorithms in Chapter 5. Using an efficient update scheme to optimize the tensor coefficients and a CTM scheme to compute expectation values, the algorithms were used to study a spin-1 bilinear-biquadratic model on the

square lattice, as well as the spin-1/2 and spin-2 Heisenberg antiferromagnets on the Kagome lattice. The overall results are compatible with other studies of the models, and with non-symmetric tensor network simulations we performed alongside the symmetric ones. The ground state of the spin-1 BLBQ model was found to cultivate anisotropic bond energies, thus breaking lattice rotation symmetry. Preserving the  $SU(2)$  symmetry in iPESS algorithms causes undesirable imbalances for half-integer systems, which counteract the benefits of the enlarged bond dimensions. For integer spin systems the iPESS algorithm with  $SU(2)$  symmetry is well suited, and predicts a quantum spin liquid for the spin-2 KHAF. Although the symmetry allows us to reach larger bond dimensions, the utility of its implementation and exploitation strongly depends on the model and the gap in the energy spectrum, as well as the tensor network ansatz. With more computational power and further optimized implementations, the full potential of symmetries in 2d tensor network algorithms is expected to unfold. These results are published in the preprint P. Schmoll and R. Orús, arXiv:2005.02748 (submitted to journal).

In Chapter 6 we proposed a new tensor network algorithm for the simulation of lattices with a high connectivity, i.e. a large number of neighbouring sites. A fine-graining approach is used to decompose the local degrees of freedom into more fundamental units in a way that allows to use a more convenient tensor network ansatz. The usefulness has been demonstrated for several magnetic and bosonic lattice models on two- and three-dimensional triangular lattices, showing excellent agreement with previous tensor network simulations and continuous unitary transformation results. The proposed method could be very relevant for the study of high-connectivity lattices, which are predestined for the cultivation of exotic phases of quantum matter. Our results are published in P. Schmoll et al., Physical Review Letters **124**, 200603 (2020).

Tensor networks can also be applied to study classical spin models. In Chapter 7 we use  $SU(2)$ -symmetric tensors to write the partition function of the classical Heisenberg model on the square lattice, and compute its relevant properties. The partition function can be represented by a contraction of an infinite 2d lattice of tensors. The tensors can be constructed analytically, their bond dimension controls the precision. The study demonstrates the versatile application of tensor networks beyond the representation of quantum states. Our tensor network approach works very well for the high-temperature limit of the Heisenberg model, it is however less conclusive in the low temperature regime due to strong, unavoidable approximations. The study of the Heisenberg model reveals a strong enhancement for the correlation length of the spin-spin correlations in the temperature range  $0.1 \leq T \leq 1$ . Further analysis of this delicate temperature region is currently performed, and the results are expected to be concluded in a soon to appear publication.

Summarizing, the  $SU(2)$ -symmetric framework has been deployed to implement well established and predominantly used tensor network algorithms for the study of one- and two-dimensional quantum many-body systems. This provides an assessment of the utility of symmetric implementations of the methods. While symmetries have enormous benefits in 1d TN algorithms, their exploitations in 2d TNs depends more on the physical settings and related factors.

## 8.2 Prospects and Outlook

The research carried out throughout the time of the PhD motivates further investigations along different directions. First and foremost, there are some technical improvements and extensions in order. An extension of the existing  $SU(2)$ -symmetric tensor network library to other commonly found symmetries – especially  $U(1)$  symmetry – is obvious. This adds valuable flexibility to the tool, which can then be used to study various symmetric phases, and also phase transitions between them. Moreover, symmetry-preserving tensor network states can be used to detect spontaneous symmetry breaking [116]. The extension of the library is also required for the simulation of lattice gauge theories, a flourishing area for the application of tensor networks [139].

Furthermore, the symmetric tensor library with the aforementioned extensions could be combined with state of the art tensor network algorithm to provide a full tensor network toolkit, that is suitable and convenient for a large audience of users. While iDMRG is certainly one of the most well-known and applied algorithms in 1d, future simulations would greatly benefit from the implementation of refined algorithms such as VUMPS [64], a fully translational invariant algorithm in the thermodynamic limit. Similarly, recent developments in 2d TN algorithms should be incorporated as well, including several proposals and refinements that increase the accuracy [72, 73], convergence [140] or stability of simulations. Particularly, more sophisticated tensor update schemes are expected to overcome the strong limitations in the space of variational parameters in symmetric TN simulations, that we have encountered in this thesis. To be more precise, they are expected to navigate better on the manifold of remaining variational parameters, therefore finding improved approximations to the ground state and surfacing the full potential of symmetric numerical simulations.

With all the proposed extensions and optimizations in place, the symmetric tensor network toolkit would provide a flexible, powerful and general utensil for future TN studies. It could be applied to study long-lasting problems in condensed matter physics, like for instance the simulation of the Hubbard model [141] in 2d. It is of particular interest since the Hubbard model might incorporate the mechanism behind high-temperature superconductivity. The ground state phase diagram is still not fully determined, and at half-filling of the lattice the Hubbard Hamiltonian has a global  $SO(4) = SU(2) \times SU(2)$  symmetry. Furthermore, a variety of different models in frustrated quantum antiferromagnetism or interacting topological materials could be embarked on with the help of symmetries.



## Appendix A

# Details for Symmetric Tensors

### A.1 Representation Theory of $SU(2)$

Group theory is a mathematical subject that has applications in physics in the form of symmetries. In this thesis we presented a formalism to exploit general symmetries in tensor network algorithms in order to reduce the variational space, and describe symmetric quantum states efficiently. To complement the discussion, we present the representation theory of the group  $SU(2)$  in this section, partly following Ref. [83]. In general, the special unitary group  $SU(n)$  denotes the group of unitary complex  $(n \times n)$ -dimensional matrices with determinant one, and matrix multiplication as the group operation. It is a subgroup of  $U(n)$ , the group of all unitary complex  $(n \times n)$ -dimensional matrices. Let us consider the case of degree  $n = 2$ , which consists of unitary matrices in the form of

$$U := \begin{pmatrix} \alpha & \beta \\ \gamma & \delta \end{pmatrix}. \quad (\text{A.1})$$

Since  $U$  is a complex square matrix with  $\det(U) = 1$  it is invertible with  $U^{-1} = U^\dagger$ . This leads to

$$\begin{pmatrix} \delta & -\beta \\ -\gamma & \alpha \end{pmatrix} = U^{-1} = U^\dagger = \begin{pmatrix} \alpha^* & \gamma^* \\ \beta^* & \delta^* \end{pmatrix}, \quad (\text{A.2})$$

which constraints the free parameters due to the conditions  $\delta = \alpha^*$  and  $\gamma = -\beta^*$ . Therefore, the group  $SU(2)$  takes the form

$$SU(2) = \left\{ \begin{pmatrix} \alpha & \beta \\ -\beta^* & \alpha^* \end{pmatrix} \in \text{Mat}(2, \mathbb{C}) : |\alpha|^2 + |\beta|^2 = 1 \right\}. \quad (\text{A.3})$$

The matrices  $U \in SU(2)$  can be conveniently parametrized by means of the Cayley-Klein parameters according to  $\alpha = x_0 + ix_3$  and  $\beta = x_2 + ix_1$ , so that we can rewrite  $U$  according to

$$U = U(x_0, \vec{x}) = x_0 \mathbb{I}_2 + i\vec{x}\vec{\sigma}, \quad (\text{A.4})$$

where  $\vec{x} = (x_1, x_2, x_3)^\top \in \mathbb{R}^3$  and  $\vec{\sigma} = (\sigma_1, \sigma_2, \sigma_3)^\top$  is the vector of Pauli matrices. In order to find representations of  $SU(2)$  it is helpful to consider the representations of  $su(2)$ , the Lie algebra of  $SU(2)$ . To this end we consider the exponential map – let  $X \in su(2)$ , then

$$\exp(tX) \in SU(2) \quad \forall t \in \mathbb{R}. \quad (\text{A.5})$$

Using  $\exp(tX)^\dagger \exp(tX) = \mathbb{I}$  and  $\det(\exp(X)) = \exp(\text{tr}(X)) = 1$ , the Lie algebra  $su(2)$  of  $SU(2)$  consists of all traceless,  $(2 \times 2)$ -dimensional skew-Hermitian matrices

$$su(2) = \left\{ X \in \text{Mat}(2, \mathbb{C}) : X = -X^\dagger, \text{tr}(X) = 0 \right\} . \quad (\text{A.6})$$

However, instead of using the basis of skew-Hermitian matrices one can work in the space of traceless, Hermitian matrices

$$H_2 = \left\{ X \in \text{Mat}(2, \mathbb{C}) : X = X^\dagger, \text{tr}(X) = 0 \right\} . \quad (\text{A.7})$$

In this space the generators of the  $su(2)$  Lie algebra can be chosen to be

$$J_\alpha = \frac{1}{2} \sigma_\alpha , \quad (\text{A.8})$$

so that the group  $SU(2)$  acts on a finite dimensional vector space unitarily by means of the transformation

$$W(\vec{r}) = e^{i\vec{r}\vec{J}} = e^{i(r_x J_x + r_y J_y + r_z J_z)} . \quad (\text{A.9})$$

Here  $\sigma_\alpha$  are the Pauli matrices,  $\vec{J} = (J_x, J_y, J_z)^\top$  and the coefficients  $r = (r_x, r_y, r_z)^\top \in \mathbb{R}^3$  parametrize the group elements. The traceless Hermitian operators are said to generate the representation  $W(\vec{r})$ . Therefore they are the generators of the Lie algebra  $su(2)$  and follow

$$[J_\alpha, J_\beta] = \sum_{\gamma=x,y,z} \epsilon_{\alpha\beta\gamma} J_\gamma \quad \alpha, \beta \in x, y, z , \quad (\text{A.10})$$

with  $\epsilon_{\alpha\beta\gamma}$  being the fully antisymmetric Levi-Civita symbol.  $J_x$ ,  $J_y$  and  $J_z$  can be associated to the projection of angular momentum along the respective real space axis. Furthermore, they fulfill the equations

$$\mathbf{J}^2 = \sum_{\alpha=x,y,z} J_\alpha^2 \quad [\mathbf{J}^2, J_\alpha] = 0 . \quad (\text{A.11})$$

### A.1.1 Irreducible Representations

Consider a vector space  $\mathbb{V}$  to transform as an irreducible representation (irrep) of  $SU(2)$  with spin- $j$ , so that the dimension of  $\mathbb{V}$  is  $2j + 1$ . Since  $\mathbf{J}^2$  commutes with all generators  $J_\alpha$  one can choose a simultaneous eigenbasis of e.g.  $\mathbf{J}^2$  and  $J_z$  as an orthonormal basis in  $\mathbb{V}$ . This leads to

$$\begin{aligned} \mathbf{J}^2 |j, m_j\rangle &= j(j+1) |j, m_j\rangle \\ J_z |j, m_j\rangle &= m_j |j, m_j\rangle , \end{aligned} \quad (\text{A.12})$$

where  $m_j$  is the spin projection along the  $z$ -axis that can take values  $m_j \in \{-j, \dots, +j\}$ . In the chosen basis we can express  $J_x$  and  $J_y$  conveniently in terms of ladder operators, i.e. raising and lowering operators  $J_\pm = (J_x \pm iJ_y)$  as

$$J_\pm |j, m_j\rangle = \sqrt{j(j+1) - m_j(m_j \pm 1)} |j, m_j \pm 1\rangle . \quad (\text{A.13})$$

Let us make a connection to the physical spin systems that are investigated in this thesis. Consider the two-dimensional vector space  $\mathbb{V}$  that transforms as a spin-1/2.

The states within this vector space can be constructed from the orthonormal basis states

$$|j = 1/2, m_j = +1/2\rangle = \begin{pmatrix} 1 \\ 0 \end{pmatrix}, \quad |j = 1/2, m_j = -1/2\rangle = \begin{pmatrix} 0 \\ 1 \end{pmatrix}. \quad (\text{A.14})$$

Choosing this basis, the operators  $J_x, J_y, J_z$  and  $\mathbf{J}^2$  are given by

$$J_x = \begin{pmatrix} 0 & \frac{1}{2} \\ \frac{1}{2} & 0 \end{pmatrix}, \quad J_y = \begin{pmatrix} 0 & -\frac{i}{2} \\ +\frac{i}{2} & 0 \end{pmatrix}, \quad J_z = \begin{pmatrix} +\frac{1}{2} & 0 \\ 0 & -\frac{1}{2} \end{pmatrix}, \quad \mathbf{J}^2 = \begin{pmatrix} \frac{3}{4} & 0 \\ 0 & \frac{3}{4} \end{pmatrix}. \quad (\text{A.15})$$

Furthermore consider a three-dimensional vector space  $\mathbb{V}$  that transforms as a spin-1. Again, by choosing a simultaneous eigenbasis of  $\mathbf{J}^2$  and  $J_z$  we can write an orthonormal basis

$$|j = 1, m_j = +1\rangle = \begin{pmatrix} 1 \\ 0 \\ 0 \end{pmatrix}, \quad |j = 1, m_j = 0\rangle = \begin{pmatrix} 0 \\ 1 \\ 0 \end{pmatrix}, \quad |j = 1, m_j = -1\rangle = \begin{pmatrix} 0 \\ 0 \\ 1 \end{pmatrix}. \quad (\text{A.16})$$

In this basis the operators  $J_x, J_y$  and  $J_z$  are given by the spin-1 Pauli matrices, and  $\mathbf{J}^2 = j(j+1)\mathbb{I}_{2j+1} = 2\mathbb{I}_{2j+1}$ .

### A.1.2 Reducible Representations

As a generalization of irreducible representations,  $SU(2)$  can act reducibly on a vector space  $\mathbb{V}$ . The vector space then generally decomposes as a direct sum of irreducible representations

$$\mathbb{V} \cong \bigoplus_j d_j \mathbb{V}_j \cong \bigoplus_j (\mathbb{D}_j \otimes \mathbb{V}_j), \quad (\text{A.17})$$

as already introduced in Sec. 3.1. Here  $\mathbb{V}_j$  is the vector space of the irreducible representation  $j$ , and  $d_j$  counts the copies of  $\mathbb{V}_j$  in  $\mathbb{V}$ . The decomposition can also be written in terms of a  $d_j$ -dimensional degeneracy subspace  $\mathbb{D}_j$ , so that irrep  $j$  is  $d_j$ -fold degenerate. The total dimension of the vector space  $\mathbb{V}$  is given by  $\sum_j d_j(2j+1)$ .

A convenient choice of a basis of  $\mathbb{V}$  is the set of orthonormal vectors  $|j, t_j, m_j\rangle$ , where  $j$  is the irreducible representation,  $t_j$  labels the states within the  $d_j$ -dimensional degeneracy subspace  $\mathbb{D}_j$  and  $m_j$  labels the states in the vector space  $\mathbb{V}_j$ . The values of  $j$  are the ones that appear in the decomposition of Eq. (A.17). The action of  $SU(2)$  on the full vector space  $\mathbb{V}$  is given by

$$W(\vec{r}) = \bigoplus_j (\mathbb{I}_{d_j} \otimes W_j(\vec{r})) , \quad (\text{A.18})$$

i.e. it acts trivially with the  $(d_j \times d_j)$ -dimensional identity on the degeneracy subspaces  $\mathbb{D}_j$  and only non-trivially with  $W_j(\vec{r})$  on  $\mathbb{V}_j$ . Furthermore, the action is generated by the operators

$$J_\alpha = \bigoplus_j (\mathbb{I}_{d_j} \otimes J_{\alpha,j}) \quad \alpha = x, y, z , \quad (\text{A.19})$$

where the operators  $J_{\alpha,j}$  generate the unitary transformations  $W_j(\vec{r})$  on  $\mathbb{V}_j$ . The total spin operator  $\mathbf{J}^2$  now takes the form

$$\mathbf{J}^2 = \bigoplus_j j(j+1) (\mathbb{I}_{j_d} \otimes \mathbb{I}_{2j+1}) . \quad (\text{A.20})$$

As an example that appears also in Chapter 5 for the simulation of the Kagome Heisenberg antiferromagnet, consider the combination of three spin-1/2s, resulting in

$$\left(\frac{1}{2}\right)^{\otimes 3} = (0_1 \oplus 1_1) \otimes \frac{1}{2}_1 = \frac{1}{2}_2 \oplus \frac{3}{2}_1 , \quad (\text{A.21})$$

where the subscript indicates the degeneracy of the irrep. The coupled vector space  $\mathbb{V}$  hence decomposes into the two irreps 1/2 and 3/2, with degeneracies two and one respectively. Therefore we have

$$\mathbb{V} \cong (\mathbb{D}_{1/2} \otimes \mathbb{V}_{1/2}) \oplus (\mathbb{D}_{3/2} \otimes \mathbb{V}_{3/2}) , \quad (\text{A.22})$$

with  $\mathbb{D}_{1/2}$  the two-dimensional degeneracy subspace of  $j = 1/2$ , and  $\mathbb{D}_{3/2}$  the one-dimensional degeneracy subspace of  $j = 3/2$ . A suitable orthonormal basis for  $\mathbb{V}$  is given by

$$\begin{aligned} (1 \ 0 \ 0 \ 0 \ 0 \ 0 \ 0 \ 0)^{\top} &= |j = 1/2, t_{1/2} = 1, m_{1/2} = +1/2\rangle \\ (0 \ 1 \ 0 \ 0 \ 0 \ 0 \ 0 \ 0)^{\top} &= |j = 1/2, t_{1/2} = 1, m_{1/2} = -1/2\rangle \\ (0 \ 0 \ 1 \ 0 \ 0 \ 0 \ 0 \ 0)^{\top} &= |j = 1/2, t_{1/2} = 2, m_{1/2} = +1/2\rangle \\ (0 \ 0 \ 0 \ 1 \ 0 \ 0 \ 0 \ 0)^{\top} &= |j = 1/2, t_{1/2} = 2, m_{1/2} = -1/2\rangle \\ (0 \ 0 \ 0 \ 0 \ 1 \ 0 \ 0 \ 0)^{\top} &= |j = 3/2, t_{3/2} = 1, m_{3/2} = +3/2\rangle \\ (0 \ 0 \ 0 \ 0 \ 0 \ 1 \ 0 \ 0)^{\top} &= |j = 3/2, t_{3/2} = 1, m_{3/2} = +1/2\rangle \\ (0 \ 0 \ 0 \ 0 \ 0 \ 0 \ 1 \ 0)^{\top} &= |j = 3/2, t_{3/2} = 1, m_{3/2} = -1/2\rangle \\ (0 \ 0 \ 0 \ 0 \ 0 \ 0 \ 0 \ 1)^{\top} &= |j = 3/2, t_{3/2} = 1, m_{3/2} = -3/2\rangle . \end{aligned} \quad (\text{A.23})$$

Following Eq. (A.19), the operators  $J_{\alpha}$  can be written in terms of generators  $J_{\alpha,1/2}$  and  $J_{\alpha,3/2}$  for irrep  $j = 1/2$  and  $j = 3/2$  as

$$J_{\alpha} = \left(\mathbb{I}_{d_{1/2}} \otimes J_{\alpha,1/2}\right) \oplus \left(\mathbb{I}_{d_{3/2}} \otimes J_{\alpha,3/2}\right) . \quad (\text{A.24})$$

For instance,  $J_z$  becomes

$$J_z = \left( \begin{pmatrix} 1 & 0 \\ 0 & 1 \end{pmatrix} \otimes \begin{pmatrix} +\frac{1}{2} & 0 \\ 0 & -\frac{1}{2} \end{pmatrix} \right) \oplus \left( (1) \otimes \begin{pmatrix} +\frac{3}{2} & 0 & 0 & 0 \\ 0 & +\frac{1}{2} & 0 & 0 \\ 0 & 0 & -\frac{1}{2} & 0 \\ 0 & 0 & 0 & -\frac{3}{2} \end{pmatrix} \right) . \quad (\text{A.25})$$

The operators  $J_x$  and  $J_y$  are constructed similarly, and following Eq. (A.20) we find

$$\mathbf{J}^2 = \frac{3}{4}\mathbb{I}_4 \oplus \frac{15}{4}\mathbb{I}_4 . \quad (\text{A.26})$$



## A.2 Fusion Tree Transformations

In Sec. 3.2.3 the  $F$ -move was introduced as a unitary change of basis for the fusion tree, that represents the group structure for the symmetric tensor. Here we are going to make the connection to the transformation of a full symmetric tensor, rather than just for the isolated fusion tree. Let us show how the  $F$ -move act on simple trees, i.e. fusion trees where incoming and outgoing indices are distinct. Fig. A.1 shows the

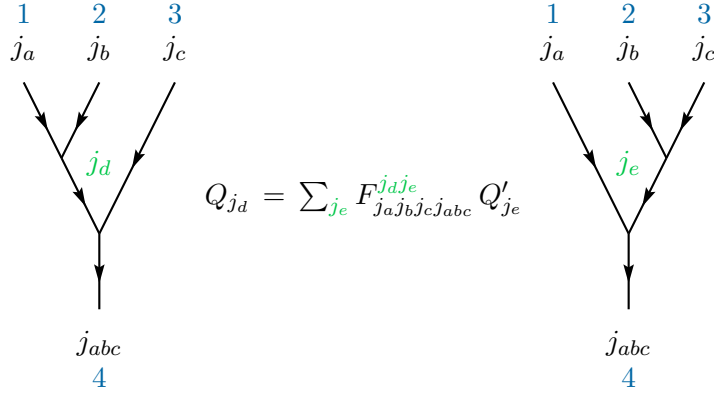


FIGURE A.1:  $F$ -move that transforms two simple trees into each other. The numerical coefficients are closely related to the Wigner 6- $j$  symbols according to Eq. (3.16). Blue labels indicate the labeling of external quantum numbers, green labels denote internal quantum numbers.

explicit relation for the transformation  $F_1$ , the remaining  $F$ -move transformations  $F_2$ ,  $F_3$  and  $F_4$  can be derived from Fig. 3.9 (see also Fig. 3.10 for the full set of possible  $F$ -moves). As stated multiple times throughout the thesis, the structural tensors  $Q$  are never explicitly stored in the symmetric tensor, and only a fusion tree in analytical form is used. Consequently, the effect of an  $F$ -move has to be incorporated into the degeneracy tensors, which are the only variational parameters. In order to show how the effect of the  $F$ -move is accounted for, consider a general decomposition of a four-index symmetric block

$$T = \sum_{j_d} P_{j_d} \otimes Q_{j_d}, \quad (\text{A.27})$$

for which all external quantum numbers are fixed. Here  $j_d$  is the internal quantum number in the four-index fusion tree. The fusion tree corresponding to tensor  $Q_{j_d}$  can be written in terms of new fusion trees  $Q'_{j_e}$  using an  $F$ -move as in Fig. A.1, so that

$$Q_{j_d} = \sum_{j_e} F^{j_d j_e} Q'_{j_e}. \quad (\text{A.28})$$

Since this transformation is formally applied on the structural part of the symmetric block  $T$ , the degeneracy part  $P_{j_d}$  can be considered constant and we find

$$T = \sum_{j_d j_e} P_{j_d} \otimes F^{j_d j_e} Q'_{j_e}. \quad (\text{A.29})$$

This transformation acts exclusively on the structural tensor and it is shown in Fig. A.2. In turn, the transformed symmetric block can again be decomposed into

degeneracy and structural parts according to

$$T = \sum_{j_e} P'_{j_e} \otimes Q'_{j_e} . \quad (\text{A.30})$$

Therefore, by writing the symmetric block  $T$  in terms of the new internal quantum numbers  $j_e$  and fusion trees  $Q_{j_e}$ , the effect of the  $F$ -move is transferred to the degeneracy tensors according to

$$P'_{j_e} = \sum_{j_d} F^{j_d j_e} P_{j_d} . \quad (\text{A.31})$$

This leaves the overall symmetric block  $T$  unchanged. Notice that the structural part

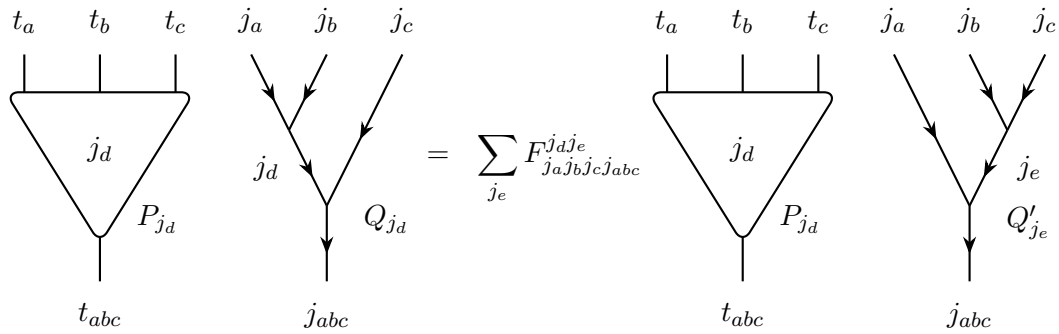


FIGURE A.2: An  $F$ -Move that solely acts on the structural part of a symmetric block.

of the symmetric tensors cannot be manipulated numerically due to its analytic array form. Therefore, the initial fusion trees  $Q_{j_d}$  will be simply replaced by the new ones  $Q'_{j_e}$ . The change of basis for the degeneracy tensors is then the inverse operation to the one of the fusion tree, in order to compensate the action. Finally, the transformed tensor  $T$  can be written as

$$T = \sum_{j_e} \left( \sum_{j_d} F^{j_e j_d} P_{j_d} \right) Q'_{j_e} , \quad (\text{A.32})$$

where the expression in parenthesis ensures that the degeneracy tensors suit the updated fusion tree.

The actual numerical factors that have to be used for the different  $F$ -moves in Fig. 3.10 can be derived from the defining spin network in Fig. 3.9.

### A.3 Construction of Matrix Product Operators

In this section we will describe in details how to construct the  $SU(2)$ -symmetric Matrix Product Operators (MPOs) used in this thesis. While matrix product states represent the actual quantum state, matrix product operators are their generalization to operators. Contrary to MPS tensors, MPO tensors have two physical indices and two virtual indices, as shown in Fig. A.3. They will be described in the same  $SU(2)$ -invariant fusion tree formalism presented in Chapter. 3. We will start with the simple Heisenberg interaction  $\vec{S} \cdot \vec{S}$ , that can be extended to the three-body chiral spin term  $\vec{S} \cdot (\vec{S} \times \vec{S})$  used in the study of the chiral ladder in Chapter 4. Furthermore

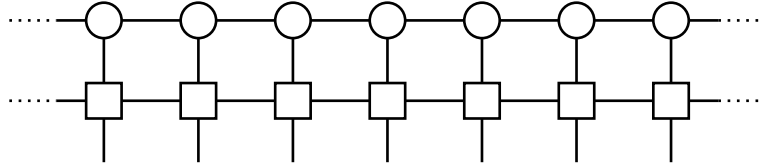


FIGURE A.3: An operator written as an MPO is applied to a quantum state written as an MPS. The absorption of the MPO into the MPS on each site yields a new MPS with enlarged bond dimensions. The MPO tensors are connected by virtual bond indices to the left and right, in complete analogy to MPS tensors.

we consider the spin-1 bilinear-biquadratic Hamiltonian used in Chapter 5 and show how the additional biquadratic interaction can be implemented. An introduction to matrix product operators can be found in Refs. [93, 60].

For the  $SU(2)$ -symmetric TN algorithms implemented in this thesis, the operators need to be written in this formalism as well, which implies a decomposition in terms of degeneracy tensors and fusion trees that represent the structure of the symmetry group. For the MPOs we will consider the action due to the structural part first, and determine afterwards the degeneracy tensors that need to give the correct weights in order to construct the interactions in the Hamiltonian. The elementary building

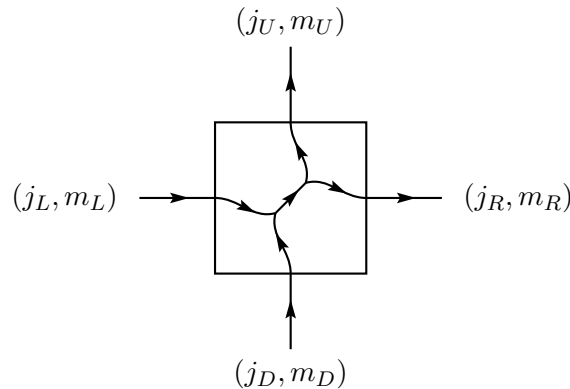


FIGURE A.4: Internal fusion tree structure for an  $SU(2)$ -symmetric MPO.

block of the  $SU(2)$ -invariant MPOs is a generic object shown in Fig. A.4, where the horizontal indices are the virtual MPO indices, and the vertical indices are those of the physical system. Due to the internal structure there are two nodes in the fusion tree, and the quantum number on the internal edge is another degree of freedom that influences the interactions that can be generated. This internal quantum number of the fusion tree will be important for the chiral spin interaction.

### A.3.1 Bilinear Interaction

Let us start with the construction of the  $SU(2)$ -invariant spin-spin interaction  $\vec{S} \cdot \vec{S}$ . This is a two-site operator that acts as a scalar, so that the corresponding MPOs need to transform as a scalar as well. Therefore the left and right ends of the two-site MPO need to have spin-0. Assuming a physical spin-1/2, the bond index connecting the two MPOs can only carry spin-0 and spin-1. Choosing spin-0 on the connecting bond index generates the trivial application of the identity operator on both spins, so that a spin-1 necessarily generates the desired dot product. The reason for this is that there are only two possible scalar operators for a spin-1/2, namely  $\mathbb{I} \otimes \mathbb{I}$  and

$\vec{S} \cdot \vec{S} = S_x \otimes S_x + S_y \otimes S_y + S_z \otimes S_z$ . We can now determine the interaction that is generated by the fusion trees, or equivalently by the Clebsch-Gordan coefficients for the left and the right MPO focusing on the spin-1 channel. The left part of the MPO is

$$\begin{array}{c}
 (S, m_S) \\
 \uparrow \\
 (0, 0) \rightarrow \boxed{S} \rightarrow (1, m) \\
 \uparrow \\
 (S, m'_S)
 \end{array}
 = \begin{cases}
 -\sqrt{\frac{1}{2S(S+1)}} \hat{S}^+ & \text{for } m = -1 \\
 +\sqrt{\frac{1}{S(S+1)}} \hat{S}^z & \text{for } m = 0 \\
 +\sqrt{\frac{1}{2S(S+1)}} \hat{S}^- & \text{for } m = +1
 \end{cases}$$

FIGURE A.5: Matrices for the MPO tensor with the left bond index fixed to spin-0 and the right bond index fixed to spin-1, leaving the freedom of choosing  $m$ . Physical indices have spin  $S = 1/2$ , the internal edge also carries spin- $S$ .

shown in Fig. A.5 and the right part of the MPO is shown in Fig. A.6. For both MPOs the internal edge can only carry the physical spin  $S$ . A contraction of the two MPOs

$$\begin{array}{c}
 (S, m_S) \\
 \uparrow \\
 (1, m) \rightarrow \boxed{S} \rightarrow (0, 0) \\
 \uparrow \\
 (S, m'_S)
 \end{array}
 = \begin{cases}
 +\sqrt{\frac{1}{2S(S+1)}} \hat{S}^- & \text{for } m = -1 \\
 -\sqrt{\frac{1}{S(S+1)}} \hat{S}^z & \text{for } m = 0 \\
 -\sqrt{\frac{1}{2S(S+1)}} \hat{S}^+ & \text{for } m = +1
 \end{cases}$$

FIGURE A.6: Matrices for the MPO tensor with the left bond index fixed to spin-1 and the right bond index fixed to spin-0, leaving the freedom of choosing  $m$ . Physical indices have spin  $S = 1/2$ , the internal edge also carries spin- $S$ .

yields the desired  $\vec{S} \cdot \vec{S}$  interaction with a prefactor of  $-1/(S(S+1))$ , as demonstrated in Fig. A.7. This prefactor is due to the Clebsch-Gordan coefficients and has to be compensated by corresponding weights in the degeneracy tensors of the full MPO. We can now proceed to the construction of the final MPO for the  $SU(2)$ -invariant

$$\begin{array}{c}
 \uparrow \quad \quad \uparrow \\
 (0, 0) \rightarrow \boxed{\phantom{S}} \rightarrow (1, m) \rightarrow \boxed{\phantom{S}} \rightarrow (0, 0) \\
 \uparrow \quad \quad \uparrow
 \end{array}
 = -\frac{1}{S(S+1)} \left( \frac{1}{2} S_i^+ S_{i+1}^- + S_i^z S_{i+1}^z + \frac{1}{2} S_i^- S_{i+1}^+ \right) = -\frac{\vec{S}_i \cdot \vec{S}_{i+1}}{S(S+1)}$$

FIGURE A.7: The contraction of the two MPOs in Figs. A.5 and A.6 produces the Heisenberg interaction with a factor of  $-1/(S(S+1))$ , that has to be compensated for in the degeneracy tensors.

Heisenberg spin chain

$$H_{\text{HB}} = J \sum_i \vec{S}_i \cdot \vec{S}_{i+1} . \quad (\text{A.33})$$

Since the term  $\vec{S}_i \cdot \vec{S}_{i+1}$  implies the application of the identity to all sites left of site  $i$  and right to site  $i+1$ , i.e.  $\vec{S}_i \cdot \vec{S}_{i+1} = \dots \mathbb{I}_{i-2} \mathbb{I}_{i-1} \vec{S}_i \cdot \vec{S}_{i+1} \mathbb{I}_{i+2} \mathbb{I}_{i+3} \dots$ , one needs two trivial spin-0 representations on the virtual bond indices, denoted by  $0_1$  and  $0_2$ . Combined with the non-degenerate spin channel  $1_1$ , the MPO can be written as a matrix-operator, i.e. a matrix of operators according to

$$\text{full MPO} = \begin{matrix} & 0_1 & 1_1 & 0_2 \\ \begin{matrix} 0_1 \\ 1_1 \\ 0_2 \end{matrix} & \left( \begin{array}{ccc} \mathbb{I} & \gamma \vec{S} & 0 \\ 0 & 0 & J\gamma \vec{S} \\ 0 & 0 & \mathbb{I} \end{array} \right) & \end{matrix}. \quad (\text{A.34})$$

In Fig. A.8 we show the full construction of the  $SU(2)$ -invariant MPO in terms of its degeneracy tensors. Here the parameter  $\gamma = i\sqrt{S(S+1)}$  cancels the unavoidable factor that appears due to the contraction of Clebsch-Gordan tensors.

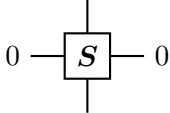
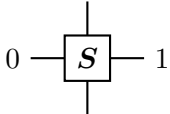
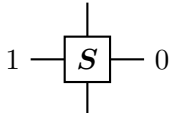
chargeSector $j_{\text{int}} j_D j_L j_R j_U$	dimensionality	degeneracyTensor	MPO
$S \ S \ 0 \ 0 \ S$	$[1, 2, 2, 1]$	$\begin{matrix} 0_1 & 0_2 \\ 0_1 \left( \begin{array}{cc} 1 & 0 \\ 0 & 1 \end{array} \right) \\ 0_2 \end{matrix}$	
$S \ S \ 0 \ 1 \ S$	$[1, 2, 1, 1]$	$\begin{matrix} 1_1 \\ 0_1 \left( \begin{array}{c} \gamma \\ 0 \end{array} \right) \\ 0_2 \end{matrix}$	
$S \ S \ 1 \ 0 \ S$	$[1, 1, 2, 1]$	$\begin{matrix} 0_1 & 0_2 \\ 1_1 \left( \begin{array}{cc} 0 & J\gamma \end{array} \right) \end{matrix}$	

FIGURE A.8: Symmetric blocks of the MPO for the Heisenberg quantum spin- $S$  chain. Each charge sector comes with a degeneracy tensor and the corresponding fusion tree generating the interaction. Spin sectors not shown have vanishing degeneracy tensors. The internal spin for every block is shown at the center of the MPOs. The labels of the MPO indices follow the convention in Fig. A.4 and  $\gamma = i\sqrt{S(S+1)}$ .

### A.3.2 Chiral Three Spin Interaction

Building on the construction of the bilinear Heisenberg interaction we can now construct the chiral three spin interaction used for the simulation of the ladder in Chapter 4. For concreteness and a better clearness of the presented construction we will consider  $S = 1/2$  now. The MPO for the chiral interaction  $\vec{S} \cdot (\vec{S} \times \vec{S})$  needs to span over three sites and a termination with spin-0 on both ends since it is a scalar operator. For  $S = 1/2$  it is clear that the interaction on the second site can only be generated by having a spin-1 representation on both virtual legs of the central tensor. A spin-2 representation is not possible since the operator can not be terminated with

a spin-0 after the third site. In contrast to the two MPOs in Sec. A.3.1, the central MPO can have different quantum numbers on the internal edge, namely

$$\frac{1}{2} \otimes 1 = \frac{1}{2} \oplus \frac{3}{2}. \quad (\text{A.35})$$

For the chiral interaction we can reuse the bilinear MPOs for the left and the right site. The full three-spin interaction can then again be constructed by evaluating the possible Clebsch-Gordan coefficients for the central MPO with fixed virtual quantum numbers. The interaction mediated by the two different internal spins is presented in Fig. A.9. In order to construct the three-site interaction one can take linear combinations of

$$\begin{aligned}
 (1, m_1) \text{ --- } \boxed{\begin{array}{c} | \\ \frac{1}{2} \\ | \end{array}} \text{ --- } (1, m_2) &= \begin{array}{c} m_1 \backslash m_2 \\ -1 \quad 0 \quad +1 \\ -1 \left( \begin{array}{ccc} -\frac{1}{3}\mathbb{I} + \frac{2}{3}S^z & \frac{\sqrt{2}}{3}S^- & 0 \\ \frac{\sqrt{2}}{3}S^+ & -\frac{1}{3}\mathbb{I} & \frac{\sqrt{2}}{3}S^- \\ 0 & \frac{\sqrt{2}}{3}S^+ & -\frac{1}{3}\mathbb{I} - \frac{2}{3}S^z \end{array} \right) \\ +1 \end{array} \equiv \mathcal{A} \\
 (1, m_1) \text{ --- } \boxed{\begin{array}{c} | \\ \frac{3}{2} \\ | \end{array}} \text{ --- } (1, m_2) &= \begin{array}{c} m_1 \backslash m_2 \\ -1 \quad 0 \quad +1 \\ -1 \left( \begin{array}{ccc} \frac{2}{3}\mathbb{I} + \frac{2}{3}S^z & \frac{\sqrt{2}}{3}S^- & 0 \\ \frac{\sqrt{2}}{3}S^+ & \frac{2}{3}\mathbb{I} & \frac{\sqrt{2}}{3}S^- \\ 0 & \frac{\sqrt{2}}{3}S^+ & \frac{2}{3}\mathbb{I} - \frac{2}{3}S^z \end{array} \right) \\ +1 \end{array} \equiv \mathcal{B}
 \end{aligned}$$

FIGURE A.9: Interactions on the central site mediated by the Clebsch-Gordan coefficients with fixed spin one representations on the virtual indices, and varying spin projections. The internal quantum number can take values  $1/2$  and  $3/2$ .

matrices  $\mathcal{A}$  and  $\mathcal{B}$ , together with the bilinear MPOs in Fig. A.5 and A.6 on both ends. This is visualized in Fig. A.10 where the interaction on the central site is given by

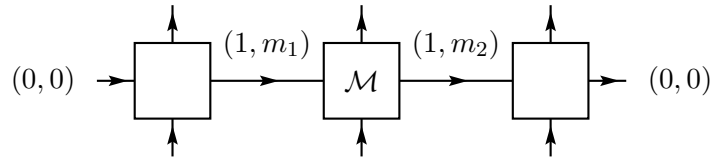


FIGURE A.10: Construction of a general three-site MPO with the linear combination  $\mathcal{M} = \alpha\mathcal{A} + \beta\mathcal{B}$ . Summation over the common indices  $m_1$  and  $m_2$  is assumed.

$\mathcal{M} = \alpha\mathcal{A} + \beta\mathcal{B}$ . The two free parameters can now be tuned to reproduce the desired interaction. For instance, the choice  $\alpha = -1$  and  $\beta = +1$  simplifies the central MPO to

$$-\mathcal{A} + \mathcal{B} = \begin{pmatrix} \mathbb{I} & 0 & 0 \\ 0 & \mathbb{I} & 0 \\ 0 & 0 & \mathbb{I} \end{pmatrix}. \quad (\text{A.36})$$

The full MPO is then in fact a scalar operator that acts trivially on the central site, and implements a next-to-nearest neighbour bilinear interaction  $\vec{S}_1 \cdot \vec{S}_3$ . For the reconstruction of the chiral triple product it is necessary to choose  $\alpha = -i$  and

$\beta = -i/2$ . The central MPO tensor then becomes

$$\mathcal{M} = -i \left( \mathcal{A} + \frac{1}{2} \mathcal{B} \right) = \begin{pmatrix} -S^z & -\frac{\sqrt{2}}{2} S^- & 0 \\ -\frac{\sqrt{2}}{2} S^+ & 0 & -\frac{\sqrt{2}}{2} S^- \\ 0 & -\frac{\sqrt{2}}{2} S^+ & S^z \end{pmatrix}. \quad (\text{A.37})$$

For this choice of parameters the three-site MPO in Fig. A.10 then evaluates to

$$\begin{aligned} H &= -\frac{4i}{6} (S^z S^+ S^- - S^z S^- S^+ + S^+ S^- S^z - S^+ S^z S^- + S^- S^z S^+ - S^- S^+ S^z) \\ &= -\frac{4}{3} \vec{S}_1 \cdot (\vec{S}_2 \times \vec{S}_3). \end{aligned} \quad (\text{A.38})$$

The factor  $1/\gamma^2 = -1/(S(S+1))$  from the Clebsch-Gordan terms of the bilinear MPOs in Sec. A.3.1 arises again, and it can be compensated with the corresponding factor  $\gamma^2$  in the degeneracy tensors.

We will now construct the MPO for a more general Hamiltonian of a quantum spin chain, that has both bilinear as well as a chiral three-site interaction. It is given by

$$H = J \sum_i \vec{S}_i \cdot \vec{S}_{i+1} + K \sum_i \vec{S}_i \cdot (\vec{S}_{i+1} \times \vec{S}_{i+2}), \quad (\text{A.39})$$

where  $J$  and  $K$  are the coupling constants respectively. Similarly to the plain bilinear MPO in Eq. (A.34), the MPO for the combined Hamiltonian has two spin-0 channels in the bond dimension of the MPO. These two channels apply the identity to all sites left and right of the sites where the interaction is applied. Furthermore we now need two spin-1 channels, one that mediates the bilinear interaction and one that mediates the three-spin interaction. The matrix-operator is given by

$$\text{full MPO} = \begin{matrix} & \begin{matrix} 0_1 & 1_1 & 1_2 & 0_2 \end{matrix} \\ \begin{matrix} 0_1 \\ 1_1 \\ 1_2 \\ 0_2 \end{matrix} & \begin{pmatrix} \mathbb{I} & \gamma \vec{S} & 0 & 0 \\ 0 & 0 & \mathcal{M} & J \gamma \vec{S} \\ 0 & 0 & 0 & K \gamma \vec{S} \\ 0 & 0 & 0 & \mathbb{I} \end{pmatrix} \end{matrix}. \quad (\text{A.40})$$

The factor  $\gamma^2$  cancels the unavoidable factor in the bilinear and the chiral three-spin term, as described above. In Fig. A.11 we show the full construction of the  $SU(2)$ -invariant MPO for the triangle ladder model, with additional bilinear terms.

### A.3.3 Bilinear-Biquadratic Interaction

In this section we will explain how the  $SU(2)$ -invariant MPO, or the two-body gate for the simple update of the spin-1 bilinear-biquadratic (BLBQ) model can be constructed. The Hamiltonian is given by

$$H = \sum_{\langle i,j \rangle} \left( \cos \theta (\vec{S}_i \cdot \vec{S}_j) + \sin \theta (\vec{S}_i \cdot \vec{S}_j)^2 \right). \quad (\text{A.41})$$

chargeSector $j_{\text{int}} j_D j_L j_R j_U$	dimensionality	degeneracyTensor	MPO
$\frac{1}{2} \frac{1}{2} 0 0 \frac{1}{2}$	$[1, 2, 2, 1]$	$\begin{matrix} 0_1 & 0_2 \\ 0_1 \begin{pmatrix} 1 & 0 \\ 0 & 1 \end{pmatrix} \\ 0_2 \end{matrix}$	
$\frac{1}{2} \frac{1}{2} 0 1 \frac{1}{2}$	$[1, 2, 2, 1]$	$\begin{matrix} 1_1 & 1_2 \\ 0_1 \begin{pmatrix} \gamma & 0 \\ 0 & 0 \end{pmatrix} \\ 0_2 \end{matrix}$	
$\frac{1}{2} \frac{1}{2} 1 0 \frac{1}{2}$	$[1, 2, 2, 1]$	$\begin{matrix} 0_1 & 0_2 \\ 1_1 \begin{pmatrix} 0 & J\gamma \\ 0 & K\gamma \end{pmatrix} \\ 1_2 \end{matrix}$	
$\frac{1}{2} \frac{1}{2} 1 1 \frac{1}{2}$	$[1, 2, 2, 1]$	$\begin{matrix} 1_1 & 1_2 \\ 1_1 \begin{pmatrix} 0 & \alpha \\ 0 & 0 \end{pmatrix} \\ 1_2 \end{matrix}$	
$\frac{3}{2} \frac{1}{2} 1 1 \frac{1}{2}$	$[1, 2, 2, 1]$	$\begin{matrix} 1_1 & 1_2 \\ 1_1 \begin{pmatrix} 0 & \beta \\ 0 & 0 \end{pmatrix} \\ 1_2 \end{matrix}$	

FIGURE A.11: Symmetric blocks of the MPO for the triangle model on a spin-1/2 ladder. Each charge sector comes with a degeneracy tensor and the corresponding fusion tree generating the interaction. The internal spin for every block is shown at the center of the MPOs. The labels of the MPO indices follow the convention in Fig. A.4 and  $\gamma = i\sqrt{S(S+1)}$ .

It is a scalar operator over two sites and it can be represented by two MPOs that are terminated with a spin-0 at both ends, as shown in Fig. A.12. We can construct

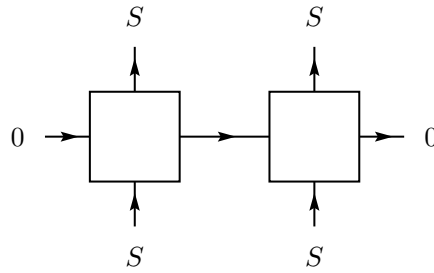


FIGURE A.12: Two-site MPO for the spin- $S$  BLBQ model, where both ends are terminated with a spin-0 to obtain a scalar operator on two sites.

the MPOs similarly to the two MPOs in the previous sections. The Clebsch-Gordan or structural tensors generate the interaction, and the degeneracy tensors give the correct weights to reproduce the exact Hamiltonian terms. In general the virtual link between the MPOs in Fig. A.12 can carry quantum numbers  $j_v = 0, \dots, 2S$  in integer steps, so that for the spin-1 BLBQ model the virtual bond quantum numbers are  $j_v = 0, 1, 2$ . In Sec. A.3.1 we have demonstrated how the identity on both sites is



generated by a spin-0 in the virtual bond index, whereas a spin-1 mediates the bilinear interaction  $\vec{S} \cdot \vec{S}$ . For a system of spin-1/2 there is no biquadratic interaction and the only scalars on two sites are the ones mentioned previously. For  $S = 1$  however, the virtual MPO bond index can carry a spin-2 which leads to the interactions in Fig. A.13 and Fig. A.14. The prefactors are explicitly written for  $S = 1$  and not

$$\begin{array}{c}
(S, m_S) \\
\uparrow \\
(0, 0) \rightarrow \boxed{S} \rightarrow (2, m) \\
\uparrow \\
(S, m'_S)
\end{array}
= \begin{cases}
+\sqrt{\frac{3}{20}} (\hat{S}^+)^2 & \text{for } m = -2 \\
-\sqrt{\frac{3}{20}} (\hat{S}^+ \hat{S}^z + \hat{S}^z \hat{S}^+) & \text{for } m = -1 \\
-\sqrt{\frac{1}{40}} (\hat{S}^+ \hat{S}^- + \hat{S}^- \hat{S}^+) + \sqrt{\frac{2}{5}} \hat{S}^z \hat{S}^z & \text{for } m = 0 \\
+\sqrt{\frac{3}{20}} (\hat{S}^- \hat{S}^z + \hat{S}^z \hat{S}^-) & \text{for } m = +1 \\
+\sqrt{\frac{3}{20}} (\hat{S}^-)^2 & \text{for } m = +2
\end{cases}$$

FIGURE A.13: Matrices for the MPO tensor with the left bond index fixed to spin-0 and the right bond index fixed to spin-2, leaving the freedom of choosing  $m$ .

Physical indices have spin  $S = 1$ , the internal edge also carries spin- $S$ .

for a general spin- $S$ , because of lengthy expressions. Contracting together these two

$$\begin{array}{c}
(S, m_S) \\
\uparrow \\
(2, m) \rightarrow \boxed{S} \rightarrow (0, 0) \\
\uparrow \\
(S, m'_S)
\end{array}
= \begin{cases}
+\sqrt{\frac{3}{20}} (\hat{S}^-)^2 & \text{for } m = -2 \\
-\sqrt{\frac{3}{20}} (\hat{S}^- \hat{S}^z + \hat{S}^z \hat{S}^-) & \text{for } m = -1 \\
-\sqrt{\frac{1}{40}} (\hat{S}^+ \hat{S}^- + \hat{S}^- \hat{S}^+) + \sqrt{\frac{2}{5}} \hat{S}^z \hat{S}^z & \text{for } m = 0 \\
+\sqrt{\frac{3}{20}} (\hat{S}^+ \hat{S}^z + \hat{S}^z \hat{S}^+) & \text{for } m = +1 \\
+\sqrt{\frac{3}{20}} (\hat{S}^+)^2 & \text{for } m = +2
\end{cases}$$

FIGURE A.14: Matrices for the MPO tensor with the left bond index fixed to spin-2 and the right bond index fixed to spin-0, leaving the freedom of choosing  $m$ .

Physical indices have spin  $S = 1$ , the internal edge also carries spin- $S$ .

MPO objects yields not only the desired biquadratic interaction. The resulting terms include a bilinear and even a constant term as well, which have to be compensated to reproduce the correct terms in the Hamiltonian. For the full MPO one then needs a degenerate channel  $0_3$ , as well as two non-degenerate channels  $1_1$  and  $2_1$  mediating the bilinear and biquadratic interaction. The constant coming from the contraction of Figs. A.13 and A.14 is compensated by one of the spin-0 channels. Working out the details one can obtain the final MPO for the Hamiltonian in Eq. (A.41) written in terms of a matrix-operator

$$\text{full MPO} = \begin{array}{c} 0_1 \\ 1_1 \\ 0_2 \\ 2_1 \\ 0_3 \end{array} \begin{pmatrix} 0_1 & 1_1 & 0_2 & 2_1 & 0_3 \\ \mathbb{I} & \gamma_1 \vec{S} & \gamma_0 & \gamma_2 \vec{Q} & 0 \\ 0 & 0 & 0 & 0 & \gamma_1 \vec{S} \\ 0 & 0 & 0 & 0 & \gamma_0 \\ 0 & 0 & 0 & 0 & \gamma_2 \vec{Q} \\ 0 & 0 & 0 & 0 & \mathbb{I} \end{pmatrix}. \quad (\text{A.42})$$

While the spin-1 channel generates the bilinear interaction  $\vec{S}_i \cdot \vec{S}_j$ , the spin-2 channels generates the biquadratic interaction  $\vec{Q}_i \cdot \vec{Q}_j \sim (\vec{S}_i \cdot \vec{S}_j)^2$ . Here  $\vec{Q}$  is the quadrupolar vector [142] with components as specified in Figs. A.13 and A.14. Finally, the full

chargeSector $j_{\text{int}} j_D j_L j_R j_U$	dimensionality	degeneracyTensor	MPO
$\mathbf{1} \ 1 \ 0 \ 0 \ 1$	$[1, 3, 3, 1]$	$\begin{matrix} & 0_1 & 0_2 & 0_3 \\ 0_1 & \left( \begin{array}{ccc} 1 & \gamma_0 & 0 \\ 0 & 0 & \gamma_0 \\ 0 & 0 & 1 \end{array} \right) \\ 0_2 & & & \\ 0_3 & & & \end{matrix}$	
$\mathbf{1} \ 1 \ 0 \ 1 \ 1$	$[1, 3, 1, 1]$	$\begin{matrix} & 1_1 \\ 0_1 & \left( \begin{array}{c} \gamma_1 \\ 0 \\ 0 \end{array} \right) \\ 0_2 & \\ 0_3 & \end{matrix}$	
$\mathbf{1} \ 1 \ 1 \ 0 \ 1$	$[1, 1, 3, 1]$	$\begin{matrix} 0_1 & 0_2 & 0_3 \\ 1_1 & \left( \begin{array}{ccc} 0 & 0 & \gamma_1 \end{array} \right) \\ & & \end{matrix}$	
$\mathbf{1} \ 1 \ 0 \ 2 \ 1$	$[1, 3, 1, 1]$	$\begin{matrix} & 2_1 \\ 0_1 & \left( \begin{array}{c} \gamma_2 \\ 0 \\ 0 \end{array} \right) \\ 0_2 & \\ 0_3 & \end{matrix}$	
$\mathbf{1} \ 1 \ 2 \ 0 \ 1$	$[1, 1, 3, 1]$	$\begin{matrix} 0_1 & 0_2 & 0_3 \\ 2_1 & \left( \begin{array}{ccc} 0 & 0 & \gamma_2 \end{array} \right) \\ & & \end{matrix}$	

FIGURE A.15: Symmetric blocks of the MPO for the spin-1 BLBQ model. Each charge sector comes with a degeneracy tensor and the corresponding fusion tree generating the interaction. The internal spin for every block is shown at the center of the MPOs. The labels of the MPO indices follows the convention in Fig. A.4.

MPO with its degeneracy tensors need to be constructed as shown in Fig. A.15. The constants are given by

$$\begin{aligned} \gamma_0 &= \left[ 1/3 \cdot \sin \theta \cdot S^2 (S+1)^2 \right]^{1/2} \\ \gamma_1 &= \left[ 1/2 \cdot (\sin \theta - 2 \cos \theta) \cdot S(S+1) \right]^{1/2} \\ \gamma_2 &= \left[ 2/3 \cdot \sin \theta \cdot (S-1/2)S(S+1)(S+3/2) \right]^{1/2}. \end{aligned} \tag{A.43}$$

As one can see from the prefactor used in the Hamiltonian, all terms except from the  $\cos \theta$ -dependent bilinear term belong to the spin-2 sector generating the biquadratic interaction.

## Appendix B

# Tensor Network Algorithms in 2d

### B.1 iPEPS Simple Update

Infinite projected entangled pair states are tensor network representations of quantum many-body systems in two and possibly higher spatial dimensions. The assumption of an infinite lattice is the closest approximation to a 2d slice of real materials that come with a certain lattice structure and a number of particles in the order of the Avogadro number  $N_0 \approx 6.022 \times 10^{23}$ . iPEPS can be used as an analytic ansatz and as a numerical tool. Some ground states of particular models such as the Toric Code [60] can be written as an exact iPEPS state, i.e. a network of tensors where the entries in the tensors are given as analytic expressions. On the other hand, iPEPS are widely used as ansätze for numerical studies, in which the entries in the tensors are optimized to represent the target state accurately. There are different algorithms to do this, such as the simple update [71] and the full update [72] based on iTEBD [50, 51], and variational update schemes [73, 74]. These methods differ in the accuracy of the ground state approximation, computational cost of the simulations and also in the complexity of the implementation. Here we focus on and describe in detail the simple update scheme, an easy to implement algorithm that is oftentimes sufficient to extract the overall physical picture, but fails to reproduce the most accurate numbers.

The simple update is based on iTEBD, a simulation technique for 1d quantum lattice systems in the thermodynamic limit. In 1d, the underlying MPS can be in its canonical form, so that the Schmidt coefficients of a bipartition of the chain appear on the links between MPS tensors (refer to Fig. 4.3). The Schmidt coefficients contain all the information about the bipartition and the diagonal tensors holding them can be interpreted as an effective environment for the MPS sites. This idea is also transferred to the 2d version of the iTEBD algorithm called the simple update, as we will describe below. Consider a Hamiltonian that is translational invariant and has the form

$$H = \sum_{\langle i,j \rangle} h_{ij} , \quad (\text{B.1})$$

i.e. it is a sum of local terms. For simplicity we will assume only nearest-neighbour interactions, but the method can be adapted to interactions that span multiple sites as well. The ground state search now starts with some initial state  $|\psi_i\rangle$  written in terms of a 2d iPEPS. For the explanation of the simple update we consider a unit cell consisting of two tensors  $A$  and  $B$  that are arranged in a checkerboard pattern, shown in Fig. B.1. Here each link of the lattice carries a diagonal tensor  $\Lambda_i$  containing singular values. Contrary to an MPS, cutting one link in the iPEPS network does not form a bipartition of the network due to the presence of loops, so that the singular values on the links are not directly related to the Schmidt coefficients of a bipartition. However the tensors  $\Lambda$  are treated as such, and they describe a sort of mean-field

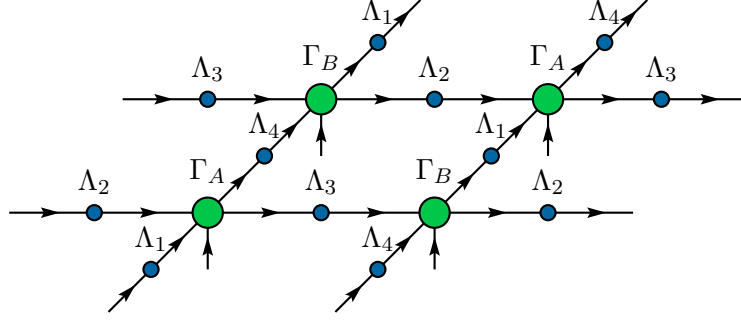


FIGURE B.1: Simple update iPEPS ansatz with a unit cell of  $N_x = 1$  and  $N_y = 2$  tensors in a checkerboard pattern.

environment for the tensors towards the four directions. A time evolution of the initial state  $|\psi_i\rangle$  with the Hamiltonian  $H$  is performed by

$$|\psi(t)\rangle = e^{-iHt} |\psi_i\rangle. \quad (\text{B.2})$$

If however the real time  $t$  is replaced by an imaginary time by making the transition  $t \rightarrow -i\tau$ , the evolution of the quantum state converges to the ground state in the limit of infinite imaginary time. This can be seen from a spectral decomposition of the imaginary time operator

$$\begin{aligned} e^{-H\tau} &= \sum_j e^{-E_j\tau} |\psi_j\rangle \langle\psi_j| = e^{-E_0\tau} \left( \sum_j e^{-(E_j-E_0)\tau} |\psi_j\rangle \langle\psi_j| \right) \\ &= e^{-E_0\tau} (|\psi_0\rangle \langle\psi_0| + e^{-\Delta\tau} |\psi_1\rangle \langle\psi_1| + \dots) \end{aligned} \quad (\text{B.3})$$

with  $\Delta = E_1 - E_0$ . Using a proper normalization of the quantum state and the assumption that the initial state  $|\psi_i\rangle$  has a finite overlap with the true ground state  $|\psi_0\rangle$  ( $\langle\psi_i|\psi_0\rangle \neq 0$ ), we find

$$|\psi_0\rangle = \lim_{\tau \rightarrow \infty} \frac{e^{-\tau H} |\psi_i\rangle}{\sqrt{\langle\psi(\tau)|\psi(\tau)\rangle}}. \quad (\text{B.4})$$

The basic idea of iTEBD and therefore also the simple update is to decompose the full imaginary time evolution into many small time steps  $\delta\tau$  according to

$$e^{-H\tau} = \left( e^{-H\delta\tau} \right)^m \quad (\text{B.5})$$

with  $m = \tau/\delta\tau$ . Furthermore, the particular form of the Hamiltonian in Eq. (B.1) can be exploited too, so that the imaginary time evolution can be written as

$$e^{-H\delta\tau} = \exp \left( -\delta\tau \sum_{\langle i,j \rangle} h_{ij} \right). \quad (\text{B.6})$$

Since the individual terms  $h_{ij}$  do not commute in general we can use a Suzuki-Trotter expansion to first (or also higher) order and rewrite Eq. (B.6) to

$$e^{-H\delta\tau} = \prod_{\langle i,j \rangle} \exp(-\delta\tau h_{ij}) + \mathcal{O}(\delta\tau^2). \quad (\text{B.7})$$

For simplicity we made the assumption that  $H$  only contains nearest-neighbour terms, so that  $g_{ij} = \exp(-\delta\tau h_{ij})$  is a two-body gate. The full imaginary time evolution can then be approximated by applying

$$U(\delta\tau) = \prod_{\langle i,j \rangle} \exp(-\delta\tau h_{ij}) \quad (\text{B.8})$$

repeatedly many times ( $m \gg 1$ ) to all two-site pairs in the tensor network. This can be easily visualized for the case of a 1d MPS that consists of a two-site unit cell as shown in Fig. B.2. The application of  $U(\delta\tau)$  then corresponds to applying the

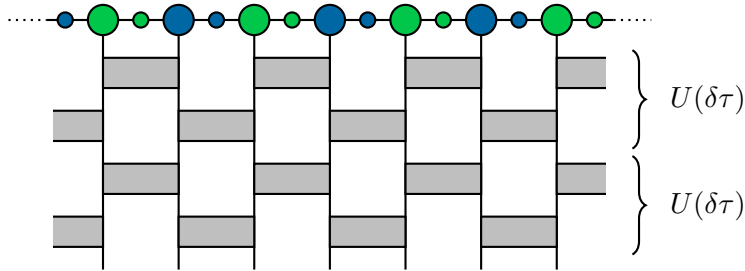


FIGURE B.2: The iTEBD two-body gate  $g_{ij}$  applied to a 1d infinite MPS with a two-site unit cell. One iTEBD step corresponds to the application of the gate to both types of links in the TN.

two-body gate  $g_{ij}$  to all different links in the network, e.g. on even and odd links in the present example. Coming back to the simple update and the iPEPS ansatz in Fig. B.1, the gates  $g_{ij}$  have to be applied to all four links in the network as shown in Fig. B.3. Now that we have described the principle setup of the iTEBD and simple

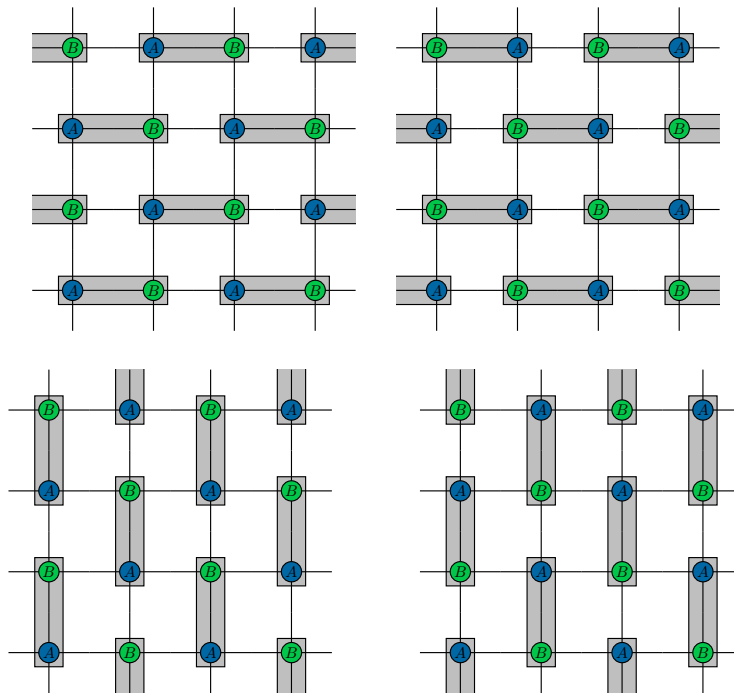


FIGURE B.3: Simple update scheme for an iPEPS ansatz with two different tensors in the unit cell. The diagonal tensors  $\Lambda$  are not shown here, they do however enter the update procedure as demonstrated in Fig. B.4 and following.

update algorithm, we can turn to the application of the two-body gate  $g_{ij}$ . We will

describe the procedure for both the 1d iTEBD case as well as for the 2d simple update because the steps are nearly identical. In two dimensions, the application of one gate  $g_{ij}$  is shown in Fig. B.4. A contraction of the full network results in an

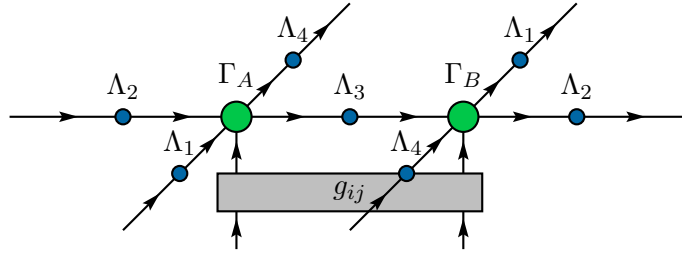


FIGURE B.4: The trotterized gate  $g_{ij}$  is applied on a horizontal link of the iPEPS network in order to update the link containing singular values  $\Lambda_3$ .

eight-index tensor that is numerically very costly. A cheaper alternative contraction and update of the link is possible if all virtual indices that are not affected, i.e. all links except for the link carrying  $\Lambda_3$  are disconnected from the update process. This

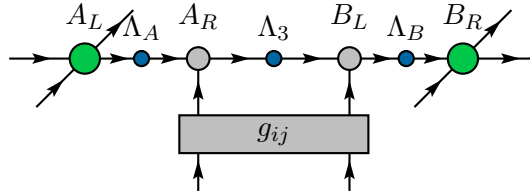


FIGURE B.5: Using a suitable decomposition, the links that are not affected by the simple update can be split away, and the two-body gate can be applied to the reduced tensors. The simple update is then similar to the 1d iTEBD algorithm.

is shown in Fig. B.5 where the gate  $g_{ij}$  can be applied to the reduced tensors  $A_R$  and  $B_L$ . From this step onwards the simple update and the 1d iTEBD algorithm are the same. Instead of working with tensors  $(\Lambda_A A_R \Lambda_3 B_L \Lambda_B)$  as in Fig. B.5, one can imagine to have a two-site translational invariant MPS with tensors  $(\Gamma\Lambda)_A$  and  $(\Gamma\Lambda)_B$  as shown in Fig. B.2. In order to update both three-index tensors as well as the singular values on the connecting link we perform the two steps in Fig. B.6. Absorbing

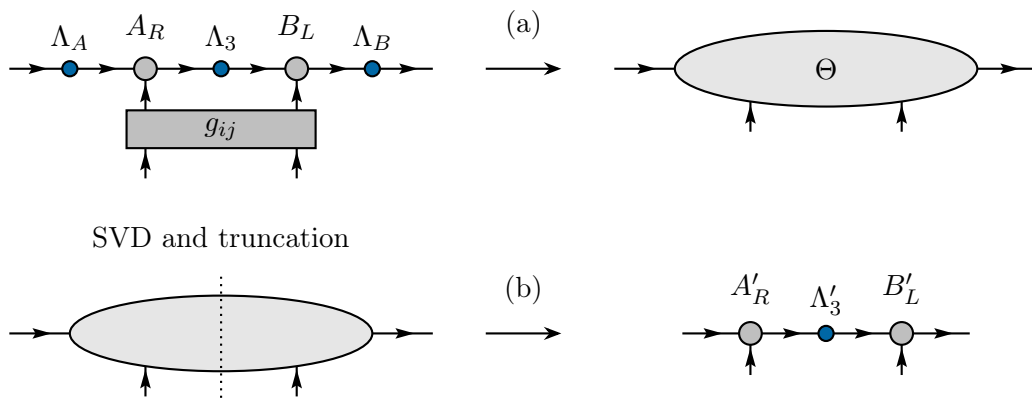


FIGURE B.6: (a) The two-body gate  $g_{ij}$  is contracted with the reduced tensors to obtain a four-index tensor  $\Theta$ . (b) Using an SVD with successive truncation in the symmetry sectors yields the updated tensors  $A'_R$ ,  $\Lambda'_3$  and  $B'_L$ .

the gate in Fig. B.6 (a) yields a four-index tensor  $\Theta$ . Notice that without splitting

away unaffected links the tensor  $\Theta$  would have eight indices instead of four. In the second step this tensor  $\Theta$  is decomposed again to retrieve the updated tensors  $A'_R$ ,  $\Lambda'_3$  and  $B'_L$  after reshaping them, see Fig. B.6 (b). This can be achieved by an SVD, where the connecting index needs to be truncated to keep a maximum of  $D$  singular values,  $D$  being the desired bond dimension. Due to the truncation, the algorithm can decide which quantum numbers are kept on the virtual index (see also Sec. 3.5.2 about SVD based truncation). In the 1d iTEBD algorithm tensors  $A'_R$  and  $B'_L$  need to be re-gauged, i.e. remove  $\Lambda_B$  on the left virtual index of  $A'_R$  and on the right virtual index of  $B'_L$ , which then represent the updated MPS tensors. For the 2d algorithm

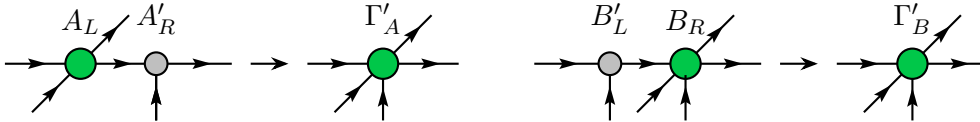


FIGURE B.7: Reconstruction of the iPEPS tensors for the simple update using reduced tensors. Notice that both  $\Gamma'_A$  and  $\Gamma'_B$  need to be re-gauged, i.e. the diagonal tensors  $\Lambda_i$  that have been absorbed while preparing the reduced tensors (see also Fig. B.4) need to be removed from the links that were split off.

the updated iPEPS tensors are constructed as demonstrated in Fig. B.7. Notice that both tensors  $\Gamma$  involved in the update need to be re-gauged as well, meaning that the diagonal tensors  $\Lambda_i$  have to be removed on all links that were not affected, similarly to the 1d iTEBD case.

One simple update step is completed after running the described procedure on all different links in the iPEPS ansatz, so that the singular values in all four tensors  $\Lambda$  have been updated once. This process is repeated until the change in singular values falls below a certain threshold, indicating that the imaginary time evolution can be refined by decreasing the Trotter step  $\delta\tau$ . Running the simple update for smaller values of the Trotter step yields better approximations to the ground state. In practice we mainly used Trotter steps of  $\delta\tau = [0.1, 0.01, 0.001, 0.0001]$  and a convergence threshold of  $\Delta = 10^{-6}$  in the singular values. When converged, the iPEPS tensor network represents the ground state of the model described by Hamiltonian  $H$ . In the final step one can absorb the singular values into the iPEPS tensors as shown in Fig. B.8. Notice that the simple update can be applied to different lattice geometries as well.

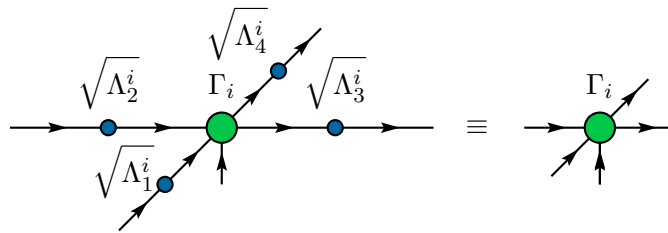


FIGURE B.8: The diagonal tensors  $\Lambda$  containing the singular values on the links are absorbed into the iPEPS tensors.

An application to a triangular lattice in two and three spatial dimensions is provided in Chapter 6.

## B.2 Effective Environments and Expectation Values

The simple update described in the previous section is an algorithm to determine the tensor network representation of the ground state of a certain lattice model. In

order to extract physical information it is necessary to compute observables in this representation. These can be local observables such as magnetization, particle density or energy, as well as non-local observables such as correlation functions. In one dimensions, expectation values of systems in the thermodynamic limit can be exactly computed due to the canonical form of the MPS. This is no longer true for two-dimensional systems, where the whole 2d plane needs to be contracted and approximations are inevitable [60]. In principle there are two different ways to compute expectation values, that are fundamentally different and vary in the accuracy of the result as well as in the computational cost.

### B.2.1 Mean-Field Environment

The iPEPS tensor network ansatz chosen for the simple update resembles the exact canonical form of 1d translational invariant MPS tensor networks. However due to the lack of a canonical form in 2d the diagonal tensors  $\Lambda$  carrying the singular values are not in direct relation to the Schmidt coefficients of a bipartition. Nevertheless the tensors represent weights on the bonds and can be interpreted as some mean-field environment surrounding every tensor. This ansatz can be readily used to compute

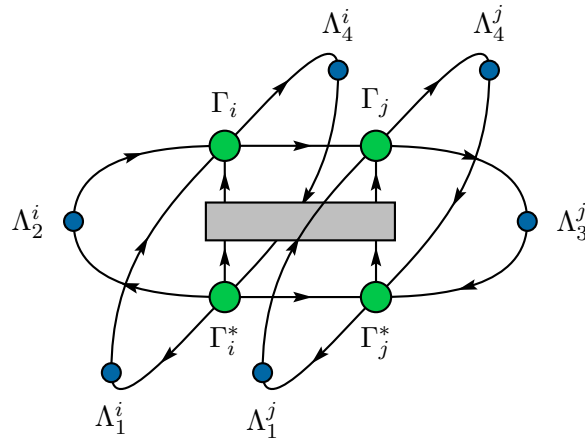


FIGURE B.9: The diagonal tensors  $\Lambda$  are used as a mean-field environment surrounding every tensor to compute expectation values.

expectation values based on this mean-field environment. An example of a two-site observable is shown in Fig. B.9. The environments of  $\Gamma_i$  and  $\Gamma_j$  are approximated by the corresponding tensors  $\Lambda$ . Since  $\Lambda^{1/2}$  has already been absorbed into each tensor  $\Gamma$  (see Fig. B.8), there is only one diagonal tensor  $\Lambda$  on the links connecting the wave function and its conjugate, and no additional tensor between the two iPEPS tensors. If only the mean-field environment is used, the network does not incorporate important quantum correlations between different sites. This way of computing expectation values should therefore only be used to get an idea of the outcome for the observables, however not to extract accurate numbers. Notice also that the mean-field ansatz is worse the more quantum correlations are present in the ground state. For a more sophisticated method we will introduce the corner transfer matrix renormalization group scheme in the following section.



### B.2.2 Corner Transfer Matrix Renormalization Group Scheme

Accurate expectation values of operators can be computed if the whole 2d iPEPS tensor network is contracted. An exact procedure to perform this contraction is exponentially hard already for finite PEPS networks, i.e. a PEPS ansatz with open boundary conditions and no translational invariance [60]. In the translational invariant case we are considering here, the situation is even more complicated and approximations are inevitable. Let us consider the computation of the norm of an iPEPS quantum state according to  $N = \langle \psi | \psi \rangle$ . Written as a contraction of the tensor network, the computation of the norm involves two infinite layers of the iPEPS as demonstrated in Fig. B.10. In order to make the description of the contraction scheme for the infinite lattice more

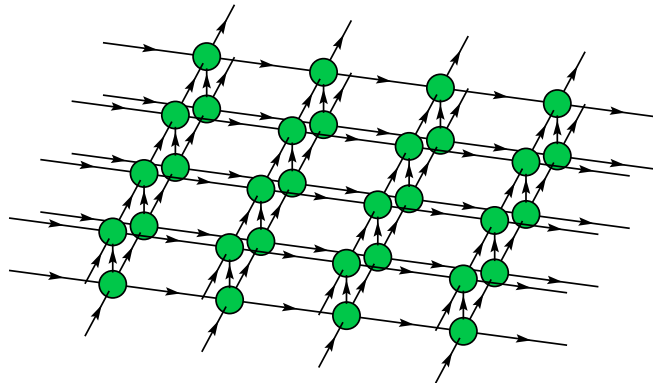


FIGURE B.10: Computing the norm of an iPEPS involves two copies of an infinite 2d lattice that need to be contracted.

clearly we will contract together the iPEPS tensor and its conjugate on every lattice site. This is shown in Fig. B.11, where the resulting lattice is a regular square lattice with a larger bond dimension of the tensors due to the index fusion. The contraction

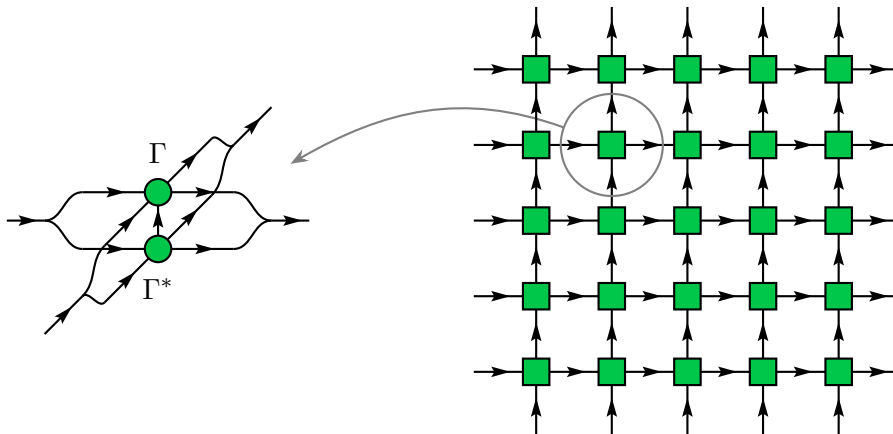


FIGURE B.11: Combining the iPEPS tensors with their conjugate version on all lattice sites results in a regular square lattice that needs to be contracted.

of the infinite lattice will be approximated by an effective environment surrounding every tensor in the unit cell. This environment consists of a set of fixed-point tensors that represent the contraction from infinite towards a certain lattice site. For the Corner Transfer Matrix Renormalization Group scheme (CTMRG) [80] used in this thesis we can define the environment as shown in Fig. B.12. It consists of four corner tensors  $\{C_1, C_2, C_3, C_4\}$  as well as four half-infinite row/column tensors  $\{T_1, T_2, T_3, T_4\}$ , that represent the contractions of all tensors in the eight areas indicated in gray. The con-

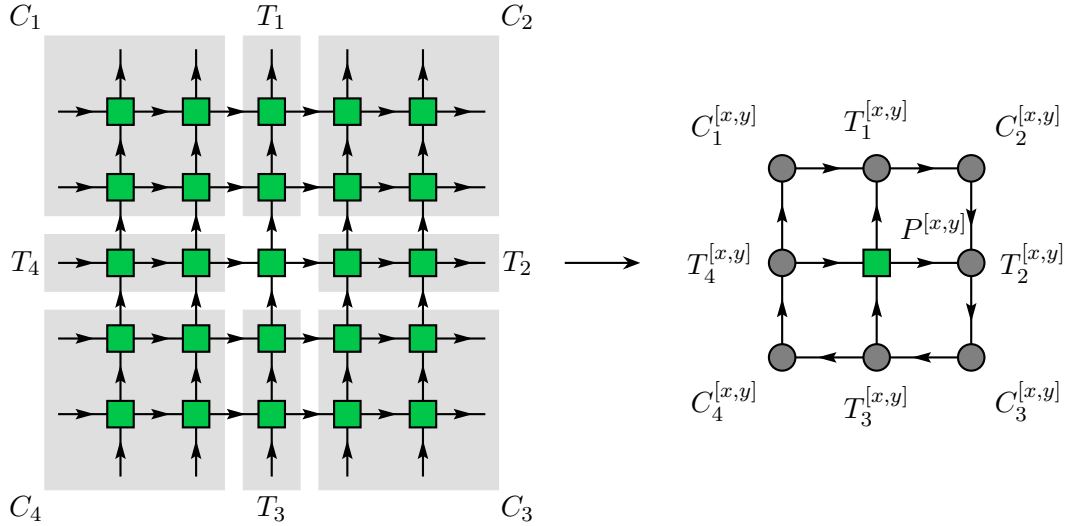


FIGURE B.12: Definition of the CTM environment tensors  $\{C_1, C_2, C_3, C_4\}$  and  $\{T_1, T_2, T_3, T_4\}$  that represent the approximated contraction of the infinite tensor network. Here  $P^{[x,y]}$  denotes the reduced tensor at position  $[x, y]$  in the unit cell.

traction of the infinite lattice is achieved by an iterative coarse-graining procedure, in which the reduced unit cell tensors  $P^{[x,y]}$  are absorbed into the environment tensors towards all lattice direction, until the environment converges to a fixed-point. In this process one has to approximate the enlarged environment tensors with a fixed bond dimension  $\chi_E$ . Without this truncation step the environment bond dimension would rapidly grow to infinity. The CTM method used in this thesis is called a *directional CTM algorithm* since the coarse-graining steps are performed sequentially in all four lattice directions. In the following we describe a left move of the CTM procedure, i.e. the absorption of a full unit cell into the left environment. This will grow and update the tensors  $C_1^{[x,y]}$ ,  $T_4^{[x,y]}$  and  $C_4^{[x,y]}$  for all  $x, y$  in the unit cell, that consists of  $N_x \times N_y$  tensors. The description of the CTM algorithm follows Refs. [143, 140].

The first step is to compute the truncation projectors which are used to reduce the enlarged bond dimension back to the desired one after the absorption. In order to

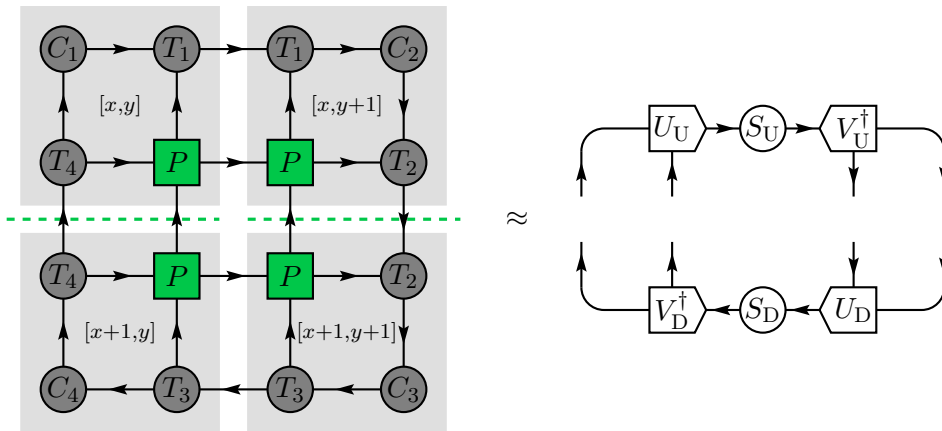


FIGURE B.13: Tensor network of  $2 \times 2$  reduced iPEPS tensors with the corresponding environments is cut along the green lines, and an SVD is performed on each half individually. The gray areas indicate the position of tensors  $P$  in the unit cell.

do this, the tensor network in Fig. B.13 is divided along the green lines, and an SVD is performed on each individual part. The gray areas indicate the position of tensors  $P$  in the unit cell as well as their corresponding environment tensors in relation to Fig. B.12. The right tensors in Fig. B.13 can be approximated if one truncates in the singular values to the desired precision. In practice we found that a truncation in  $S_U$  and  $S_D$  is however not necessary and does not improve the speed of the procedure significantly. The singular values in  $S_U$  and  $S_D$  are absorbed into the unitary tensors  $U$  and  $V^\dagger$ , as shown in Fig. B.14. Here we define  $F_{UL} = U_U S_U^{1/2}$ ,  $F_{UR} = S_U^{1/2} V_U^\dagger$ ,

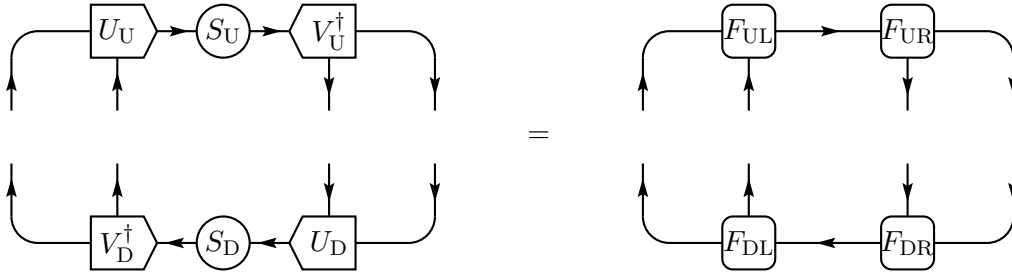


FIGURE B.14: The singular values  $S_U$  and  $S_D$  are absorbed into the corresponding unitary tensors  $U$  and  $V^\dagger$ .

$F_{DR} = U_D S_D^{1/2}$  and  $F_{DL} = S_D^{1/2} V_D^\dagger$ . In the next step we compute the projectors by using a biorthogonalization of the tensors  $F_{UL}$  and  $F_{DL}$  according to Fig. B.15. In

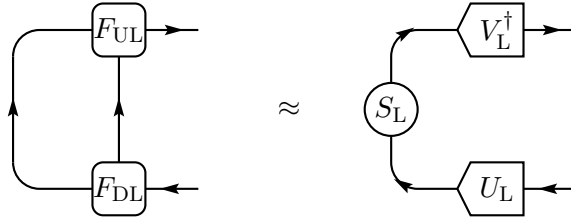


FIGURE B.15: In order to compute the projectors to truncate the environment we use a biorthogonalization procedure that involves the SVD of  $F_{DL} \cdot F_{UL}$ . The singular values  $S_L$  are truncated to the desired environment bond dimension  $\chi_E$ .

this step the singular values  $S_L$  are truncated to the desired environment bond dimension  $\chi_E$  and the tensor  $S_L$  needs to be inverted. In the following figure we define  $S_L^+ = \text{inv}(S_L^{1/2})$ , where a pseudo-inverse with a fixed threshold is used. Finally, the projectors  $P$  can be computed as shown in Fig. B.16. In order to compute all the

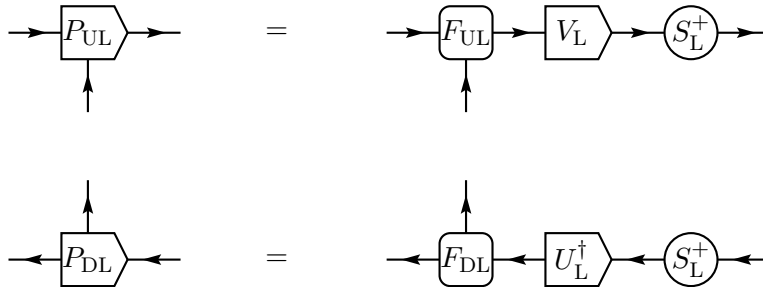


FIGURE B.16: Projectors to truncate the environment bond dimension for a left CTM move.

projectors necessary for the absorption of one column at fixed  $y$ , one can run over all tensors in the unit cell in  $x$ -direction, such that the projectors for every row, and

therefore for every subspace is computed. After this first step one can continue with the actual absorption of the tensors, as described below.

By absorbing more and more unit cell tensors into the environment in each direction, the environment tensors eventually represent the contraction of the infinite lattice once they are converged to a fixed-point. A left CTM move absorbs all columns of the iPEPS unit cell to the left environment, one after the other. Using the projectors computed in the first step, the updated and approximated corner tensors  $C'_1$  can be computed as shown in Fig. B.17. In the same way we can absorb a reduced iPEPS

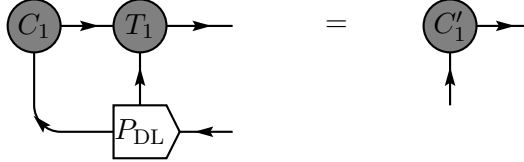


FIGURE B.17: Update of the upper corner tensor  $C_1$  in the left CTM step.

tensor into the environment tensor  $T_4$ , and use two projectors of different environment subspaces to truncate the enlarged bond dimension back to the desired one. In this

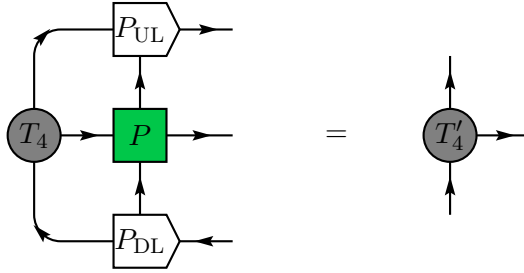


FIGURE B.18: Update of the half-infinite row tensors  $T_4$  in the left CTM step. Here  $P_{UL}$  and  $P_{DL}$  belong to different subspaces.

update step every tensor  $P^{[x,y]}$  has to be absorbed into the corresponding tensor  $T_4^{[x,y]}$  for fixed  $y$ . The last update is for the bottom corner tensor  $C_4$ , using again the projectors. Performing one complete left CTM moves involves the absorption of a complete

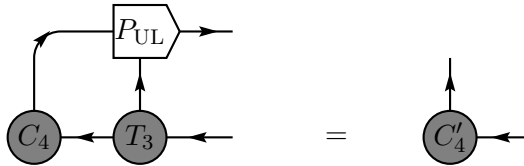


FIGURE B.19: Update of the lower corner tensor  $C_4$  in the left CTM step.

unit cell into the environment. So far we have only absorbed one column, i.e. tensors  $P^{[x,y]}$  for all  $x$  and one fixed  $y$ . The updated tensors  $C'_1$ ,  $T'_4$  and  $C'_4$  are then the new environment tensors for tensors  $P^{[x,y+1]}$ . Therefore one also has to iterate over all  $y$  to complete the left CTM step. After one left absorption step the environment is grown to the top, right, bottom and this full procedure is iterated until convergence is reached. A good, yet not the cheapest way to determine convergence is to check the spectrum of singular values of the corner tensors  $C_i^{[x,y]}$ , for all  $i$ ,  $x$  and  $y$ . Once the difference between successive CTM steps falls below a certain threshold one can stop the iteration. We noticed that the ground state energy, computed from the CTM tensors as described below, can also serve as an indication of convergence. However,

since the ground state energy typically converges rather quickly compared to other observables it might not be the best check.

### B.2.3 Computation of Expectation Values using CTM Environments

Expectation values for the iPEPS ground state can now be readily computed. Since operators typically only act on a limited number of iPEPS sites, the rest of the whole 2d network is similar to the one of the norm of the state, and can therefore be approximated by the CTM tensors. Expectation values of local observables are then computed as shown in Fig. B.20. Since the iPEPS wave function is not necessarily

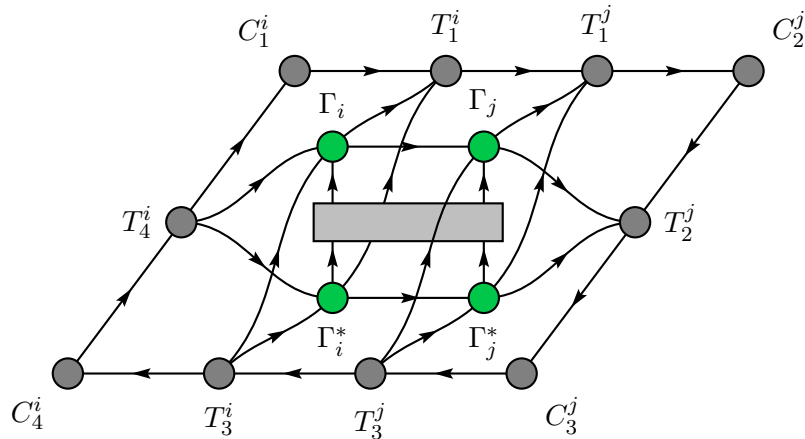


FIGURE B.20: Expectation values can be computed by sandwiching the operator between the iPEPS tensors and their fixed-point environment tensors, that represent the contraction of the whole 2d plane around that particular link or patch of tensors.

normalized we have to divide the expectation value by the norm of the state, given by the contraction in Fig. B.20 without the operator. Expectation values for one-site or multi-site operators are computed in a similar way.

## B.3 iPESS Simple Update

The Kagome lattice is a particularly interesting structure. It features corner-sharing triangles, which can lead to geometric frustration and hence an extended number of competing ground state configurations. For numerical tensor network simulations one typically favors an ansatz that resembles the lattice structure, in order to capture the correct entanglement pattern. Often though a mapping is used that transforms the original lattice to a more convenient structure that is more amenable to tensor network techniques. For instance, the Kagome lattice can be mapped to the square lattice by a coarse-graining of three physical sites into one, as done for instance in Ref. [116]. This mapping is however not very suitable, at least not for the optimization of the iPEPS tensors. Here we will present a mixed approach, in which the ground state wave function is obtained on the honeycomb lattice, the dual of the original Kagome lattice. This does not preserve the direct entanglement structure but proves to be very beneficial. In order to compute effective environments and expectation values a suitable coarse-graining to the square lattice is adopted.

### B.3.1 General iPESS Algorithm

The infinite Projected Entangled Simplex State (iPESS) tensor network has been proposed in Ref. [101]. It exploits the honeycomb lattice structure for the simulation of the Kagome lattice. The two structures are shown in Fig. B.21. Although this ansatz

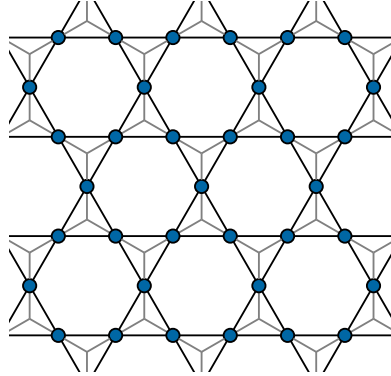


FIGURE B.21: Kagome lattice shown in black and its dual honeycomb lattice shown in gray.

does not resemble the entanglement pattern of the original lattice, it is well suited because it captures the correlation on the triangles in the Kagome lattice, i.e. the correlations between three sites at a time. The iPESS ansatz consists of three-index tensors for the lattice sites, as well as additional three-index *simplex tensors* that connect them among each other. The smallest unit cell of three-sites is shown in

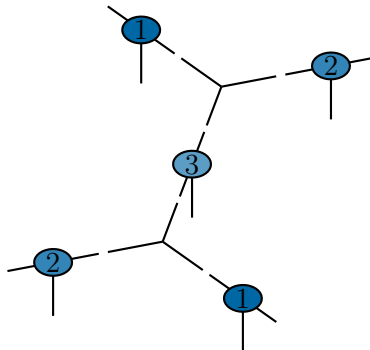


FIGURE B.22: iPESS ansatz with a unit cell of three tensors. The three-index tensors for the physical sites are connected by three-index virtual simplex tensors.

Fig. B.22, where one simplex builds the upper triangle and another simplex tensor builds the lower triangle. Both simplex tensors carry only virtual indices. In order to determine the tensor coefficients that represent the ground state of a certain Hamiltonian we use again a simple update scheme, illustrated in Fig. B.23. This time the simple update acts on all three sites connected to one simplex with the Hamiltonian

$$H_S = h_{12} + h_{13} + h_{23} . \quad (\text{B.9})$$

In order to reconstruct the iPESS tensors a higher-order SVD is used. Based on the singular values of this decomposition we can use a subsequent truncation to obtain the updated iPESS tensors. Importantly, the algorithm can be adapted to symmetry-preserving tensors as well, so that the truncation is performed in the individual sectors on the virtual indices. Both the non-symmetric and the  $SU(2)$ -symmetric version of the iPESS algorithm have been implemented for a three-site and a six-site unit cell.

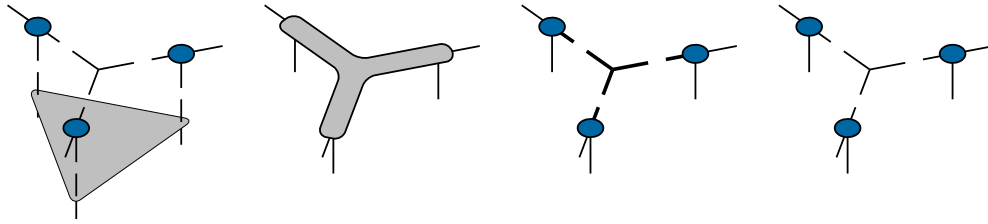


FIGURE B.23: Simple update in the iPESS scheme. A three-body Trotter gate (gray triangle) is applied to three sites attached to a simplex tensor. Using a higher-order SVD the resulting six-index tensor is decomposed again, and a truncation to the desired bond dimension yields the updated iPESS tensors. The second type of simplex tensor and its surrounding lattice sites are updated similarly.

### B.3.2 $SU(2)$ -Symmetric iPESS Algorithm

The iPESS algorithm presented in the previous section can be implemented using symmetry-preserving tensors in terms of networks of degeneracy tensors and corresponding fusion trees, that account for the group structure.

#### Integer Spin Systems

For the simulations of integer spin systems we can directly use the three-site iPESS ansatz with either only integer representations or both integer and half-integer representations on the virtual bond indices. Choosing only half-integer representations on the virtual bonds is not possible here due to the three-index simplex tensors, that could not satisfy the fusion rules in this case.

#### Half-Integer Spin Systems

For a half-integer spin system the three-site iPESS ansatz is not suitable. The reason for this is that the fusion rules cannot be satisfied simultaneously on all nodes in the network. This is illustrated in Fig. B.24, where the translational invariance of the unit cell fixes all spins on the virtual indices to a spin-0. The translational invariance is

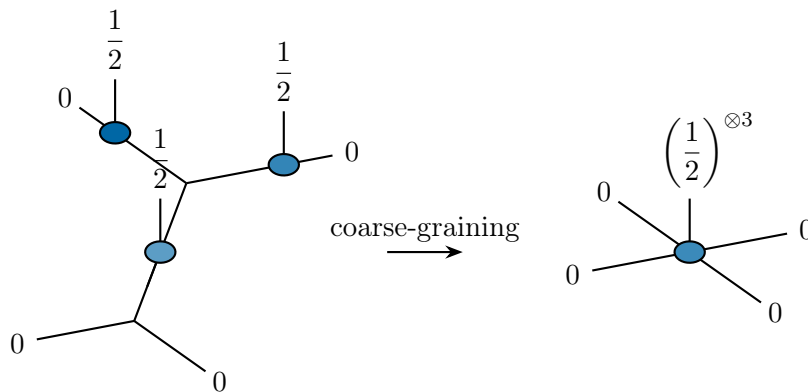


FIGURE B.24: Conflict between a decoration of the three-site iPESS with  $SU(2)$  quantum numbers and translational invariance. The problem can only be solved by enlarging the unit cell. Physical indices are drawn upwards for more clarity.

however not compatible with half-integer quantum numbers on the physical degrees of freedom. A coarse-graining of the iPESS tensors into a single iPEPS tensor with only integer spins on the virtual indices and half-integer spins on the physical indices makes the problem more evident. The mismatch for half-integer spins can only be resolved by enlarging the unit cell of iPESS tensors to an even number of sites, e.g. a six-site

unit cell. In this case the virtual bond indices necessarily carry both integer and half-integer quantum numbers. A possible implementation for six lattice site tensors in the unit cell alongside four different simplex tensors is shown in Fig. B.25. The

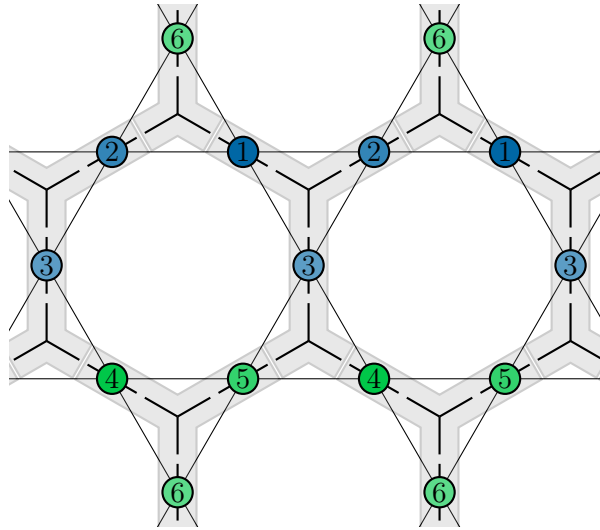


FIGURE B.25: Unit cell and lattice structure for the six-site iPESS. Four different simplex tensors connect the tensors on the lattice sites.

simple update for a six-site unit cell involves the update of all four simplex tensors together with their surrounding lattice site tensors.

## B.4 Effective Environments and Expectation Values

### B.4.1 iPESS Coarse-Graining

The simulation of ground states using iPESS as a TN ansatz has been described in Sec. B.3. In order to compute effective environments and expectation values ultimately, we resort to a coarse-graining to a square lattice iPEPS. Here we present one possible coarse-graining of the original TN ansatz on the honeycomb lattice, however the mapping is not unique. Consider the six-site iPESS ansatz shown in Fig. B.26. A coarse-graining of tensors in the gray-shaded areas leads to two different iPEPS

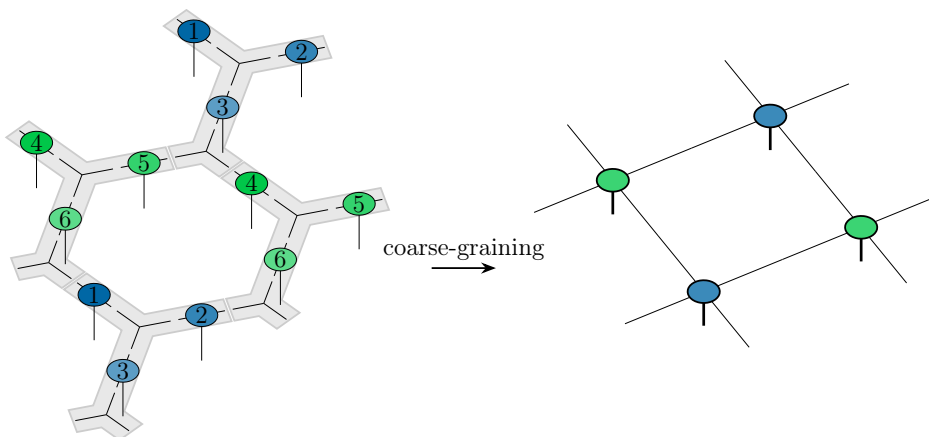


FIGURE B.26: Coarse-graining of the six-site iPESS ansatz into a two-site iPEPS ansatz with a checkerboard pattern of the tensors. The coarse-graining is performed for the gray-shaded regions.



tensors, one for iPESS sites  $(1, 2, 3)$  with two simplex tensors, and one for iPESS sites  $(4, 5, 6)$  with the remaining two simplex tensors. For the three-site iPESS network in Fig. B.22 the coarse-graining results in a translational invariant iPEPS network with a single tensor in the unit cell instead. The coarse-grained tensors can then be used in standard TN techniques to contract the infinite 2d layer, for instance in a CTM procedure as presented in Sec. B.2.

### B.4.2 Computation of Expectation Values using CTM Environments

The computation of expectation values for coarse-grained iPESS tensors is very similar to regular iPEPS tensors as described in Sec. B.2.3. Since the contraction of the infinite lattice is approximated by the CTM environment tensors, evaluating local observables can be done efficiently. Let us consider the energy per Kagome triangle, a three-body operator similar to the Trotter gate in the iPESS simple update. Measuring the energy on sites  $(1, 2, 3)$  or sites  $(4, 5, 6)$  in Fig. B.26 involves the evaluation of a single-site operator in the fine-grained picture, shown in Fig. B.27. If instead the energy is

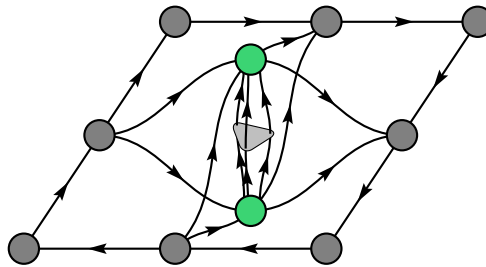


FIGURE B.27: A three-body iPESS operator becomes a single-site iPEPS operator if it acts on three sites that are coarse-grained together.

computed for sites  $(3, 5, 4)$  or sites  $(6, 2, 1)$  on the second type of triangles, the three-body iPESS operator remains a three-body operator for the coarse-grained tensors. This is shown in Fig. B.28, and the expectation value then includes the four iPEPS tensors and their respective environment. Two-body operators like the bond energy

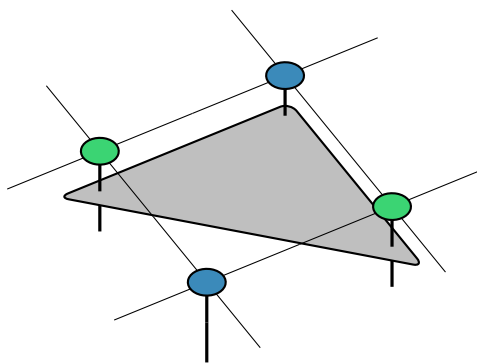


FIGURE B.28: A three-body iPESS operator that acts on three different coarse-grained iPEPS tensors.

$\vec{S}_i \cdot \vec{S}_j$  for nearest neighbours  $\langle i, j \rangle$  become either a single-site operator, or they remain a two-site operator in the coarse-grained picture.



# Bibliography

- [1] G. E. Moore, *Cramming more components onto integrated circuits*, Reprinted from *Electronics*, volume 38, number 8, April 19, 1965, pp.114 ff., IEEE Solid-State Circuits Society Newsletter **11**(3), 33 (2006), doi:[10.1109/NSSC.2006.4785860](https://doi.org/10.1109/NSSC.2006.4785860).
- [2] M. Lewenstein, A. Sanpera, V. Ahufinger, B. Damski, A. Sen(De) and U. Sen, *Ultracold atomic gases in optical lattices: mimicking condensed matter physics and beyond*, Advances in Physics **56**(2), 243 (2007), doi:[10.1080/00018730701223200](https://doi.org/10.1080/00018730701223200).
- [3] X. G. Wen, *Topological Orders in Rigid States*, International Journal of Modern Physics B **04**(02), 239 (1990), doi:[10.1142/S0217979290000139](https://doi.org/10.1142/S0217979290000139).
- [4] X.-G. Wen, *Topological Order: From Long-Range Entangled Quantum Matter to a Unified Origin of Light and Electrons*, ISRN Condensed Matter Physics **2013**, 1 (2013), doi:[10.1155/2013/198710](https://doi.org/10.1155/2013/198710).
- [5] A. Kitaev and C. Laumann, *Topological phases and quantum computation* (2009), [arXiv:0904.2771](https://arxiv.org/abs/0904.2771).
- [6] H. P. Nautrup and T.-C. Wei, *Symmetry-protected topologically ordered states for universal quantum computation*, Phys. Rev. A **92**, 052309 (2015), doi:[10.1103/PhysRevA.92.052309](https://doi.org/10.1103/PhysRevA.92.052309).
- [7] M. A. Nielsen and I. L. Chuang, *Quantum Computation and Quantum Information*, Cambridge University Press, doi:[10.1017/cbo9780511976667](https://doi.org/10.1017/cbo9780511976667) (2009).
- [8] Nobelprize.org [Online], *The Nobel Prize in Physics 2016* (2020).
- [9] R. Orús, *Tensor networks for complex quantum systems*, Nature Reviews Physics **1**(9), 538 (2019), doi:[10.1038/s42254-019-0086-7](https://doi.org/10.1038/s42254-019-0086-7).
- [10] J. Eisert, *Entanglement and tensor network states* (2013), [arXiv:1308.3318](https://arxiv.org/abs/1308.3318).
- [11] S. Singh, R. N. C. Pfeifer and G. Vidal, *Tensor network decompositions in the presence of a global symmetry*, Phys. Rev. A **82**, 050301 (2010), doi:[10.1103/PhysRevA.82.050301](https://doi.org/10.1103/PhysRevA.82.050301).
- [12] W. Pauli, *Über das Wasserstoffspektrum vom Standpunkt der neuen Quantenmechanik*, Zeitschrift für Physik A Hadrons and nuclei **36**(5), 336 (1926), doi:[10.1007/bf01450175](https://doi.org/10.1007/bf01450175).
- [13] X. Chen, Z.-C. Gu and X.-G. Wen, *Classification of gapped symmetric phases in one-dimensional spin systems*, Phys. Rev. B **83**, 035107 (2011), doi:[10.1103/PhysRevB.83.035107](https://doi.org/10.1103/PhysRevB.83.035107).
- [14] N. Schuch, D. Pérez-García and I. Cirac, *Classifying quantum phases using matrix product states and projected entangled pair states*, Phys. Rev. B **84**, 165139 (2011), doi:[10.1103/PhysRevB.84.165139](https://doi.org/10.1103/PhysRevB.84.165139).

- [15] K. Landsman, *Foundations of Quantum Theory*, Springer International Publishing, doi:[10.1007/978-3-319-51777-3](https://doi.org/10.1007/978-3-319-51777-3) (2017).
- [16] P. Anderson, *Resonating valence bonds: A new kind of insulator?*, Materials Research Bulletin **8**(2), 153 (1973), doi:[10.1016/0025-5408\(73\)90167-0](https://doi.org/10.1016/0025-5408(73)90167-0).
- [17] P. Silvi, F. Tschirsich, M. Gerster, J. Jünemann, D. Jaschke, M. Rizzi and S. Montangero, *The Tensor Networks Anthology: Simulation techniques for many-body quantum lattice systems*, SciPost Phys. Lect. Notes p. 8 (2019), doi:[10.21468/SciPostPhysLectNotes.8](https://doi.org/10.21468/SciPostPhysLectNotes.8).
- [18] C. R. Dean, *Even denominators in odd places*, Nature Physics **11**(4), 298 (2015), doi:[10.1038/nphys3298](https://doi.org/10.1038/nphys3298).
- [19] P. Mendels and F. Bert, *Quantum kagome frustrated antiferromagnets: One route to quantum spin liquids*, Comptes Rendus Physique **17**(3-4), 455 (2016), doi:[10.1016/j.crhy.2015.12.001](https://doi.org/10.1016/j.crhy.2015.12.001).
- [20] A. Einstein, B. Podolsky and N. Rosen, *Can Quantum-Mechanical Description of Physical Reality Be Considered Complete?*, Phys. Rev. **47**, 777 (1935), doi:[10.1103/PhysRev.47.777](https://doi.org/10.1103/PhysRev.47.777).
- [21] M. J. Klein, *Briefwechsel, 1916-1955. Albert Einstein and Hedwig and Max Born. Commentary by Max Born. Nymphenburger, Munich, 1969. 332 pp. DM 24.80*, Science **169**(3943), 360 (1970), doi:[10.1126/science.169.3943.360-b](https://doi.org/10.1126/science.169.3943.360-b).
- [22] J. S. Bell, *On the Einstein Podolsky Rosen paradox*, Physics Physique Fizika **1**(3), 195 (1964), doi:[10.1103/physicsphysiquefizika.1.195](https://doi.org/10.1103/physicsphysiquefizika.1.195).
- [23] A. Aspect, P. Grangier and G. Roger, *Experimental Realization of Einstein-Podolsky-Rosen-Bohm Gedankenexperiment: A New Violation of Bell's Inequalities*, Phys. Rev. Lett. **49**, 91 (1982), doi:[10.1103/PhysRevLett.49.91](https://doi.org/10.1103/PhysRevLett.49.91).
- [24] J. F. Clauser, M. A. Horne, A. Shimony and R. A. Holt, *Proposed Experiment to Test Local Hidden-Variable Theories*, Phys. Rev. Lett. **23**, 880 (1969), doi:[10.1103/PhysRevLett.23.880](https://doi.org/10.1103/PhysRevLett.23.880).
- [25] P. A. Hiskett, D. Rosenberg, C. G. Peterson, R. J. Hughes, S. Nam, A. E. Lita, A. J. Miller and J. E. Nordholt, *Long-distance quantum key distribution in optical fibre*, New Journal of Physics **8**(9), 193 (2006), doi:[10.1088/1367-2630/8/9/193](https://doi.org/10.1088/1367-2630/8/9/193).
- [26] R. Ursin, F. Tiefenbacher, T. Schmitt-Manderbach, H. Weier, T. Scheidl, M. Lindenthal, B. Blauensteiner, T. Jennewein, J. Perdigues, P. Trojek, B. Ömer, M. Fürst *et al.*, *Entanglement-based quantum communication over 144 km*, Nature Physics **3**(7), 481 (2007), doi:[10.1038/nphys629](https://doi.org/10.1038/nphys629).
- [27] D. Boschi, S. Branca, F. De Martini, L. Hardy and S. Popescu, *Experimental Realization of Teleporting an Unknown Pure Quantum State via Dual Classical and Einstein-Podolsky-Rosen Channels*, Phys. Rev. Lett. **80**, 1121 (1998), doi:[10.1103/PhysRevLett.80.1121](https://doi.org/10.1103/PhysRevLett.80.1121).
- [28] L. K. Grover, *A Fast Quantum Mechanical Algorithm for Database Search*, In *Proceedings of the Twenty-Eighth Annual ACM Symposium on Theory of Computing*, STOC '96, p. 212–219. Association for Computing Machinery, New York, NY, USA, ISBN 0897917855, doi:[10.1145/237814.237866](https://doi.org/10.1145/237814.237866) (1996).

- [29] P. W. Shor, *Algorithms for quantum computation: discrete logarithms and factoring*, In *Proceedings 35th Annual Symposium on Foundations of Computer Science*, pp. 124–134. IEEE Comput. Soc. Press, doi:[10.1109/sfcs.1994.365700](https://doi.org/10.1109/sfcs.1994.365700) (1994).
- [30] T.-C. Wei and P. M. Goldbart, *Geometric measure of entanglement and applications to bipartite and multipartite quantum states*, *Phys. Rev. A* **68**, 042307 (2003), doi:[10.1103/PhysRevA.68.042307](https://doi.org/10.1103/PhysRevA.68.042307).
- [31] V. Coffman, J. Kundu and W. K. Wootters, *Distributed entanglement*, *Phys. Rev. A* **61**, 052306 (2000), doi:[10.1103/PhysRevA.61.052306](https://doi.org/10.1103/PhysRevA.61.052306).
- [32] A. Rényi, *On Measures of Entropy and Information*, In *Proceedings of the Fourth Berkeley Symposium on Mathematical Statistics and Probability, Volume 1: Contributions to the Theory of Statistics*, pp. 547–561. University of California Press, Berkeley, Calif. (1961).
- [33] J. Eisert and M. Cramer, *Single-copy entanglement in critical quantum spin chains*, *Phys. Rev. A* **72**, 042112 (2005), doi:[10.1103/PhysRevA.72.042112](https://doi.org/10.1103/PhysRevA.72.042112).
- [34] I. Peschel and J. Zhao, *On single-copy entanglement*, *Journal of Statistical Mechanics: Theory and Experiment* **2005**(11), P11002 (2005), doi:[10.1088/1742-5468/2005/11/p11002](https://doi.org/10.1088/1742-5468/2005/11/p11002).
- [35] S. Sachdev, *Quantum Phase Transitions*, Cambridge University Press, doi:[10.1017/cbo9780511973765](https://doi.org/10.1017/cbo9780511973765) (2009).
- [36] S. Suzuki, J. ichi Inoue and B. K. Chakrabarti, *Quantum Ising Phases and Transitions in Transverse Ising Models*, Springer Berlin Heidelberg, doi:[10.1007/978-3-642-33039-1](https://doi.org/10.1007/978-3-642-33039-1) (2013).
- [37] D.-H. Lee, *Routes to High-Temperature Superconductivity: A Lesson from FeSe/SrTiO<sub>3</sub>*, *Annual Review of Condensed Matter Physics* **9**(1), 261 (2018), doi:[10.1146/annurev-conmatphys-033117-053942](https://doi.org/10.1146/annurev-conmatphys-033117-053942).
- [38] H. Fehske, R. Schneider and A. Weiße, eds., *Computational Many-Particle Physics*, Springer Berlin Heidelberg, doi:[10.1007/978-3-540-74686-7](https://doi.org/10.1007/978-3-540-74686-7) (2008).
- [39] F. Becca and S. Sorella, *Quantum Monte Carlo Approaches for Correlated Systems*, Cambridge University Press, doi:[10.1017/9781316417041](https://doi.org/10.1017/9781316417041) (2017).
- [40] R. M. Dreizler and E. K. U. Gross, *Density Functional Theory*, Springer Berlin Heidelberg, doi:[10.1007/978-3-642-86105-5](https://doi.org/10.1007/978-3-642-86105-5) (1990).
- [41] D. Vollhardt, V. Anisimov, S. Skornyakov and I. Leonov, *Dynamical Mean-Field Theory for Correlated Electron Materials*, *Materials Today: Proceedings* **14**, 176 (2019), doi:[10.1016/j.matpr.2019.05.080](https://doi.org/10.1016/j.matpr.2019.05.080).
- [42] J. Oitmaa, C. Hamer and W. Zheng, *Series Expansion Methods for Strongly Interacting Lattice Models*, Cambridge University Press, doi:[10.1017/cbo9780511584398](https://doi.org/10.1017/cbo9780511584398) (2006).
- [43] J. Stein, *Flow equations and the strong-coupling expansion for the hubbard model*, *Journal of Statistical Physics* **88**(1-2), 487 (1997), doi:[10.1007/bf02508481](https://doi.org/10.1007/bf02508481).

- [44] S. Szalay, M. Pfeffer, V. Murg, G. Barcza, F. Verstraete, R. Schneider and Örs Legeza, *Tensor product methods and entanglement optimization for ab initio quantum chemistry*, International Journal of Quantum Chemistry **115**(19), 1342 (2015), doi:[10.1002/qua.24898](https://doi.org/10.1002/qua.24898).
- [45] W. Huggins, P. Patil, B. Mitchell, K. B. Whaley and E. M. Stoudenmire, *Towards quantum machine learning with tensor networks*, Quantum Science and Technology **4**(2), 024001 (2019), doi:[10.1088/2058-9565/aaea94](https://doi.org/10.1088/2058-9565/aaea94).
- [46] A. Jahn, M. Gluza, F. Pastawski and J. Eisert, *Holography and criticality in matchgate tensor networks*, Science Advances **5**(8) (2019), doi:[10.1126/sciadv.aaw0092](https://doi.org/10.1126/sciadv.aaw0092).
- [47] A. Gallego and R. Orus, *Language design as information renormalization*. (2017), [arXiv:1708.01525](https://arxiv.org/abs/1708.01525).
- [48] S. R. White, *Density matrix formulation for quantum renormalization groups*, Phys. Rev. Lett. **69**, 2863 (1992), doi:[10.1103/PhysRevLett.69.2863](https://doi.org/10.1103/PhysRevLett.69.2863).
- [49] S. R. White, *Density-matrix algorithms for quantum renormalization groups*, Phys. Rev. B **48**, 10345 (1993), doi:[10.1103/PhysRevB.48.10345](https://doi.org/10.1103/PhysRevB.48.10345).
- [50] G. Vidal, *Efficient Classical Simulation of Slightly Entangled Quantum Computations*, Phys. Rev. Lett. **91**, 147902 (2003), doi:[10.1103/PhysRevLett.91.147902](https://doi.org/10.1103/PhysRevLett.91.147902).
- [51] G. Vidal, *Efficient Simulation of One-Dimensional Quantum Many-Body Systems*, Phys. Rev. Lett. **93**, 040502 (2004), doi:[10.1103/PhysRevLett.93.040502](https://doi.org/10.1103/PhysRevLett.93.040502).
- [52] F. Verstraete and J. I. Cirac, *Renormalization algorithms for Quantum-Many Body Systems in two and higher dimensions* (2004), [arXiv:cond-mat/0407066](https://arxiv.org/abs/cond-mat/0407066).
- [53] G. Evenbly and G. Vidal, *Class of Highly Entangled Many-Body States that can be Efficiently Simulated*, Phys. Rev. Lett. **112**, 240502 (2014), doi:[10.1103/PhysRevLett.112.240502](https://doi.org/10.1103/PhysRevLett.112.240502).
- [54] Y.-Y. Shi, L.-M. Duan and G. Vidal, *Classical simulation of quantum many-body systems with a tree tensor network*, Phys. Rev. A **74**, 022320 (2006), doi:[10.1103/PhysRevA.74.022320](https://doi.org/10.1103/PhysRevA.74.022320).
- [55] L. Tagliacozzo, G. Evenbly and G. Vidal, *Simulation of two-dimensional quantum systems using a tree tensor network that exploits the entropic area law*, Phys. Rev. B **80**, 235127 (2009), doi:[10.1103/PhysRevB.80.235127](https://doi.org/10.1103/PhysRevB.80.235127).
- [56] P. Silvi, V. Giovannetti, S. Montangero, M. Rizzi, J. I. Cirac and R. Fazio, *Homogeneous binary trees as ground states of quantum critical Hamiltonians*, Phys. Rev. A **81**, 062335 (2010), doi:[10.1103/PhysRevA.81.062335](https://doi.org/10.1103/PhysRevA.81.062335).
- [57] F. Verstraete and J. I. Cirac, *Continuous Matrix Product States for Quantum Fields*, Phys. Rev. Lett. **104**, 190405 (2010), doi:[10.1103/PhysRevLett.104.190405](https://doi.org/10.1103/PhysRevLett.104.190405).
- [58] A. Franco-Rubio and G. Vidal, *Entanglement and correlations in the continuous multi-scale entanglement renormalization ansatz*, Journal of High Energy Physics **2017**(12) (2017), doi:[10.1007/jhep12\(2017\)129](https://doi.org/10.1007/jhep12(2017)129).

- [59] F. Verstraete, V. Murg and J. Cirac, *Matrix product states, projected entangled pair states, and variational renormalization group methods for quantum spin systems*, *Advances in Physics* **57**(2), 143 (2008), doi:[10.1080/14789940801912366](https://doi.org/10.1080/14789940801912366).
- [60] R. Orús, *A practical introduction to tensor networks: Matrix product states and projected entangled pair states*, *Annals of Physics* **349**, 117 (2014), doi:[10.1016/j.aop.2014.06.013](https://doi.org/10.1016/j.aop.2014.06.013).
- [61] P. Corboz, *Improved energy extrapolation with infinite projected entangled-pair states applied to the two-dimensional Hubbard model*, *Phys. Rev. B* **93**, 045116 (2016), doi:[10.1103/PhysRevB.93.045116](https://doi.org/10.1103/PhysRevB.93.045116).
- [62] L. Chi-Chung, P. Sadayappan and R. Wenger, *On Optimizing a Class of Multi-Dimensional Loops with Reduction for Parallel Execution*, *Parallel Processing Letters* **07**(02), 157 (1997), doi:[10.1142/s0129626497000176](https://doi.org/10.1142/s0129626497000176).
- [63] J. Xu, L. Liang, L. Deng, C. Wen, Y. Xie and G. Li, *Towards a polynomial algorithm for optimal contraction sequence of tensor networks from trees*, *Phys. Rev. E* **100**, 043309 (2019), doi:[10.1103/PhysRevE.100.043309](https://doi.org/10.1103/PhysRevE.100.043309).
- [64] V. Zauner-Stauber, L. Vanderstraeten, M. T. Fishman, F. Verstraete and J. Haegeman, *Variational optimization algorithms for uniform matrix product states*, *Phys. Rev. B* **97**, 045145 (2018), doi:[10.1103/PhysRevB.97.045145](https://doi.org/10.1103/PhysRevB.97.045145).
- [65] F. Verstraete and J. I. Cirac, *Matrix product states represent ground states faithfully*, *Phys. Rev. B* **73**, 094423 (2006), doi:[10.1103/PhysRevB.73.094423](https://doi.org/10.1103/PhysRevB.73.094423).
- [66] U. Schollwöck, *The density-matrix renormalization group*, *Rev. Mod. Phys.* **77**, 259 (2005), doi:[10.1103/RevModPhys.77.259](https://doi.org/10.1103/RevModPhys.77.259).
- [67] B. Pirvu, G. Vidal, F. Verstraete and L. Tagliacozzo, *Matrix product states for critical spin chains: Finite-size versus finite-entanglement scaling*, *Phys. Rev. B* **86**, 075117 (2012), doi:[10.1103/PhysRevB.86.075117](https://doi.org/10.1103/PhysRevB.86.075117).
- [68] P. Schmoll, A. Haller, M. Rizzi and R. Orús, *Quantum criticality on a chiral ladder: An  $SU(2)$  infinite density matrix renormalization group study*, *Phys. Rev. B* **99**, 205121 (2019), doi:[10.1103/PhysRevB.99.205121](https://doi.org/10.1103/PhysRevB.99.205121).
- [69] E. Stoudenmire and S. R. White, *Studying Two-Dimensional Systems with the Density Matrix Renormalization Group*, *Annual Review of Condensed Matter Physics* **3**(1), 111 (2012), doi:[10.1146/annurev-conmatphys-020911-125018](https://doi.org/10.1146/annurev-conmatphys-020911-125018).
- [70] L. Vanderstraeten, *Tensor Network States and Effective Particles for Low-Dimensional Quantum Spin Systems*, Springer International Publishing, doi:[10.1007/978-3-319-64191-1](https://doi.org/10.1007/978-3-319-64191-1) (2017).
- [71] J. Jordan, R. Orús, G. Vidal, F. Verstraete and J. I. Cirac, *Classical Simulation of Infinite-Size Quantum Lattice Systems in Two Spatial Dimensions*, *Phys. Rev. Lett.* **101**, 250602 (2008), doi:[10.1103/PhysRevLett.101.250602](https://doi.org/10.1103/PhysRevLett.101.250602).
- [72] H. N. Phien, J. A. Bengua, H. D. Tuan, P. Corboz and R. Orús, *Infinite projected entangled pair states algorithm improved: Fast full update and gauge fixing*, *Phys. Rev. B* **92**, 035142 (2015), doi:[10.1103/PhysRevB.92.035142](https://doi.org/10.1103/PhysRevB.92.035142).
- [73] P. Corboz, *Variational optimization with infinite projected entangled-pair states*, *Phys. Rev. B* **94**, 035133 (2016), doi:[10.1103/PhysRevB.94.035133](https://doi.org/10.1103/PhysRevB.94.035133).



- [74] L. Vanderstraeten, J. Haegeman, P. Corboz and F. Verstraete, *Gradient methods for variational optimization of projected entangled-pair states*, Phys. Rev. B **94**, 155123 (2016), doi:[10.1103/PhysRevB.94.155123](https://doi.org/10.1103/PhysRevB.94.155123).
- [75] M. Levin and C. P. Nave, *Tensor Renormalization Group Approach to Two-Dimensional Classical Lattice Models*, Phys. Rev. Lett. **99**, 120601 (2007), doi:[10.1103/PhysRevLett.99.120601](https://doi.org/10.1103/PhysRevLett.99.120601).
- [76] Z. Y. Xie, H. C. Jiang, Q. N. Chen, Z. Y. Weng and T. Xiang, *Second Renormalization of Tensor-Network States*, Phys. Rev. Lett. **103**, 160601 (2009), doi:[10.1103/PhysRevLett.103.160601](https://doi.org/10.1103/PhysRevLett.103.160601).
- [77] Z. Y. Xie, J. Chen, M. P. Qin, J. W. Zhu, L. P. Yang and T. Xiang, *Coarse-graining renormalization by higher-order singular value decomposition*, Phys. Rev. B **86**, 045139 (2012), doi:[10.1103/PhysRevB.86.045139](https://doi.org/10.1103/PhysRevB.86.045139).
- [78] T. Nishino and K. Okunishi, *Corner Transfer Matrix Renormalization Group Method*, Journal of the Physical Society of Japan **65**(4), 891 (1996), doi:[10.1143/jpsj.65.891](https://doi.org/10.1143/jpsj.65.891).
- [79] T. Nishino and K. Okunishi, *Corner Transfer Matrix Algorithm for Classical Renormalization Group*, Journal of the Physical Society of Japan **66**(10), 3040 (1997), doi:[10.1143/jpsj.66.3040](https://doi.org/10.1143/jpsj.66.3040).
- [80] R. Orús and G. Vidal, *Simulation of two-dimensional quantum systems on an infinite lattice revisited: Corner transfer matrix for tensor contraction*, Phys. Rev. B **80**, 094403 (2009), doi:[10.1103/PhysRevB.80.094403](https://doi.org/10.1103/PhysRevB.80.094403).
- [81] R. Orús, *Exploring corner transfer matrices and corner tensors for the classical simulation of quantum lattice systems*, Phys. Rev. B **85**, 205117 (2012), doi:[10.1103/PhysRevB.85.205117](https://doi.org/10.1103/PhysRevB.85.205117).
- [82] M. Robinson, *Symmetry and the Standard Model*, Springer New York, doi:[10.1007/978-1-4419-8267-4](https://doi.org/10.1007/978-1-4419-8267-4) (2011).
- [83] S. Singh and G. Vidal, *Tensor network states and algorithms in the presence of a global  $SU(2)$  symmetry*, Phys. Rev. B **86**, 195114 (2012), doi:[10.1103/PhysRevB.86.195114](https://doi.org/10.1103/PhysRevB.86.195114).
- [84] M. Hamermesh and A. A. Mullin, *Group Theory and its Applications to Physical Problems*, American Journal of Physics **30**(10), 774 (1962), doi:[10.1119/1.1941790](https://doi.org/10.1119/1.1941790).
- [85] P. Schmoll, S. Singh, M. Rizzi and R. Orús, *A programming guide for tensor networks with global  $su(2)$  symmetry*, Annals of Physics **419**, 168232 (2020), doi:<https://doi.org/10.1016/j.aop.2020.168232>.
- [86] H. C. Jiang, Z. Y. Weng and T. Xiang, *Accurate Determination of Tensor Network State of Quantum Lattice Models in Two Dimensions*, Phys. Rev. Lett. **101**, 090603 (2008), doi:[10.1103/PhysRevLett.101.090603](https://doi.org/10.1103/PhysRevLett.101.090603).
- [87] S. Singh, *Identifying quantum phases from the injectivity of symmetric matrix product states*, Phys. Rev. B **91**, 115145 (2015), doi:[10.1103/PhysRevB.91.115145](https://doi.org/10.1103/PhysRevB.91.115145).



- [88] S. Trebst, M. Troyer, Z. Wang and A. W. W. Ludwig, *A Short Introduction to Fibonacci Anyon Models*, Progress of Theoretical Physics Supplement **176**, 384 (2008), doi:[10.1143/ptps.176.384](https://doi.org/10.1143/ptps.176.384).
- [89] I. Affleck, D. Gepner, H. J. Schulz and T. Ziman, *Critical behaviour of spin- $s$  Heisenberg antiferromagnetic chains: analytic and numerical results*, Journal of Physics A: Mathematical and General **22**(5), 511 (1989), doi:[10.1088/0305-4470/22/5/015](https://doi.org/10.1088/0305-4470/22/5/015).
- [90] O. I. Motrunich, *Orbital magnetic field effects in spin liquid with spinon Fermi sea: Possible application to  $\kappa$ -(ET) $_2$ Cu $_2$ (CN) $_3$* , Phys. Rev. B **73**, 155115 (2006), doi:[10.1103/PhysRevB.73.155115](https://doi.org/10.1103/PhysRevB.73.155115).
- [91] B. Bauer, L. Cincio, B. Keller, M. Dolfi, G. Vidal, S. Trebst and A. Ludwig, *Chiral spin liquid and emergent anyons in a Kagome lattice Mott insulator*, Nature Communications **5**(1) (2014), doi:[10.1038/ncomms6137](https://doi.org/10.1038/ncomms6137).
- [92] F. Görg, K. Sandholzer, J. Minguzzi, R. Desbuquois, M. Messer and T. Esslinger, *Realization of density-dependent Peierls phases to engineer quantized gauge fields coupled to ultracold matter*, Nature Physics **15**(11), 1161 (2019), doi:[10.1038/s41567-019-0615-4](https://doi.org/10.1038/s41567-019-0615-4).
- [93] U. Schollwöck, *The density-matrix renormalization group in the age of matrix product states*, Annals of Physics **326**(1), 96 (2011), doi:[10.1016/j.aop.2010.09.012](https://doi.org/10.1016/j.aop.2010.09.012).
- [94] C. Holzhey, F. Larsen and F. Wilczek, *Geometric and renormalized entropy in conformal field theory*, Nuclear Physics B **424**(3), 443 (1994), doi:[10.1016/0550-3213\(94\)90402-2](https://doi.org/10.1016/0550-3213(94)90402-2).
- [95] G. Vidal, J. I. Latorre, E. Rico and A. Kitaev, *Entanglement in Quantum Critical Phenomena*, Phys. Rev. Lett. **90**, 227902 (2003), doi:[10.1103/PhysRevLett.90.227902](https://doi.org/10.1103/PhysRevLett.90.227902).
- [96] P. Calabrese and J. Cardy, *Entanglement entropy and quantum field theory*, Journal of Statistical Mechanics: Theory and Experiment **2004**(06), P06002 (2004), doi:[10.1088/1742-5468/2004/06/p06002](https://doi.org/10.1088/1742-5468/2004/06/p06002).
- [97] L. Tagliacozzo, T. R. de Oliveira, S. Iblisdir and J. I. Latorre, *Scaling of entanglement support for matrix product states*, Phys. Rev. B **78**, 024410 (2008), doi:[10.1103/PhysRevB.78.024410](https://doi.org/10.1103/PhysRevB.78.024410).
- [98] T. Vekua and G. Sun, *Exact asymptotic correlation functions of bilinear spin operators of the Heisenberg antiferromagnetic spin- $\frac{1}{2}$  chain*, Phys. Rev. B **94**, 014417 (2016), doi:[10.1103/PhysRevB.94.014417](https://doi.org/10.1103/PhysRevB.94.014417).
- [99] J. Cardy and E. Tonni, *Entanglement Hamiltonians in two-dimensional conformal field theory*, Journal of Statistical Mechanics: Theory and Experiment **2016**(12), 123103 (2016), doi:[10.1088/1742-5468/2016/12/123103](https://doi.org/10.1088/1742-5468/2016/12/123103).
- [100] P.-H. Huang, J.-H. Chen, A. E. Feiguin, C. Chamon and C. Mudry, *Coupled spin- $\frac{1}{2}$  ladders as microscopic models for non-Abelian chiral spin liquids*, Phys. Rev. B **95**, 144413 (2017), doi:[10.1103/PhysRevB.95.144413](https://doi.org/10.1103/PhysRevB.95.144413).

- [101] Z. Y. Xie, J. Chen, J. F. Yu, X. Kong, B. Normand and T. Xiang, *Tensor Renormalization of Quantum Many-Body Systems Using Projected Entangled Simplex States*, Phys. Rev. X **4**, 011025 (2014), doi:[10.1103/PhysRevX.4.011025](https://doi.org/10.1103/PhysRevX.4.011025).
- [102] I. Niesen and P. Corboz, *A tensor network study of the complete ground state phase diagram of the spin-1 bilinear-biquadratic Heisenberg model on the square lattice*, SciPost Phys. **3**, 030 (2017), doi:[10.21468/SciPostPhys.3.4.030](https://doi.org/10.21468/SciPostPhys.3.4.030).
- [103] S. Bhattacharjee, V. B. Shenoy and T. Senthil, *Possible ferro-spin nematic order in NiGa<sub>2</sub>S<sub>4</sub>*, Phys. Rev. B **74**, 092406 (2006), doi:[10.1103/PhysRevB.74.092406](https://doi.org/10.1103/PhysRevB.74.092406).
- [104] J. G. Cheng, G. Li, L. Balicas, J. S. Zhou, J. B. Goodenough, C. Xu and H. D. Zhou, *High-Pressure Sequence of Ba<sub>3</sub>NiSb<sub>2</sub>O<sub>9</sub> Structural Phases: New S = 1 Quantum Spin Liquids Based on Ni<sup>2+</sup>*, Phys. Rev. Lett. **107**, 197204 (2011), doi:[10.1103/PhysRevLett.107.197204](https://doi.org/10.1103/PhysRevLett.107.197204).
- [105] J. B. Marston and C. Zeng, *Spin-Peierls and spin-liquid phases of Kagomé quantum antiferromagnets*, Journal of Applied Physics **69**(8), 5962 (1991), doi:[10.1063/1.347830](https://doi.org/10.1063/1.347830).
- [106] K. Yang, L. K. Warman and S. M. Girvin, *Possible spin-liquid states on the triangular and Kagomé lattices*, Phys. Rev. Lett. **70**, 2641 (1993), doi:[10.1103/PhysRevLett.70.2641](https://doi.org/10.1103/PhysRevLett.70.2641).
- [107] M. B. Hastings, *Dirac structure, RVB, and Goldstone modes in the kagomé antiferromagnet*, Phys. Rev. B **63**, 014413 (2000), doi:[10.1103/PhysRevB.63.014413](https://doi.org/10.1103/PhysRevB.63.014413).
- [108] Y. Ran, M. Hermele, P. A. Lee and X.-G. Wen, *Projected-Wave-Function Study of the Spin-1/2 Heisenberg Model on the Kagomé Lattice*, Phys. Rev. Lett. **98**, 117205 (2007), doi:[10.1103/PhysRevLett.98.117205](https://doi.org/10.1103/PhysRevLett.98.117205).
- [109] R. R. P. Singh and D. A. Huse, *Triplet and singlet excitations in the valence bond crystal phase of the kagome lattice Heisenberg model*, Phys. Rev. B **77**, 144415 (2008), doi:[10.1103/PhysRevB.77.144415](https://doi.org/10.1103/PhysRevB.77.144415).
- [110] G. Evenbly and G. Vidal, *Frustrated Antiferromagnets with Entanglement Renormalization: Ground State of the Spin- $\frac{1}{2}$  Heisenberg Model on a Kagome Lattice*, Phys. Rev. Lett. **104**, 187203 (2010), doi:[10.1103/PhysRevLett.104.187203](https://doi.org/10.1103/PhysRevLett.104.187203).
- [111] L. Savary and L. Balents, *Quantum spin liquids: a review*, Reports on Progress in Physics **80**(1), 016502 (2016), doi:[10.1088/0034-4885/80/1/016502](https://doi.org/10.1088/0034-4885/80/1/016502).
- [112] S. Depenbrock, I. P. McCulloch and U. Schollwöck, *Nature of the Spin-Liquid Ground State of the S = 1/2 Heisenberg Model on the Kagome Lattice*, Phys. Rev. Lett. **109**, 067201 (2012), doi:[10.1103/PhysRevLett.109.067201](https://doi.org/10.1103/PhysRevLett.109.067201).
- [113] R. R. P. Singh and D. A. Huse, *Ground state of the spin-1/2 kagome-lattice Heisenberg antiferromagnet*, Phys. Rev. B **76**, 180407 (2007), doi:[10.1103/PhysRevB.76.180407](https://doi.org/10.1103/PhysRevB.76.180407).
- [114] H. J. Liao, Z. Y. Xie, J. Chen, Z. Y. Liu, H. D. Xie, R. Z. Huang, B. Normand and T. Xiang, *Gapless Spin-Liquid Ground State in the S = 1/2 Kagome Antiferromagnet*, Phys. Rev. Lett. **118**, 137202 (2017), doi:[10.1103/PhysRevLett.118.137202](https://doi.org/10.1103/PhysRevLett.118.137202).

- [115] S. Yan, D. A. Huse and S. R. White, *Spin-Liquid Ground State of the  $S = 1/2$  Kagome Heisenberg Antiferromagnet*, *Science* **332**(6034), 1173 (2011), doi:[10.1126/science.1201080](https://doi.org/10.1126/science.1201080).
- [116] C. Hubig, *Abelian and non-abelian symmetries in infinite projected entangled pair states*, *SciPost Phys.* **5**, 47 (2018), doi:[10.21468/SciPostPhys.5.5.047](https://doi.org/10.21468/SciPostPhys.5.5.047).
- [117] A. Kshetrimayum, T. Picot, R. Orús and D. Poilblanc, *Spin- $\frac{1}{2}$  kagome XXZ model in a field: Competition between lattice nematic and solid orders*, *Phys. Rev. B* **94**, 235146 (2016), doi:[10.1103/PhysRevB.94.235146](https://doi.org/10.1103/PhysRevB.94.235146).
- [118] T. Liu, W. Li, A. Weichselbaum, J. von Delft and G. Su, *Simplex valence-bond crystal in the spin-1 kagome Heisenberg antiferromagnet*, *Phys. Rev. B* **91**, 060403 (2015), doi:[10.1103/PhysRevB.91.060403](https://doi.org/10.1103/PhysRevB.91.060403).
- [119] L. Balents, *Spin liquids in frustrated magnets*, *Nature* **464**(7286), 199 (2010), doi:[10.1038/nature08917](https://doi.org/10.1038/nature08917).
- [120] P. Scholl, S. S. Jahromi, M. Hörmann, M. Mühlhauser, K. P. Schmidt and R. Orús, *Fine Grained Tensor Network Methods*, *Phys. Rev. Lett.* **124**, 200603 (2020), doi:[10.1103/PhysRevLett.124.200603](https://doi.org/10.1103/PhysRevLett.124.200603).
- [121] S. S. Jahromi and R. Orús, *Universal tensor-network algorithm for any infinite lattice*, *Phys. Rev. B* **99**, 195105 (2019), doi:[10.1103/PhysRevB.99.195105](https://doi.org/10.1103/PhysRevB.99.195105).
- [122] M. P. A. Fisher, P. B. Weichman, G. Grinstein and D. S. Fisher, *Boson localization and the superfluid-insulator transition*, *Phys. Rev. B* **40**, 546 (1989), doi:[10.1103/PhysRevB.40.546](https://doi.org/10.1103/PhysRevB.40.546).
- [123] C. N. Yang, *Concept of Off-Diagonal Long-Range Order and the Quantum Phases of Liquid He and of Superconductors*, *Rev. Mod. Phys.* **34**, 694 (1962), doi:[10.1103/RevModPhys.34.694](https://doi.org/10.1103/RevModPhys.34.694).
- [124] M. P. Qin, Q. N. Chen, Z. Y. Xie, J. Chen, J. F. Yu, H. H. Zhao, B. Normand and T. Xiang, *Partial long-range order in antiferromagnetic Potts models*, *Phys. Rev. B* **90**, 144424 (2014), doi:[10.1103/PhysRevB.90.144424](https://doi.org/10.1103/PhysRevB.90.144424).
- [125] J. F. Yu, Z. Y. Xie, Y. Meurice, Y. Liu, A. Denblyker, H. Zou, M. P. Qin, J. Chen and T. Xiang, *Tensor renormalization group study of classical XY model on the square lattice*, *Phys. Rev. E* **89**, 013308 (2014), doi:[10.1103/PhysRevE.89.013308](https://doi.org/10.1103/PhysRevE.89.013308).
- [126] L. Vanderstraeten, B. Vanhecke, A. M. Läuchli and F. Verstraete, *Approaching the Kosterlitz-Thouless transition for the classical XY model with tensor networks*, *Phys. Rev. E* **100**, 062136 (2019), doi:[10.1103/PhysRevE.100.062136](https://doi.org/10.1103/PhysRevE.100.062136).
- [127] N. D. Mermin and H. Wagner, *Absence of Ferromagnetism or Antiferromagnetism in One- or Two-Dimensional Isotropic Heisenberg Models*, *Phys. Rev. Lett.* **17**, 1133 (1966), doi:[10.1103/PhysRevLett.17.1133](https://doi.org/10.1103/PhysRevLett.17.1133).
- [128] H. E. Stanley and T. A. Kaplan, *Possibility of a Phase Transition for the Two-Dimensional Heisenberg Model*, *Phys. Rev. Lett.* **17**, 913 (1966), doi:[10.1103/PhysRevLett.17.913](https://doi.org/10.1103/PhysRevLett.17.913).
- [129] H. E. Stanley and T. A. Kaplan, *On the Possible Phase Transition for Two-Dimensional Heisenberg Models*, *Journal of Applied Physics* **38**(3), 975 (1967), doi:[10.1063/1.1709708](https://doi.org/10.1063/1.1709708).

- [130] V. Berezinsky, *Destruction of long range order in one-dimensional and two-dimensional systems having a continuous symmetry group. I. Classical systems*, Sov. Phys. JETP **32**, 493 (1971).
- [131] J. M. Kosterlitz and D. J. Thouless, *Ordering, metastability and phase transitions in two-dimensional systems*, Journal of Physics C: Solid State Physics **6**(7), 1181 (1973), doi:[10.1088/0022-3719/6/7/010](https://doi.org/10.1088/0022-3719/6/7/010).
- [132] R. G. Brown and M. Ciftan, *The 2d/3d classical heisenberg ferromagnet*, In D. P. Landau, K. K. Mon and H.-B. Schüttler, eds., *Computer Simulation Studies in Condensed-Matter Physics V*, pp. 150–154. Springer Berlin Heidelberg, ISBN 978-3-642-78083-7 (1993).
- [133] Y. Tomita, *Finite-size scaling analysis of pseudocritical region in two-dimensional continuous-spin systems*, Phys. Rev. E **90**, 032109 (2014), doi:[10.1103/PhysRevE.90.032109](https://doi.org/10.1103/PhysRevE.90.032109).
- [134] O. Kapikranian, B. Berche and Y. Holovatch, *Quasi-long-range ordering in a finite-size 2d classical heisenberg model*, Journal of Physics A: Mathematical and Theoretical **40**(14), 3741 (2007), doi:[10.1088/1751-8113/40/14/001](https://doi.org/10.1088/1751-8113/40/14/001).
- [135] T. Nakamura, *Statistical Theory of Hindered Rotation in Molecular Crystals*, Journal of the Physical Society of Japan **7**(3), 264 (1952), doi:[10.1143/JPSJ.7.264](https://doi.org/10.1143/JPSJ.7.264).
- [136] M. E. Fisher, *Magnetism in One-Dimensional Systems - The Heisenberg Model for Infinite Spin*, American Journal of Physics **32**(5), 343 (1964), doi:[10.1119/1.1970340](https://doi.org/10.1119/1.1970340).
- [137] G. S. Joyce, *Classical Heisenberg Model*, Phys. Rev. **155**, 478 (1967), doi:[10.1103/PhysRev.155.478](https://doi.org/10.1103/PhysRev.155.478).
- [138] P. van Dongen, *Statistische Physik*, Springer Berlin Heidelberg, doi:[10.1007/978-3-662-55500-2](https://doi.org/10.1007/978-3-662-55500-2) (2017).
- [139] M. Bañuls, R. Blatt, J. Catani, A. Celi, J. Cirac, M. Dalmonte, L. Fallani, K. Jansen, M. Lewenstein, S. Montangero, C. Muschik, B. Reznik *et al.*, *Simulating Lattice Gauge Theories within Quantum Technologies* (2019), [arXiv: 1911.00003](https://arxiv.org/abs/1911.00003).
- [140] M. T. Fishman, L. Vanderstraeten, V. Zauner-Stauber, J. Haegeman and F. Verstraete, *Faster methods for contracting infinite two-dimensional tensor networks*, Phys. Rev. B **98**, 235148 (2018), doi:[10.1103/PhysRevB.98.235148](https://doi.org/10.1103/PhysRevB.98.235148).
- [141] J. Hubbard, *Electron correlations in narrow energy bands*, Proceedings of the Royal Society of London. Series A. Mathematical and Physical Sciences **276**(1365), 238 (1963), doi:[10.1098/rspa.1963.0204](https://doi.org/10.1098/rspa.1963.0204).
- [142] C. Lacroix, P. Mendels and F. Mila, eds., *Introduction to Frustrated Magnetism*, Springer Berlin Heidelberg, doi:[10.1007/978-3-642-10589-0](https://doi.org/10.1007/978-3-642-10589-0) (2011).
- [143] P. Corboz, T. M. Rice and M. Troyer, *Competing States in the  $t$ - $J$  Model: Uniform  $d$ -Wave State versus Stripe State*, Phys. Rev. Lett. **113**, 046402 (2014), doi:[10.1103/PhysRevLett.113.046402](https://doi.org/10.1103/PhysRevLett.113.046402).